CERN Yellow Reports: Monographs CERN-2025-007

The DEFT facility

An accelerator for very-high-energy electron FLASH radiotherapy

Technical design report

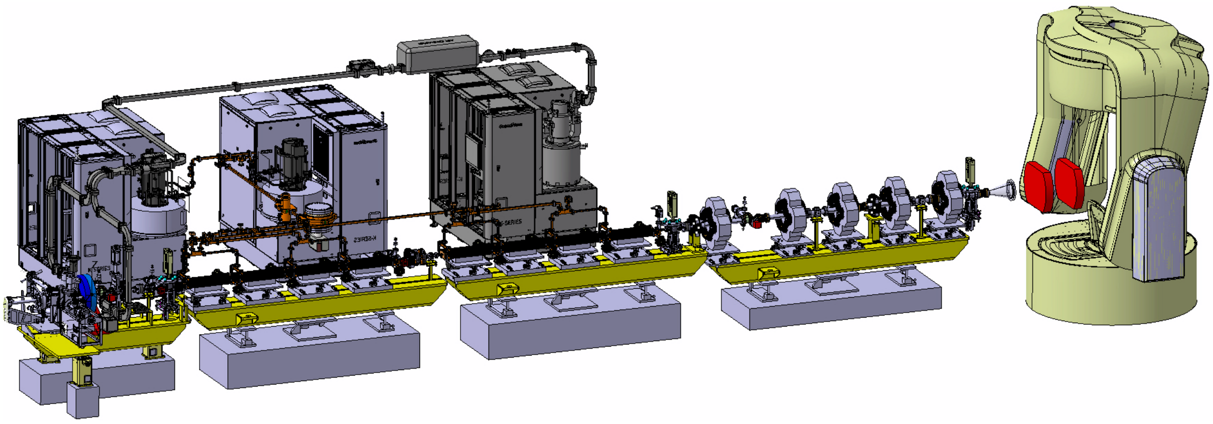

Maria Elena Angoletta, Jeremie Bauche, Olivier Brunner, Sergio Calatroni, Roberto Corsini, Jean-Marc Cravero, Steffen Doebert, Jose Antonio Ferreira Somoza, Maria Carmen Giordano, Eduardo Granados, Alexej Grudiev (Corresp. Ed.), Raul Key, Andrea Latina (Corresp. Ed.), Thibaut Lefevre, Stephane Burger, Michal Krupa, Alexander Malyzhenkov, Pablo Martinez Reviriego, Carlo Rossi, Igor Syratchev, Ping Wang, Markus Widorski, Benjamin Woolley, and Walter Wuensch

CERN

CERN Yellow Reports: Monographs
Published by CERN, CH-1211 Geneva 23, Switzerland

ISBN 978-92-9083-703-9 (paperback)
ISBN 978-92-9083-704-6 (PDF)
ISSN 2519-8068 (Print)
ISSN 2519-8076 (Online)
DOI `https://doi.org/10.23731/CYRM-2025-007`

This volume should be cited as:

The DEFT facility: An accelerator for very-high-energy electron FLASH radiotherapy—Technical design report
Maria Elena Angoletta *et al.*,
CERN Yellow Reports: Monographs, CERN-2025-007 (CERN, Geneva, 2025),
DOI 10.23731/CYRM-2025-007.

Corresponding editors: Alexej.Grudiev@cern.ch and Andrea.Latina@cern.ch.

Accepted in Sep. 2025, by the CERN Reports Editorial Board (contact Carlos.Lourenco@cern.ch).

Published by the CERN Scientific Information Service (contact Jens.Vigen@cern.ch).

Indexed in the CERN Document Server and in INSPIRE.

Published Open Access to permit its wide dissemination, as knowledge transfer is an integral part of the mission of CERN.

Abstract

The design of an accelerator facility capable of delivering FLASH radiotherapy to large, deep-seated tumours is presented. The facility, called DEFT (Deep Electron Flash Therapy), produces 140 MeV electrons so is capable of treating tumours located at depths up to 25 cm. It is capable of delivering sufficient electron intensity to treat tumours up to 20 cm in diameter, in less than 0.1 s with doses up to 20 to 30 Gy. The full facility, including electron source, accelerator and beam delivery system are described along with extensive performance simulations.

Contents

Chapter 1

Introduction

Radiation therapy (RT) is one of the main methods used in treating cancer, together with surgery, chemotherapy and immunotherapy. The workhorse of modern external beam RT is MV photo beam therapy. In addition, there is particle-based therapy, which includes protons, light ions, and low energy electrons. All of these treatment modalities must confront the conflicting requirement of sparing the healthy tissues that surround the tumour while maximizing the effectiveness in tumour control. This requirement has pushed RT technologies toward fractionated dose administration together with highly conformal dose delivery systems.

While such modern high-precision RT treatments can provide acceptable clinical outcomes with limited side effects for many patients, there is still a clinical care gap and a resulting clinical need for numerous cancer patients. For such cases, hope is being generated by the observation that doses delivered at ultra-high dose rates (UHDR, average dose rate $\gtrsim$50 Gy/s) can produce a sparing effect on healthy tissues while maintaining the effectiveness on tumour cells compared with irradiations delivered at conventional dose rates (average dose rate $\sim$0.05 Gy/s) [1, 2]. This increase of the therapeutic index by the ultra-fast dose delivery, commonly referred to as "FLASH effect", was initially observed in the 1970s, first proposed in 2014 and has since then been independently confirmed in numerous studies using different radiation modalities and preclinical models.

These initial investigations have all used low energy electrons, which limits applicability to near-surface treatment. In order to extend FLASH therapy to large, deep-seated tumours in humans, Very High Energy Electrons, roughly defined as having energies above 100 MV/m, are a natural choice since they penetrate deep enough into the body and intense enough electron beams can now be produced in relatively compact accelerator complexes. In particular, the use of high-gradient RF technology developed at CERN for the realization of the high-energy linear collider CLIC appeared to be the logical choice for designing a compact FLASH-RT device capable of producing penetrating very high-energy electron (VHEE, 100–250 MeV) beams at UHDR to treat deep-seated tumours. In addition, supporting experiments are being carried out at the CERN facility CLEAR in relation to the creation and detection of UHDR and to the characterization of the FLASH effect.

A comprehensive design of an accelerator complex optimized for delivering FLASH radiation therapy has been carried out by a team at CERN. This report describes the Deep Electron Flash Therapy (DEFT) accelerator complex.

The DEFT beam facility consists of an injector, a linac and a beam delivery system (BDS). The objectives that drive the design of the beam facility are the need to provide an electron beam, with an energy of 140 MeV, in a compact facility, with a high delivered total charge, of the order of a few micro-Coulombs, over a large and well-controlled field that meets clinical requirements, with a diameter of at least 20 cm, within FLASH timescales. These objectives can be achieved in a novel and high-performance DEFT facility in part by adopting high-gradient linac technology developed in the framework of the CLIC project [3]. CLIC targets TeV-range electron-positron collisions and requires a collider several kilometres long, which is clearly at a far larger scale than a FLASH facility but shares with FLASH the requirements for high accelerating gradients, high instantaneous beam current and well-controlled beam characteristics. The CLIC project has invested significant resources over the past two decades in developing high-gradient and high-current linac technologies and has successfully carried out extensive testing of prototype systems and components. The CLIC project has also developed an extensive beam dynamics simulation capability, which has been benchmarked against experiments carried out at numerous laboratories. Much of this technology and simulation capability is directly applicable to a FLASH facility, and a highly compelling design of a FLASH accelerator has been produced. Accelerator parameter choices for this FLASH accelerator are largely supported by experimental results or extensive studies within the CLIC project and the larger electron linac community.

This chapter describes the basic features of the beam facility, its underlying motivations, and its connection to developments in the CLIC study. A baseline design has been elaborated, for which all key elements have been specified, and a consistent set of simulations has been carried out.

The linac consists of X-band, 12 GHz, accelerating structures operating at an accelerating gradient of 30 MV/m. A high accelerating gradient is important to minimize the size of the facility. Gradient of 30 MV/m is high compared to the typical 15 MV/m range of most current electron linacs, but is quite conservative compared to the 100 MV/m achieved in CLIC prototypes. A higher gradient requires more RF power from the klystron and modulator systems, which will be described below, and thus increases their cost, but results in a shorter linac and smaller facility and which lower bunker and building costs. The optimized total cost has a broad minimum around 30 MV/m.

The operating frequency of 12 GHz is the same as the main linac of CLIC and is thus a natural choice for this facility. The relatively high frequency (most electron linacs operate at 3 GHz) has the advantage that the stored energy needed to establish a specific gradient is lower, thus lowering the RF power system cost. Higher frequencies, however, require tighter mechanical tolerances in components; consequently, until now, the use of X-band has been limited. The CLIC project has been instrumental in driving the development of X-band technology and its commercialization, and is at the centre of an international collaboration developing and adopting the technology. The collaboration includes a steadily increasing number of advanced accelerator projects, including CompactLight (a free electron laser) [4], Smart*Light (an Inverse Compton Scattering X-ray source), POLARIX (short-bunch diagnostic)[5], in addition to CLIC and FLASH-eRT. The CLIC and other projects worldwide have now received over twenty X-band klystrons from commercial suppliers, so the commercialization of X-band is well underway.

The focus at CERN in developing high-gradient X-band systems over the past few years has been building and operating four klystron-driven X-band test stands, known as the XBoxes. The XBoxes have been built to operate and validate all the major RF parts of an X-band linac, including RF power sources, pulse compressors, waveguide systems and accelerating structures. The test stands are also used to study the fundamental performance limitations and to develop optimized operational algorithms. Together, the XBoxes have been operated for over 50 000 hours. The XBoxes are quite similar in layout and composition to the linac units, which are foreseen for DEFT and provide the basis for estimations of performance and cost.

The linac for DEFT consists of eight 0.6 m long accelerating structures which are driven by two klystron/modulator units and an RF pulse compressor. The beam gains energy in the accelerating structures through the synchronization of the electromagnetic (RF) wave travelling through the structures and the subsequent conversion of electromagnetic energy into increased kinetic energy of the beam. There are also important interactions of the beam with the accelerating structure that can lead to beam instabilities and loss of beam quality. The beam parameters and accelerating design and optimization process are highly complex and determine, to a large extent, the overall performance achievable in the facility. Significant resources in the CLIC study have been dedicated to the development of design tools and experimental validation of this subject. To highlight one aspect, the objective to treat large tumours requires accelerating a high total charge in FLASH timescales. The result is that the instantaneous current in the linac is approximately one Amp, which is very close to the current in the CLIC main linac. Maintaining beam stability requires accelerating structures with higher-order mode suppression, and over twenty such structures have been tested for extended periods in the XBoxes.

After acceleration, the beam is manipulated in the beam delivery system. A magnetic lattice controls the transverse beam size and uniformity to produce the desired radiation dose at the patient. The electron beam uniformities derived in this section are calculated by propagating the beam forward through vacuum to the isocenter. The effects of beam scattering by the output vacuum window, air and patient are considered in the medical physics section of this report. The lattice of the beam delivery system is composed of conventional normal conducting magnets with quite conservative specifications. The lattice optics have been optimized using the simulation tools developed for beam dynamics simulation in CLIC.

The electron beam is generated in a laser-driven photoinjector. This type of electron source is used in numerous accelerators around the world, for example, in X-ray free electron lasers, although DEFT shares with CLIC the requirement of a very high current. CERN has studied different injector technologies and built and operated numerous high-current photoinjectors in successive generations of beam test facilities: CTF2, CTF3, PHIN and CLEAR. The photoinjector for DEFT is based on the measured characteristics and performances of these facilities, optimized using well understood and benchmarked simulation tools. The required beam parameters are achievable.

The components, systems and issues will be elaborated in the sections below. The components and systems will be described in detail, and motivations for specific design choices will be given. The simulation tools used to address critical issues will be described, results presented, and conclusions drawn. Examples of existing components and systems are given, as well as test and operational results which support simulation results. Alternatives and variants will be described where relevant.

Chapter 2

Beam parameters and design strategy

1 Beam parameters and machine layout

The overall layout of the beam facility, including electron source, linac and beam delivery system (BDS), is illustrated in Fig. 2.1. During one treatment session, up to 40 bunch trains are created in a photoinjector RF gun, accelerated in a short X-band linac up to 140 MeV, then transported through a magnetic system that delivers the electron beams to the target within a time of less than 100 ms.

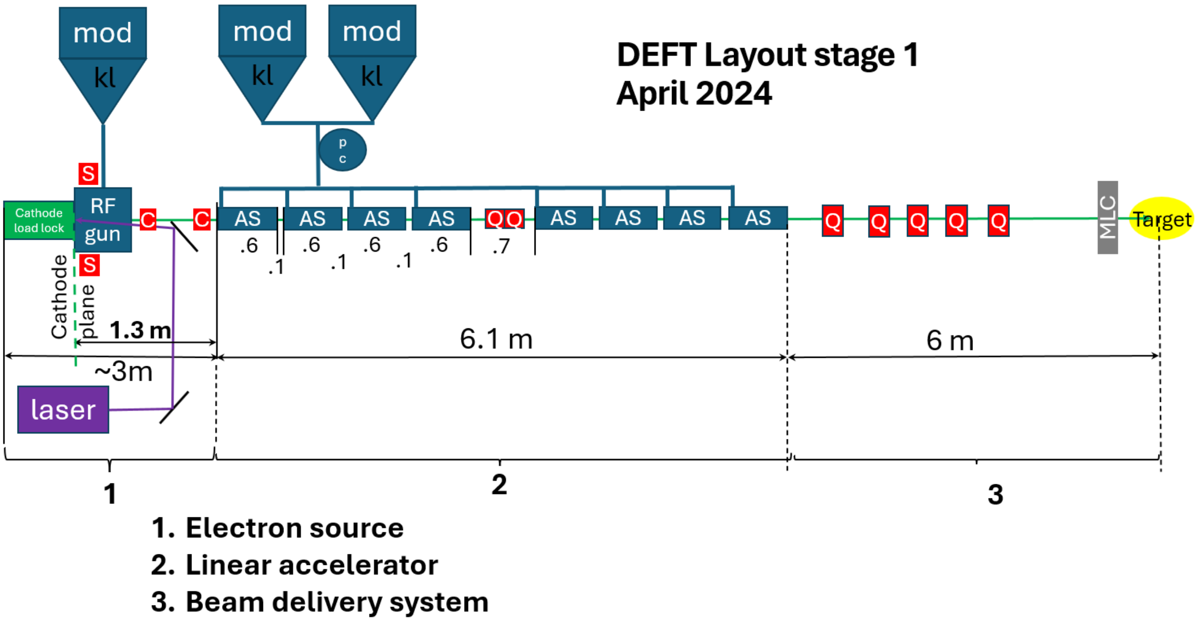

Figure 2.1: Overall layout of the accelerator and the beam delivery system.

The electron source consists of an S-band photocathode gun, immersed in a solenoidal magnetic field, that produces trains of up to 507 electron bunches with a nominal charge of 190 pC per bunch and energy of about 7 MeV. The cathode is hit with a laser with a spot size radius of 0.8 mm for an RMS emission time of 1 ps, corresponding to a bunch length of about 300 μm. The phase and the amplitude of the RF in the gun, as well as the amplitude of the solenoid field, are tuned to prepare the beam for transport through the linac optimally.

The linac starts 1.3 m downstream of the cathode and consists of two groups of four 60 cm-long X-band accelerating structures placed on a girder and spaced by 10 cm, which we call RF units later on. Two combined RF power sources feed the two RF units. The RF units have 70 cm drift space in between, where two quadrupoles are placed. The first RF unit fully relies on RF focusing provided by the strong accelerating field at the entrance of each structure. The RF focusing is sufficient for transverse stability and transport of the beam in the first RF unit, where beam energy is relatively low, from 7 to 75 MeV. In the second RF unit, the RF focusing is not strong enough and must be complemented by the focusing provided by the two quadrupoles placed upstream.

The primary function of the BDS is to transport the beam to the target and provide the required transverse beam distribution. It consists of a beam line composed of individually powered conventional electromagnets. The beam is transported through a beam line featuring five quadrupoles. At the end of the beam lines, a multi-leaf collimator (MLC) is used to provide the best possible conformity of the beams to the shape of the target. The MLC provides the important safety feature of ensuring that the patient is not accidentally irradiated away from the target region.

2 Beam dynamics design strategy

In the DEFT facility, a high-intensity electron beam is accelerated from the cathode to ultra-relativistic energies in a short distance of just a few metres. The unconventional requirements for beam uniformity and large fields at the patient, as well as the simultaneous presence of collective effects, including space charge, beam loading, and wakefields, render conventional concepts such as emittance and Twiss parameters ineffective.

The Twiss formalism comes from the second-order moments of the phase-space distribution, such as the sigma matrix, the rms ellipse, or the emittance. A description using Twiss parameters is therefore *complete* only for Gaussian beams, which are fully described by their second-order moments [6]. If the beam is not Gaussian, second moments alone do not capture the full distribution: two very different distributions can have the same rms emittance and Twiss parameters. As it will be shown in the following paragraphs, features such as uniformity are associated with higher moments than the second ones and are not encoded in the sigma matrix. The Twiss parameters are therefore unsuitable for assessing and treating uniformity.

For these reasons, the DEFT design was based on realistic multi-particle beam tracking and a numerical assessment of uniformity. In this fashion, the mentioned collective effects were incorporated by design. The distinctive nature and challenges of the DEFT project have led to the development of an in-house beam dynamics code, RF-Track [7], as the design tool for the facility.

RF-Track is a versatile particle tracking code developed by one of the authors of this document. Initially created for the simulation of hadron medical linacs, it was subsequently developed to provide the functionalities required by the DEFT project, making it the optimal choice for DEFT. Its most notable features are as follows:

1. It implements space-charge forces, which are crucial to accurate tracking in the injector.
2. It implements wakefield and beam-loading effects, which are crucial for assessing the beam evolution along the linac.
3. It implements single-bunch and multi-bunch effects, which is crucial for assessing beam stability in the linac.
4. It tracks particles through conventional elements, such as quadrupoles and sector bends, and through 1D, 2D, or 3D field maps of static and oscillating electromagnetic fields. This is essential for accurately describing the particles' motion in the electron gun field, the solenoid, and the linac accelerator structures.
5. It implements particle generation in photocathodes using pseudo-random or quasi-random number generators.
6. It implements particle scattering through materials, which allows for assessing the properties of the beam travelling through air and water.
7. It implements orbit correction algorithms, which enable testing beam-based alignment procedures and realistic operational scenarios.

2.1 Field uniformity

Crucial to the successful design of the DEFT facility was the capability to quantify the uniformity of the distribution of particles at the patient location. A measure of uniformity was found in the fourth standardised moment of a distribution, called "kurtosis". Kurtosis measures the narrowness of the tails of a distribution. It is defined as

$$\text{Kurtosis}\left[X\right] = E\left[\left(\frac{X-\mu}{\sigma}\right)^4\right] = \frac{E\left[(X-\mu)^4\right]}{\left(E\left[(X-\mu)^2\right]\right)^2} = \frac{\mu_4}{\sigma^4} \quad , \tag{2.1}$$

where μ is the average, μ_4 is the fourth central moment, and σ is the standard deviation of the distribution. Figure 2.2 shows the kurtosis of different probability density functions. In the red box, two cases of interest: "U", which is the 1D uniform distribution, corresponding to kurtosis of 1.8; and "W", which is the "Wigner semicircle distribution", corresponding to kurtosis of 2. The Wigner semicircle distribution describes the projection of a uniform disc over a line. Figure 2.3 shows an example of the two distributions based on the simulation of a particle beam at DEFT.

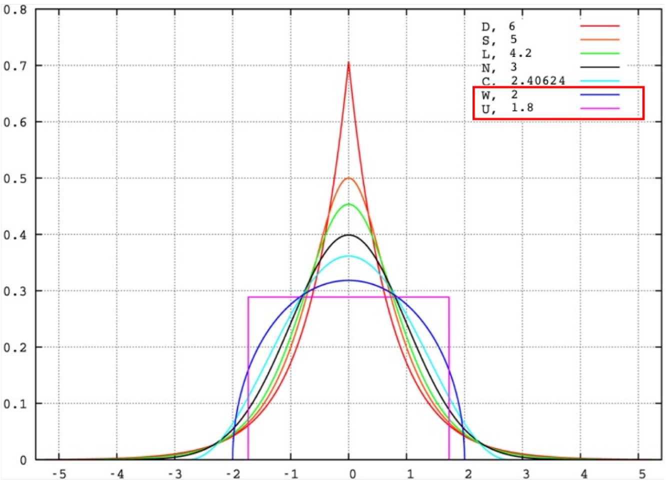

Figure 2.2: Kurtosis of different probability density functions for selected distributions with mean 0, variance 1. The two cases of interest are in the red box. [Image © Wikipedia.]

Kurtosis is an estimator readily available through common numeric computing environments, such as Octave and Python, and it became a crucial quantity in designing the DEFT injector and the linac optics. However, kurtosis is quite sensitive to the distribution's tails and has proved inaccurate in achieving and assessing the target beam quality at the patient location. Therefore, we elaborated a more sophisticated and robust definition of "uniformity" based on the concepts of percentile and cumulative distribution function (CDF). In statistics, a *k*-th percentile is a score below which a given percentage *k* of items falls. For example, the 50th percentile of a distribution is the median, whereas the 100th percentile corresponds to its maximum value. The curve with all percentiles, from 0th to 100th, is the inverse of the CDF. We used the Euclidean difference between the inverse CDF of a given distribution and the inverse CDF of an ideal uniform distribution as a refined measure of uniformity. Uniformity is then evaluated as a χ^2

$$\chi^2 = \sum_{8\text{ angles}} \left\| \text{CDF}\left(\text{Projected } XY\right)^{-1} - \text{CDF}\left(\text{Uniform disc}\right)^{-1} \right\|^2,$$

where $\text{CDF}\left(\ldots\right)^{-1}$ denotes the inverse CDF of a distribution, "Projected XY" is the tracked XY distribution at the patient's location, projected onto a line in the XY plane tilted by a certain angle, and "Uniform disc” is the ideal uniform disc. To sample the distribution over different angles, we sum the contributions of eight directions in the XY plane, from 0° to 180° in steps of 22.5°. The result is that the closer a distribution is to an ideal uniform disc, the smaller the χ^2. Compared to kurtosis, this method allows for a more accurate handling of the tails, as the inverse CDF functions can be arbitrarily truncated to exclude the tails.

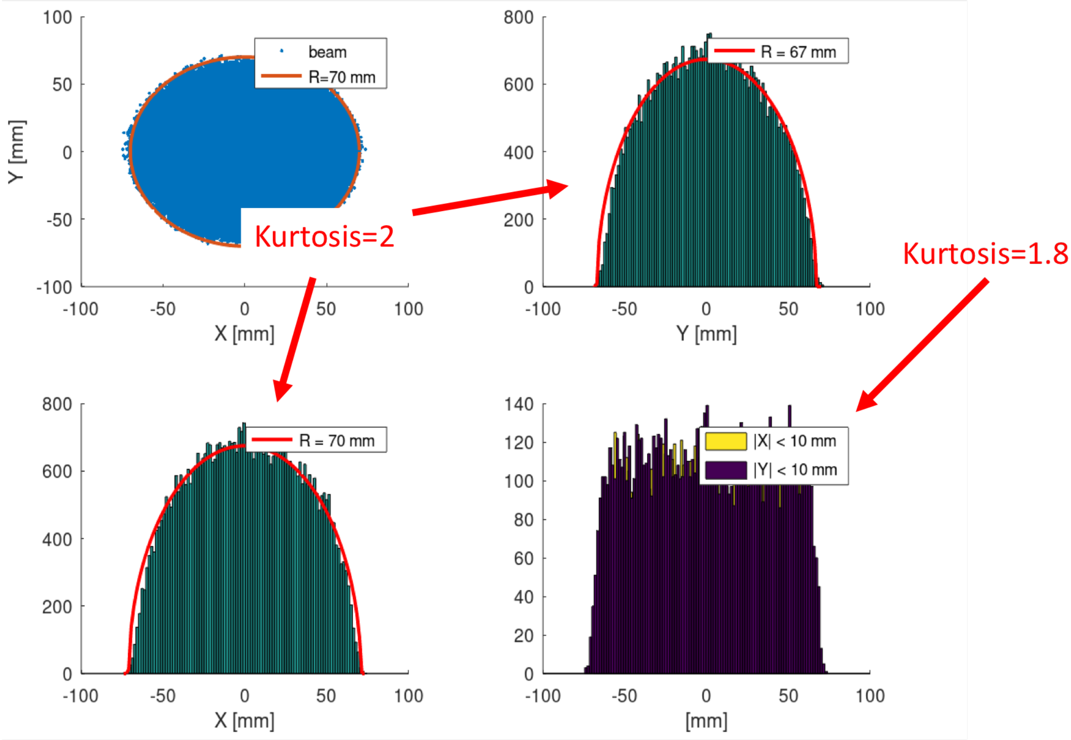

Figure 2.3: The projection of a uniform disc is a Wigner semicircle distribution, with kurtosis = 2. The projection of a uniform distribution has kurtosis = 1.8.

2.2 Stabilising randomness

The impact of statistical noise needed to be reduced to assess uniformity reliably. We used two methods to reduce the noise:

1. Simulating 1 million particles.
2. Using “quasi-random” distributions.

A “quasi-random” distribution is a fully deterministic low-discrepancy sequence of points covering a multi-dimensional space as uniformly as possible.

The first method reduces the statistical error but increases the simulation time. The second, where the particle distribution is created using a quasi-random sequence, is key to ensuring stable results free of statistical errors while enabling faster simulation times. We used the second method to design the optics throughout the machine and the first to compute the final particle distributions for dose-delivery simulations.

2.3 Design strategy

The design strategy is based on four consecutive steps addressing as many key aspects:

Injector and linac optics. Utilise the space-charge force, balanced by the focusing effects of the injector solenoid and the linac optics, to obtain beam uniformity at the linac end. This is achieved with a multi-objective optimisation using the following degrees of freedom: the laser spot size and pulse length at the cathode, the RF gun phase, the solenoid strength, the linac accelerating gradient, and the linac's quadrupole strengths and positions. Beam uniformity at the linac end is assessed as previously described.

Beam stability. Evaluate the impact of short- and long-range wakefields on the beam stability. The impact of wakefields is primarily assessed in terms of transverse beam jitter amplification. Too-large jitter amplification can lead to beam break-up and must be avoided by increasing the linac's quadrupole strength, which in turn compromises the fine balance between the different knobs obtained in the previous step to achieve uniformity. A compromise between beam uniformity and beam stability must be reached.

Beam delivery. The five quadrupoles of the beam delivery line are optimised to transport uniformity from the linac end to the isocentre, fulfilling all beam requirements: 20 cm diameter, circular shape, uniformity, and equal divergence in both horizontal and vertical directions (homothety). The optimisation uses both the strengths and the positions of the quadrupoles as degrees of freedom and includes constraints such as sufficient spacing for accommodating correctors and beam position monitors, as well as the position of the vacuum window.

Robustness. Assess the impact of static elements misalignment and dynamic imperfections, such as jitter, to ensure a robust solution and an effective beam-based correction strategy. Beam-based alignment techniques are tested in simulation under realistic imperfections, and an analysis of the response matrix is performed to identify the number and the position of correctors and beam position monitors required.

These steps are usually performed in the order presented and can be repeated and reiterated until a satisfactory solution is found.

Except for the fact that, in this optimisation, the position of the elements is a degree of freedom and is used to achieve the beam parameters at the patient, the methodology presented here anticipates practical commissioning, operation and tuning procedures for the proposed machine. Indeed, the position where the screens will be installed corresponds to the points where the uniformity point is imposed by the design in the simulation. The operation will consist of assessing and maintaining uniformity at these positions.

Figure 2.4 shows the overall layout of the full DEFT facility from a beam dynamics perspective, including the electron gun, the linac, and the beam delivery system.

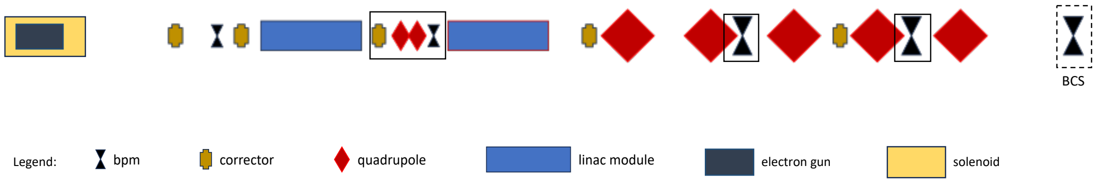

Figure 2.4: Schematic layout of the DEFT facility, from a beam dynamics perspective. The beam goes left to right. The BCS element is a screen located after the vacuum window, providing information for the beam setup and beam-based alignment.

3 Beam dynamics and estimated performance

3.1 Gun section

The main parameters of the photoinjector are summarised in Table 2.1. The injector consists of a 3 GHz 2.5-cell standing-wave structure, operated at 90 MV/m gradient, and a solenoid magnet integrating the primary and bucking coils to provide zero magnetic field at the cathode. The gradient of the RF gun, together with its operating phase and the solenoid magnet, is tuned to provide beam uniformity at the linac entrance, 1.3 m downstream of the cathode.

Table 2.1: Main laser and beam parameters at the cathode and beam's time structure.

Parameter	Symbol	Units	Value
Bunch charge	Q	pC	190
Photon energy	E_{phot}	eV	4.73
Effective work function	Φ_{eff}	eV	3.5
Laser spot size at cathode, rms	σ_x, σ_y	mm	0.8
Laser pulse length, rms	σ_t	ps	1.6
Bunch repetition rate	t_{rep}	GHz	3
Number of bunches per train	n_{b}	-	$\sim$507

Table 2.2 summarises the operational setup of the photoinjector, while Fig. 2.5 shows the uniform transverse beam profile at the linac start.

Table 2.2: Operational parameters of the RF gun.

Parameter	Symbol	Units	Value
RF gradient	E_z	MV/m	90
RF phase	Φ_{RF}	deg	-139.975
Solenoid peak field	B_{sol}	T	0.2197

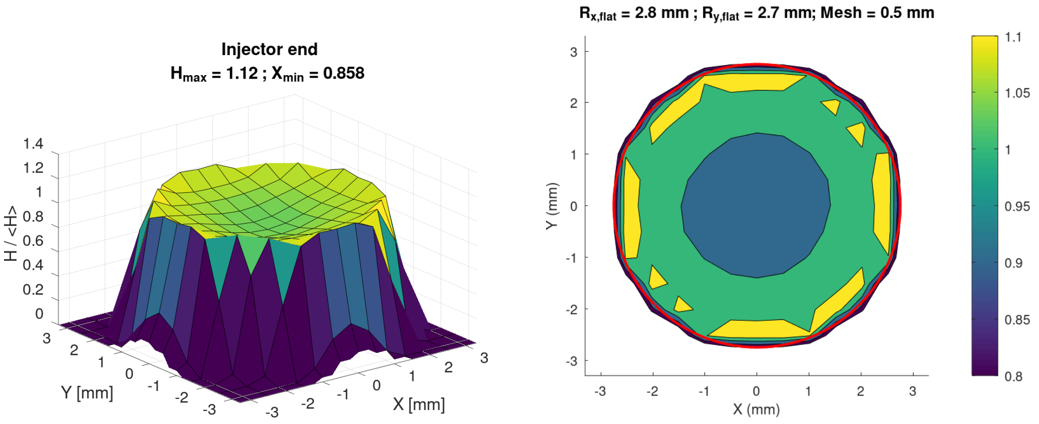

Figure 2.5: Bunch transverse profile (left) and 2D density histogram (right) at longitudinal position S = 1.3 m from the cathode (the linac start), normalised to the average density.

The beam profile evolution along the injector is depicted in Fig. 2.6. The beam envelope, including all particles denoted as $R = 100\,\%$ in the plot, determines the required minimum aperture in the injector part.

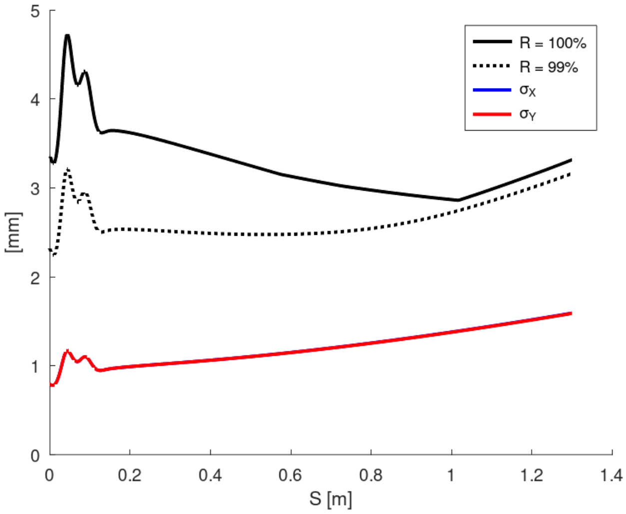

Figure 2.6: Transverse beam profile evolution from the cathode, $S = 0\,\mathrm{m}$, to the main linac entrance, $S = 1.3\,\mathrm{m}$.

The evolution of the transverse beam distribution from the cathode surface to the end of the injector section is visualised in Fig. 2.7. Initially, the Gaussian beam profile originated by a corresponding shape of the laser at the photocathode becomes uniform before the end of the injector, 0.6 m. Such an evolution is possible due to a tailored combination of the repulsive Coulomb interaction between the electrons (transverse space charge effects), the RF focusing in the standing wave structure, and the magnetic focusing from the solenoid. First uniformity point at 0.6 m is an ideal location for the transverse profile monitor to measure and control the uniformity of the electron beam in the injector. If location of the monitor is upstream or downstream from 0.6 m due to integration requirements, the uniformity point can be shifted precisely to its location by tuning the magnetic field of the solenoid according to the values predicted with numerical simulations.

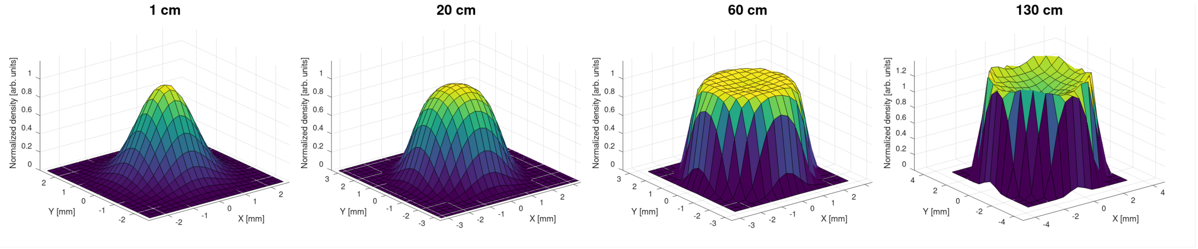

Figure 2.7: Bunch transverse profile evolution in the injector section.

As shown in Fig. 2.5, the beam at the injector end, 1.3 m, is not uniform. Here, uniformity would be desirable; however, more stringent requirements must be met. Firstly, the bunch must enter the first structure's iris comfortably to minimise the impact of short-range transverse wakefields and nonlinearities. A maximum beam radius of 3.2 mm is imposed as a hard constraint of the injector+linac optimisation. Secondly, the beam must enter the structure as a diverging beam to counteract the strong RF focusing at the structure entrance. The beam's transverse uniformity is achieved at the linac end as the primary objective of the optimisation process.

Two correctors and one beam position monitor are placed between the gun's solenoid and the linac start for beam-based alignment purposes.

3.2 Linac sections

The linac consists of two sections separated by a 70 cm gap where a quadrupole doublet focuses the beam, ensuring beam stability and providing uniformity at the screen downstream of the linac. The two linac sections comprise four X-band structures each, spaced 10 cm from each other. A pulse compressor feeds the eight accelerating structures by combining the output of two klystrons to increase the peak power. A single klystron can power four structures in each section. In the gap between the two linac modules, a corrector steerer magnet precedes the quadrupole doublet, and a beam position monitor follows it for beam-based alignment procedures.

The linac is conceived to accelerate the beam up to 140 MeV. Lower operating beam energies are also easily achievable. In this case, properly adjusting the magnet settings along the machine would be essential to recover the required uniformity at the beam field size at the patient location.

All linac structures are operated on-crest with a fixed gradient; see Table 2.3. The RF phase is one of the degrees of freedom utilised to achieve beam uniformity in the XY-plane at the linac end, together with the quadrupole doublet's strength and position. The optimum corresponds to on-crest acceleration.

The quadrupole parameters relevant to beam dynamics are summarised in Table 2.4. Figures 2.8 and 2.9 show the beam longitudinal momentum and the transverse beam profiles along the linac for the target beam energy of 140 MeV.

Table 2.3: Setup of the RF structures in the linac.

Parameter	**Symbol**	**Units**	**Value**
Linac phase	Φ_{RF}	deg	0.0
Linac unloaded avg. gradient	E_z	MV/m	34.4 (96.3% max. field)

Table 2.4: Linac quadrupole doublet parameters. The total length of this section is 70 cm, corresponding to the distance between the two linac modules.

Parameter	**Symbol**	**Units**	**Value**
QA gradient	G_A	T/m	14.36
QB gradient	G_B	T/m	-14.53
Length	L	cm	4.5
Aperture radius	a	mm	6
Distance 4th structure to QA	$L1$	cm	37
Distance from QA to QB	$L2$	cm	4
Distance from QB to 5th structure	$L3$	cm	20

3.2.1 Single-bunch effects

Short-range wakefields in the X-band structures introduce head-to-tail effects within the bunch. Longitudinally, they introduce correlated energy spread, usually utilised to compensate for the RF-induced energy spread. Transversely, they produce a head-to-tail deflection correlated with the beam offset in the structure, which harms the bunch, defocusing and kicking it out of its trajectory.

In our simulations and design optimisation, we used a widely adopted numerical model to describe the short-range wakefield effects [8]. This model computes the Wakefield function based on three structure parameters: a, the iris aperture radius in meters; l, the cell length in meters; and g, the gap length in meters. The parameters (a, g, l) of the DEFT X-band structure are summarised in Table 2.5, and displayed in Fig. 2.10.

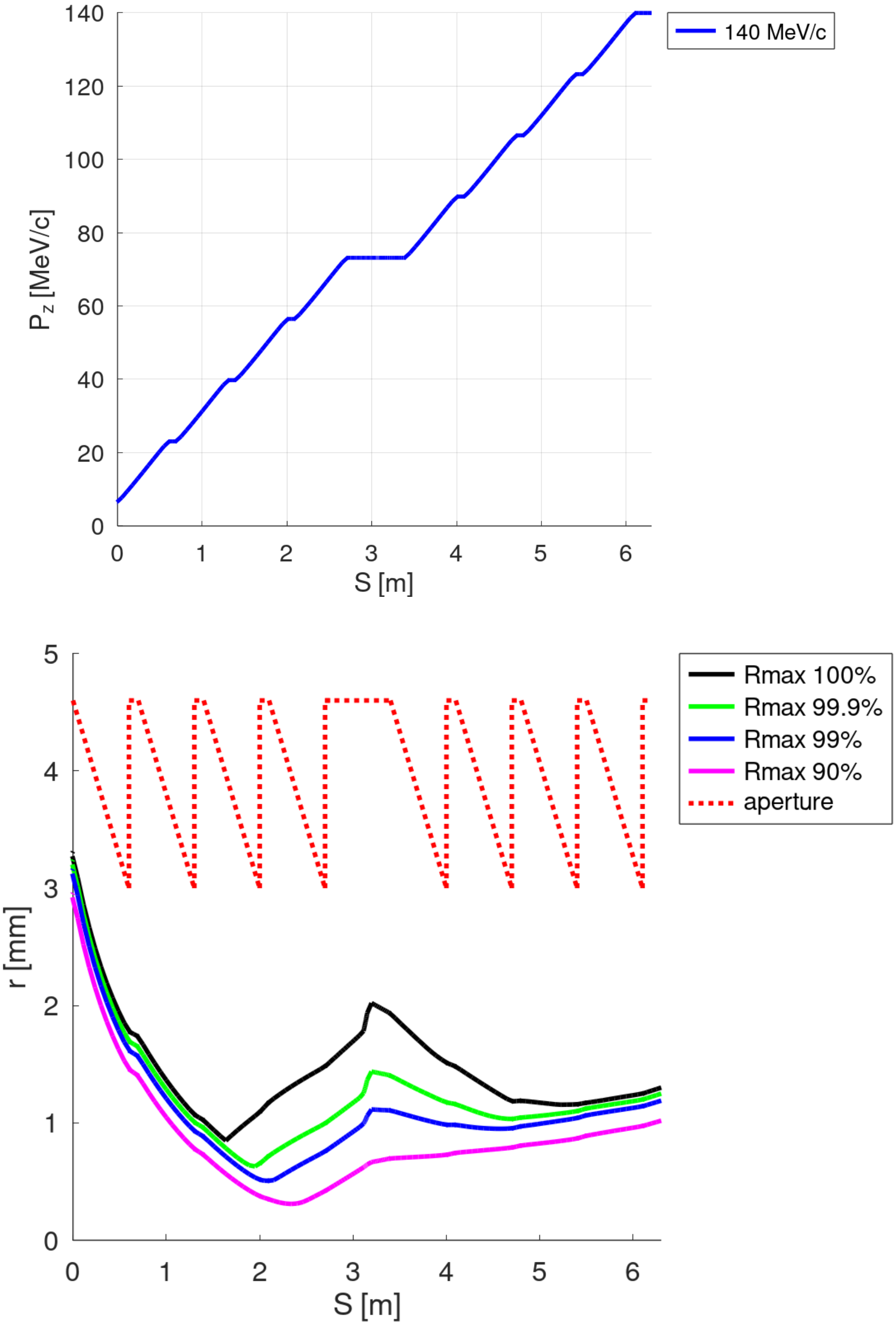

Figure 2.8: The average longitudinal momentum of the bunches along the linac for the three energies (top). The curved momentum profile, shown at high energy, is due to beam-loading effects. Bunch profile along the linac, including the envelope at different percentiles (bottom).

In the presence of an incoming transverse beam jitter, the transverse short-range wakefields amplify the jitter-induced betatron oscillation, deflecting the beam off-axis further and increasing the amplitude of the oscillation. The ratio between the oscillation amplitude at the linac entrance and the amplitude at the linac end is called the “amplification factor”. We designed the RF structures and the linac optics to keep it below 1.2, that is, less than 20% amplitude increase.

A convenient technique to evaluate the amplification factor is through the “action” variable, as the “action” gauges an oscillation amplitude in the phase space. Using the beam, one paints an ellipse in the

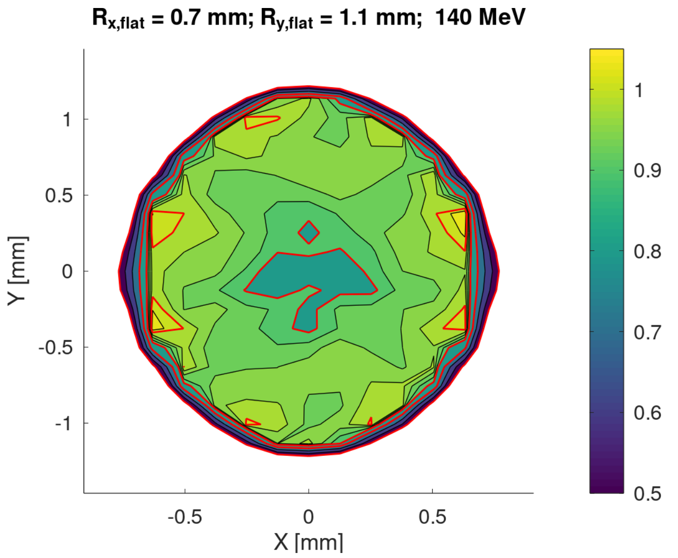

$R_{x,flat}$ = 0.7 mm; $R_{y,flat}$ = 1.1 mm; 140 MeV

Figure 2.9: Bunch transverse profile on the screen at the linac end. The average bunch energy is 140 MeV.

Table 2.5: The X-band cell parameters.

Parameter	Symbol	Units	First cell	Last cell
Iris aperture radius	a	mm	4.6	3.0
Gap length	g	mm	6.83	
Cell length	l	mm	10.41	

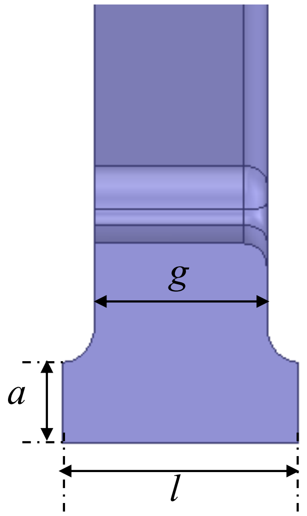

Figure 2.10: Pictorial representation of the RF accelerating structure's cell parameters: a, iris aperture radius; g, gap length; and l, cell length.

phase space at injection and then measures the variation of the ellipse's area through the linac. The area of the ellipse in the phase space is the "action". The jitter amplification factor, JA, is the square root of the ratio between the “action” at the linac end and the “action” at the linac start,

$$\mathrm{JA} = \sqrt{\frac{A_{\text{final}}}{A_{\text{initial}}}}.$$

For oscillations well within the beam pipe aperture, this quantity is independent of the oscillation amplitude, providing a robust and general indicator of beam stability.

In a lattice with only linear elements, the “action” is preserved throughout the system. Nevertheless, the “action” increases with wakefield and nonlinear effects. Figure 2.11 shows an example of “action” evolution along the linac with and without wakefields. The focusing effect of the quadrupole doublet in the middle of the linac counteracts such an amplification. Figure 2.12 shows the amplification factor at the linac end as a function of the quadrupole doublet’s gradient. Figure 2.13 shows the amplification factor at the linac end as a function of the average iris aperture in the RF structures.

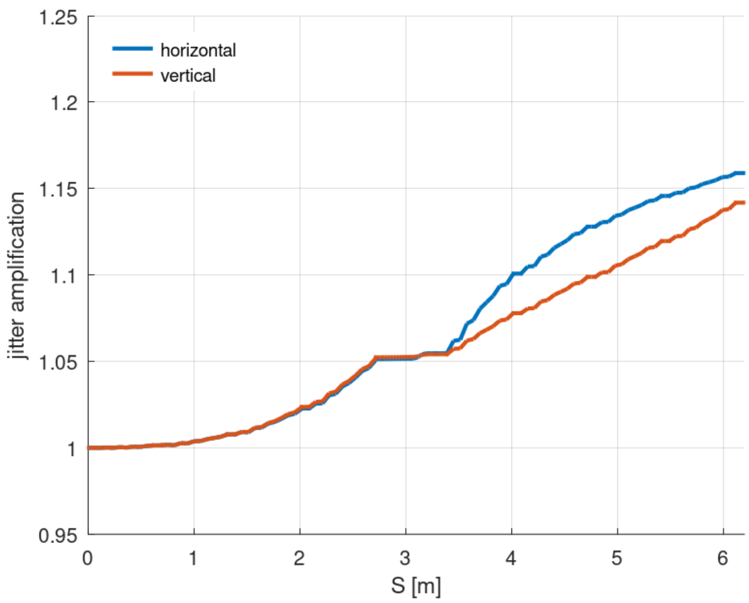

Figure 2.11: Jitter amplification factor along the linac. This factor grows where transverse short-range wakefields are strong. The flat part in the middle of the linac corresponds to the quadrupole doublet.

3.2.2 Multi-bunch effects

The excitation of high-order modes by bunches passing off-axis through an accelerating structure can persist for sufficient time to deflect the subsequent bunches along the train and induce transverse oscillations, leading to jitter amplification or even beam breakup. For this reason, the higher-order modes must be damped and reduced to be harmless.

From a beam dynamics viewpoint, the high-order modes are modelled as the summation of damped oscillations computed with electromagnetic 3D solvers:

$$w_{\perp}(s) = \sum_{i\,\in\,\text{all modes}} A_i\, e^{\frac{\pi s}{Q_i \lambda_i}}\, \sin\left(-2\pi \frac{s}{\lambda_i}\right). \qquad [\mathrm{V/pC/m^2}] \tag{2.2}$$

Three quantities describe each i-th mode: A_i, the amplitude in V/pC/m/mm; Q_i, the damping factor; and λ_i, the wavelength in metres of the mode. The independent variable s is the distance in metres from the

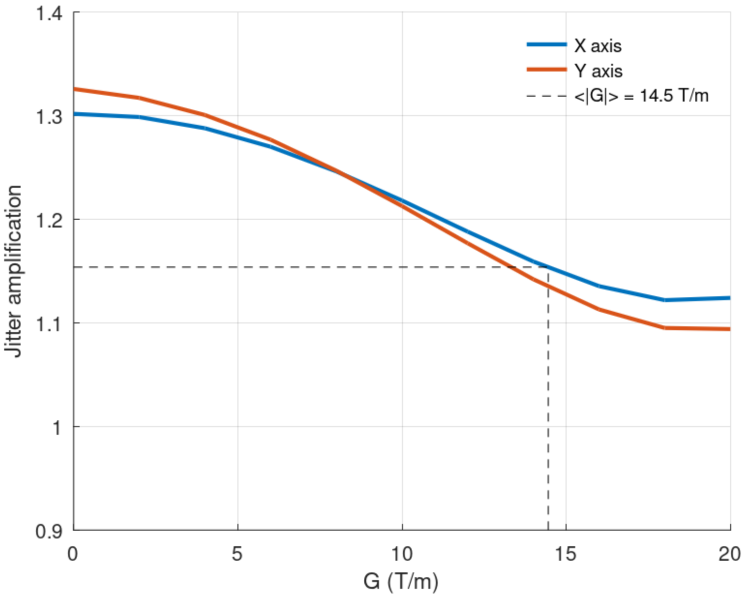

Figure 2.12: Jitter amplification factor in the linac as a function of average quadrupole gradient in the quadrupole doublet. The dashed line indicates the nominal average gradient.

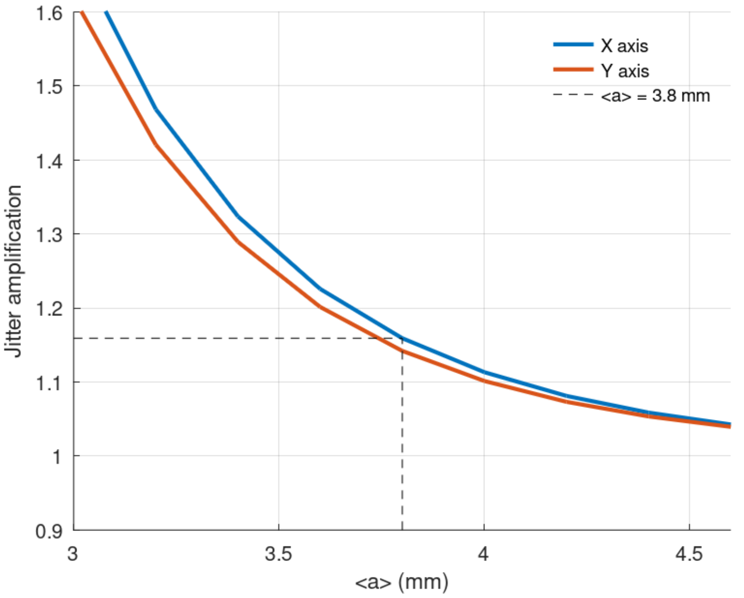

Figure 2.13: Jitter amplification factor as a function of the average iris aperture of the structures. The dashed line indicates the baseline average aperture.

driving bunch, and it's always negative, as the witness bunch always follows the driving bunch. Table 2.6, in the following chapter, summarises these parameters for the DEFT accelerating structure.

Assuming that the long-range effect only affects the first following bunch, a scan of the threshold kick that a bunch in the train can sustain without amplifying too much the oscillation of the trailing bunches was performed. The result is shown in Fig. 2.14. The threshold kick targets the jitter amplification factor to be less than 1.1, which determines the kick to be less than ~ 50 V/pC/m/mm in its absolute value.

Table 2.6: Table of the high-order modes considered in the beam dynamics simulations. The two main modes in each cell are denoted as #1 and #2.

	Input coupler	**First cell**		**Middle cell**		**Last cell**		**Output coupler**	**Units**
		#1	**#2**	**#1**	**#2**	**#1**	**#2**		
Amplitude	163	63.2	-	105.0	2.39	145.5	3.04	185	V/pC/m/mm
frequency	15.42	14.88	-	15.75	21.01	16.82	21.59	16.82	GHz
Q factor	160	19.6	-	10.3	60.3	7.1	119.4	80	-

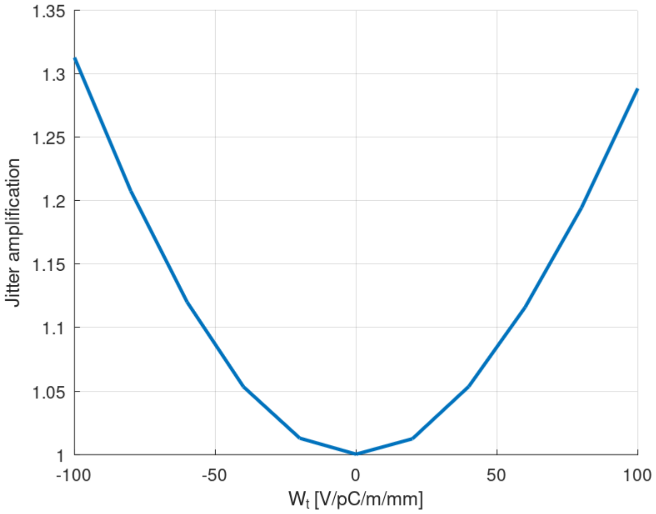

Figure 2.14: Jitter amplification factor at linac end as a function of the transverse kick at the following bunch. Targeting 1.1 or below drives the design of the HOM suppressors in the RF structures.

The maximum kick that the following bunch can sustain drives the RF design. Figure 2.15 shows the jitter amplification due to the high-order modes in the table, along the first 30 bunches of a train entering the linac with an offset; 72 modes per structure were considered, 1 for each cell.

One would normally want the JA to be as small as possible; however, achieving this objective is not possible given the several constraints in the optimisation. Indeed, the baseline steady-state JA is approximately 1.16 on the horizontal axis and 1.14 on the vertical axis. These values were deemed an acceptable compromise, and the sensitivity studies presented in the following sections confirmed this.

3.3 Beam delivery

3.3.1 Beam transport to window

Twenty cm downstream of the last structure's exit, a beam screen allows for measuring the beam properties and assessing uniformity. Following this screen is the beam delivery system (BDS), which prepares the beam for delivery to the patient. The BDS system is defined as that section from the end of the linac to the vacuum window, located 1.3 m ahead of the isocenter.

The beam delivery system comprises five quadrupole magnets, two magnetic correctors (steerers), and two beam position monitors (BPMs). The distance from the linac end to the isocenter is exactly six meters. The vacuum window is located 1.3 m ahead of the isocenter. A third beam position information, necessary for beam-based alignment beside the two BPMs, is provided by the BCS screen located between the vacuum window and the isocenter. The position and the strength of the quadrupoles are ob-

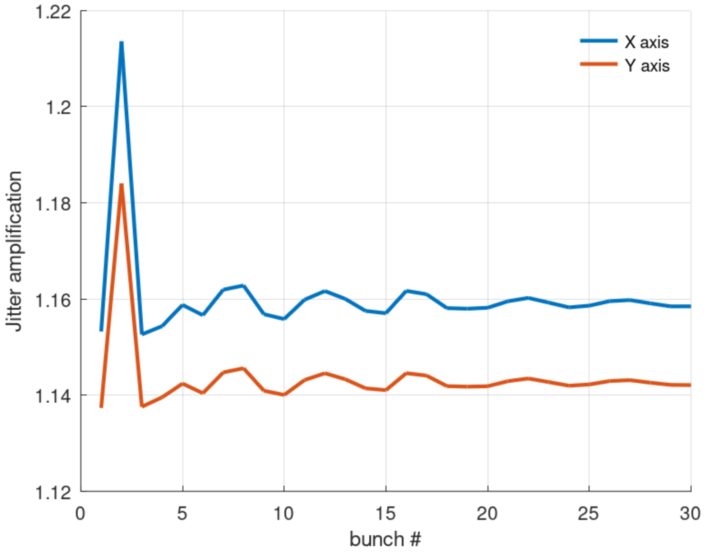

Figure 2.15: The jitter amplification factor in the linac due to short- and long-range transverse wakefield effects for the first 30 bunches of the train, using the realistic long-range wakefields from the final structure design.

tained via a multi-objective optimisation aimed to achieve the following five objectives simultaneously:

1. The best possible uniformity.
2. A field radius between 100 and 105 mm.
3. Homothety of the outgoing beam.
4. A transmission larger than 98%.
5. Fulfilling integration space requirements.

The search for the optimum is performed while maintaining the peak field at the cathode in the electron gun at 90 MV/m to limit the required input power to the gun. The result of this multi-objective optimisation is shown in Figs. 2.16 and 2.17. The optimisation achieves its objectives with 100 % transmission. Figure 2.16 shows the beam envelope along the beam delivery system. Figure 2.17 shows the beam profile at the isocentre. Tables 2.7 and 2.8 summarise the machine setup resulting from the optimisation.

3.4 Preserving the beam quality

Unwanted effects due to the unavoidable installation misalignments of the accelerator components or variations in time of the operating conditions affect the beam quality at the patient location. To counteract "static" effects such as misalignments, we adopted strategies and methods developed in the context of linear collider R&D, like automatic orbit steering and beam-based alignment. "Dynamic" effects, such as time-dependent variations, can be separated into two regimes: high-frequency variations, i.e., jitter of various machine parameters, and low-frequency variations, i.e., slow drifts of key system quantities. The aim of reducing the jitter amplification led to key design choices, like reducing the single-bunch charge to reduce the impact of wakefields. The effect of jitter was already assessed in the previous sections; see the jitter amplification studies. Slow variations of key quantities can be addressed using feedback loops that apply the automatic correction methods described in the following paragraphs.

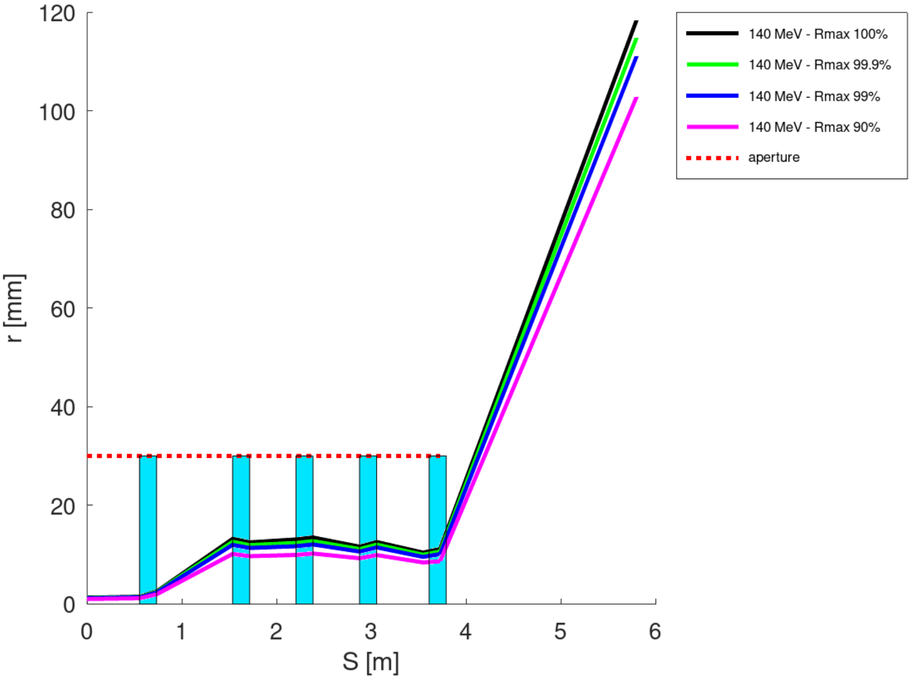

Figure 2.16: Transverse envelope along the beam delivery system.

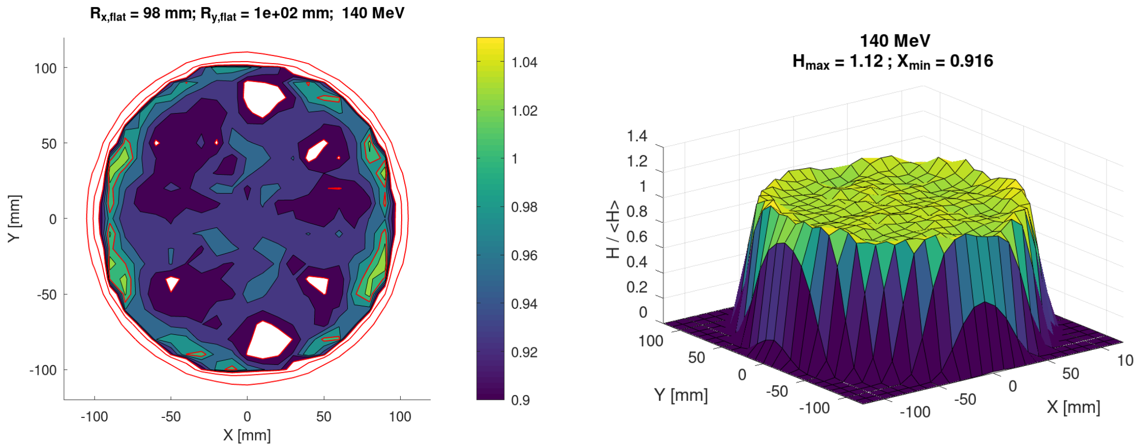

Figure 2.17: Transverse density profile and 2D histogram of the beams delivered to the patient.

3.4.1 Automatic orbit correction and beam-based alignment

Unwanted but unavoidable offsets of the accelerator components installed induce beam degradation through mechanisms like spurious dispersion due to misaligned quadrupoles and transverse wakefield effects from off-axis accelerating structures, which impart transverse deflections to the beam that degrade its quality and harm uniformity.

Over the last decades, automatic beam-based steering procedures have been devised for linear colliders, like CLIC or ILC. The large number of correctors (hundreds or more) in such large-scale facilities makes manual orbit correction impossible.

Beam-based techniques allow for automatic correction based on trajectory measurements. Given an estimate of the orbit distortions due to element misalignment, χ^2 in the formula below, one can compute the required corrector strengths to steer the trajectory and make it closer to the ideal one.

Table 2.7: Parameters of the DEFT accelerator, section by section.

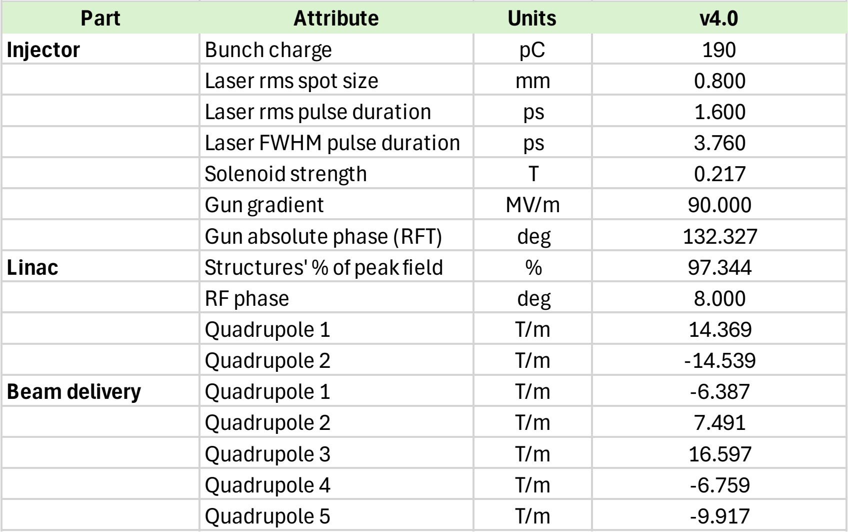

Part	Attribute	Units	v4.0
Injector	Bunch charge	pC	190
	Laser rms spot size	mm	0.800
	Laser rms pulse duration	ps	1.600
	Laser FWHM pulse duration	ps	3.760
	Solenoid strength	T	0.217
	Gun gradient	MV/m	90.000
	Gun absolute phase (RFT)	deg	132.327
Linac	Structures' % of peak field	%	97.344
	RF phase	deg	8.000
	Quadrupole 1	T/m	14.369
	Quadrupole 2	T/m	-14.539
Beam delivery	Quadrupole 1	T/m	-6.387
	Quadrupole 2	T/m	7.491
	Quadrupole 3	T/m	16.597
	Quadrupole 4	T/m	-6.759
	Quadrupole 5	T/m	-9.917

The trajectory distortion can be quantified as,

$$\begin{aligned}\chi^2 = {} & \omega_1^2 \sum_{\forall i \in \text{bpms}} x_{\text{nominal},i}^2 + \dots \\ & \omega_2^2 \sum_{\forall i \in \text{bpms}} \left(x_{\text{nominal},i} - x_{\text{off-energy},i}\right)^2 + \dots \\ & \omega_2^2 \sum_{\forall i \in \text{bpms}} \left(x_{\text{nominal},i} - x_{\text{off-charge},i}\right)^2 \quad .\end{aligned} \tag{2.3}$$

where

$$\omega_1^2 = \left(\sigma_{\text{bpm offset}}^2 + \sigma_{\text{bpm resolution}}^2\right)^{-1} \quad , \tag{2.4}$$

$$\omega_2^2 = \left(2\sigma_{\text{bpm resolution}}^2\right)^{-1} \quad . \tag{2.5}$$

Minimising χ^2 in Eq. (2.3) corresponds to applying the Dispersion-Free Steering (DFS) and the Wakefield-Free Steering (WFS) methods to correct the beam trajectory dispersion and wakefield effects simultaneously.

Given a set of orbit measurements, the corrector settings that minimise χ^2 are the solution of the following system of equations:

$$\mathbf{x} = \mathbf{R} \cdot \theta, \tag{2.6}$$

where $\mathbf{x}$ is the vector of orbit measurements, θ is the unknown vector of corrector strengths to be found, and $\mathbf{R}$ is the global response matrix of the system, which contains the response of the trajectory and the dispersion to correctors:

$$\mathbf{x} = \begin{bmatrix} \mathbf{x}_{\text{nominal}} \\ \omega_D \cdot \left(\mathbf{x}_{\text{off-energy}} - \mathbf{x}_{\text{nominal}}\right) \\ \omega_W \cdot \left(\mathbf{x}_{\text{off-charge}} - \mathbf{x}_{\text{nominal}}\right) \end{bmatrix}, \quad \mathbf{R} = \begin{bmatrix} \mathbf{R}_{\text{nominal}} \\ \omega_D \cdot \left(\mathbf{R}_{\text{off-energy}} - \mathbf{R}_{\text{nominal}}\right) \\ \omega_W \cdot \left(\mathbf{R}_{\text{off-charge}} - \mathbf{R}_{\text{nominal}}\right) \end{bmatrix}.$$

$\mathbf{R}_{\text{nominal}}$, $\mathbf{R}_{\text{off-energy}}$, and $\mathbf{R}_{\text{off-charge}}$ are respectively the orbit, the dispersive, and the wakefield response matrices, containing the response of each BPM along each beamline to each corrector in the three differ-

Table 2.8: Elements position in the DEFT accelerator, section by section.

Injector	**Mid-point position [cm] (*)**	**Length [cm] (**)**
Corrector 1	52.6	10
Bpm 1	85.00	10
Corrector 2	122.00	10
Linac	**Mid-point position (*)**	
Acc. Structure 1	160.00	62.4
Acc. Structure 2	230.00	62.4
Acc. Structure 3	300.00	62.4
Acc. Structure 4	370.00	62.4
Corrector 3	432.00	10
Quadrupole	439.25	4.5
Quadrupole	447.75	4.5
Bpm 2	452.80	10
Acc. Structure 5	500.00	62.4
Acc. Structure 6	570.00	62.4
Acc. Structure 7	640.00	62.4
Acc. Structure 8	710.00	62.4
Beam Delivery	**Mid-point position (*)**	
Corrector 4	796.0	18
Quadrupole	824.0	18
Quadrupole	922.0	18
Bpm 3	955.5	20
Quadrupole	990.0	18
Corrector 5	1030.0	18
Quadrupole	1058.0	18
Bpm 4	1091.50	20
Quadrupole	1126.0	18
Window	1210	0
Beam position measurement	1240.0	20
Isocenter	1340	0
(*) relative to the cathode		
(**) beam-dynamics length		

ent cases; the weights, ω_D and ω_W, are:

$$\omega_D = \omega_W = \frac{\omega_2}{\omega_1},$$

or can be adjusted to match specific cases.

The solution of the linear system of equations in Eq. (2.6) can be found using the least-squares method:

$$\theta = -\mathbf{R}^{-1} \cdot \mathbf{x},$$

where $\mathbf{R}^{-1}$ is the pseudo-inverse of the matrix $\mathbf{R}$, and θ is the vector of required variation of the corrector strengths to achieve correction.

3.4.2 Implementation of the orbit correction procedure

Magnetic steering and BPMs allow automatic trajectory correction according to the described correction strategy. Two BPMs with a resolution of 10 μm are located in the injector and in the linac, where the beam size is small. The beam delivery system has two BPMs with a larger aperture and, therefore, a degraded resolution of 100 μm. An additional beam position information with a larger lever arm after the vacuum window is also required to reach the isocentre with the required accuracy. Five correctors (magnetic steerers) are required to perform the orbit correction. BPMs and correctors are distributed along the beam line as shown in Fig. 2.4.

The implementation of realistic misalignments in the simulation was discussed with the team responsible for the prealignment of the elements in the tunnel. The key quantities used in this context were two: (1) the transverse alignment accuracy for the two points at each end of an object, σ_t; and (2) the distance between these two points, ΔL. It should be noted that this distance often differs from the actual length of the physical object, as these two points refer to the rigid support underneath the object rather than the object itself. Figure 2.18 gives a pictorial representation of the key quantities involved.

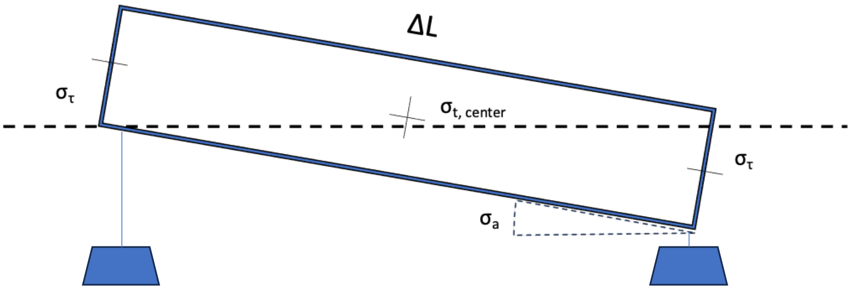

Figure 2.18: Misalignment model used in the simulations.

The rms transverse misalignment of the centre of an object is

$$\sigma_{\mathrm{t,\,centre}} = \frac{\sigma_\mathrm{t}}{\sqrt{2}}.$$

One can compute its rms pitch/yaw misalignment angles using the ends' rms transverse misalignment, σ_t and an object's length, ΔL:

$$\sigma_\mathrm{a} = \frac{\sqrt{2}\sigma_\mathrm{t}}{\Delta L}.$$

To assess the effectiveness of the correction procedure, we created 100 randomly misaligned configurations of the machine, according to the rms offsets shown in Table 2.9. Then, we applied the correction procedure to each machine and evaluated the performance by looking at three parameters:

1. Uniformity, which is defined as

$$\chi^2 = \sum_{8\text{ angles}} \|\mathrm{CDF}\,(\text{Projected } XY) - \mathrm{CDF}\,(\text{Uniform disk})\|^2, \tag{2.7}$$

   where the first term is the cumulative distribution function of the simulated XY distribution at the patient location projected against an angle in the plane, and the second term is the target CDF, that is, the cumulative distribution function of an ideal uniform disk. We sum up the contributions of eight directions in the XY-plane, from 0° to 180° in steps of 22.5°. The smaller the χ^2, the closer the distribution to an ideal uniform disk. The χ^2 for the ideal machine has a value of about 10.

2. The horizontal and vertical beam position at the patient.

3. The horizontal and vertical beam radii at the patient.

Our simulations showed that the effect of wakefields in the accelerating structures is much stronger than the dispersion introduced by misaligned quadrupoles. For this reason, we decided to use only WFS and not DFS (i.e., ω_D was set to 0). As a test beam to estimate the impact of wakefields in WFS, we used a bunch charge of 100 pC, almost half the nominal charge.

3.4.3 Results of the orbit correction simulations and discussion

Figure 2.19 shows the results of the simulations. We display the results of the 100 randomly misaligned machines sorted from small to large, to give a visual insight into their statistical distributions. As shown in the plots, WFS effectively recovers all the critical parameters in most of the 100 simulated machines: uniformity, transverse position, and beam radii. This confirms that wakefield effects are the most crucial ones, as well as the choice of algorithm. In the plots, the dashed lines show the result for 90% of the simulated machines. The corresponding values are within the specified tolerances. Figure 2.19 also shows that some random seeds can be particularly unlucky, missing one or more targets completely. This should not be alarming: These results are from a beam-based correction procedure designed to be fast and fully automatic in the interest of short simulation time. Should the real machine be one of the unlucky seeds, one could always imagine applying specific corrections on a case-by-case basis. For example, if an element was found to be “too off-axis”, there would be no automatic correction better than to go into the tunnel and realign it.

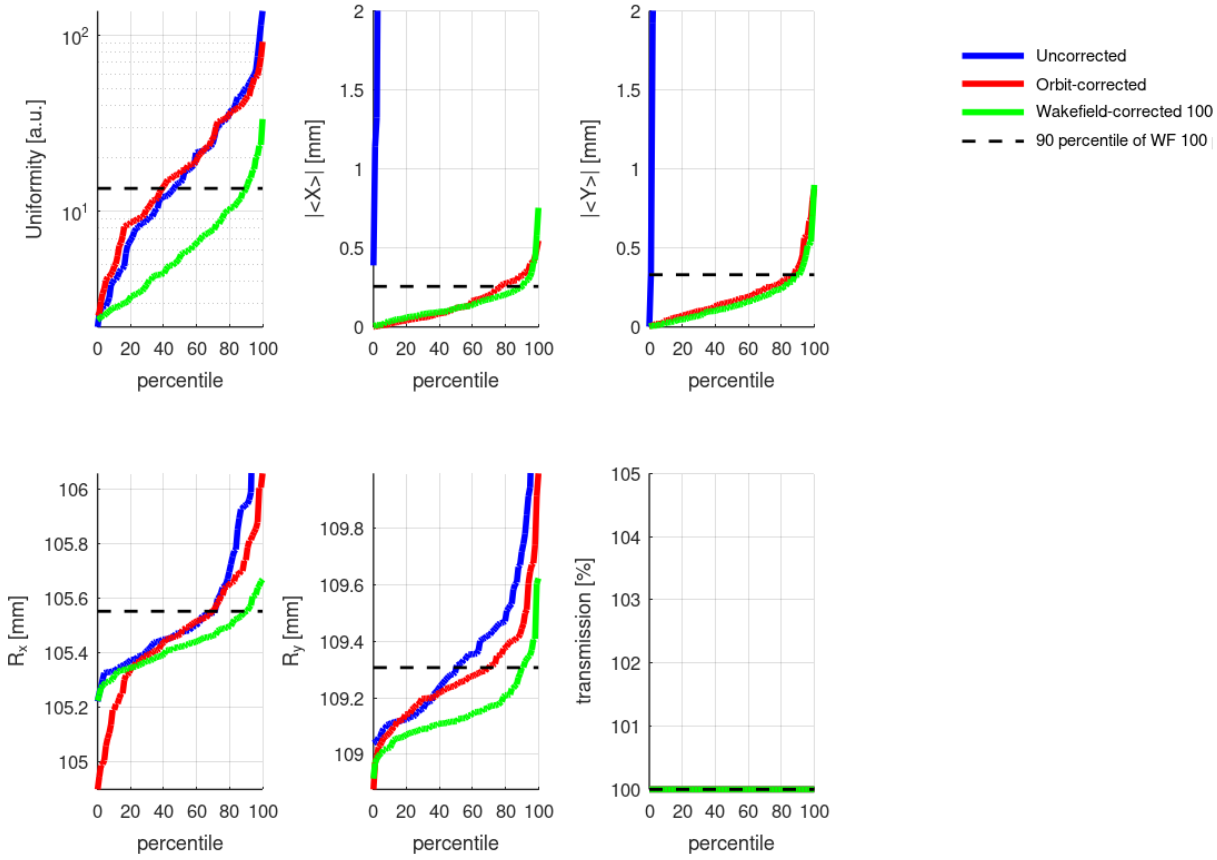

Figure 2.19: Performance of the beam-based alignment technique proposed. The “Uniformity” parameter for the ideal machine is about 10.

Figure 2.20 shows the corrector strengths in both transverse planes required by all machines. In

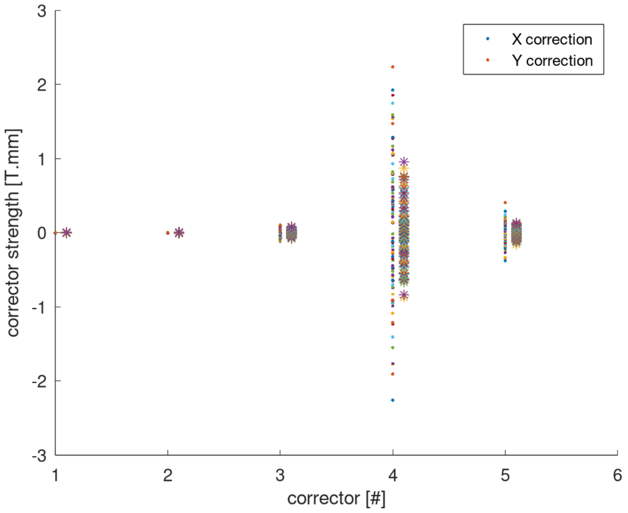

Figure 2.20: Required corrector strengths for the simulated 100 machines.

this plot, the peak-to-peak values are most relevant. As can be seen, the peak-to-peak is within a range of ±3 T · mm, which is perfectly acceptable from a magnet design point of view.

Table 2.9: Root-mean-squared values of the offsets considered in the simulations.

Component	σ_t [μm] (assumed)	ΔL [cm] (assumed)	$\sigma_{t,\text{centre}}$ [μm] (computed)	σ_a [μrad] (computed)	σ_{roll} [μrad] (assumed)
Electron gun	40	-	28.2	-	300
Solenoid	40	25	28.2	226.2	300
Injector BPM	40	10	28.2	565.7	300
Injector correctors	40	10	28.2	565.7	300
Linac structures	40	70	28.2	80.8	300
Linac corrector	40	10	28.2	565.7	300
BDS quadrupoles	40	20	28.2	282.8	300
BDS BPMs	40	20	28.2	282.8	300
BDS corrector	40	20	28.2	282.8	300
Injector girder	100	130	70.7	108.8	300
Linac module girders	100	300	70.7	47.1	300
BDS girder	100	400	70.7	35.3	300

3.5 Sensitivities studies to the injector parameters

Sensitivity studies are dedicated to imposing limitations on the acceptable variations in the parameters of the machine, within which reaching the requested performance at the patient location is feasible. Furthermore, they allow for fine-tuning of the optimal operational parameters. In this section, we discuss limitations on the required parameters of the injector part. In this simplified analysis, we neglect the beam collimator before the patient's location in the beam line delivery system. Acceptable fluctuations of the beam parameters at the patient location are summarised in Table 2.10. These values are not obsolete but rather provide some guidance for the design of the machine and define the limitations on the acceptable variation of the critical machine parameters. The results presented below are for simulations with 10 000 particles. In limited cases, these findings are cross-checked and validated by simulations with one million particles.

Table 2.10: Acceptable fluctuations of the beam parameters at the patient location used for the sensitivity studies.

Parameter	**Symbol**	**Units**	**Fluctuation**
Flat area radius	ΔR_x, ΔR_y	mm	± 1
Position X-Y	ΔX, ΔY	mm	± 1
Uniformity	U	%	0–15
Homothety	H	%	± 2
Symmetry	S	%	± 1
Transmission	T	%	> 98
Flat area charge	q	%	> 85
Beam energy mean	E	MeV	± 2
Beam energy 5 pct.	$E_{5\text{pct}}$	MeV	± 2
Divergence	D	mrad/cm	± 0.5

3.5.1 Impact of errors in laser parameters

Laser spot offset at the cathode in horizontal/vertical direction mostly impacts the beam spot offset at the vertical/horizontal direction correspondingly, as can be seen in Figs. 2.21 and 2.22. The required stability for the laser spot position is $\pm 3.4\%$ from the rms spot size, which corresponds to $\pm 27\,\mu$m.

Laser spot size variations are depicted in Fig. 2.23 and should be limited to $\pm 1.2\,\%$.

Impact of the laser pulse duration fluctuation is depicted in Fig. 2.24. The variations should be limited to $\pm 1.6\,\%$ or $\pm 26\,$fs.

3.5.2 Impact of errors in charge at the cathode

The charge variations at the cathode (i.e. due to laser power fluctuations or rapid changes in the quantum efficiency) can significantly impact the total delivered charge and the beam quality at the patient location. Allowed fluctuation of the total charge critical for space-charge dominated beam dynamics should be within 2%. The total charge delivered to the patient in the flat area must be more than 85%. We check the initial variations of the charge at the cathode within the $\pm 20\%$ range. We find that required charge stability at the cathode should remain within $\pm 1\%$ or $\pm 1.9\,$pC as depicted in Fig. 2.25 due to horizontal size variation at the patient location.

3.5.3 Impact of errors in solenoid parameters

Figure 2.26 indicates a critical impact of the variations in the solenoid magnetic field on the beam quality at the patient location. As mentioned in Section 3.1, the solenoid's magnetic field is tuned to achieve uniformity at the injector part for a selected gun gradient and phase. The fluctuations of the flat area radii, R_x and R_y, impose severe limitations on the magnetic field stability of $\pm 0.1\,\%$ from the nominal value.

3.5.4 Impact of errors in gun parameters

Figure 2.27 shows the dependence of the fluctuations of the critical beam parameters at the patient location on the variations in the gun gradient. This defines the admissible variations of the gun gradient:

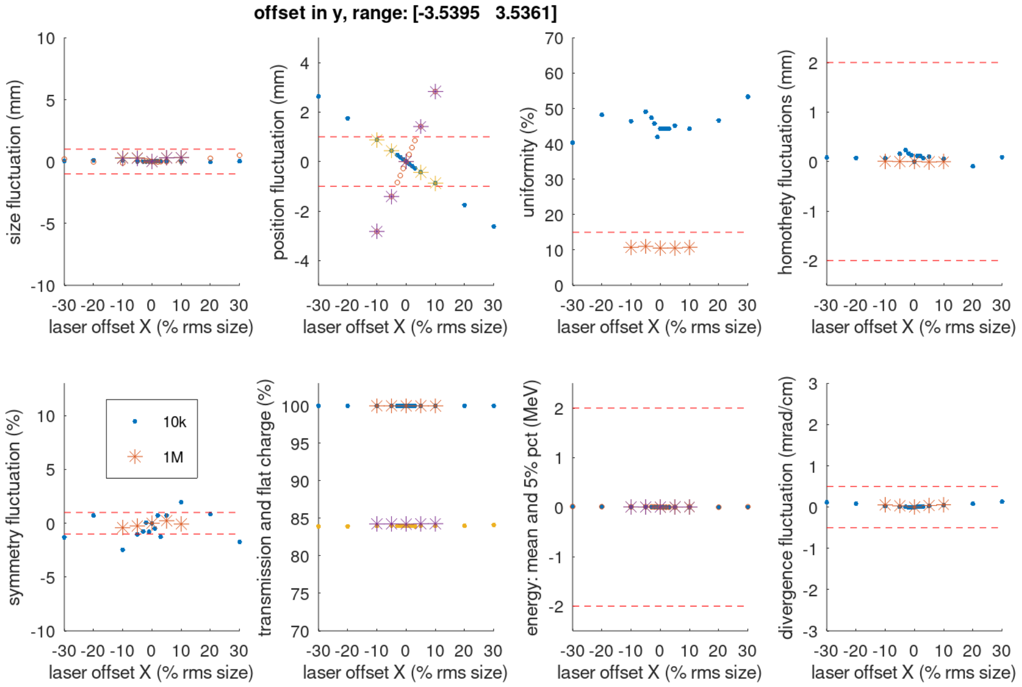

Figure 2.21: Deviation of the critical beam parameters at the patient location with the horizontal laser spot position fluctuations. Required laser spot stability is ±28 μm to remain within the acceptable fluctuations of the vertical position at the patient location (dashed red lines).

±0.1 MV/m to remain within the limitations at the patient location dictated by the size fluctuation at the patient location.

The impact of the phase stability of the RF gun is depicted in Fig. 2.28. The required phase stability is $\pm 3^\circ$ again limited by the size fluctuation at the patient location.

3.5.5 Summary of injector errors

Table 2.11 summarizes the maximum acceptable variations of the injector parameters to satisfy the requirements of the beam quality at the patient location (see Table 2.10). It also highlights the most critical parameters of the final beam, defining the limitations.

3.6 Sensitivities studies to the linac and beam delivery system parameters

3.6.1 Impact of RF errors in the linac section

The effect of RF gradients and phase errors is shown in Figs. 2.29 and 2.30.

3.6.2 Impact of quadrupole errors

Figures 2.31 and 2.32 show the impact of linac quadrupole strength errors. The acceptable variations are 0.4% and 0.2% correspondingly in 1st and 2nd quadrupole.

For beamline quadrupoles the results are shown in Figs. 2.33– 2.37.

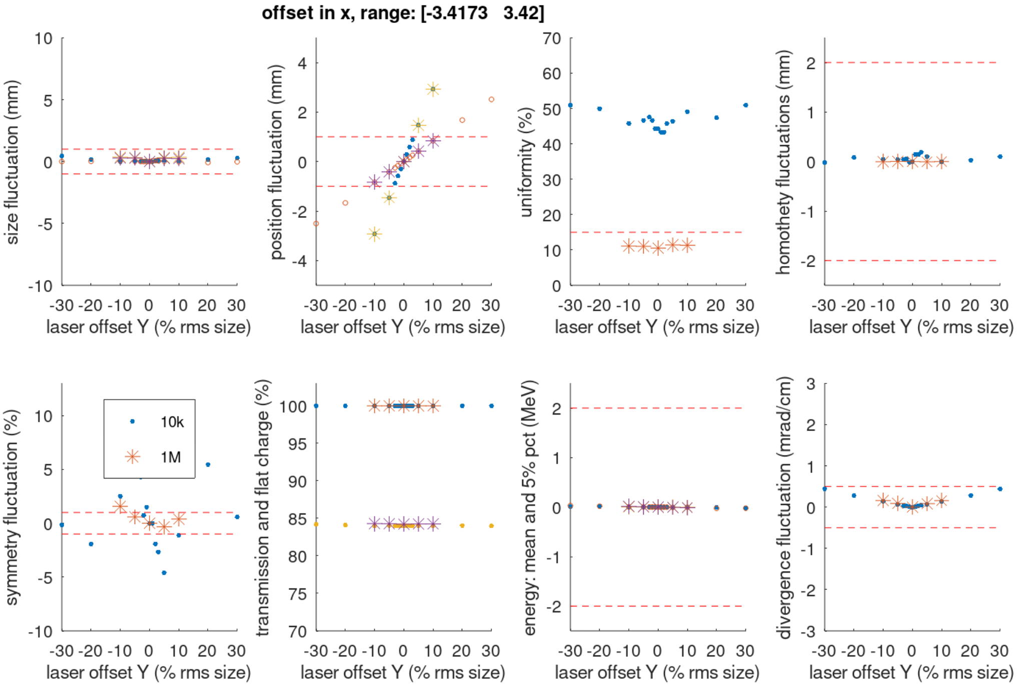

Figure 2.22: Deviation of the critical beam parameters at the patient location with the vertical laser spot position fluctuations. Required laser spot stability is ±27 μm to remain within the acceptable fluctuations of the horizontal position at the patient location (dashed red lines).

Table 2.11: Acceptable fluctuations of the parameters in the injector section to satisfy the stability requirements at the patient location listed in Table 2.10.

Parameter	Symbol	Units	Target	Max. variation	Limitation
			Laser		
Offset	X, Y	μm	0	±28,±27	ΔY, ΔX
Size	$\sigma_{x,y}$	μm	800	±9.6	ΔR_x, ΔR_y
Duration	σ_t	fs	1600	±25.6	ΔR_y
Charge	Q	pC	190	±1.9	ΔR_y
			Solenoid		
Amplitude	B	mT	219.7	±0.2	ΔR_x, ΔR_y
			Gun		
Gradient	E_z	MV/m	90	±0.1	ΔR_x, ΔR_y
Phase	Φ	degree	-140	±3	ΔR_x, ΔR_y

3.6.3 Summary of linac and beamlines errors

Table 2.12 summarizes acceptable maximum variations of the linac and beamlines parameters to satisfy the requirements of the beam quality at the patient location (see Table 2.10). It also highlights the most critical parameters of the final beam, defining the limitations.

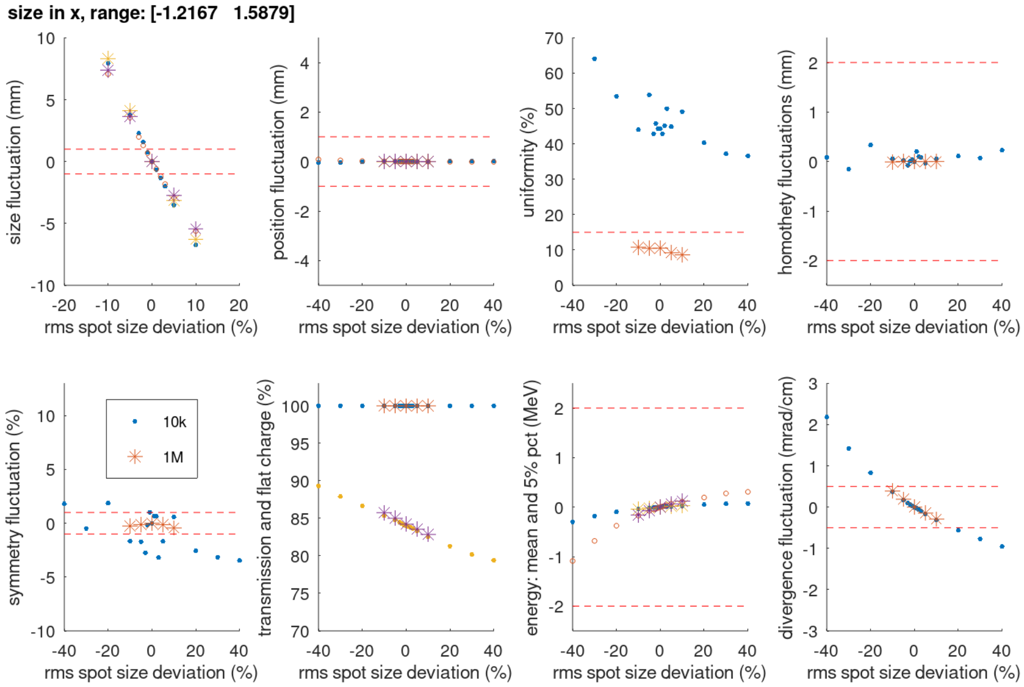

Figure 2.23: Deviation of the critical beam parameters at the patient location with the laser spot size fluctuations. Required laser spot stability is ±1.2 % to remain within the acceptable horizontal flat area radius fluctuations at the patient location (dashed red lines).

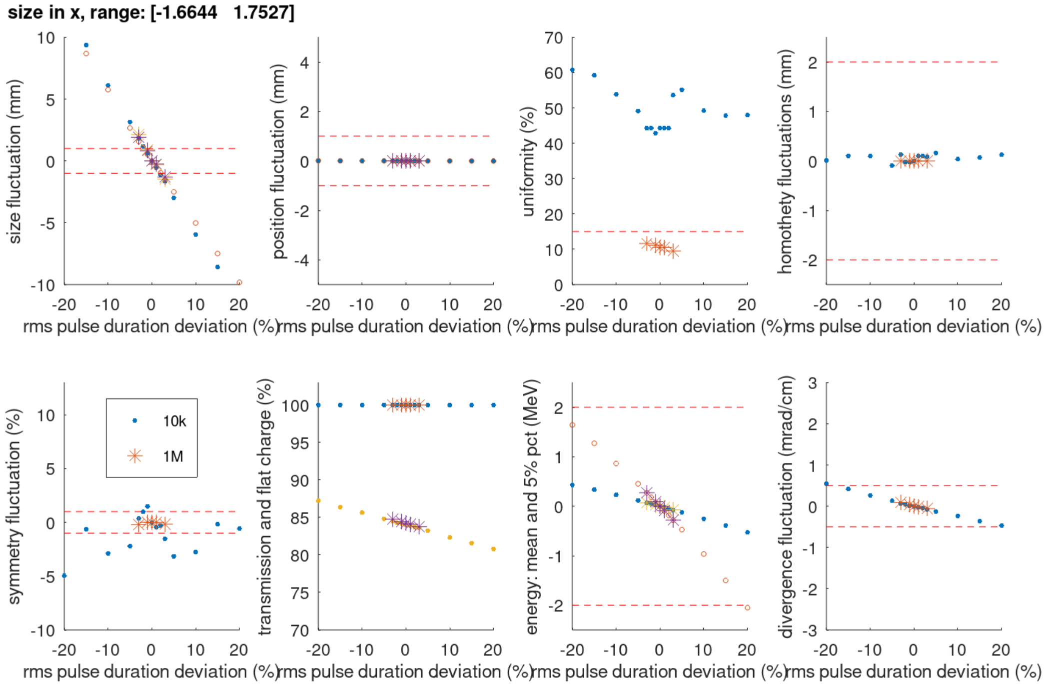

Figure 2.24: Deviation of the critical beam parameters at the patient location with the laser pulse duration fluctuations. Required stability is ±1.6 %.

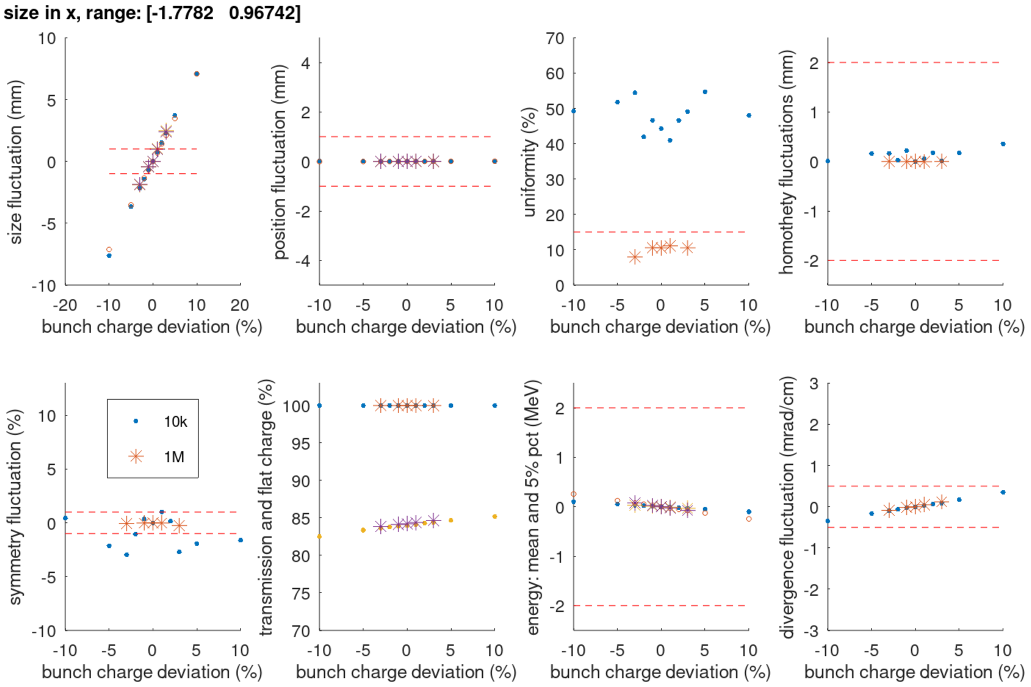

Figure 2.25: Deviation of the critical beam parameters at the patient location with the fluctuations of the bunch charge at the cathode. Required stability is ±1 % to remain within the acceptable horizontal flat area radius fluctuations at the patient location (dashed red lines).

Table 2.12: Acceptable fluctuations of the parameters in the linac and beam delivery sections to satisfy the stability requirements at the patient location listed in Table 2.10.

Parameter	**Symbol**	**Units**	**Target**	**Range, %**	**Limitation**
			Linac		
Gradient	E_z	MV/m	33.7	±0.3	ΔR_x, ΔR_y
Phase	Φ	degree	0	$\pm 1^\circ$	ΔR_x, ΔR_y
Quadrupole 1	QA	T/m	14.4	±0.4	ΔR_x, ΔR_y
Quadrupole 2	QB	T/m	-14.6	±0.2	ΔR_x, ΔR_y
			BDS		
Quadrupole 1	$Q1$	T/m	-18.5	±0.7	ΔR_x, ΔR_y
Quadrupole 2	$Q2$	T/m	6.6	±0.5	ΔR_x, ΔR_y
Quadrupole 3	$Q3$	T/m	-5.1	±0.12	ΔR_x, ΔR_y
Quadrupole 4	$Q4$	T/m	6.3	±0.3	ΔR_y, ΔR_x
Quadrupole 5	$Q5$	T/m	-18.5	±0.5	ΔR_y, ΔR_x

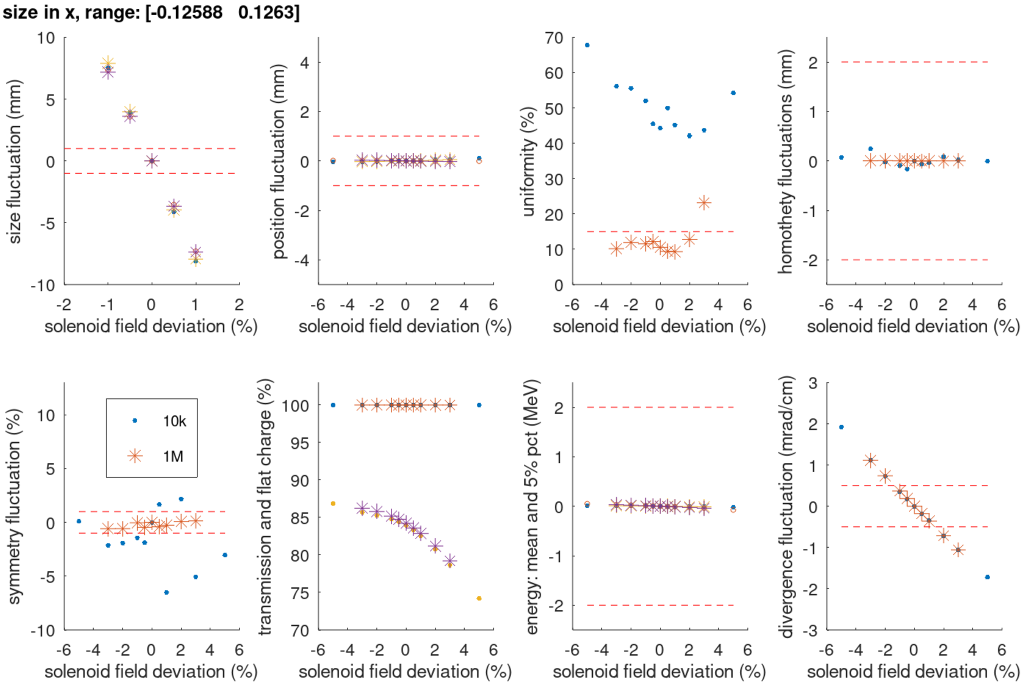

Figure 2.26: Deviation of the critical beam parameters at the patient location with the magnetic field fluctuations of the injector solenoid. Required solenoid stability is ±0.1 % to remain within the acceptable fluctuations at the patient location (dashed red lines).

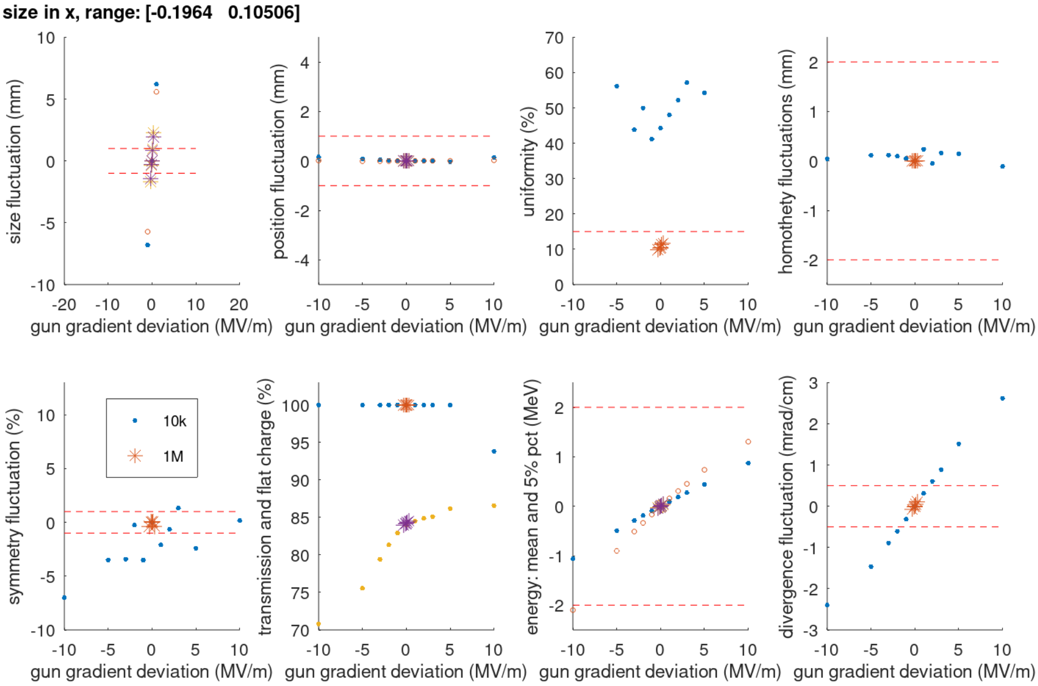

Figure 2.27: Deviation of the critical beam parameters at the patient location with the fluctuations of the gun gradient. Required gun gradient stability is ±0.1 MV/m to remain within the acceptable fluctuations at the patient location (dashed red lines).

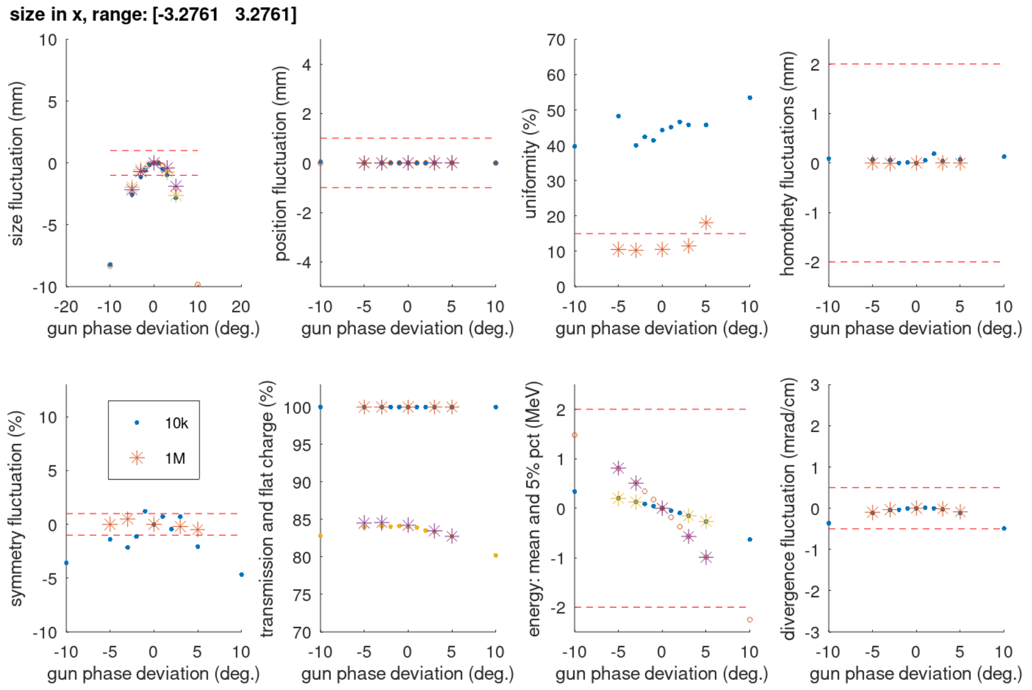

Figure 2.28: Deviation of the critical beam parameters at the patient location with the fluctuations of the gun phase. Required gun phase stability is ±3.0° degrees to remain within the acceptable fluctuations at the patient location (dashed red lines).

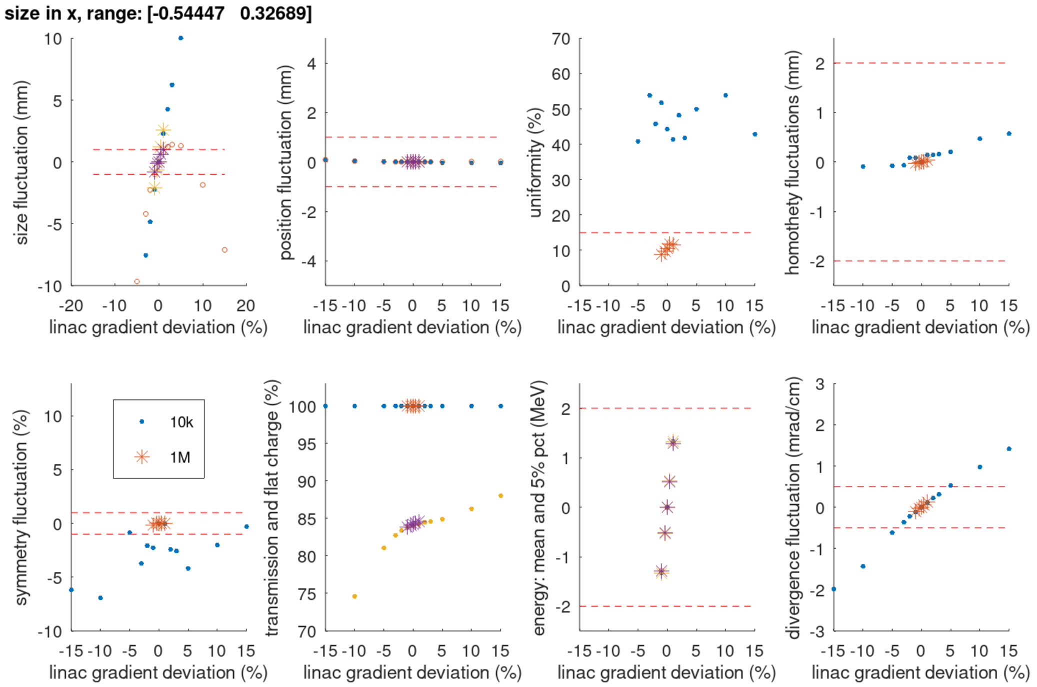

Figure 2.29: Deviation of the beam parameters at the patient location with variations of the gradient in all accelerating structures of the linac. Maximum affordable variation is ±0.3% .

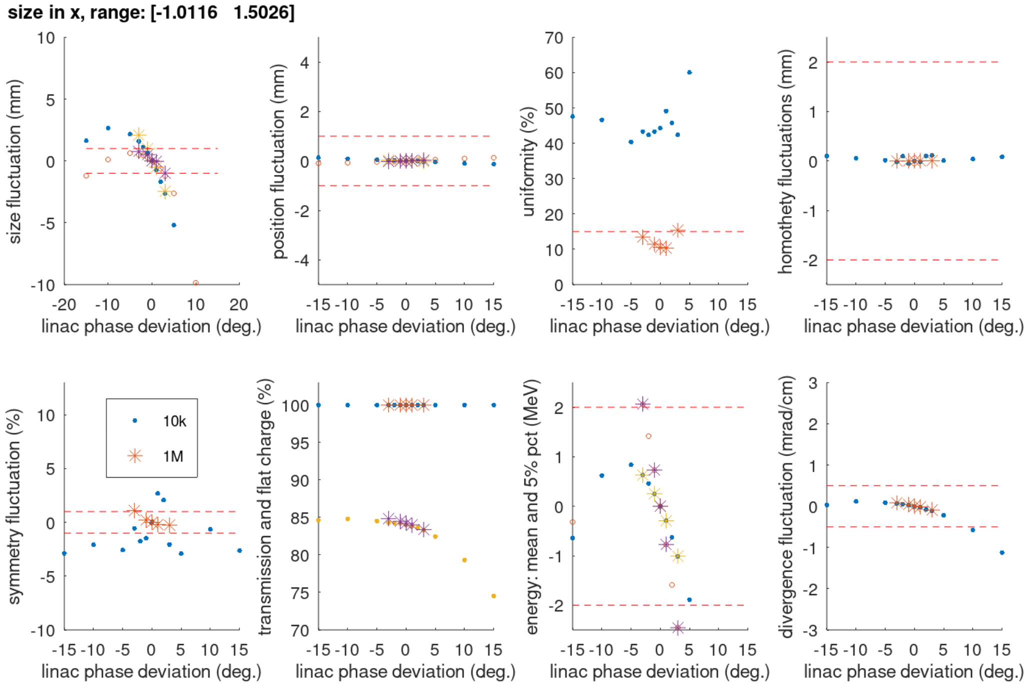

Figure 2.30: Deviation of the beam parameters at the patient location with variations of the phase in all linac structures. Maximum affordable fluctuation is ±1 degree.

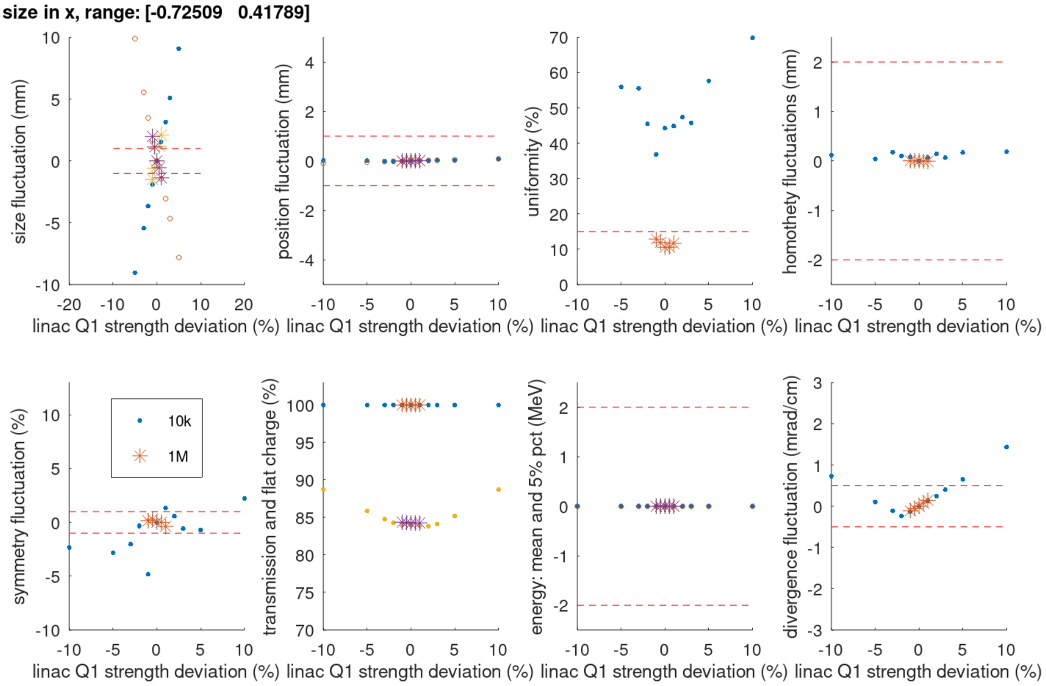

Figure 2.31: Deviation of the beam parameters at the patient location with variations of the strength in the 1st quadrupole between two linac modules.

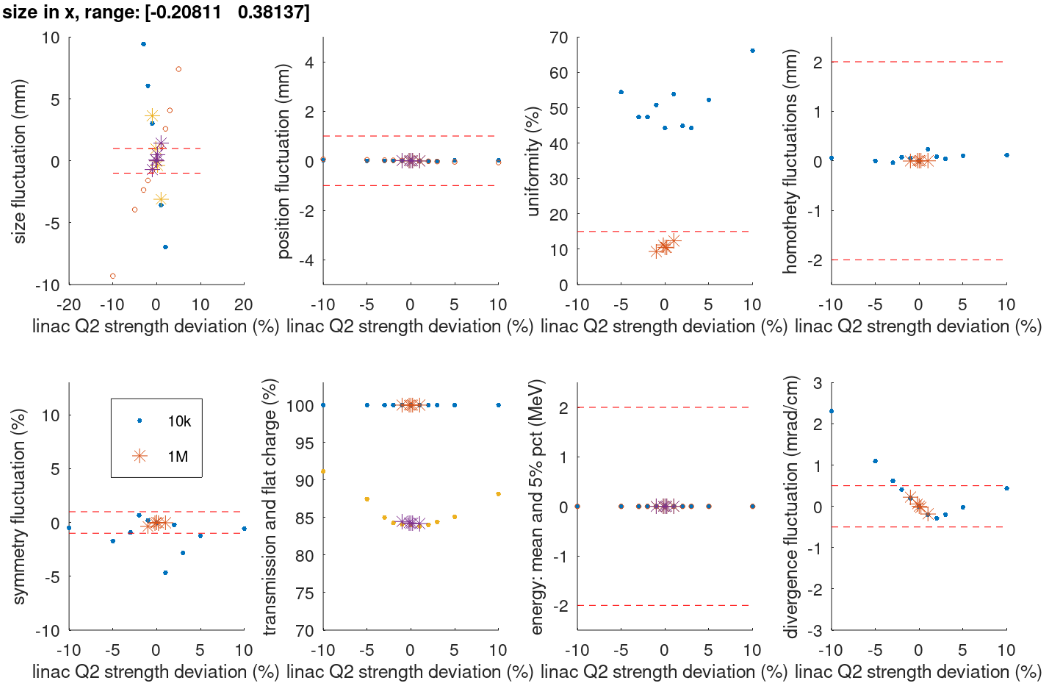

Figure 2.32: Deviation of the beam parameters at the patient location with variations of the strength of the 2^{nd} quadrupole between two linac modules.

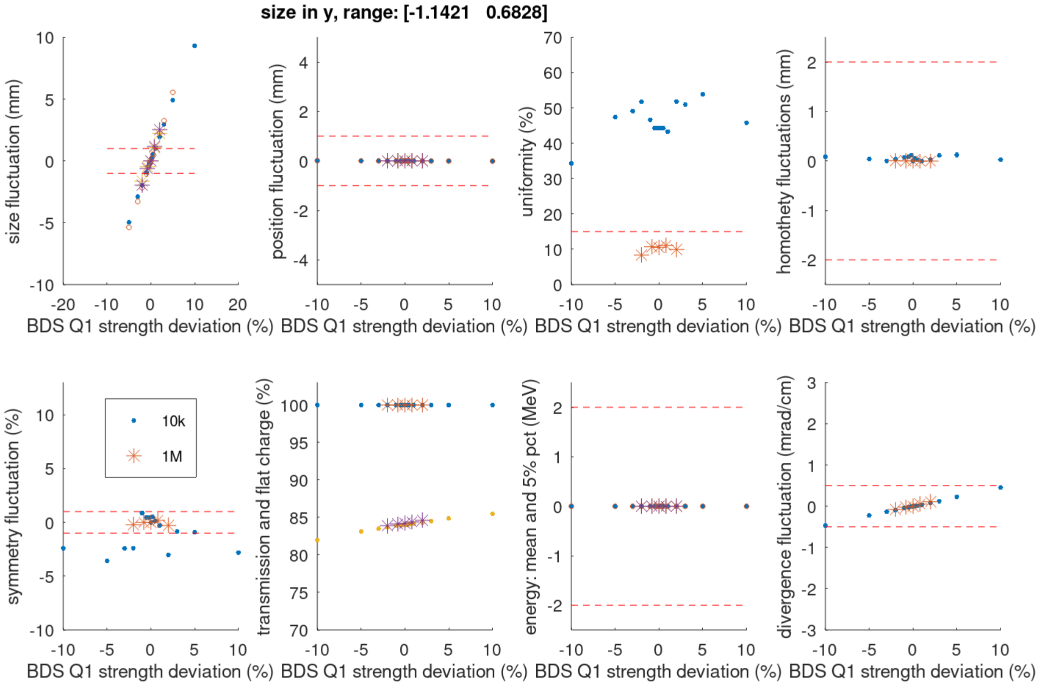

Figure 2.33: Deviation of the beam parameters at the patient location with variations of the strength of the 1^{st} quadrupole in the beam delivery system.

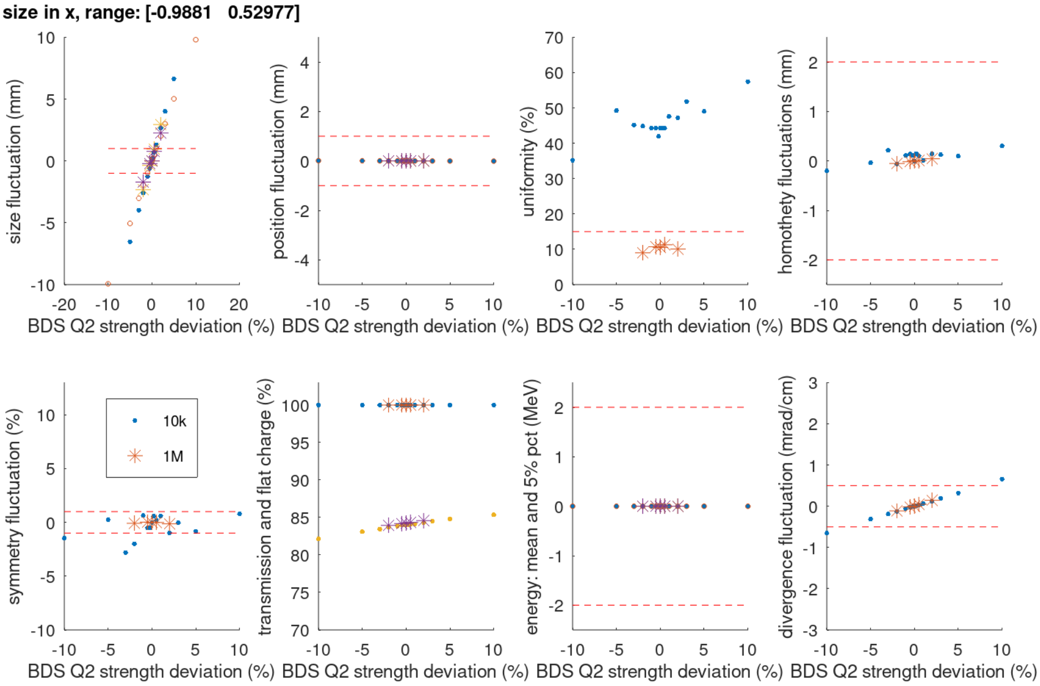

Figure 2.34: Deviation of the beam parameters at the patient location with variations of the strength of the 2nd quadrupole in the beam delivery system.

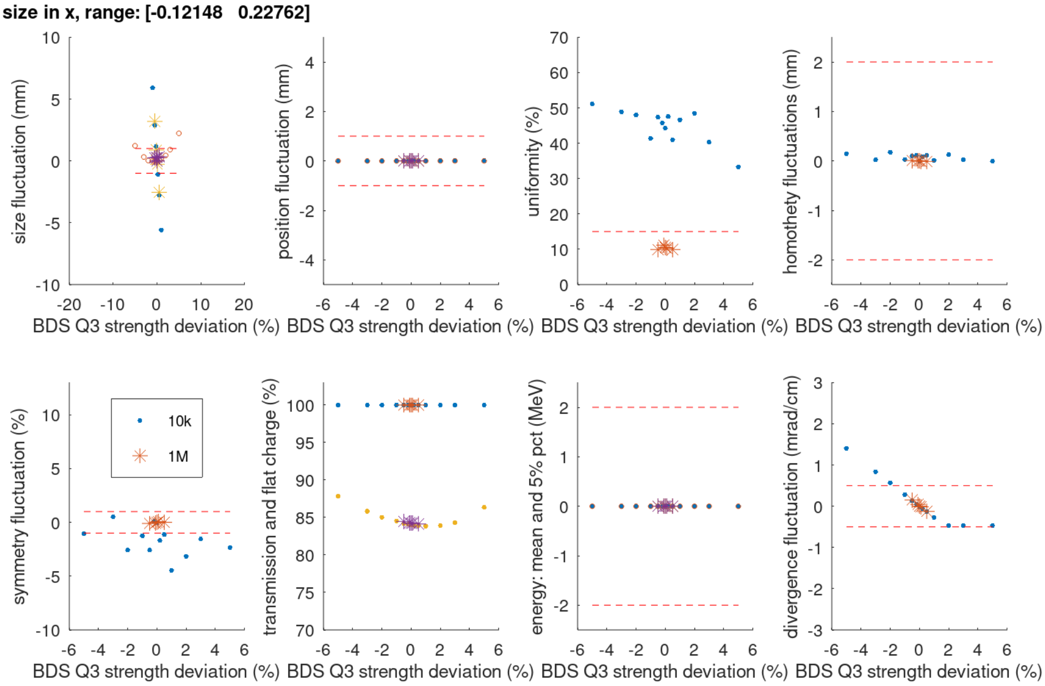

Figure 2.35: Deviation of the beam parameters at the patient location with variations of the strength of the 3rd quadrupole in the beam delivery system.

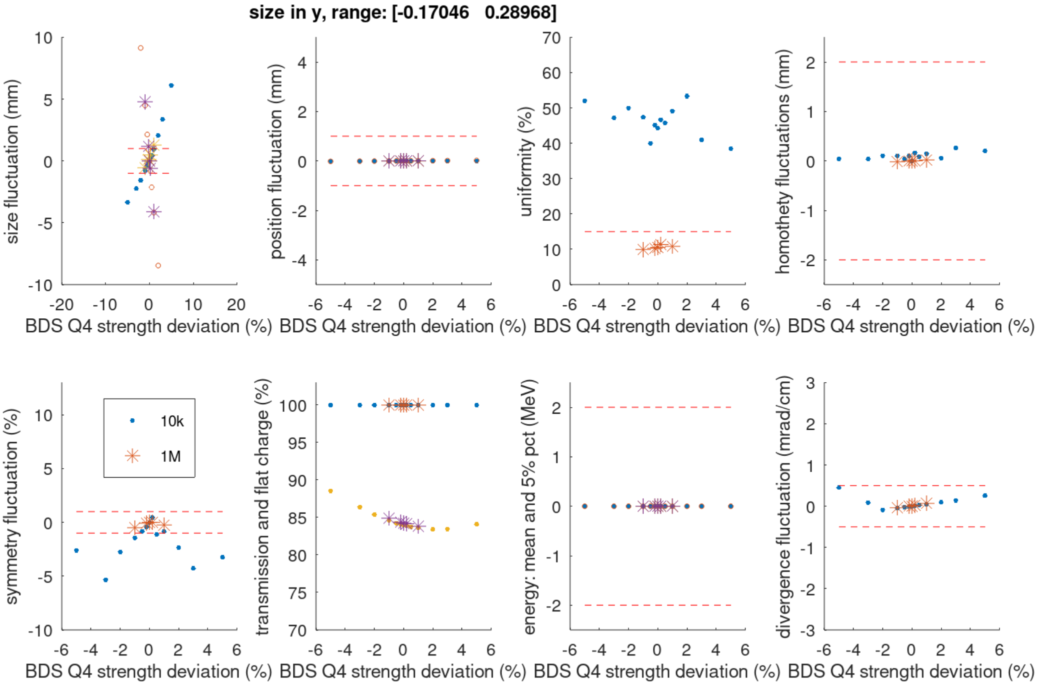

Figure 2.36: Deviation of the beam parameters at the patient location with variations of the strength of the 4th quadrupole in the beam delivery system.

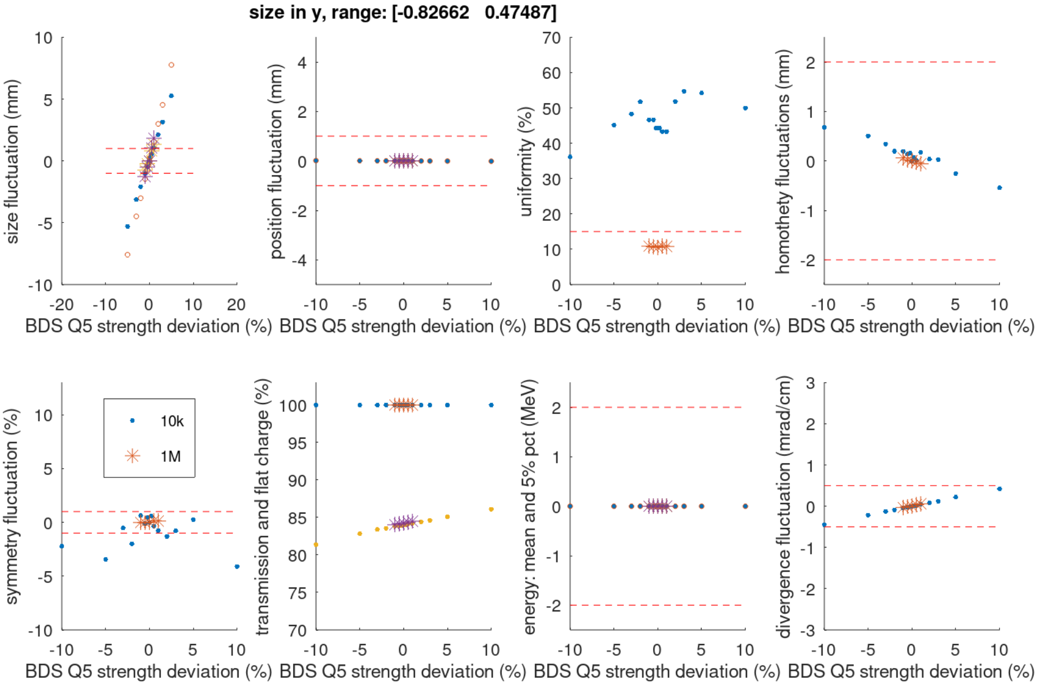

Figure 2.37: Deviation of the beam parameters at the patient location with variations of the strength of the 5th quadrupole in the beam delivery system.

Chapter 3

Linac components

1 Photoinjector

1.1 Introduction

The DEFT injector must fulfil several requirements; it must generate a train of electron bunches with a specific and variable time structure to deliver a well-defined radiation dose to the patient. The transverse emittance of the beam and the longitudinal bunch length must be reasonably small, as the following acceleration is accomplished by X-band accelerating structures. And finally, a homogeneous transverse beam distribution is required at the treatment location. The most important beam parameters at the end of the injector are summarized in Table 3.1.

Table 3.1: Beam parameters at the end of the injector.

Parameter	**Value**
Gradient in the gun (MV/m)	90
RF pulse length (μs)	1.5
Momentum (MeV/c)	6.5
Charge per bunch (nC)	0.190
Bunches per train (max)	507
Bunch spacing (ns)	0.333
Number of trains (max)	40
Charge per treatment (max) (μC)	3.8
Homogenity of the beam (%)	0.1
Emittance (μm)	5.8
Energy spread (%)	1
Repetition rate (Hz)	400
Bunch length (mm)	0.35
Laser spot size rms (mm)	0.8
Laser duration rms (ps)	1.6

The above-mentioned requirements make a photoinjector the electron source of choice for this application. A laser impinges on a photocathode placed in a short standing wave cavity, allowing immediate acceleration and emittance preservation. Those guns can deliver nC-type bunches with an emittance of the order of a few μm [9, 10]. The downside is the sensitivity of the high quantum efficiency (QE) cathodes, which require a very good vacuum of the order of 10^{-10} mbar and have a limited lifetime. The laser determines the time structure of the beam and allows therefore to the creation of X-band suitable short bunches right from the cathode and flexibility to choose the length of the bunch train. The intense electron bunches are liberated via the photo effect from the cathode with a short laser duration and a small transverse spot size. Therefore, the electrons are exposed to a significant space charge force, which lets the bunch expand longitudinally and transversely. The expansion is counteracted somewhat by a magnetic solenoidal field within the gun. Given a well-defined transverse distribution of the laser, this space charge expansion process generates the homogeneous distribution required for the treatment. Once generated in the injector, the distribution can be preserved in the linac and beam transport.

We distinguish between two main types of cathodes relevant for those applications. Metal cathodes, where copper is most common, but magnesium and iridium have also been used. They reach typical quantum efficiencies in the 10^{-5}–10^{-4} range but are quite robust and do not need extremely small pressures. Particularly in the case of copper, they are straightforward to use in an RF cavity and can be part of the cavity wall. A limitation of metallic cathodes is their ablation threshold if high charge and small spot sizes are required.

The second type of cathodes are semiconductors like Cs_2Te, $CsSb$, Cs_3Nb or $GaAs$. The semiconductors are produced as a thin layer on a metallic substrate and then introduced as a part of the cavity wall into the RF gun. They promise much higher quantum efficiencies of the order of up to 0.1–0.2. The thin film layers are very sensitive to the gun's residual gas pressure and particle back bombardment. Typically, a static vacuum of $< 10^{-10}$ mbar is needed for those cathodes in the gun. Therefore, the high quantum efficiencies have a limited lifetime, which depends on the charge extracted and the dynamic vacuum during operation [11, 12]. These cathodes require a sophisticated infrastructure for fabrication and transfer under vacuum into the RF guns for operation.

For DEFT, we have chosen to use Cs_2Te cathodes because of the small laser spot size needed and the power requirements for the laser. The power density on the cathode would exceed the ablation threshold of copper.

The injector of the DEFT medical treatment accelerator consists of an RF photoinjector and a diagnostic section before the LINAC starts with the first X-band accelerating structure. The photoinjector is a 3 GHz, 2.5 cell standing wave cavity with a photocathode placed in the centre of the half cell. The cathode gets illuminated with a short pulse UV laser to liberate electrons via photo-effect. A solenoid is used to focus the beam right after the cathode while being accelerated with high-gradient RF fields. The RF gun is followed by a beam line section, which provides pumping to reach a good vacuum and charge, beam position and profile, and measurements. A layout of the injector can be seen in Fig. 3.1.

Two pairs of corrector magnets allow the precise alignment of the beam coming out of the electron source within the first accelerating structure based on the beam position information produced by the BPM and the screen. The screen in front of the first accelerating structure allows for checking the uniformity of the transverse beam distribution. This is a critical measurement. An ICT gives a reliable charge measurement before acceleration. The laser input port allows the laser to be sent via an adjustable mirror outside the vacuum to the centre of the cathode. The RF gun itself needs a very good vacuum of the order of $< 10^{-10}$ mbar; therefore, it is separated by a gate valve from the rest of the beamline, and massive pumping is deployed right outside the RF cavity, including NEG pumping.

The key elements of the injector are described in more detail in the following sections.

1.2 S-band RF cavity

The 2D RF design of the RF gun for the DEFT project is shown in Fig. 3.2, and the field distribution on the axis as well as the surface electric field are shown in Fig.3.3. The Superfish code was used to do the 2D design. The parameters of the RF gun are listed in Table 3.2. The efficiency of the RF gun can benefit from a small beam aperture. However, the small aperture is bad for the vacuum pumping. As the klystron can provide a peak power of 23 MW, taking into account the RF loss in the RF system and the 10% operation margin of the klystron, the efficiency of the RF gun is not a limitation. In this case, a larger beam aperture can be an option. The RF gun for the DEFT project has a beam aperture with a radius of 20 mm. To reduce the surface fields, the elliptical iris was applied for the DEFT gun. The mode separation of the DEFT Gun is 42.1 MHz.

The coupling factor of the RF gun is 1.98. Based on the coupling factor, the field on the cathode versus time for the 90 MV/m case can be calculated and is shown in Fig. 3.4. From the curve, the filling time and the unloaded field can be obtained. The field on the cathode has a range of 80–110 MV/m. All

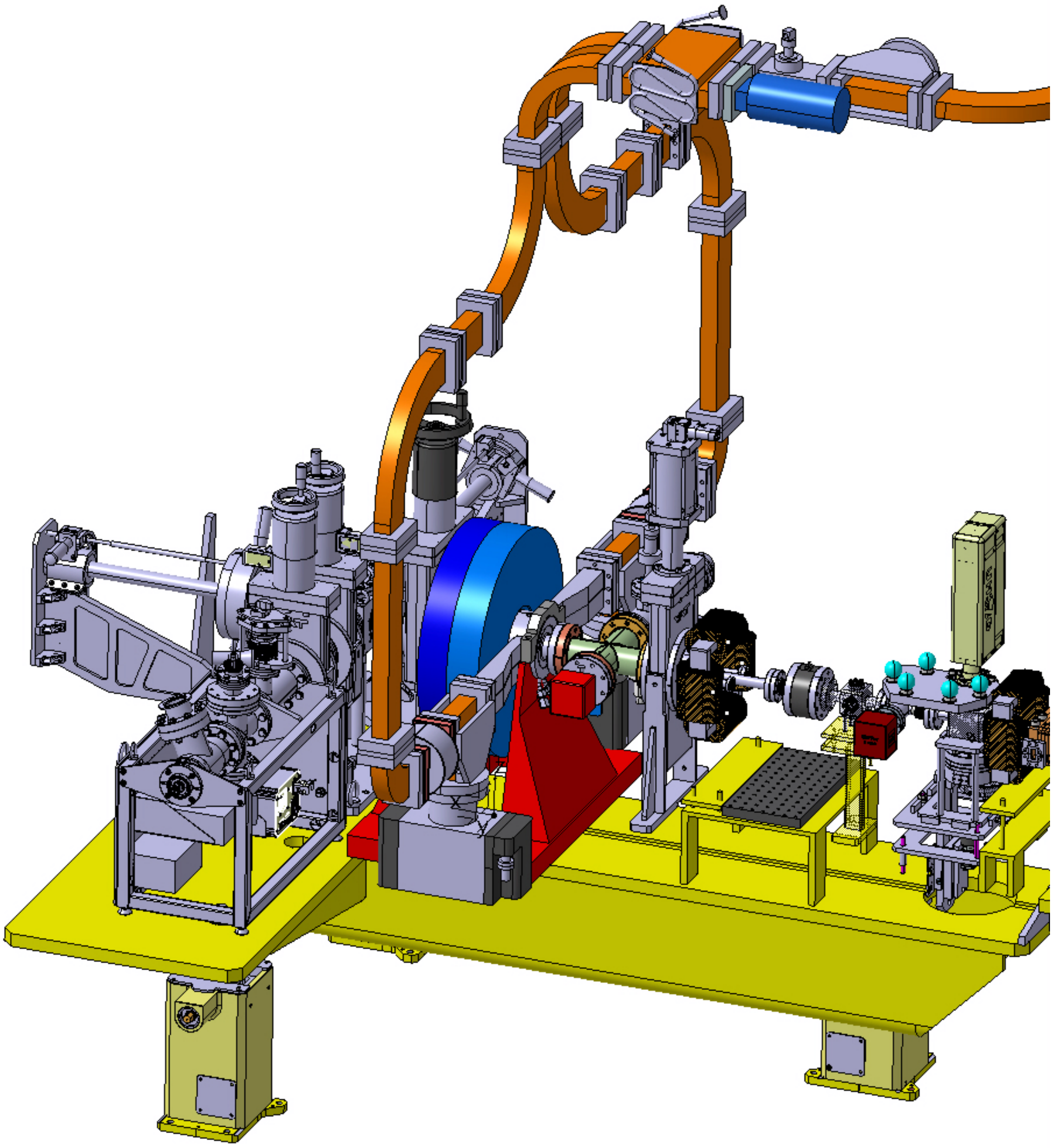

Figure 3.1: Layout of the DEFT injector region, including a load lock system for the cathodes.

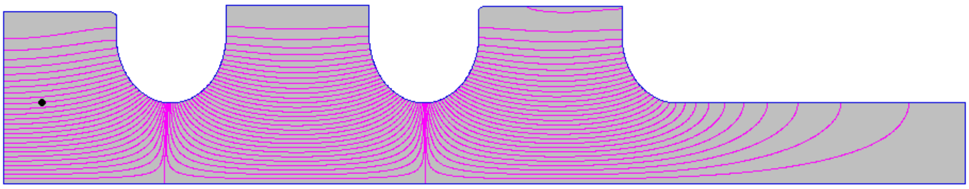

Figure 3.2: Preliminary 2D RF design of the RF gun.

the parameters for different fields on the cathode are calculated and listed in Table 3.3.

Based on the 2D model mentioned above, the 3D RF model was designed using HFSS software. The 3D model, the field on the axis, as well as the wide and narrow band S11 curves are shown in Fig. 3.5.

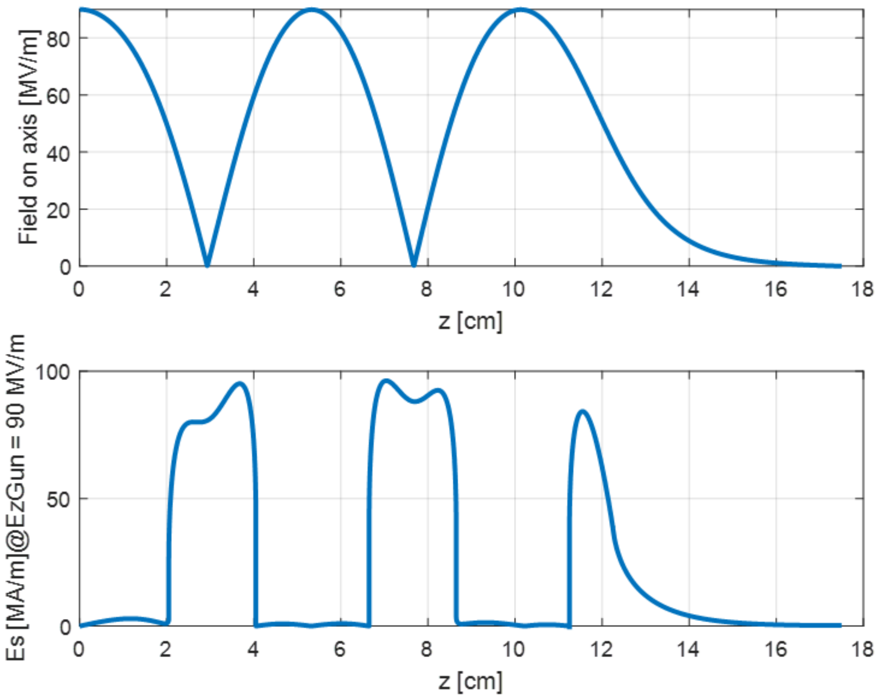

Figure 3.3: Nominal electric field on axis (top) and on the surface (bottom) of the RF gun.

Table 3.2: RF parameters of the RF gun.

RF frequency [MHz]	Em/Es	Hm/Es [kA/(MV)]	Q_0	Mode separation [MHz]
2998	1.07	2.34	14121	42.1

Table 3.3: Parameters of the RF gun for operation at different fields on the cathode.

Ez Gun [MV/m]	Eunloaded [MV/m]	Ebeam [MeV]	Pbeam[MW]	Ploss [MW]	Prf [MW]	Tf [ns]	Tp [ns]
80	83.32	5.84	3.33	8.49	12.19	1071.2	1241.2
90 (Nominal case)	**93.30**	**6.53**	**3.72**	**10.75**	**15.01**	**1126.1**	**1296.1**
100	103.28	7.20	4.10	13.27	18.13	1176.8	1346.8
110	113.26	7.87	4.48	16.06	21.54	1222.9	1392.9

The asymmetry introduced by the two waveguides connected to the coupler cell results in a quadrupolar kick F_2 of the RF accelerating field affecting the beam dynamics. It is defined as

$$F_2 \cdot r^2 = \frac{1}{\pi} \int_0^{2\pi} V_{\mathrm{acc}}(r,\phi)\cos(2\phi)d\phi \quad ,$$

where $V_{\mathrm{acc}}(r,\phi)$ is the voltage along the z direction, with respect to the offset of r and an angle of ϕ. Race-Track shape for the coupler cell was introduced to compensate for the effect of the waveguide coupling holes and minimize the quadrupolar kick F_2 as shown in Fig. 3.6. A parameter of Cd was introduced to define the Race-Track shape, and it is the distance between the centre of the coupler cell and the centres of the arcs. The Cd was optimized to minimise the quadrupolar kick F_2.

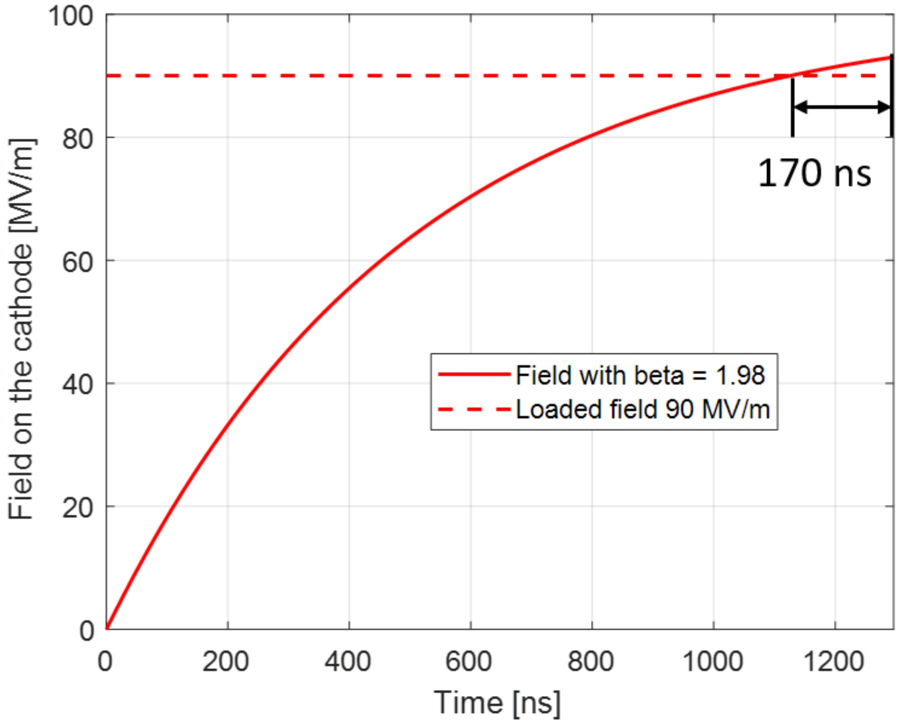

Figure 3.4: Field on the cathode vs. time for 90 MV/m operation.

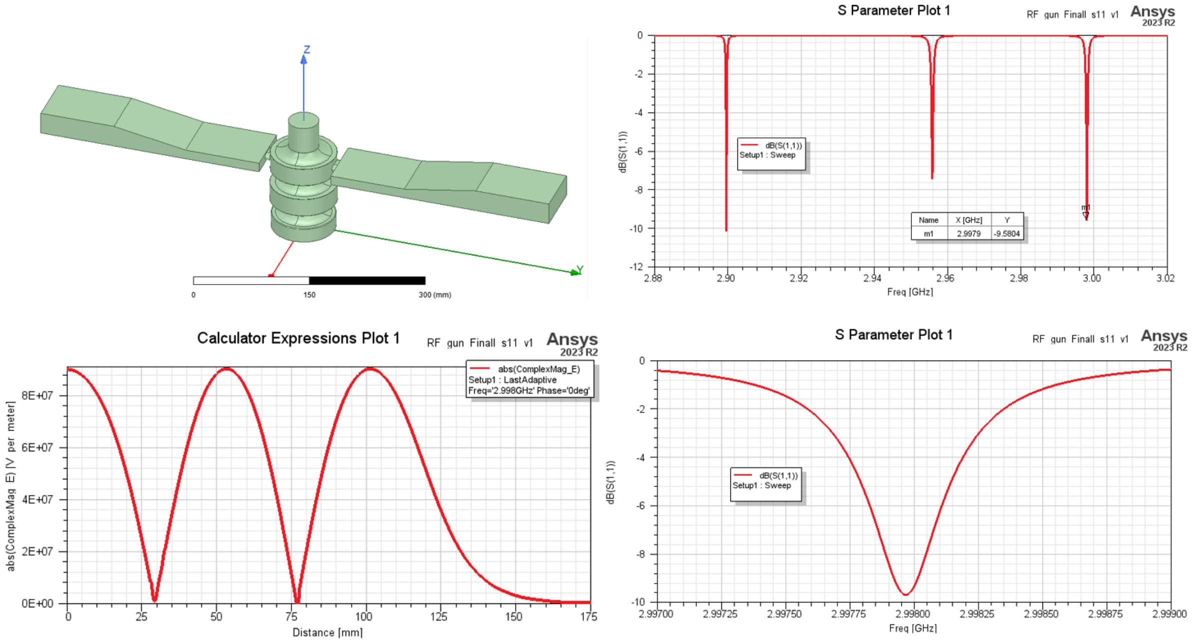

Figure 3.5: The 3D RF model, the field distribution on the axis, as well as the wide and narrow band reflection curves.

1.2.1 *Thermal analysis for the S-band RF gun*

In this subsection, we will discuss the thermal analysis of the RF gun. The methods and formulas are the same as for the accelerating structure and the pulse compression system; for more details, please see Sections 3.1 and 2. The lost power of the RF gun with surface field of 90 MV/m versus time is shown

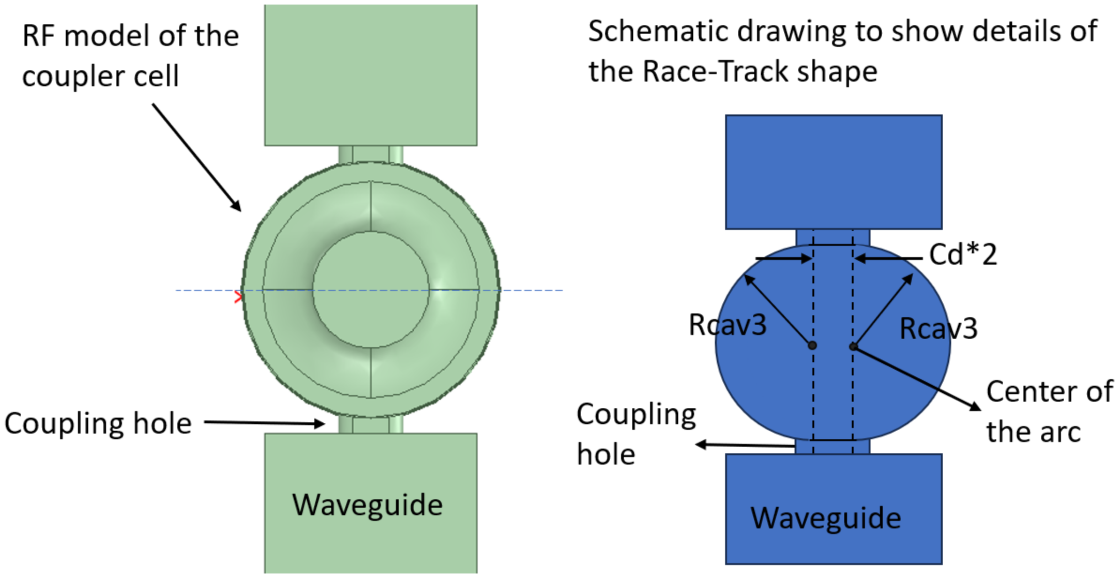

Figure 3.6: RF design and schematic drawing of the coupler cell.

in Fig. 3.7. The lost energy per RF pulse is 9.05 J, which is calculated by integrating the lost power over time. In the 10 Hz case, the average lost power is 90.5 W. In burst mode, the overall lost energy is 362 J. The preliminary mechanical design of the RF gun is shown in Fig. 3.8. The mass of the RF gun is 27.7 kg and the cross section of the cooling pipe is 50.27 mm^2. Based on these parameters, the temperature rise of the cooling water in 10 Hz as well as the temperature rise of the RF gun in burst mode can be calculated. The results are listed in Table 3.4.

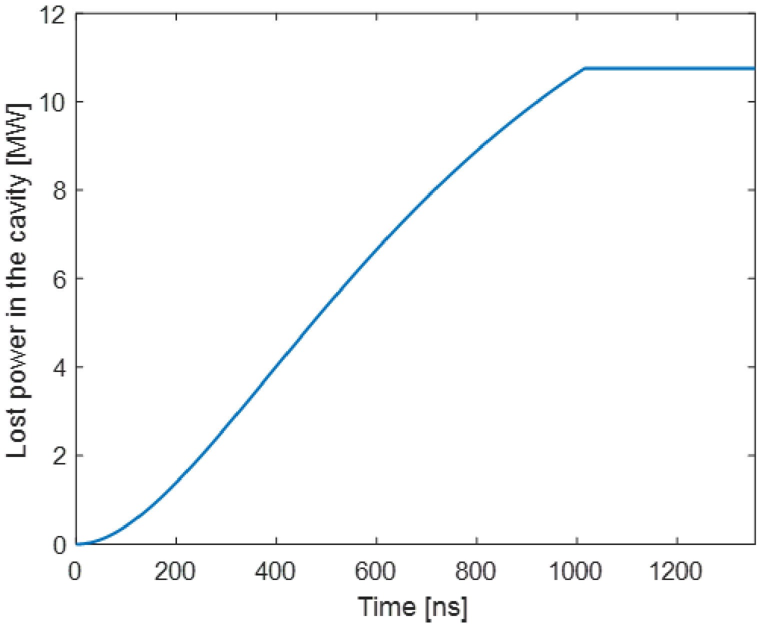

Figure 3.7: Lost power in the RF gun versus time for the surface field of 90 MV/m.

RF sensitivity studies for the S-band gun were carried out to estimate the variation of the RF parameters with temperature. A temperature variation in the cavity will induce a frequency shift due to

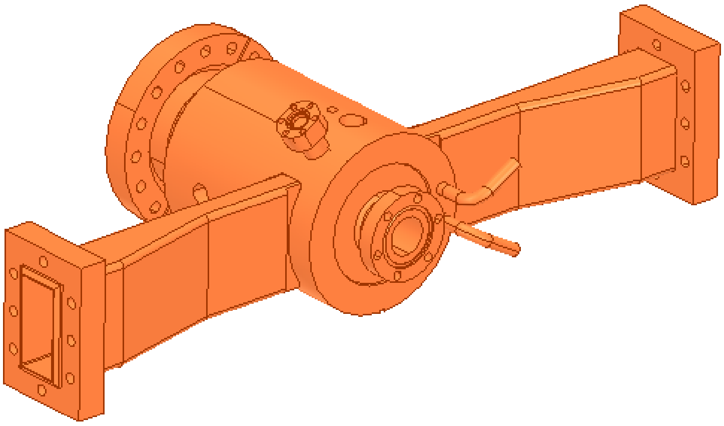

Figure 3.8: Preliminary mechanical model of the RF gun.

Table 3.4: Thermal parameters of the RF gun with surface field of 90 MV/m.

Mass [kg]	27.7
Lost energy per RF pulse [J]	9.05
δT of cooling water in 10 Hz [K]	0.43
δT of component in burst mode [K]	0.034

thermal expansion, given by

$$\frac{\Delta f}{f} = -\frac{\Delta l}{l} = -\alpha \Delta T \quad , \tag{3.1}$$

where Δf is the frequency shift, f is the resonant frequency, $\Delta l/l$ is the scale of the shape due to thermal expansion caused by the temperature variation, $\alpha = 17 \times 10^{-6}$ 1/K is the copper thermal expansion coefficient, and ΔT is the temperature variation.

Then, the amplitude and the phase of the accelerating voltage along the full structure can be computed for different temperature variations, assuming the input frequency of the RF is fixed at $f_0 =$ 2.998 GHz and relativistic $\beta = 1$. The results can be seen in Fig. 3.9.

From Fig. 3.9, it can be obtained that, close to the resonant frequency, the phase of the voltage increases linearly with the temperature by

$$\frac{\Delta \phi}{\Delta T} = 9.1286 \, \frac{\text{deg}}{\text{K}} \quad . \tag{3.2}$$

However, the amplitude shows a non-linear behaviour. In this case, a tolerance in amplitude of ±0.1% corresponds to a temperature change of ±0.06 K.

1.3 Photocathode and preparation chamber

Taking the specification requirements discussed in the introduction (Section 1.1) into account and based on operational experience at CERN, a compromise solution between operational parameters and maintainability is reviewed. As per given specifications, the quantum efficiency (QE) of a photocathode should range above 1% over a lifetime of one year, driven by a robust laser system working in the UV

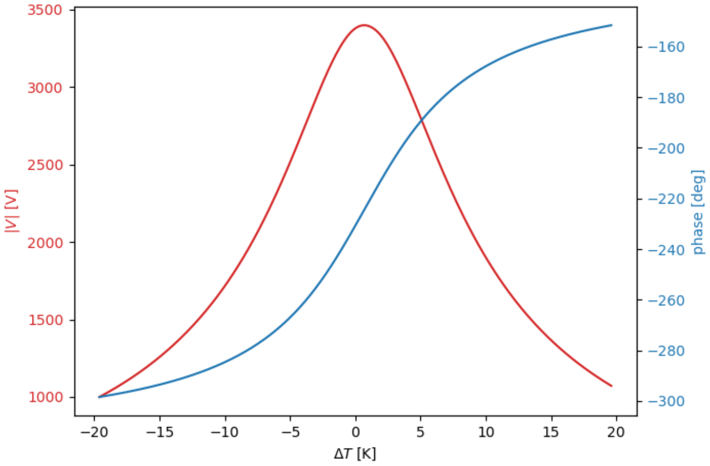

Figure 3.9: Thermal sensitivity study of the accelerating voltage in the S-band RF gun for $\beta = 1$ and $f_0 = 2.998$ GHz.

range and should present a manageable vacuum system and maintenance demands suitable for a medical facility.

Operating an RF photoinjector requires balanced considerations of available photocathode materials, desired quantum efficiency, corresponding laser system requirements, and the projected lifetime of the source. Table 3.5 shows a comparison of common photocathode materials utilised in RF photoinjectors, alongside their QE, laser wavelength ranges, and applications.

Table 3.5: Overview of photocathode types and materials.

Class	Material	QE (per unit)	Wavelength	Gun	Application
Normal conducting metals	Cu, Mg	10^{-5}–10^{-4}	UV	NC-RF	Low rep-rate FELs
Superconducting metals	Nb, Pb	10^{-5}–10^{-4}	UV	SC-RF	High rep-rate FELs
Positive electron affinity semiconductor	Cs_2Te, Cs_3Sb, K_2CsSb and others	0.1–0.2	Visible UV	NC-RF, DC	FELs, ERLs
Negative-electron-affinity semiconductor	GaAs, etc.	0.1–0.35	IR-Visible	DC(XHV)	Polarised Sources, ERLs (ALICE)

As bare metal photocathodes only provide comparatively low quantum efficiencies in the range of 10^{-5}–10^{-4} when irradiated with deep UV laser wavelengths, they are not suitable for the charge demand within this project. Antimonide-based semiconductor photocathodes provide a higher QE and can be illuminated with visible laser wavelengths. However, they typically have very stringent vacuum requirements of $< 10^{-10}$ mbar and limited lifetimes. Taking these considerations into account, selecting copper substrate photocathodes with a thin-film coating of Cs_2Te represents a balanced choice between laser illumination and vacuum requirements with a proven track record and longer lifetimes than

Antimonide-based photocathodes. This choice also determines the required laser system in the UV range with manageable setup, operational, and maintenance parameters (see Section 1.4).

1.3.1 Cs_2Te photocathode production

For the production of Cs_2Te photocathodes at CERN, there are two main Physical Vapour Deposition (PVD) techniques established: Traditional dual-layer sequential deposition (max. initial QE up to 10%) or co-deposition (max. initial QE up to 25%) of Tellurium (Te) and Caesium (Cs) onto a metallic substrate (plug), typically oxygen-free copper or molybdenum similar to the examples shown in Fig. 3.10.

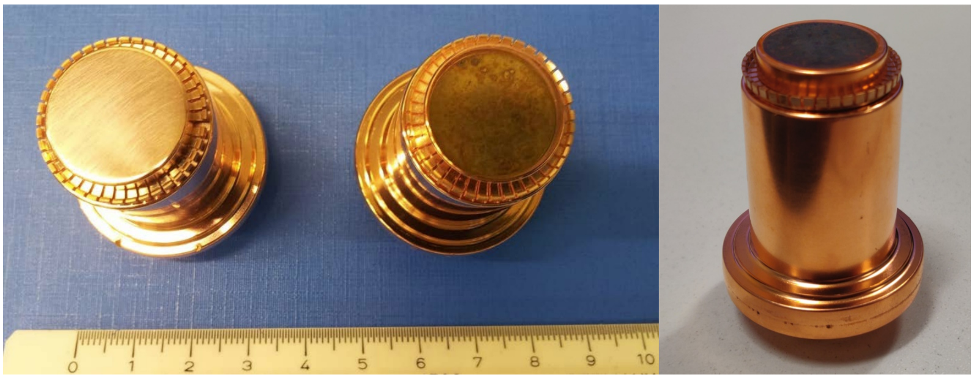

Figure 3.10: Photocathode plugs before Cs_2Te deposition (left), after Cs_2Te deposition (middle), and after extended use in an RF gun (right).

The co-deposition process aims to produce the nm-thickness photoemissive alloy by simultaneously evaporating and mixing the vapours of the two compounds, Te and Cs, before deposition on the substrate. This process can be more efficient since the stoichiometric ratio can be optimised to maximise the QE of the resulting alloy. However, to properly execute this production procedure, real-time monitoring and control of the PVD process, layer thickness measurement with independent quartz crystal microbalances, and laser measurement of the estimated QE value, all under well-maintained Ultra-High Vacuum (UHV) conditions with pressures below 10^{-10} mbar, are crucial requirements. After the production process, the finished photocathode needs to be verified and characterised with a dedicated laser system and DC gun under 'near operational' conditions. A dedicated external laboratory, such as the CERN Photoemission Laboratory, is typically required to ensure the availability of dedicated instrumentation and quality control, as well as complementary services and facilities for machining, metrology, and cleaning of the production components. A simplified schematic overview of the key components of the setup is given in Fig. 3.11.

Besides requiring an additional production facility, this technique also presents the challenge of transporting the finished photocathode plug(s) under UHV conditions to the operational facility using a specialised vacuum vessel ('suitcase') compatible with both installations. These transport vessels must be equipped with active UHV pumping and monitoring devices to ensure the quality and traceability of the photocathode status in transit, especially when transport routes extend beyond the production site. The target operational facility must support a transfer port or load lock system and bake-out equipment to ensure the safe installation of the photocathode. Finally, RF conditioning and QE measurement verification with the local laser system and instrumentation are required to ensure the compliance of the production parameters with the operational parameters.

As an alternative and more direct approach, sequential deposition of Te and Cs can be performed *in-situ* by integrating a preparation chamber, power supplies, and equipment necessary for the PVD process connected directly behind the RF gun. The photocathode plug can be transferred directly in vacuum between the *gun* position and the *PVD* position using suitable built-in manipulators. In this setup,

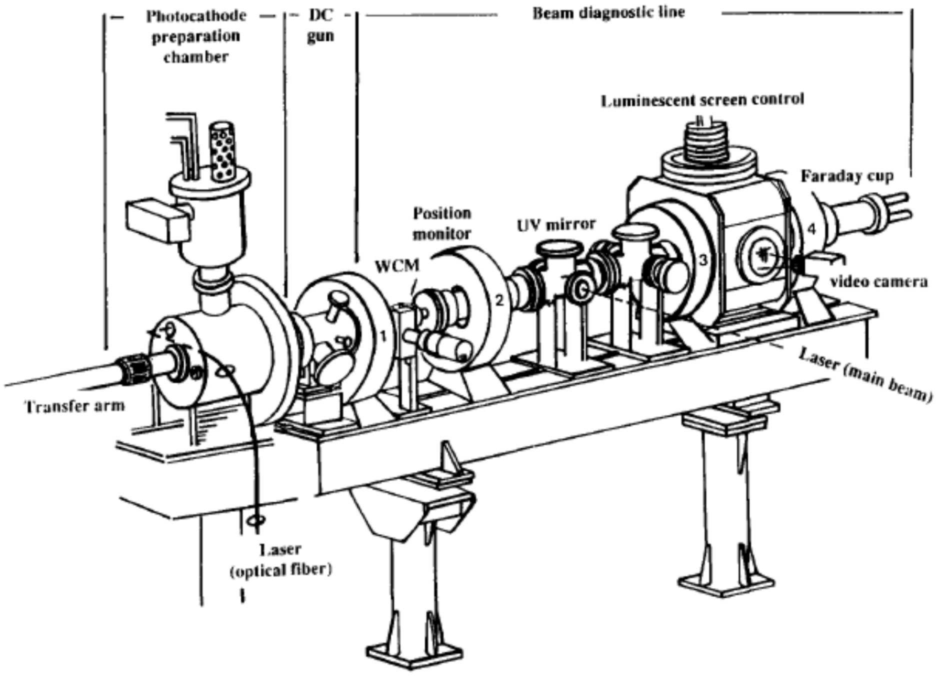

Fig. 1. The dc test bench.

Figure 3.11: Schematic view of the CERN Photoemission Laboratory photocathode production and characterisation setup [13].

the PVD preparation chamber position facilitates the exchange of new and expired photocathode plugs (e.g. too many stacked dual-evaporation layers), as well as the exchange of spent Te and Cs and evaporator crucibles. An example design of such a preparation chamber is shown in Fig. 3.12. This integrated PVD principle is employed for the CLEAR gun at CERN, where a 'rejuvenation' of the photocathode is scheduled during a yearly maintenance period of typically 3–5 days. This work consists of first evaporating a nm-thickness layer of Tellurium and subsequently evaporating a nm-thickness layer of Caesium while monitoring the thickness of the respective layers with a built-in quartz crystal microbalance. This process typically yields a slightly lower QE than co-deposition, as no stoichiometric mixture of Te and Cs takes place. Also, the QE diagnostic capabilities during the evaporation process are limited. After the evaporation process, the photocathode is transferred back into the RF gun position, where it is subsequently conditioned for operation. Typical Cs_2Te photocathodes at CLEAR are operated with QE ranges higher than 1% and lifetime ranges of around a year.

With both approaches to photocathode production, the following key requirements in terms of maintainability and documentation must be taken into account: The dispensers for Te and Cs must be well accessible to facilitate easy exchange and replenishment. The design should offer the option to isolate the preparation chamber housing the PVD process and corresponding instrumentation from the operational components of the RF gun. In addition, the exchange of an expired photocathode should be feasible with minimal downtime and impact on the operation of the facility. Monitoring and control hardware and software for the preparation chamber and production process are crucial elements in advancing towards an industrial approach to both operation and production of the electron source.

1.3.2 Photocathode lifetime

Based on CERN operational experiences, the lifetime of Cs_2Te photocathodes produced using sequential deposition should offer a good compromise for handling, rejuvenation, and conditioning. Photocathodes from Cs_2Te have been the primary choice for electron sources by worldwide accelerators, also due to

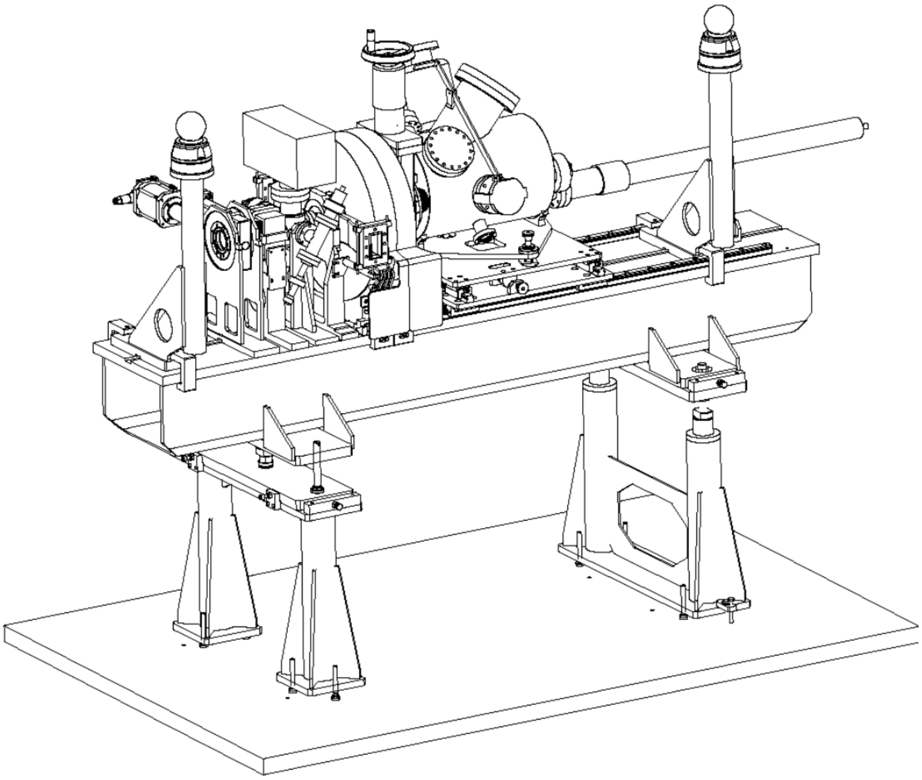

Figure 3.12: Schematic of the CLEAR RF gun on the left and the integrated PVD preparation chamber on the right [13].

their stable performance in complex operation environments and long lifetime [14, 15, 16, 17, 18, 19]. Corresponding studies were done mostly for the PHIN photoinjector (currently being operated at the AWAKE experiment [20]) and photocathodes fabricated via co-evaporation at the CERN Photoemission Laboratory [12, 21]. These photocathodes traditionally present an initial QE$>$ 10% after fabrication when illuminated with a UV-wavelength laser beam. The lifetime is defined as the time during which the cathode can produce the nominal charge with the nominal (or less) laser energy. During continued operation and charge extraction, the QE decreases, and the photocathode must either be 'rejuvenated' or exchanged with a new one. Photocathode lifetime is typically defined as the time taken for the QE to fall to $1/e$ of its initial value, and the decay can be represented as the sum of two exponentials with a fast and slow decay:

$$\mathrm{QE}(t) = \mathrm{C}_1 e^{-\frac{t}{\tau_1}} + \mathrm{C}_2 e^{-\frac{t}{\tau_2}} \tag{3.3}$$

with τ_2 of the slow decay representing the dominant time constant for defining the lifetime of the photocathode as an exponential law, and C_1 and C_2 fitting constants to the decay curve and proportional to the fresh photocathode QE. In one of the first CERN studies of $\mathrm{Cs_2Te}$ photocathode lifetime under controlled conditions in a real RF photoinjector (PHIN), the photocathode was used for producing an electron beam with 2.3 nC per bunch, 350 ns macropulse duration, and 0.8 Hz macro-pulse repetition rate. The QE data from this experiment, displayed in Fig. 3.13, is well represented by a double exponential leading to an estimated lifetime of 304 ± 20 hours.

In Fig. 3.14 (a), a lifetime study performed with a longer train length of 1.6 µs, 2.3 nC per bunch and 0.8 Hz macro-pulse repetition rate showed that a QE higher than 8% was maintained over more than 110h. An exponential QE decay was not evident in this study, indicating that the $1/e$ lifetime would

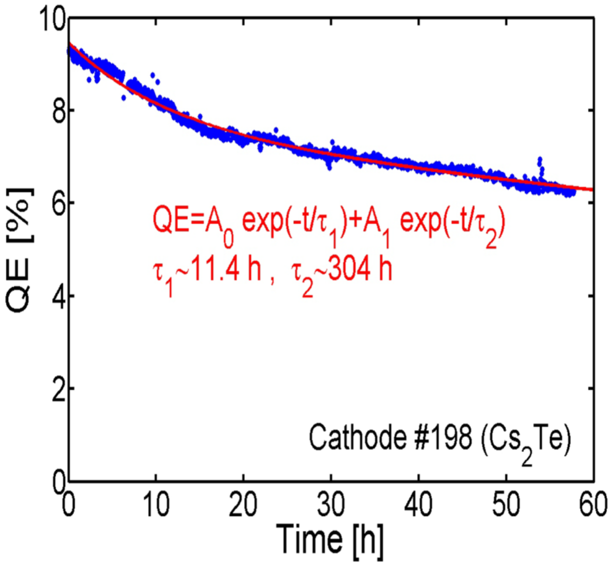

Figure 3.13: Lifetime study of a Cs_2Te photocathode.

easily exceed 300h when compared to the previously described study. Another lifetime measurement was performed with the same train length (1.6 µs and 2 nC per bunch charge but a higher macro-pulse repetition rate of 5 Hz. The results presented in Fig. 3.14 (b) show a very similar trend, where the QE seemed initially to decrease, but this was only caused by a drifting RF phase. By correcting the phase, the initial QE value could be restored and kept constant over a long period. The total extracted charge for these experiments ranges from 1.7 to 2.6 C.

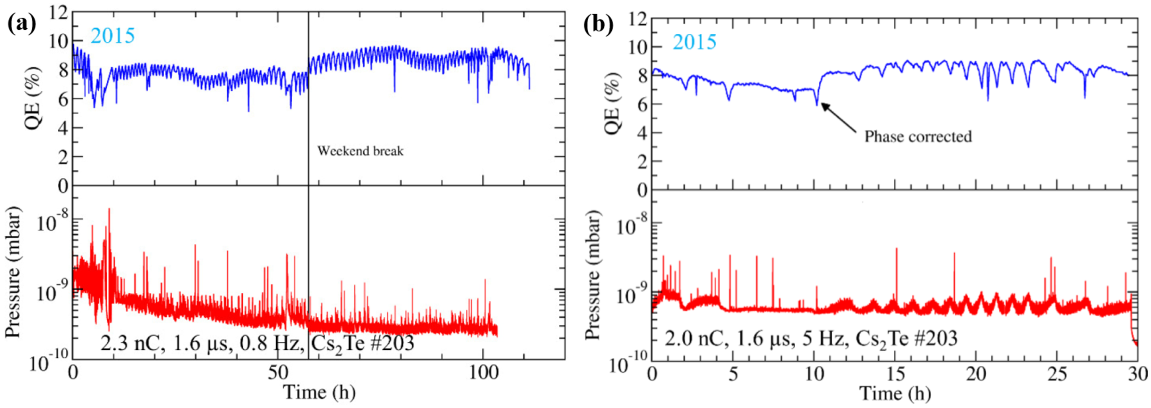

Figure 3.14: Lifetime studies of a Cs_2Te photocathode exposed to long pulse train lengths and high macro-pulse repetition rates.

Cs_2Te photocathodes produced with the co-deposition process and subsequently operated at the AWAKE experiment on a routine basis were showing QE values higher than 5% during all experiment runs. The sequentially deposited Cs_2Te photocathodes installed at the CERN CLEAR facility typically show an initial maximum QE value of up to 4–6% after production and rejuvenation, which then maintains a steady QE level of over 0.5% during all experiment runs throughout the year. Additional experimental information on the rejuvenation processes can be found in Ref. [22]. While no specific lifetime studies have been performed for the CLEAR facility, the corresponding operational hours can be approximated to similar results as for the AWAKE experiment.

The operating lifetime and performance of Cs_2Te photocathodes are critically dependent on well-maintained static and dynamic vacuum levels, as well as differing beam properties such as bunch charge, train length, and repetition rate. These operational factors must be taken into consideration as they contribute mainly to the dynamic vacuum levels and the deterioration of the photocathode. The photocathode deterioration processes can be divided into two families: *chemical poisoning* (residual gas contamination) and *radiation damage* (ion and electron bombardment).

1. **Chemical poisoning** is associated with chemical reactions of the photocathode surface with the residual gases remaining in the vacuum chamber and creating mainly oxides but also other compounds which reduce the photoemissive yield. In addition to a good static vacuum (background pressure), the dynamic vacuum level (i.e., during operation) should be monitored and maintained as well as possible. Many phenomena can originate pressure bursts, such as field emitted electron stimulated desorption (ESD) and desorption induced by beam losses, meaning direct interaction of the beam with the inner walls of the vacuum chambers.

2. **Radiation damage** includes both the impact of ions and electrons onto the photocathode surface. This ion back bombardment is associated with the ionisation of residual gases by the created electron beam within the gun. These positive ions are accelerated by the electric field *towards* the cathode surface at high energy, depending on the gun peak gradient, where their impact can cause physical damage and material ablation. If the beam transport can be optimised to minimise beam losses, the vacuum can be maintained at a constant level, which will be beneficial in terms of preserving the photocathode lifetime and performance.

1.4 Laser system

In this section, the main components of the photoinjector laser system are described. The optical chain of the laser is based on the one implemented in the CLEAR facility at CERN. This description aims to give a comprehensive view of the necessary performance parameters of each of the elements of the laser system and their overall expected performance. The choice of laser technology, however, is not unique, and other systems with similar parameters can be used as long as they meet the final specifications.

The widely available laser systems are typically operating in the near-IR spectral region, which requires frequency conversion to access DUV wavelengths necessary for photoemission.

Following the requirements for bunch train temporal structure and charge, and assuming that the photocathode of choice is made out of Cs_2Te, the requirements of the laser system are specified in Table 3.6. These parameters assume a quantum efficiency of at least 1%, and unsaturated photoemission conditions. The proposed system, however, will need to have a pulse energy considerably larger to accommodate potential losses in the laser beam delivery chain, as well as saturation and ageing effects on the cathode.

Common technologies capable of satisfying the requirements of the photoinjector laid out in Table 3.6 include Neodimium-doped and Ytterbium-doped laser materials. Here, we describe a system based on Nd:YLF, which is currently used at CERN. A schematic of such a laser is shown in Fig. 3.15. In the following, we describe the expected performance of each component separately, although the final solution can be either implemented separately or altogether, depending on the laser technology chosen. In most cases, the system is composed of a master oscillator locked to the RF reference (either at 1.5 or 3 GHz), a pulse picking system, an amplification chain, a harmonic conversion stage, and a beam delivery system to the cathode.

For some laser technologies, the laser may include an additional pulse stretcher and compressor to perform what is known as Chirped Pulse Amplification (CPA). This is the case for Yb-doped laser media. Additionally, the pulse picking system may be located at the output of the oscillator or the front-end amplifier. This choice depends on the specific performance of the pulse picker system in terms of

Table 3.6: Main specifications of the laser and beam delivery system.

Laser specifications	**Value range**
Wavelength	< 270 nm
Minimum single pulse UV energy	135 nJ
Typical single pulse UV energy	1 µJ
Bunch spacing	1/3 ns
Minimum burst UV energy	$\sim$ 135 µJ
Typical burst UV energy	1 mJ
Max. number of bunches	1100
Max. number of trains / s	400
IR to DUV Conversion efficiency	$> 10\%$
Minimum UV average power	54 mW (full repetition rate)
Typical UV average power	400 mW (full repetition rate)
Typical UV average power	40 mW (10% duty cycle)
Pulse duration (FWHM)	3–7 ps
Train energy stability (RMS)	$< 1\%$
Laser beam delivery	**Value range**
Beam size on cathode (RMS)	1.6 mm
Beam quality	$M^2 < 2$
Fluence on cathode	~ 2 µJ/cm^2

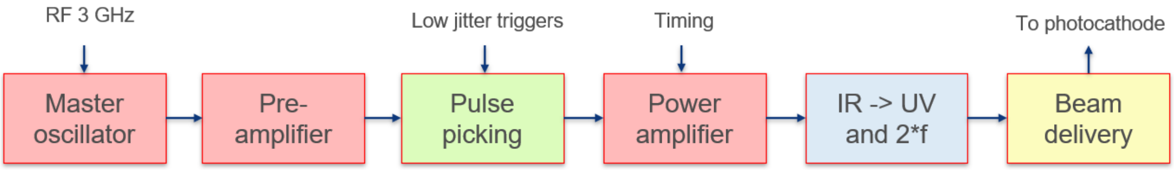

Figure 3.15: Main components of the laser systems.

train-to-train stability and the amplitude noise characteristics of the laser oscillator.

The train “flatness” is also affected by the location of the pulse picking system. In this regard, modulators used at the output of the oscillator normally have a temporal transfer function with a ramp profile to compensate for loading (or saturation) effects in the laser amplifier chain. A simpler scheme is to use the pulse picking after the front-end and use square gate functions instead. This arrangement can be used when the pre-amplifier operates continuously to a high average power, although the resulting train usually has a slight amplitude negative slope, resulting from the aforementioned loading effects. The most robust solution is to then design the power amplifiers so that the loading effect is minimal, which is normally achieved by heavily saturating the gain of the amplifiers.

1.4.1 Master oscillator and pre-amplifier

The overall stability of the photoinjector laser relies heavily on the stability of the front-end laser. We propose to use Neodymium-doped laser materials due to their durability, reliability and availability, but other laser materials can perform the task too. Here, we propose to use a front-end photoinjector laser composed of a Nd:YLF oscillator and pre-amplifier, with the specifications shown in Table 3.7. The seed pulses are produced by a diode-pumped Nd:YLF mode-locked oscillator at a repetition rate of 1.5 GHz with an average power of ∼300 mW at 1047 nm. The output pulse duration is of the order of ∼5 ps.

Table 3.7: Front-end laser main performance parameters.

Laser parameter	**Value range**
Laser gain medium	Nd:YLF or similar
Wavelength	1030–1047 nm
Operation mode	CW mode-locked
Pulse repetition rate (locked)	1.5 GHz ± few Hz
Average power oscillator	∼100 mW
Average power pre-amplifier	∼10 W
Pulse width (FWHM)	3–7 ps
Timing jitter	< 0.3 ps RMS integrated over [1 kHz–100 MHz]
Beam quality	$M^2 = 1.1$
Power stability (after warm-up time)	<0.5% over long periods of time

The synchronization with the RF reference is obtained at the laser oscillator level. The frequency (or repetition rate) of the oscillator is compared to the RF reference, and a PLL acts on the laser cavity end-mirror through a fast piezo-controller to stabilize it (with a feedback loop bandwidth of up to several 10 kHz). Because of the small tuning range of the laser oscillator, the cavity length needs an additional actuator to adjust coarsely the cavity length to a value close to the RF reference to be able to lock it (with a precision of the order of a few kHz). The base plate of the front-end laser is temperature stabilized by water cooling using a chiller with a temperature stability of 0.01 K, ensuring stable operation of the locking system.

The typical time jitter is of the order of <100 fs RMS. However, the requirement for operations is of the order of ∼ 300 fs RMS. The laser oscillator requires periodic intervention (about ∼1 per month) to ensure reliable long-term operation.

The oscillator output pulses are amplified by a pre-amplifier to boost the available average power up to ∼10 W. The pulses delivered by the pre-amplifier have the same temporal characteristics as the oscillator pulses. The tuning of the wavelength of the pumping diodes of the pre-amplifier is performed by temperature adjustment of its chiller with 0.1 K increments. This chiller actively stabilizes the temperature of the pumping diode stack enclosure. As the diodes degrade with use, it is required to adjust the temperature set point (usually by lowering it) in order to match the emission wavelength of the diode stack to the peak of the absorption cross-section spectrum of the laser gain medium.

1.4.2 Pulse picking and interleaving system

The pulse picker should be designed to allow discrimination of single pulses from the laser front-end at 1.5 GHz repetition rate (this is achieved with a rise-time < 400 ps). An additional pulse picker is normally used in series with the variable pulse picker to limit the maximum train length in case of failure. Note that in the proposed scheme, the oscillator is running at 1.5 GHz, but the final repetition rate of the UV laser is 3 GHz. This is because we use an inter-leaver at the last stage of the laser to split and recombine the output. The consequence of this arrangement is that the resolution for the pulse picking scheme is 2 UV pulses. Since the trains have around 1000 pulses, this represents 0.2% of the integrated train charge. This scheme is depicted in Fig. 3.16.

The pulse picker is typically composed of Pockels Cells and polarizers as depicted in Fig. 3.17. As shown, the input polarization into the first polarizing beam splitter (P1) is vertical. This polarizer defines the input polarization into the fast pulse picker. The polarization is then rotated by 90° when PC1

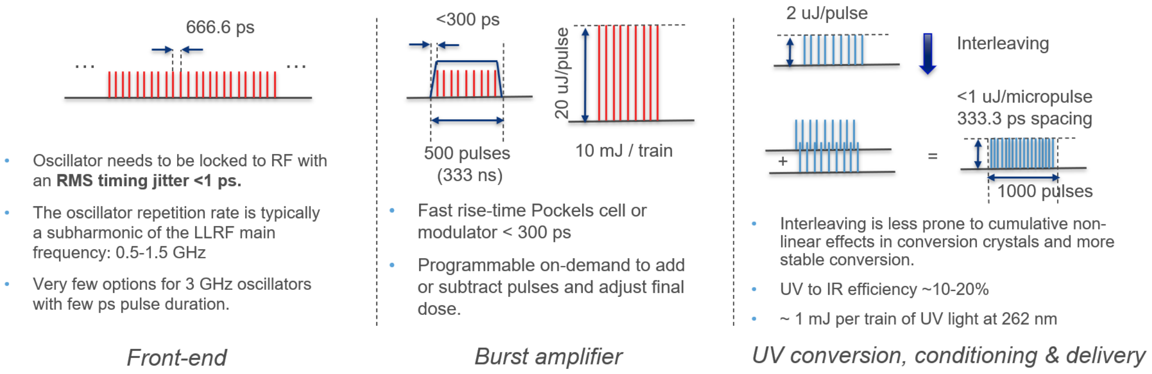

- Oscillator needs to be locked to RF with an **RMS timing jitter <1 ps.**
- The oscillator repetition rate is typically a subharmonic of the LLRF main frequency: 0.5-1.5 GHz
- Very few options for 3 GHz oscillators with few ps pulse duration.

- Fast rise-time Pockels cell or modulator < 300 ps
- Programmable on-demand to add or subtract pulses and adjust final dose.

- Interleaving is less prone to cumulative non-linear effects in conversion crystals and more stable conversion.
- UV to IR efficiency ~10-20%
- ~ 1 mJ per train of UV light at 262 nm

Figure 3.16: Scheme for laser pulse train generation in the Front-end, amplification in the burst mode, and conversion to the DUV and interleaving of trains to produce the 3 GHz repetition rate beam.

is triggered. Under this configuration, all the pulses propagating through PC1 are normally reflected by P2, except during the time that the voltage is applied to PC1, being transmitted by P2.

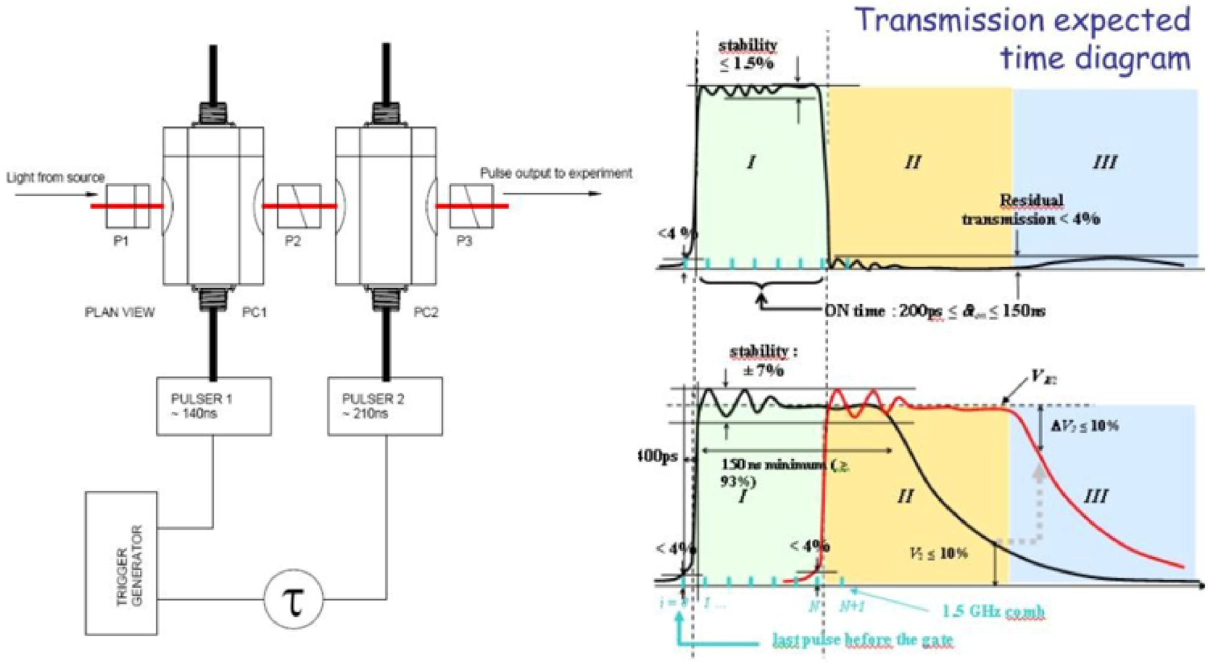

Figure 3.17: A pulse picking system based on Pockels cells (PC1 and PC2) and polarizers (P1, P2 and P3) can produce the necessary rise time of <300 ps. The pulsers are high-voltage power supplies triggered by the generator with a variable delay τ. On the right is an expected temporal transfer function of a similar pulse picker.

The pulse duration of the voltage signal applied to PC1 is usually fixed (and longer than the train length), and the number of pulses transmitted through P2 remains constant.

The PC2 timing defines the closure of the time window for the pulse picker. When the transmitted pulses via P2 impinge PC2, their polarization is again turned by 90° while the voltage is applied to PC2. Analogously to P2, P3 selects the horizontally polarised portion of the incoming pulse train.

PC1 and PC2 are driven by a high-voltage pulse generator. The pulse generators are triggered externally by a low-timing jitter (< 30 ps) trigger from the timing rack. This requirement is normally enforced due to the “non-flat” nature of the pulse picker temporal transfer function. Although reproducible, it tends to have ripples with a few % amplitude variations. To avoid additional micro-pulse instability, it is usually required that the timing jitter of the pulse picker be lower than the temporal waveform of these ripples. The transmission function profile of the pulse picker arises from the impedance characteristics and bandwidth of the Pockels cell circuit and load. The electrical parameters of the cell were matched to 50 Ω to ensure that the waveform suffers no distortions due to electrical mismatch and cable reflections (large enough reflections can partially re-open the cell after a short time delay). Unfortunately, the internal connections of the Pockels cell typically present a high inductance to truly match 50 Ω, which makes the appearance of the aforementioned ripples inevitable.

The main specifications for the fast pulse picker include a sharp rise time of less than 300 ps, with an amplitude stability or modulation within the transmission window of <1%. In terms of residual transmission, it was required to be <4% for the region outside the window. Each Pockels cell had a contrast rejection outside the selected train of 10 000:1, which theoretically leads to 0.7% RMS modulation in the transmission window (4% peak to valley). These specifications are included in Table 3.8. The transmission of each Pockels cell is normally around 92%, whereas each polarizing beam splitter has a transmission of 95% for most suppliers. The cumulative power transmission of the fast pulse picker should be more than 75%.

Table 3.8: Pulse picker system main requirements.

Pulse picker parameters	**Value range**
Rise/Fall time	<300 ps
Duration “open” gate	Variable and up to 333.3 ns
Step resolution	30 ps
Repeatability	< 1% RMS
Overall contrast	> 1000:1
Overall transmission	> 75%
Repetition rate	single-shot to 400 Hz
Trigger timing jitter (RMS)	<30 ps

The interleaver is based on a common concept around the photoinjector community: pulse stacking. Traditionally, pulse stackers are used in order to achieve high-brilliance and ultra-short FEL pulses by shaping the profile of the UV pulses. The so-called pulse stacking technique involves the production of replicas of a single UV laser pulse. The temporal superposition of these gives the picosecond a flat-top amplitude when the various pulses partially overlap in time, reducing space charge effects. As the delay between replicas is increased beyond the pulse duration, multiple electron bunches can be generated within the same RF cycle.

For splitting and recombining the UV pulses, a modified Mach-Zender interferometer was used (see Fig. 3.18). The laser pulse was first divided into two by a polarizing beam splitter (PBS1) so that the P-polarised beam goes straight and the S-polarised beam is reflected sideways. The ratio of power between each beam is controlled by the half-waveplate HWP1. Each of the beams (P and S) hits the set of mirrors, and then they are recombined by another polarizing beam splitter cube (PBS2). One set of mirrors was positioned on a movable platform so that the delay between the two beams could be adjusted. A second half-wave plate (HWP2) provided adjustment of the intensity of the main beam.

Both wave-plates and the delay stage are motorized for remote control, while PBS2 has 2-axis motorization (tip-tilt) in order to gain independent alignment of the two beams on the cathode. The delay stage provides a temporal resolution of 17 fs, with a delay range of up to 1 ns. This wide range opens the possibility of doubling the repetition rate of the laser to 3 GHz, if a delay of 333 ps is set. The tip-tilt of

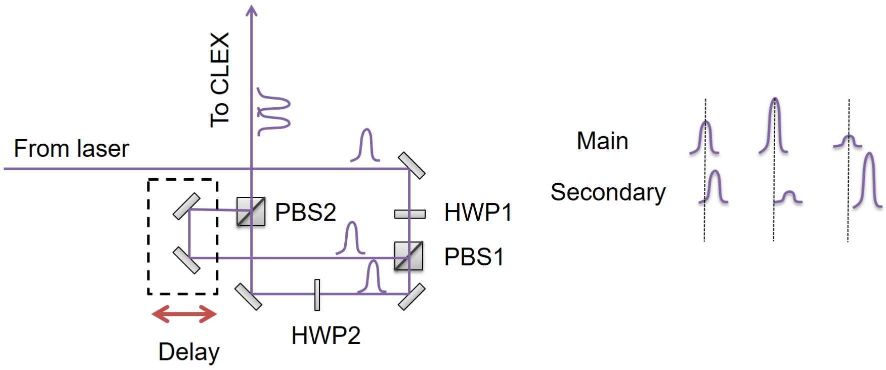

Figure 3.18: Interleaver or double UV pulse generation setup.

PBS2 is performed using a stepper motor actuated high precision mount, with a resolution of 0.0016°.

In terms of contrast, the PBS should have a contrast of 100:1 between the transmission of P-polarised light and the reflection of S-polarised light. This means that, in the best-case scenario, a leak of 1% from one of the arms will always leak through the double-pulse generation setup onto the cathode. To avoid this scenario, remote-controlled motorized beam stoppers have been installed in each arm. The double-pulse setup also serves as power control for the UV beam by tuning either HWP1 or HWP2.

It is important to note that the output pulses from the stacker have P and S polarization. A summary of the specifications required for the pulse interleaver is given in Table 3.9.

Table 3.9: Interleaver system main requirements.

Interleaver parameters	**Value range**
Temporal step resolution	$<$100 fs
Polarizers contrast	$>$100:1
Transmission losses	$<$10% in the UV
Beam pointing overlap	$<$ 1 mrad

1.4.3 Amplification chain

The output from the pulse picker system is usually an image relayed onto the main amplifier head by employing a 4f telescope. An isolator needs to be placed before the amplifier to avoid potential back-reflections. The beam is then passed through the gain media to amplify it (a few passes maximizes the extraction efficiency of the amplifier without diffraction effects and a reasonable footprint of 0.5 × 1.5 m).

The amplifier is typically a Nd:YLF rod housed in a water-cooled copper mount. The rod is side pumped (300–400 μs pulses with a few kW average power during the pulse) at a maximum repetition rate of 400 Hz. After amplification, the pulses had an energy of approximately 20 μJ at 1047 nm (10 mJ for a train of 500 pulses). The resulting specifications are summarized in Table 3.10.

Since the aperture of the gain medium is relatively small compared to its length, the multi-pass amplifier was designed in a way such that each pass impinges the laser medium with the minimum angle of incidence possible. This was achieved by utilising both azimuthal and tangential planes for each pass through the gain medium.

Table 3.10: Amplifier chain performance requirements.

Interleaver parameters	Value range
Single output pulse energy	20 µJ
Burst output energy (500 pulses)	10 mJ
Burst-to-burst energy stability	<0.5% RMS
Burst repetition rate (full)	400 Hz
Output average power (Max.)	4 W
Output average power (Typ.)	0.4 W
Pump pulse duration	300–500 µs

1.4.4 UV harmonic conversion

Frequency conversion is performed with standard non-linear optical crystals. For the second harmonic generation (from 1047 to 527 nm), type II conversion in a 10 mm long KTP crystal yields a conversion efficiency of 35%. The spot size in the crystal is approximately 3 mm in diameter ($1/e^2$) with vertical polarisation. The output at 527 nm is horizontally polarised with a maximum pulse energy of 5 μJ.

Conversion to the UV is performed in a 12 mm long BBO (type I phase matching), utilising directly the output from the KTP crystal (similar beam diameter of around 3 mm). The typical efficiency of the process is approximately 40%, bringing the overall efficiency to 20% from IR to UV. The conversion efficiency from IR to UV is summarized in Table 3.11 both for the single pulse and for the long train cases. A slightly different conversion efficiency was measured for long trains of 100 ns, where the existence of short life-time (ns to ps) colour centres in the BBO crystal may play a role.

Table 3.11: Summary of conversion efficiency from IR to UV.

Parameter	Single pulse	Long train (333 ns)
IR to VIS conversion	50%	50%
VIS to UV conversion	Up to 40%	Up to 20%
Typ. IR-UV conversion	Up to 20%	Up to 10%
Typ. UV pulse energy	$\sim 4\mu$J	$\sim 2\mu$J
Max UV energy/bunch at cathode	$\sim 2\mu$J	$\sim 1\mu$J

1.4.5 UV beam delivery to the photocathode

The distance from the laser room to the photocathode is typically about 10s of meters. An optical relay was needed to minimize the consequences of disturbances of the beam alignment along the path (tilt of mirrors, displacement of components by vibration, thermal expansions, as well as turbulence). The design for the laser diameter on the photocathode was 1.6 mm ± 10% RMS with position instability of less than 10% of the diameter (i.e. 0.1 mm RMS).

The magnification of the telescope relay is typically 1. Transverse adjustment of the UV laser beam is done in order to optimize the laser fluence in the photocathode. Variation of the spot size may be required, for example, to minimize electron beam emittance or to obtain a higher charge per bunch (by maximizing the charge yield of the RF gun). Several approaches exist to achieve this, for instance image relaying a variable diameter aperture onto the photocathode or a variable mismatched telescope can be introduced. Further details on existing UV beam delivery systems are available in the reports on the AWAKE [20] and CLEAR [23] facilities.

The conditioning of the UV beam is critical for optimization of accelerator performance. Steering of the UV beam on the photocathode is performed using a motorized mirror mount. A motorized filter wheel equipped with a set of neutral density filters is used for varying the energy of UV laser pulses, while the laser energy meter provides a reading of the pulse energy. The length of the UV optical path is adjusted to match the desired timing of the electron bunches. A motorized aperture enables remote control of the laser beam spot size on the photocathode. Examples of laser beam images recorded with the virtual cathode camera are presented in Fig. 3.19. In combination with control of the pulse energy delivered to the cathode, it was possible to perform measurements of electron bunch charge and emittance versus the laser beam size and pulse energy.

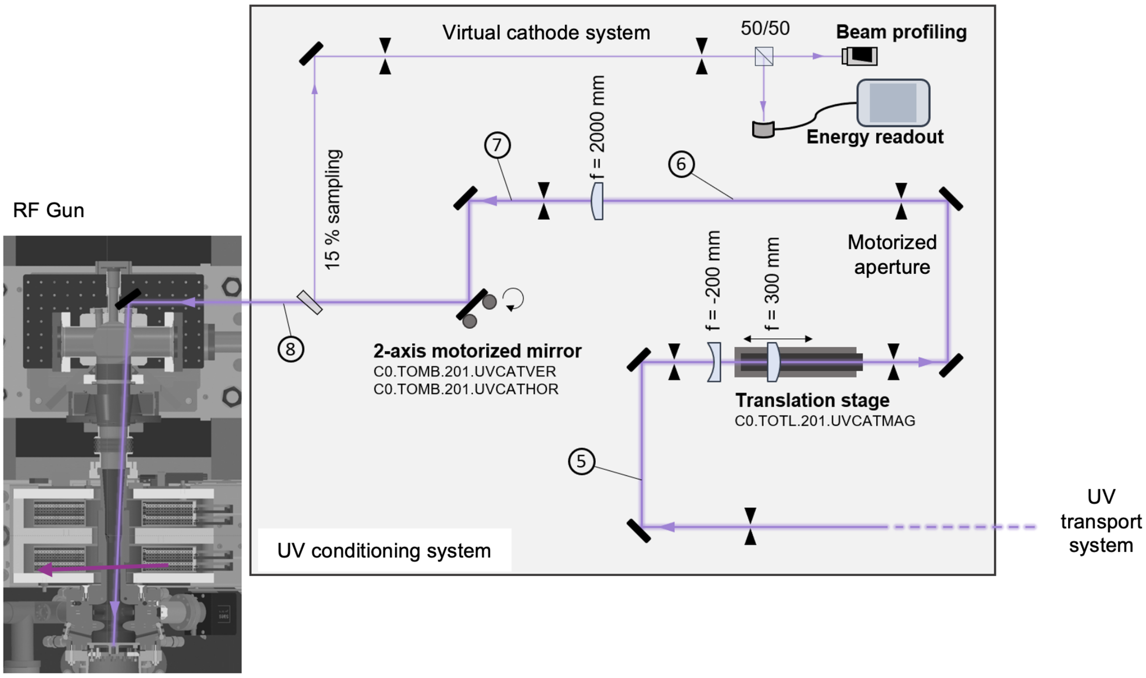

Figure 3.19: Schematic of a UV laser conditioning system, including virtual cathode and control systems.

2 The X-band accelerating structure

2.1 RF design and parameters

The accelerating structure is a strongly tapered travelling wave disk-loaded waveguide structure which consists of 70 regular cells with RF phase advance per cell of 120° and two coupler cells at the input and output of the structure.

2.1.1 Single cell design

The geometry (an inside vacuum shape) of a regular cell is shown in Fig. 3.20. It consists of a central cavity (cell) and four damping waveguides attached to it. The shape of the outer wall of the cell is optimized to reduce the surface magnetic field. The iris on the x-z plane (z is the direction of the beam path) has an elliptical shape to minimize surface electric field and the modified Poynting Vector S_c. The distribution of the surface electric and magnetic fields, as well as that of the S_c, is shown in Fig. 3.21.

The shape of the iris on the x-y plane is shown in Fig. 3.20 left. It is not round but consists of 8 arcs of two different radii. It is optimized to minimize the octupole (F_4) and sixteen order multipole (F_8), defined as

$$F_4 \cdot r^4 = \frac{1}{\pi} \int_0^{2\pi} V_{\text{acc}}(r,\phi) \cos(4\phi) d\phi$$

and

$$F_8 \cdot r^8 = \frac{1}{\pi} \int_0^{2\pi} V_{\text{acc}}(r,\phi) \cos(8\phi) d\phi \quad ,$$

where $V_{\text{acc}}(r,\phi)$ is the voltage along the z direction, for an offset of r and an angle of ϕ. The geometry of the first, middle and last cells of the tapered structure has been optimized individually, and their parameters are listed in Table 3.12.

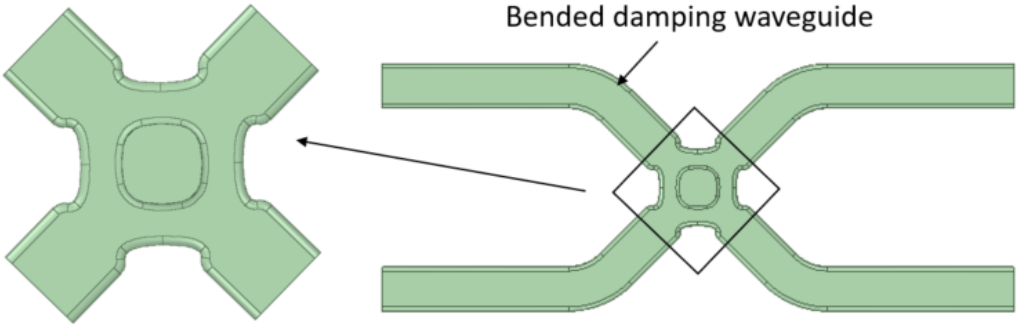

Figure 3.20: Geometry of the internal (vacuum) volume of a regular cell.

Table 3.12: RF parameters of the first, middle, and last cells.

Parameters	**First cell**	**Middle cell**	**Last cell**
Aperture radius [mm]	4.6	3.8	3.0
Frequency [GHz]	11.994	11.994	11.994
E_s/E_a	2.61	2.37	2.15
H_s/E_a [mA/V]	4.55	4.29	4.10
S_c/E_a^2 [mA/V]	1.29	0.78	0.45
R'/Q [kΩ/m]	9.963	12.249	14.807
Q	5844.8	5722.7	5639.1
v_g/c [%]	6.791	3.770	1.689
$F_4[V/m^4]@35[MV/m]$	4.6	-2.9	9.6
$F_8[V/m^4]@35[MV/m]$	2.1e9	31.9e9	-116.8e9

2.1.2 Tapered structure design

Each accelerating structure consists of 72 cells, which gives a total active length of 0.6 m. For each of the 72 cells RF parameters have been calculated based on the interpolation of the parameters of the three cells from Table 3.12 and used to calculate analytically the distribution of the loaded and unloaded accelerating gradients along the structure which are shown in red solid and dashed lines, respectively, in Fig. 3.22. The distributions of the surface electric and magnetic fields, as well as those of the S_c and power flow Pz along the structure, are also shown for loaded and unloaded conditions in Fig. 3.22.

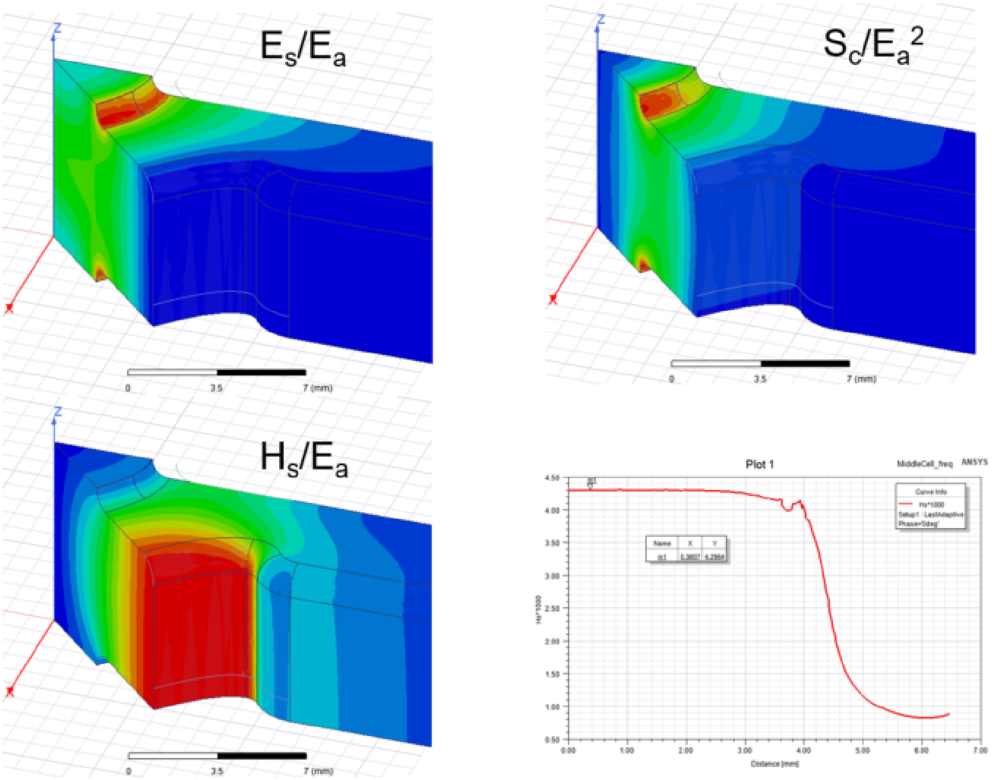

Figure 3.21: Distributions of surface electric and magnetic fields and the modified Poynting vector S_c of the middle cell (1/8 view). The distribution of the magnetic field along the cell wall is also plotted.

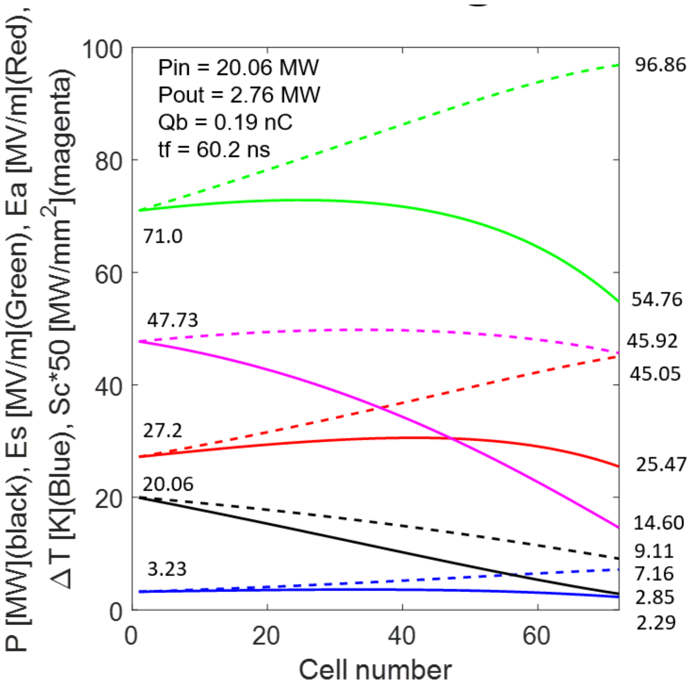

Figure 3.22: Distribution of accelerating gradient (red), power flow (black), surface electric (green), magnetic (blue) fields and S_c (magenta) for loaded (solid) and unloaded (dashed) conditions.

The calculations have been done for the nominal bunch charge of 190 pC, bunch spacing of 1/3 ns and nominal average loaded accelerating gradient of 29.17 MV/m. This analytical model has been used to optimize the design of the tapered structure. Many different structures have been considered. Only the final result is presented.

2.1.3 3D RF design

Based on the analytical design, a full 3D model of the accelerating structure has been created and simulated in ANSYS-EM electromagnetic simulator and CST Microwave Studio. The 3D model of the accelerating structure is shown in Fig. 3.23. A taper is needed to provide a smooth transition of waveguide height from 6.8317 mm to 10.16 mm. The RF design of the RF taper and the S-parameters are shown in Fig. 3.24.

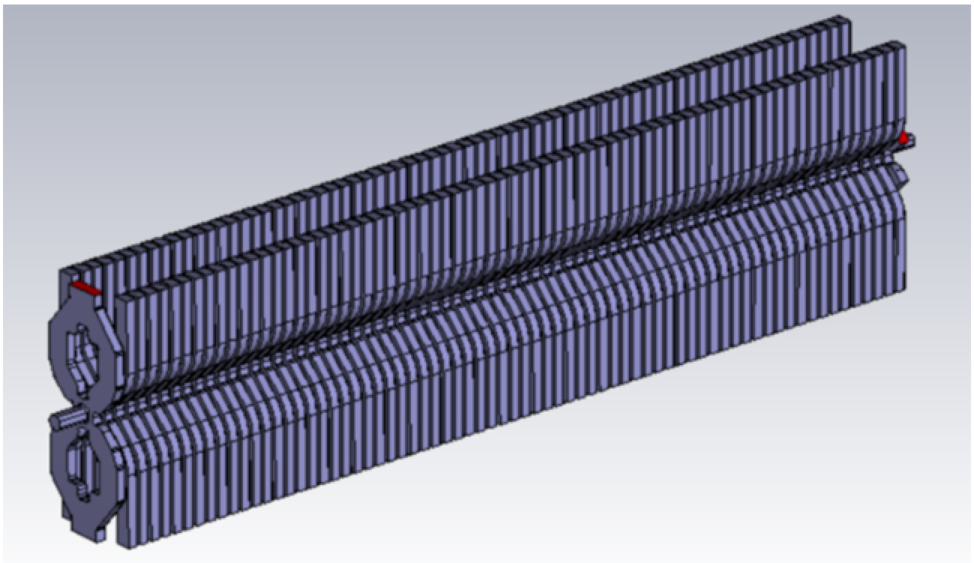

Figure 3.23: 3D model of the internal volume of the accelerating structure.

The full 3D model has been optimized at the nominal RF frequency of 11.994 GHz to minimize the reflections of both the input and the coupler. The nominal RF phase advance per cell of 120° in the regular cells is also a major merit function for the optimization. The results are shown in Fig. 3.25, where the complex electric field on the axis along the structure is plotted on the complex plane to show the RF phase (left) as well as the complex magnitude versus Z to show the pure travelling wave without reflections (right). Scattering parameters of the structure are shown in Fig. 3.26, both from the input (S11, red) and the output (S22, blue) of the structure as a function of RF frequency.

In Fig. 3.27, the unloaded accelerating voltage is plotted versus RF frequency of the input power of 1 W. It has been calculated in the 3D simulation model, taking into account the exact geometry of the structure as well as realistic copper losses. At the nominal RF frequency of 11.994 GHz, input power of 1 W results in an unloaded accelerating voltage of 4.79 kV. The nominal accelerating voltage of the structure is 17.5 MV (29.17 MV/m over 0.6 m). Based on these calculations nominal input power for the unloaded condition is calculated to be 13.35 MW. For the nominal loaded operation condition, the beam loading voltage of 4.1 MV, which is calculated using the analytical model described in the previous subsection, has been taken into account. This results in the input power of 20.3 MW for the nominal loaded operation condition.

In Fig. 3.28, the transmission (S21), the filling time, and the average Q-factor of the structure calculated based on the 3D simulations are plotted versus RF frequency. The filing time at the nominal RF frequency is τ_f = 60.8 ns. In Fig. 3.29, the schematic shape of the input RF pulse is illustrated. It

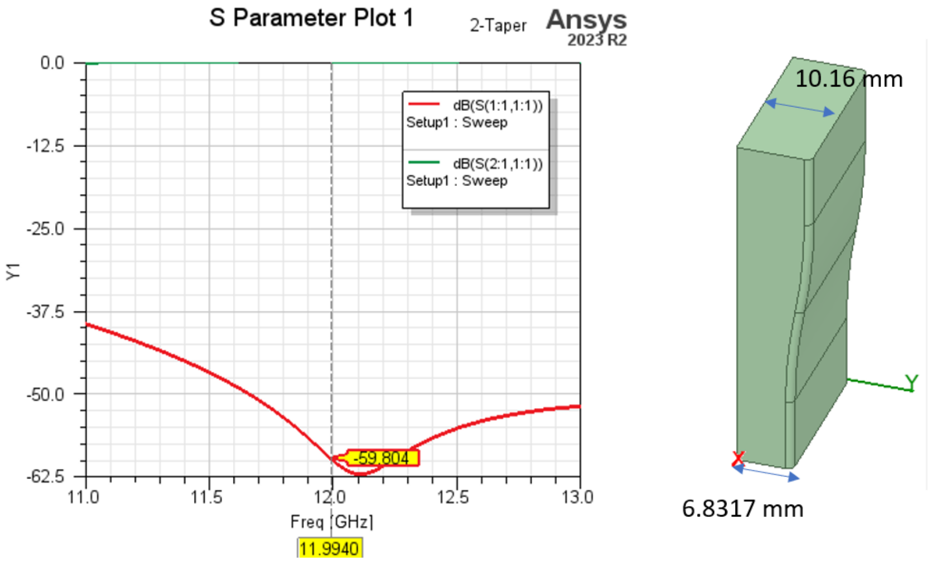

Figure 3.24: RF taper for the accelerating structure.

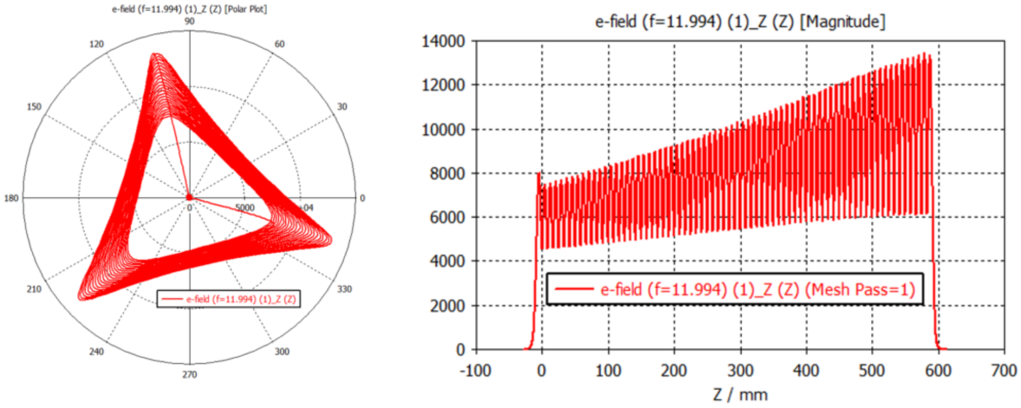

Figure 3.25: Complex electric field distribution along the accelerating structure axis. Real and imaginary parts on the complex plane (left) and complex magnitude versus Z (right).

shows a special ramp of the input power to fill the structure in a correct way before the first bunch goes through the structure at the beginning of the flat top. This ramp is necessary for compensation of the bunch-to-bunch energy spread due to the transient beam-loading effect.

Finally, the accelerating structure, the nominal beam and the corresponding overall system parameters are presented in the Table 3.13. The total dose per pulse is calculated based on the total charge per pulse and the charge-to-dose conversion factor of 0.011 Gy/nC. The overall RF-to-beam efficiency of 16%, which is the ratio of the energy in one bunch train to the energy in one RF pulse from the two klystrons, is calculated assuming the RF pulse compression efficiency of 43%, calculated in Section 3.1.

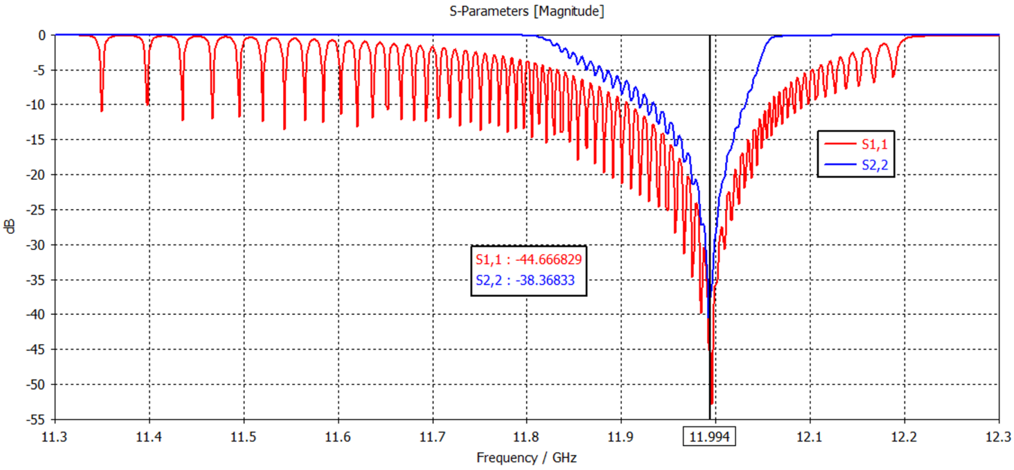

Figure 3.26: S-parameters of the structure from the input (red) and the output (blue) ports.

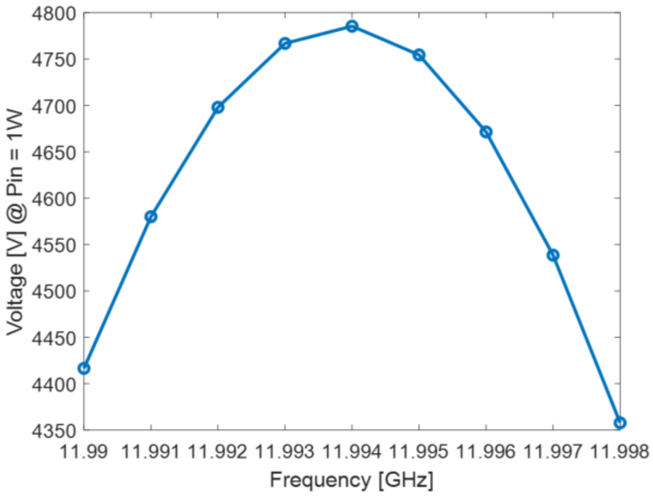

Figure 3.27: Accelerating voltage versus frequency is calculated for the input power of 1 W in the 3D simulation model.

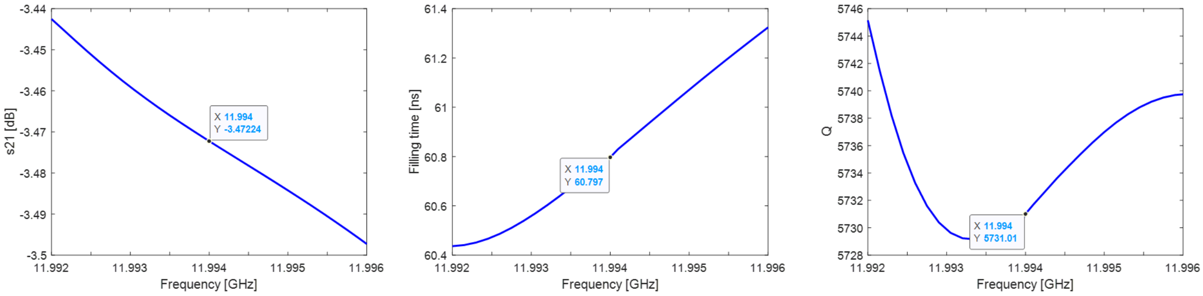

Figure 3.28: The transmission, filling time and average Q-factor of the accelerating structure.

2.1.4 Wakefields

Each regular cell is coupled to 4 damping waveguides used for long-range wakefield suppression, which is necessary for the stability of the high-current electron beam accelerated in the structure. The damping waveguides are terminated by the RF load, which absorbs the power of high order modes (HOMs) cou-

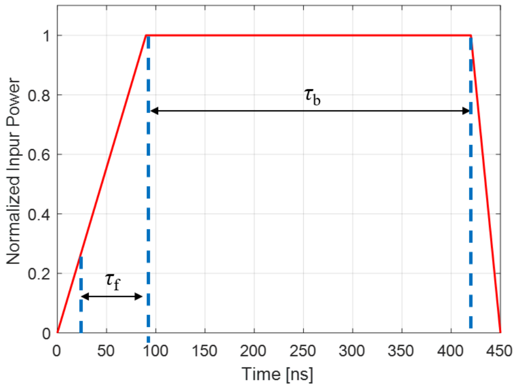

Figure 3.29: Schematic shape of the input RF pulse.

Table 3.13: Parameters of the accelerating structures, nominal beam parameters and corresponding overall system parameters.

Parameters	Units	Value
Active length	m	0.6
$\langle E_{\mathrm{acc}} \rangle$ loaded	MV/m	29.2
Bunch charge	nC	0.19
Bunch spacing	ns	1/3
Pin	MW	20.3
τ_f	ns	61
$\tau_f+\tau_b$	ns	230
Number of bunches	–	507
Pulse charge	nC	96
Dose per pulse	Gy	0.85
Steady state RF-to-beam efficiency	%	49.7
RF pulse efficiency :$\tau_b/(\tau_f+\tau_b)$	%	73.7
Structure RF-to-beam efficiency	%	36.6
Overall RF-to-beam efficiency	%	16

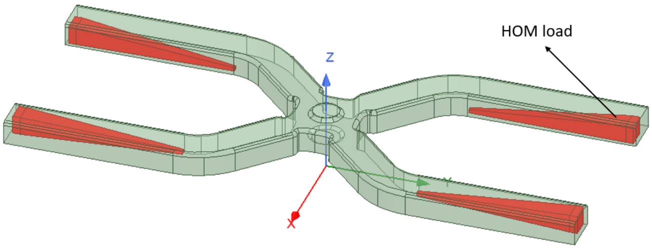

Figure 3.30: Regular cell with 4 high-order mode (HOM) damping loads.

pled out of the cell. The geometry of a regular cell equipped with HOM loads is shown in Fig. 3.30. As an example, the performance of the damping is demonstrated in Fig. 3.31, where the transverse wakefields and corresponding impedance of the last regular cell are shown. The parameters of the most significant dipole HOM are extracted from the wakefield curve by fitting an exponential function shown in the dashed line in Fig. 3.31. The HOM parameters extracted for the wakefields of the first, middle and last cells are shown in Table 3.14. These parameters of the three cells are used to calculate HOM parameters in all cells by interpolation for the beam dynamics simulation of the transverse stability of the beam in the linac.

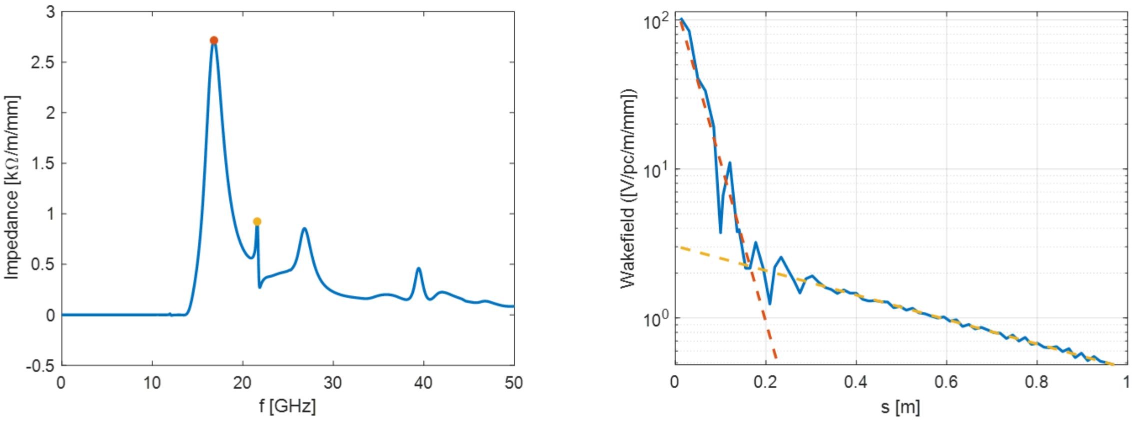

Figure 3.31: Transverse impedance (left) and wakefield (right) of the last regular cell.

Table 3.14: HOM parameters of the first, middle, and last regular cells, as well as the input and output coupler cells.

	f [GHz]	Q	A [V/pC/mm/m]
First-cell Mode 1	14.88	19.6	63.2
First-cell Mode 2	–	–	0
Middle-cell Mode 1	15.75	10.3	105.0
Middle-cell Mode 2	21.01	60.3	2.39
Last-cell Mode 1	16.82	7.1	145.5
Last-cell Mode 2	21.59	119.4	3.04
Input coupler	15.42	160	163
Output coupler	16.82	80	3.04

The wakefields of the full model in Fig. 3.32 are calculated by using two settings for the damping waveguides. For the first setting defined in the blue zone, the input and output couplers, as well as the damping waveguides, deploy the perfect matching loads (PML). For the second one, the input and output couplers deploy an RF splitter while the damping waveguides deploy PMLs. The wakefields of the two cases and the wakefields calculated by using the interpolation of the single cells are shown in Fig. 3.32. The RF splitters of the input and output RF couplers cause the reflection of the wakefields from the input and output RF couplers and resulting in the enhancement of the wakefield. However, the level of the wakefield is still much smaller than the wakefields at the position of the second bunch (0.1 m).

Several materials were analysed for the design of the HOM loads by measuring the relative electric permittivity, ε, and loss tangent, $\tan\delta$. The best performance was obtained for the Rocar S1 material from Ceramtec and Hexoloy SP SiC from Coorstek. The measurements and the fit computed by the simulation tool can be seen in Fig. 3.33.

In order to minimize reflections from the loads, the tip and the taper of the geometry must be carefully studied. In addition, the load must absorb most of the input power to minimize reflections from the end of the waveguide. Since the electrical permittivity in both materials is rather similar, the optimum design found does not depend on the material choice. The final design can be seen in Fig. 3.34 and parameters can be found in Table 3.15.

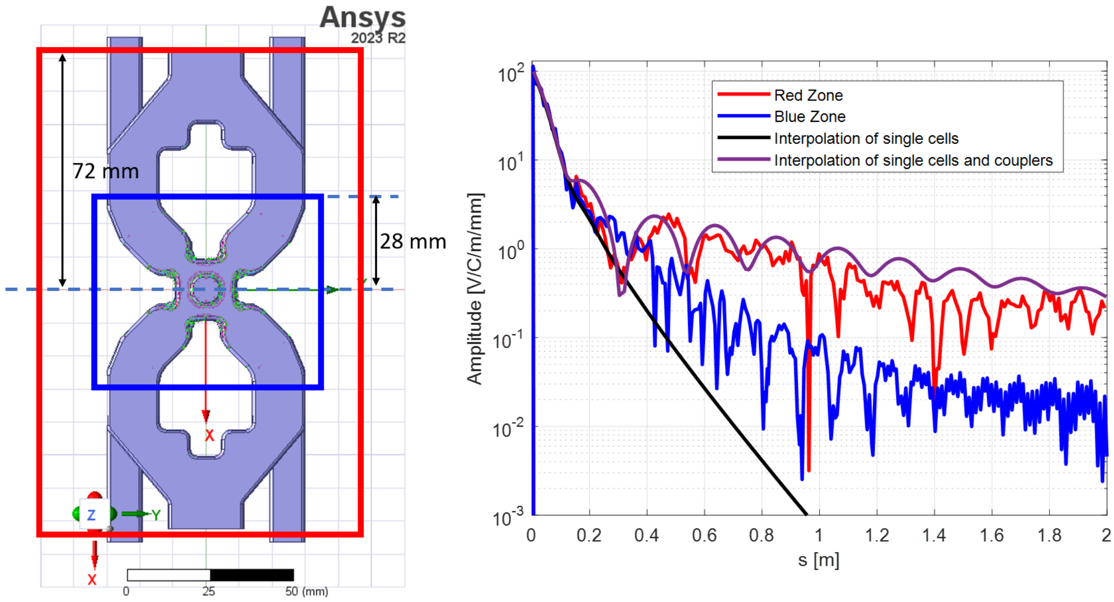

Figure 3.32: Wakefields of the full tapered structure with RF couplers and wakefields calculated by using the interpolation of the single cells.

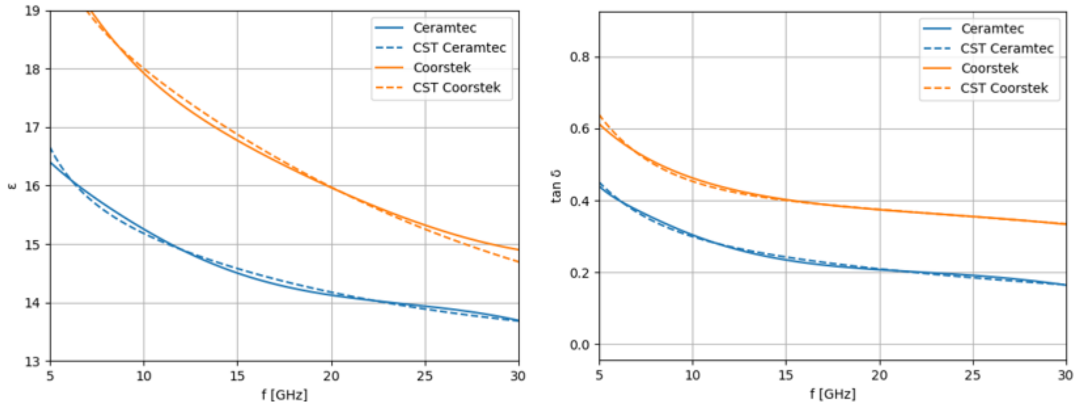

Figure 3.33: Comparison between material measurement and numerical fit for relative permittivity (left) and loss tangent (right) for SiC materials.

A comparison of the total wake with the SiC loads and using PML boundary condition is shown in Fig. 3.35.

2.2 Thermo-mechanical design

2.2.1 Thermal analysis for the accelerating structure

In this subsection, we discuss the thermal analysis for the accelerating structure, including the temperature stability tolerance, the temperature rise of the cooling water in 10 Hz operation and the temperature rise of the accelerating structure in burst mode.

The mechanical design of the CLIC-K accelerating structure is shown in Fig. 3.36. The accelerating structure for the DEFT project has similar discs and cooling pipes as CLIC-K. The temperature rise of the cooling water in 10 Hz and the temperature rise of the accelerating structure in burst mode can be roughly calculated based on the CLIC-K mechanical model.

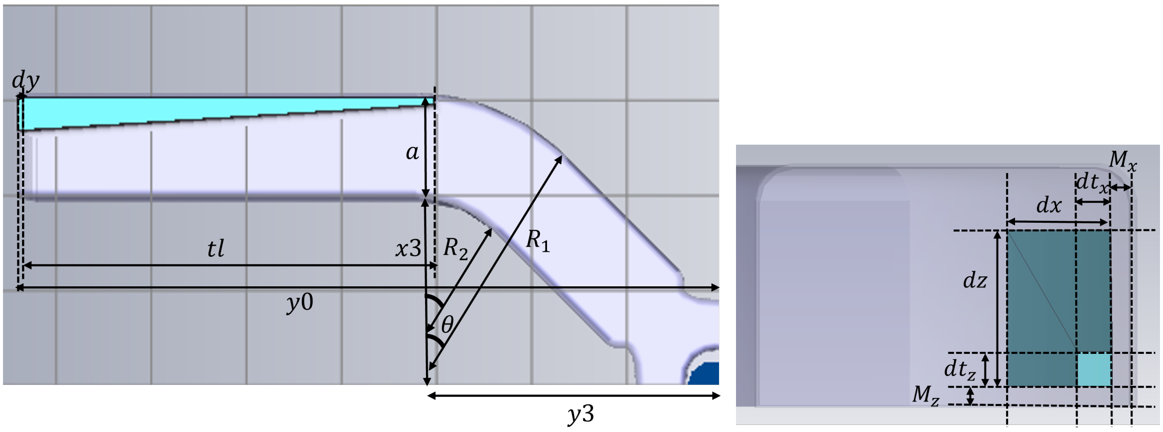

Figure 3.34: Final SiC HOM load design for both materials.

Table 3.15: Parameters of the SiC HOM load design.

Parameter	Value [mm]
dy	0.5
tl	42
$y0$	72
dx	3.433
dz	3.746
dt_x	0.8
dt_z	0.8
M_x	0.4
M_z	0.4
a	10.7
$x3$	19.238
$y3$	31.360
R_2	11
R_1	R_2+a
θ	45 [deg]

For the calculation of the temperature rise of the cooling water in 10 Hz, there are two cases with different cross sections for cooling. As shown in Fig. 3.36, there are eight holes in the disc, which correspond to eight cooling pipes in the accelerating structure. If the water pipes work in parallel, the cooling area is 226.2 mm^2. If the water pipes work in series, the area for cooling is 28.3 mm^2. The lost power in the accelerating structure is 11.2 MW, which can maintain the nominal average gradient of 29.17 MV/m. The pulse length of the RF pulses that go into the accelerating structure is 229.2 ns $\tau_f+\tau_b$. The lost energy per RF pulse is 4.48 J calculated by 11.2 MW·400 ns. In the case of 10 Hz operation, the average lost power in the accelerating structure is 44.8 W. The temperature rise of the cooling water can be calculated by δT = P$_{AS}$/(A·v·ρ·C$_p$), where P$_{AS}$ is equal to 44.8 W, A is 226.3 or 28.3 mm^2, v is the speed of water with 1 m/s, ρ is the water density with 997 kg/m^3, and C$_p$ is the water heat capacity with 4182 J/(kg·K). For the two cases, the temperature rise is 0.048 K or 0.384 K.

For the calculation of the temperature rise of the accelerating structure in burst mode, 41 RF pulses will be generated in 0.1 s. We assume that no heat will be taken away by the cooling system within 0.1 s and the temperature is the same everywhere in the accelerating structure. The overall lost energy in burst mode is 179.2 J calculated by 40 $\times$ 4.48 J. The mass of the accelerating structure is. Based on the

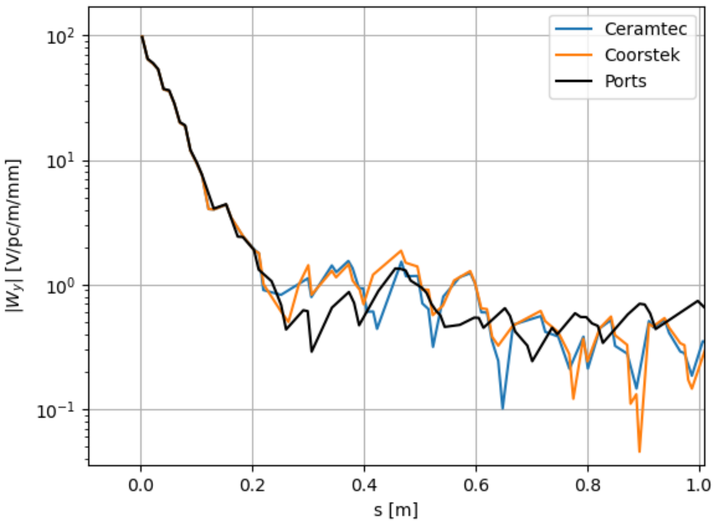

Figure 3.35: Comparison of the total wake with the SiC HOM loads and using PML boundary condition.

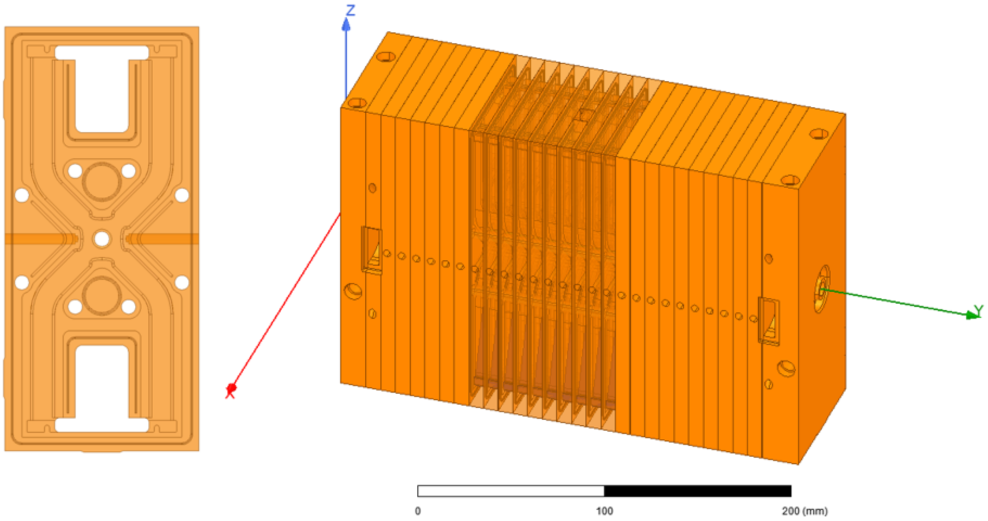

Figure 3.36: Mechanical model of the CLIC-K as well as a disc.

definition of the specific heat capacity, the temperature rise of the accelerating structure can be calculated by $\delta T = dQ\ /(\mathrm{c{\cdot}M})$, where dQ is 179.2 J, c is the specific heat capacity of copper with 0.385 KJ/(kg·K) and M = 44 kg is the mass of the accelerating structure which is about two times that of the CLIC-K. The resulting temperature rise is 0.012 K.

Sensitivity studies on RF parameters for the X-band AS were carried out to estimate the alteration of RF parameters due to thermal variation. A temperature variation of the cavity will cause the thermal expansion of the structure, which will induce a frequency shift given by Eq. (3.1). Then, the amplitude and phase of the accelerating voltage can be computed for different thermal variations assuming the input frequency of the RF is fixed at $f_0 = 11.994$ GHz. The results can be seen in Fig. 3.37.

From Fig. 3.37, it can be obtained that the phase of the voltage increases linearly with the temperature by

$$\frac{\Delta\phi}{\Delta T} = 1.823\ \frac{\mathrm{deg}}{\mathrm{K}} \quad . \tag{3.4}$$

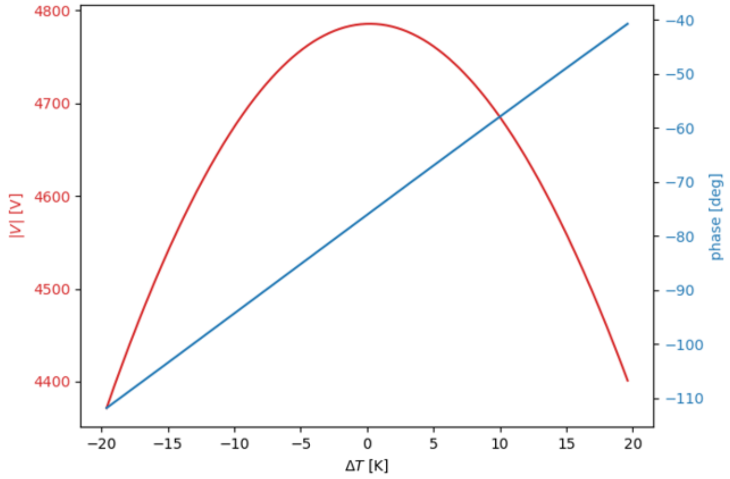

Figure 3.37: Thermal sensitivity study of the accelerating voltage in the X-band AS for $f_0 = 11.994$ GHz.

However, the amplitude shows a non-linear behaviour. In this case, a tolerance in amplitude of ±0.1% corresponds to a temperature change of ±2 K.

3 RF pulse-compressor and waveguide distribution systems

3.1 X-band RF pulse compression system

The RF pulse compression system increases the RF power for the accelerating structures compared to the available RF power of the RF power source, resulting in a significant reduction in the number of RF power sources and the overall cost. A novel X-band RF pulse compression system was designed for the klystron-based CLIC. After adjusting the frequencies of the correction cavities, this RF pulse compression system can meet the requirements of the DEFT project.

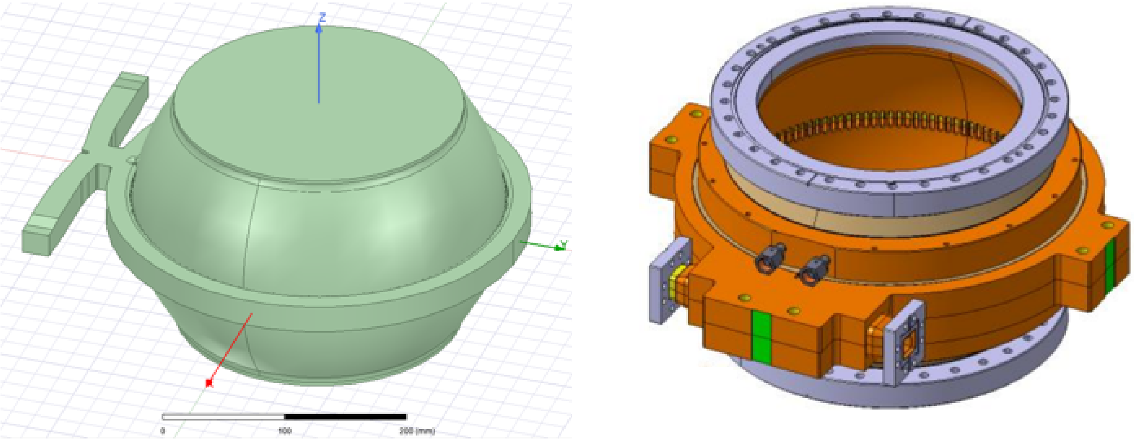

Figure 3.38: RF and mechanical designs of the barrel open cavity pulse compressor.

The RF pulse compression system of the DEFT project consists of a barrel open cavity (BOC) pulse compressor and a correction cavity chain with four correction cavities. The RF and mechanical models of the BOC pulse compressor are shown in Fig. 3.38. The working mode of the BOC pulse compressor is $TM_{1,1,32}$ and is illustrated in Fig. 3.39. One of the features of this mode is that there are no

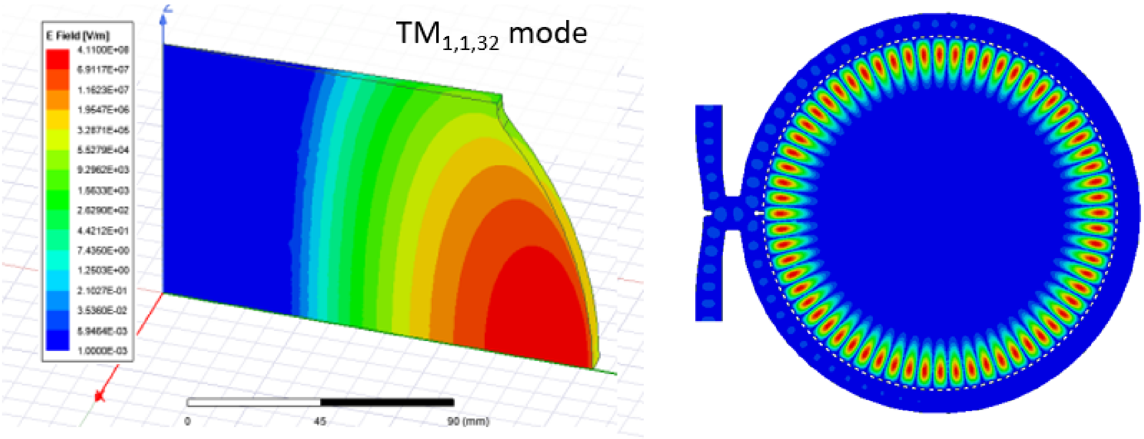

Figure 3.39: RF field distribution of the TM$_{1,1,32}$ mode of the barrel open cavity pulse compressor.

fields at the top and bottom of the cavity, resulting in a very high unloaded quality factor of 235 000. A vacuum port can be added on the top or bottom of the cavity, benefiting from the fact that there is no field on the central axis of the cavity. Around the cavity, there are 128 (4 times the mode index 32) coupling holes. The RF power in the RF coupler is coupled with the TM$_{1,1,32}$ mode in the cavity by the coupling holes. The optimized coupling factor for the klystron-based CLIC is 6.6. This coupling factor is close enough to what is necessary for the DEFT pulse compression system, thus no redesign of the BOC is needed.

The core part of the RF coupler of the BOC pulse compressor is shown in Fig. 3.40. It consists of four ports. All the RF power from Port-1 goes into Port-2. Port-3 and Port-4 are isolated from Port-1 and Port-2. Connecting Port-2 with Port-3 results in the final RF coupler with two ports, as seen in Fig. 3.41 that illustrates that all the RF power from Port-1 goes into Port-2 with nearly no reflection after making a round trip around the BOC. The double-height WR-90 waveguide is used for the input and output of the BOC pulse compressor.

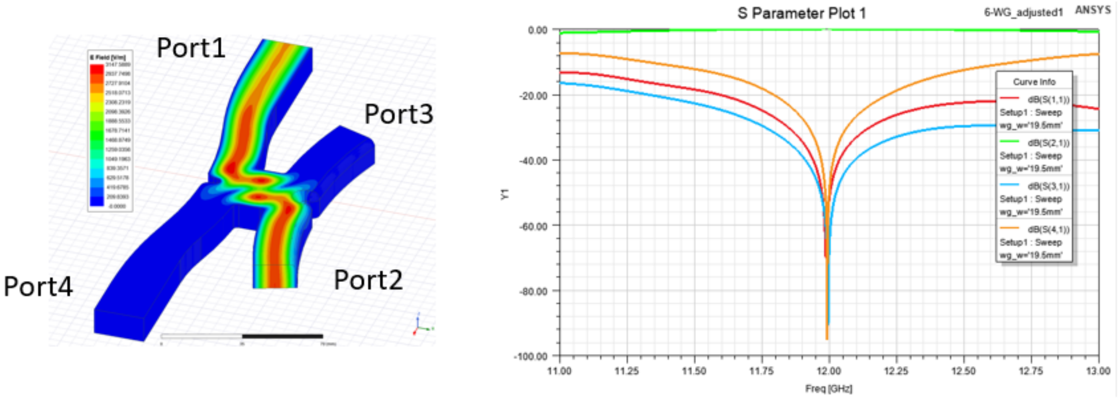

Figure 3.40: Core part of the RF coupler for the BOC pulse compressor on the left. S-parameters are shown on the right.

The RF design of the correction cavity (CC) chain is shown in Fig. 3.42. The correction cavity chain deploys two identical RF rotators with height of the input and output waveguides of 12 mm, each of which feeds RF power to two spherical cavities with different frequencies through the circular waveguide ports. The double-height WR-90 waveguide is used for the input and output of the CC chain. Two RF

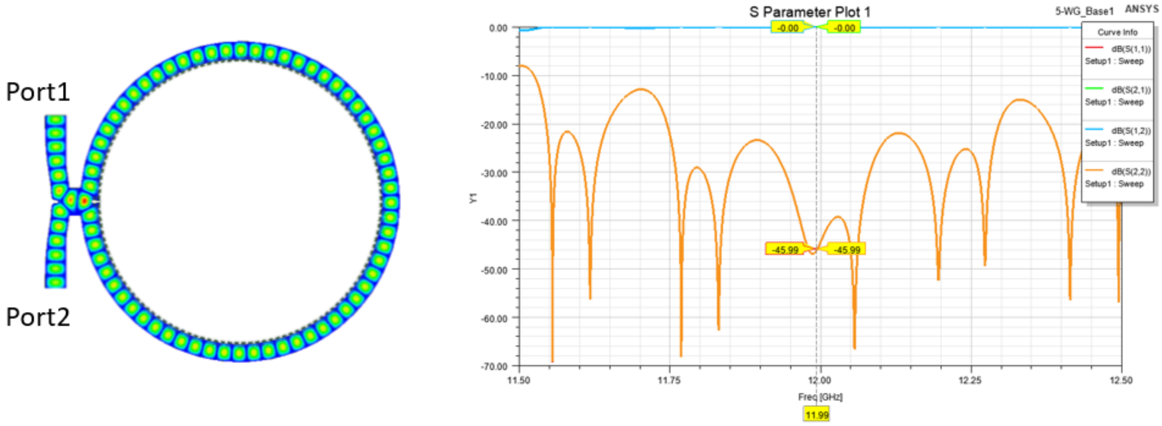

Figure 3.41: Full RF coupler of the BOC pulse compressor on the left. S-parameters are shown on the right.

tapers are used to transform the cross-section from 12 mm to double height (20.32 mm) of the WR-90 waveguide. The lengths of the circular waveguides between the spherical cavities and the RF rotators are carefully calculated to minimize the reflection of the CC chain.

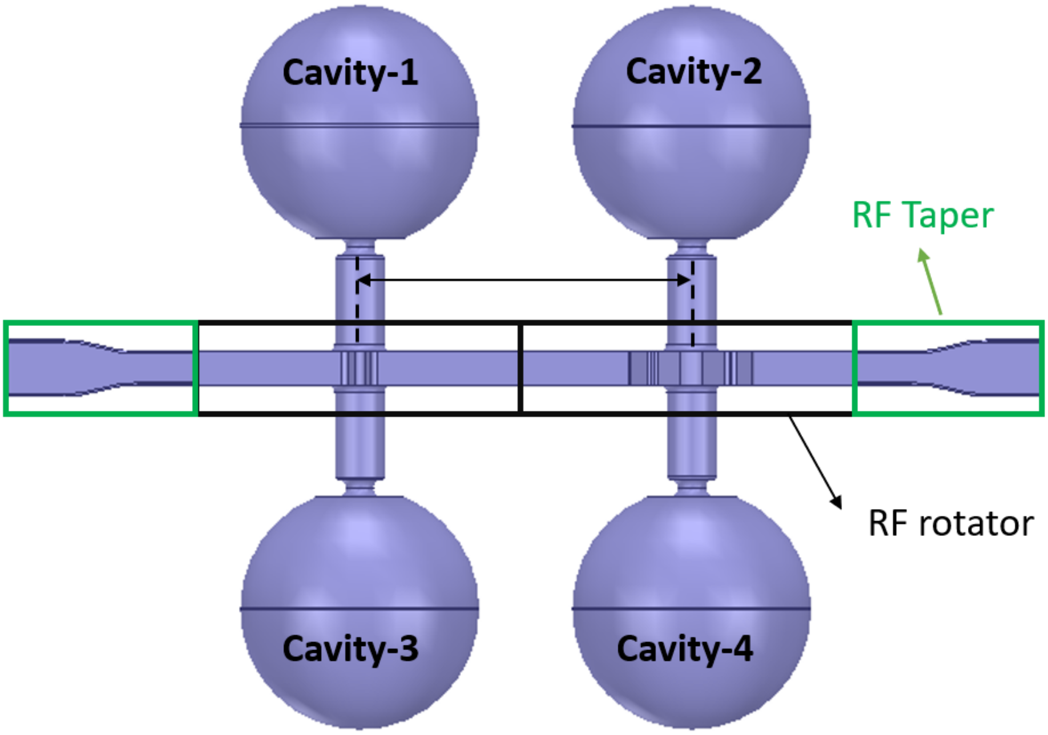

Figure 3.42: RF design of the correction cavity chain.

The mode of the spherical cavity is $TE_{1,1,3}$, as shown in Fig. 3.43. All four spherical cavities have the same unloaded quality factors and coupling factors, which are 71 400 and 1.9, respectively. The frequencies of the correction cavities will be discussed in the following.

The RF design and the S-parameters of the RF rotator are shown in Fig. 3.44. In the circular waveguide, there are two polarised TE_{11} modes. If each polarised TE_{11} mode is seen as a port, the

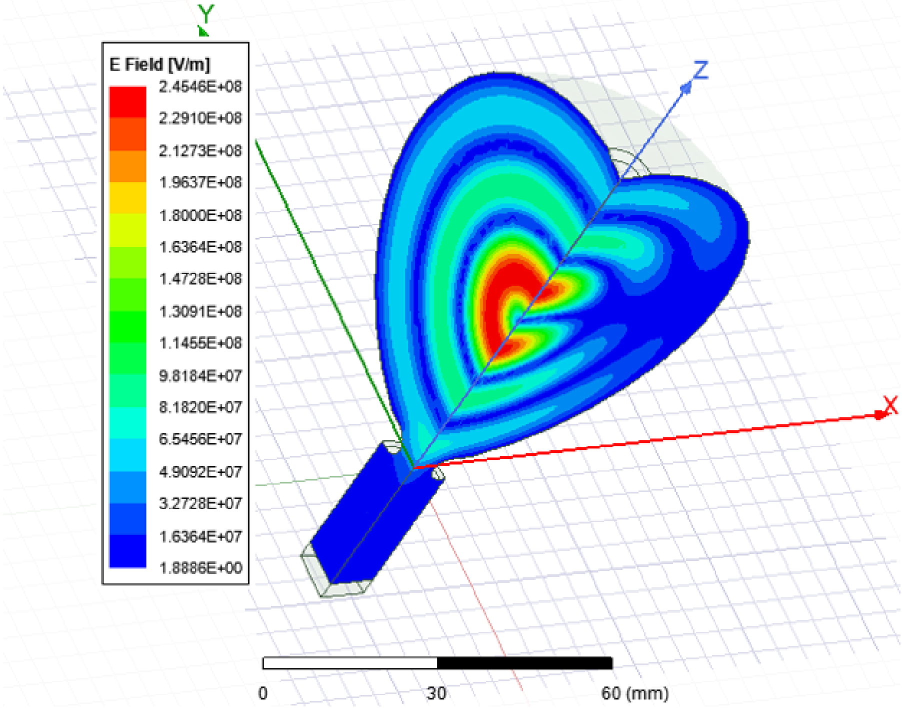

Figure 3.43: RF field distribution of the $\mathrm{TE}_{1,1,3}$ mode of the correction cavity.

S-parameters of the RF rotator are the same as those of a standard 3-dB hybrid. Each polarised mode can excite a corresponding $\mathrm{TE}_{1,1,3}$ mode in the spherical cavity.

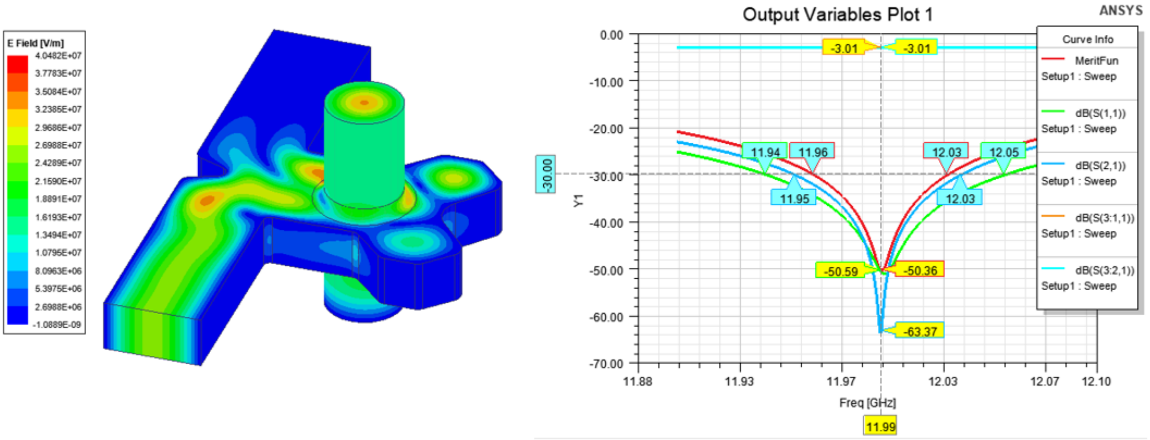

Figure 3.44: RF design of the RF rotator.

The spectrum and the waveforms related to the pulse compression system are shown in Fig. 3.45. In the spectrum, there are five peaks that correspond to five cavities in the pulse compression system. The RF parameters of the five cavities are listed in Table 3.16. All correction cavities have the same unloaded quality factor (Q_0) and coupling factor (β), while the storage cavity (the BOC pulse compressor) has a much larger unloaded quality factor. The external quality factor defined by Q_0/β of the correction cavities and the storage cavity has similar values. The frequency difference of the adjacent peaks is 3.68 MHz, which is approximately equal to $1/(\tau_b+\tau_f)$, where τ_b and τ_f are defined in Table 3.13.

The compressed RF pulse coming from the pulse compression system should have a specific shape that satisfies the requirement of the linac, as shown in Fig. 3.29. To achieve this, the input pulse needs

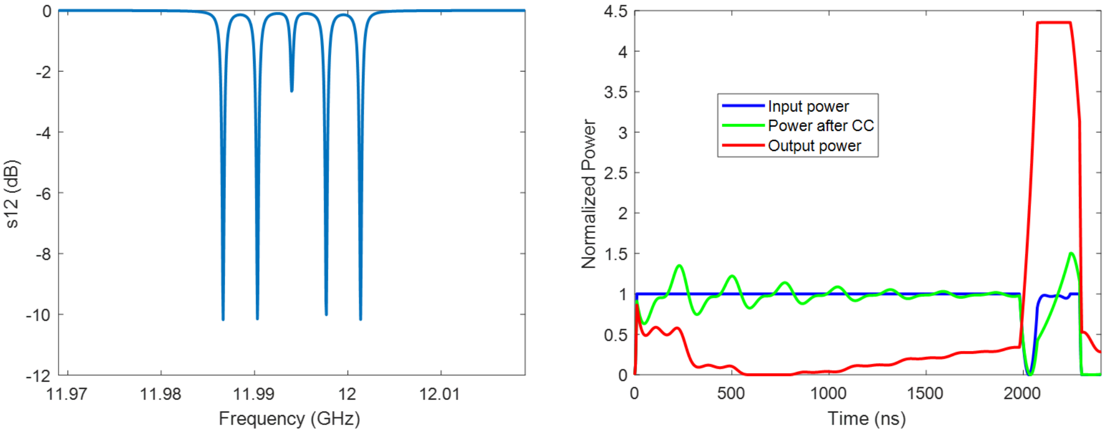

Figure 3.45: Spectrum and the waveforms of the pulse compression system.

Table 3.16: RF Parameters of the storage (SC) and correction (CC) cavities.

	f [GHz]	Q	β
CC-1	11.98664	71 000	1.9
CC-2	11.99032	71 000	1.9
SC	11.99400	235 000	6.6
CC-3	11.99768	71 000	1.9
CC-4	12.00136	71 000	1.9

to be modulated with several ripples at the end of the pulse. The CC chain modulates the amplitude of the input pulse. The BOC pulse compressor then compresses the RF pulse and generates the RF pulse with much larger peak power and the required shape. The ratio of the peak power in the compressed pulse to the peak power from the RF power source is the power gain. It is the key parameter of the pulse compression system, which is listed together with the other parameters of the pulse compression system in Table 3.17. The compression ratio is defined as (2300 ns)/(τ_b+τ_f), where 2300 ns is the pulse length from the RF power source into the pulse compression system, and the pulse compression efficiency is defined as the ratio of the power gain and the compression ratio.

Table 3.17: Parameters of the pulse compression system.

Parameter	Value
Power gain	4.35
Compression ratio	10
τ_b+τ_f [ns]	230
Pulse compression efficiency [%]	43

3.1.1 Thermal analysis for the pulse compression system

The pulse compression system is based on resonant cavities with very large unloaded quality factors (Q_0). The performance of the pulse compression system is sensitive to the temperature of the resonant cavities. In this subsection, we discuss the thermal analysis for the pulse compression system.

As we show in Fig. 3.45, there are 5 RF peaks in the spectrum of the pulse compression system. Each RF peak corresponds to one resonant cavity. The temperature changes of the resonant cavities cause the offsets of the RF peaks in the spectrum, which reduce the power gain and change the phase of the output RF pulses. Figure 3.46 shows the power gain and output phase versus the temperature change of the BOC pulse compressor. Within the range of ± 0.1 K, the reduction of the power gain is smaller than 1% and the phase change is within ± 3.5 deg of RF phase. The power gain and output RF phase versus the temperature of the correction cavity chain are shown in the Fig. 3.47. Within the range of ± 0.2 K, the reduction of the power gain is smaller than 0.5 % and the RF phase change is within ± 0.7 degrees.

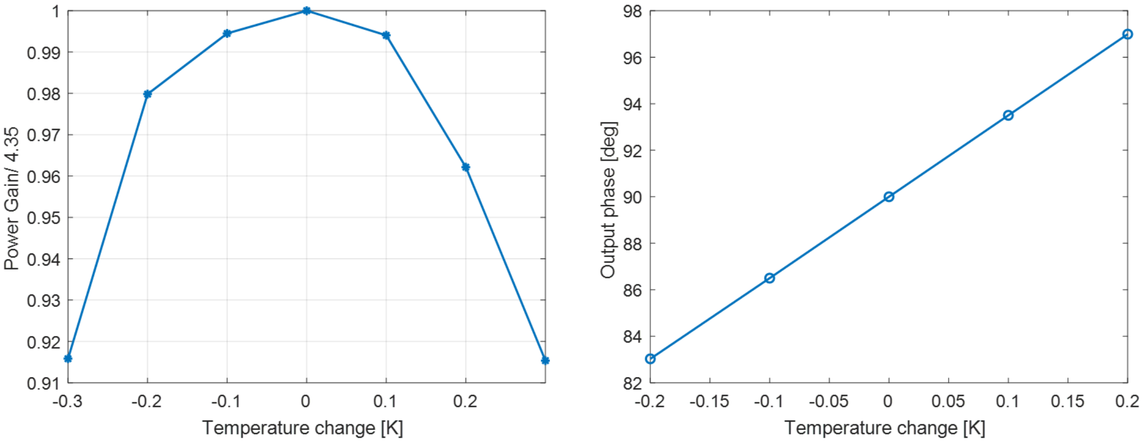

Figure 3.46: Power gain and phase versus temperature change of the BOC pulse compressor.

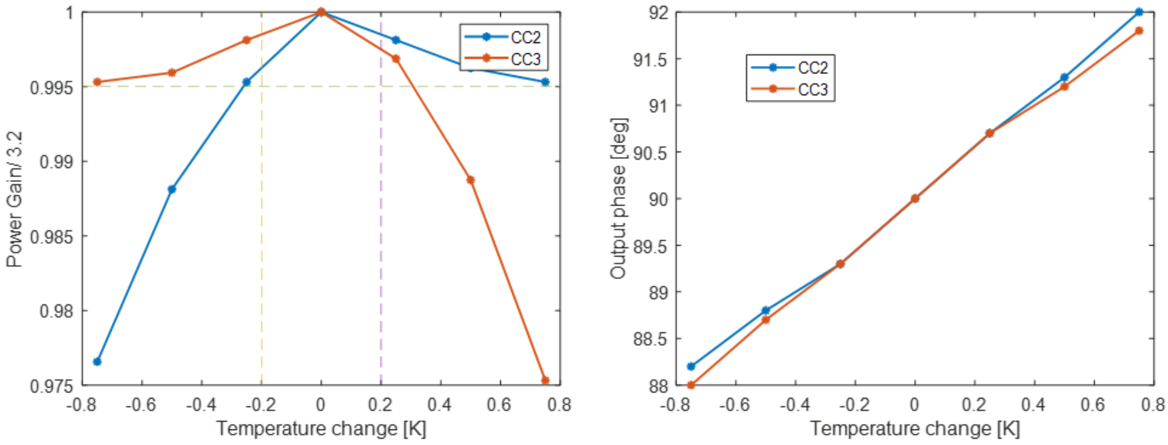

Figure 3.47: Power gain and phase versus temperature change of the correction cavity chain.

The RF power losses of the BOC pulse compressor and the correction cavity chain can be calculated using the waveforms in Fig. 3.45. The RF power losses of the BOC pulse compressor are 20.3%, and the RF power losses of the correction cavity chain are 3.9%. Based on the power losses, the input power of the klystron and the pulse length of the RF pulse, the lost energies per RF pulse of the BOC pulse compressor and the correction cavity chain are calculated 25.46 J and 5.09 J. In the 10 Hz case, the average power lost of the BOC pulse compressor and the correction cavity chain are 254.6 W and 50.9 W. The temperature distribution of the BOC pulse compressor and the correction cavity chain can be calculated based on the lost powers mentioned above. The temperature distribution, the deformation and the stress intensity of the BOC pulse compressor are shown in Fig. 3.48. The difference between the maximum and minimum temperature is 0.92 K, causing the maximum deformation of 2.2 μm. This deformation is much smaller than the mechanical tolerance of the BOC pulse compressor and will not have a significant effect on the operation of the BOC pulse compressor. The maximum stress intensity is 2.3 MPa, which is negligible. For the correction cavity chain, the average power lost is 12.7 W in one cavity.

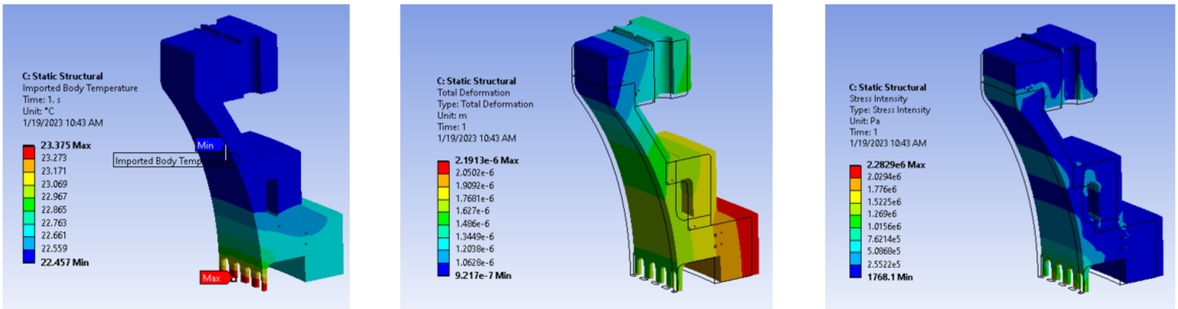

Figure 3.48: The temperature distribution, the deformation and the stress intensity of the BOC pulse compressor.

The BOC pulse compressor has two cooling rings with a cross section of 100.7 mm^2 and the cavity of the correction cavity chain has only one cooling ring with a cross section of 212.2 mm^2. On the basis of the cross sections and the average lost powers, the temperature rises of the cooling water can be calculated. The calculation is the same as that for the accelerating structure. The speed of the water is also 1 m/s in this calculation. The temperature increases are 0.3 K and 0.014 K for the BOC pulse compressor and the cavity in the correction cavity chain.

For the burst mode, the temperature rises of the BOC pulse compressor and the correction cavity chain can be calculated as we discussed for the accelerating structure. The total lost energies are 1018.4 J and 50.8 J for the BOC pulse compressor and the cavity in the correction cavity chain. The mass of the BOC pulse compressor is about 55 kg, while the mass of the cavity in the correction cavity chain is 19.8 kg. Based on the lost powers and the masses, the temperature rises can be calculated. They are 0.048 K and 0.0067 K for the BOC pulse compressor and the cavity in the correction cavity chain.

In summary, the results discussed above are listed in Table 3.18.

Table 3.18: Thermal parameters of the pulse compression system.

	BOC pulse compressor	Correction cavity chain
Mass [kg]	55.14	72.9
Lost energy per RF pulse [J]	25.46	5.08
δT of cooling water in 10 Hz [K]	0.3	0.014
δT of component in burst mode [K]	0.048	6.7e-3
δT of temperature distribution [K]	0.92	0.1

The RF sensitivity studies for the pulse compressor system were carried out to estimate the effect of thermal variation on the RF parameters. A temperature variation in the cavity will cause its expansion or contraction, which will induce a frequency shift given by Eq. (3.1). Then, the amplitude and phase of the output signal can be computed for different thermal variations, assuming the input frequency of the RF is fixed at $f_0 = 11.994$ GHz.

For the CC, the results can be seen in Fig. 3.49. It can be observed that the amplitude shows a symmetric behaviour with the sign of the temperature modification, doing one oscillation around the ideal case. Regarding the phase, an anti-symmetric behaviour can be observed, where the maximum variation is reached at the end of the compressed pulse.

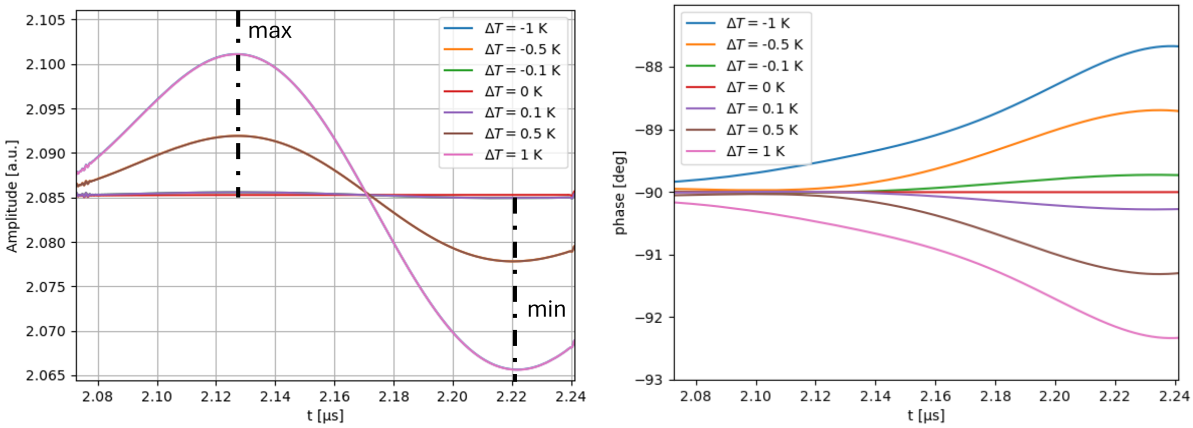

Figure 3.49: Thermal sensitivity study of the amplitude (left) and phase (right) of the compressed pulse changing the temperature in the CC chain.

From Fig. 3.49, it can be obtained that the maximum variation of the phase of the output signal decreases linearly with the temperature by

$$\frac{\Delta\phi}{\Delta T} = -2.33\ \frac{\text{deg}}{\text{K}} \quad . \tag{3.5}$$

However, the amplitude shows a non-linear behaviour. In this case, a tolerance in amplitude of ±0.1% corresponds to a temperature change of ±0.2 K.

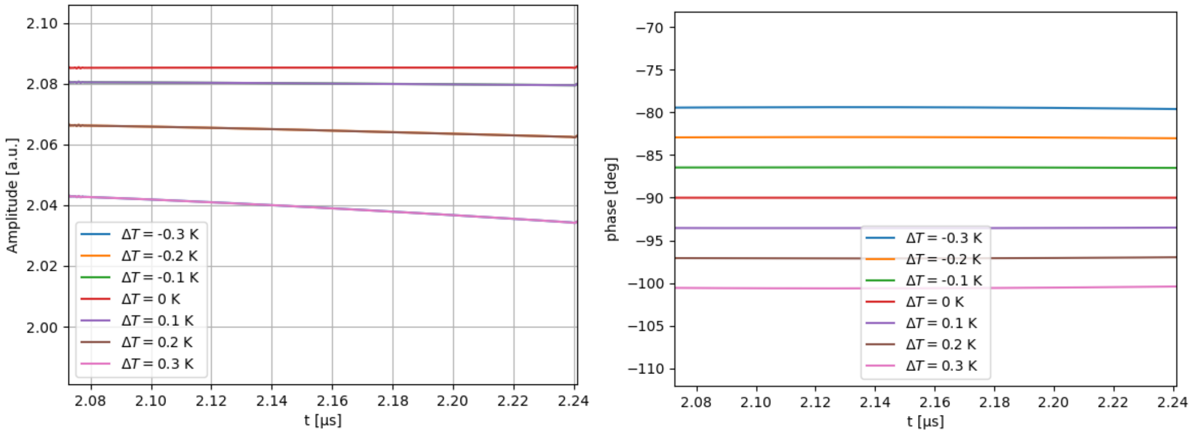

Figure 3.50: Thermal sensitivity study of the amplitude (left) and phase (right) of the compressed pulse changing the temperature in the BOC.

For the BOC, the results can be seen in Fig. 3.50. It can be observed that the amplitude shows a symmetric behaviour with the sign of the temperature modification, decreasing the amplitude of the pulse in a non-linear way. Regarding the phase, an anti-symmetric behaviour can be observed, where the maximum variation is reached at the end of the compressed pulse. Similarly to the case of CC, the maximum variation of the RF phase of the BOC output signal decreases linearly with the temperature by

$$\frac{\Delta\phi}{\Delta T} = -35.67\ \frac{\text{deg}}{\text{K}} \quad . \tag{3.6}$$

and the amplitude shows a non-linear behaviour with the tolerance in amplitude of ±0.1% corresponds to a temperature change of ±0.04 K. The BOC shows a more sensitive behaviour than the CC cavity chain.

3.2 X-band RF waveguide distribution system

The schematic layout of the X-band RF unit is shown in Fig. 3.51. It consists of two klystrons, a pulse compression system, eight X-band accelerating structures and some RF components for RF power combination, transmission and absorption. The DEFT project can share a lot of the RF components with the klystron-based CLIC. The main parameters of the X-band RF unit are shown in Table 3.19. In this section, we discuss these RF components in detail.

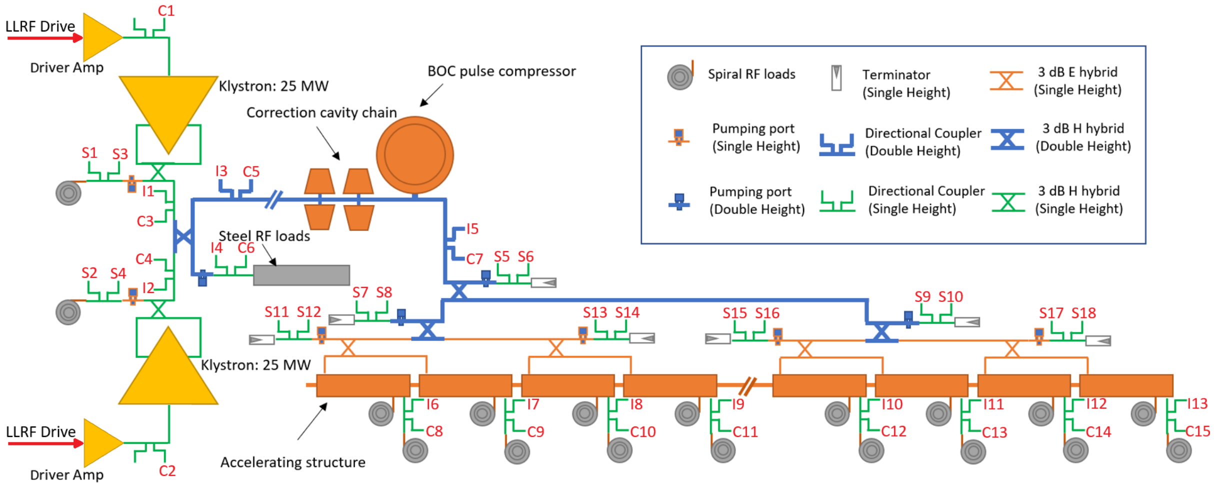

Figure 3.51: Schematic layout of the X-band RF unit.

Table 3.19: Parameters of the DEFT X-band RF unit.

Parameter	Value
No. of klystrons per RF unit	2
Klystron maximum peak power [MW]	25
Klystron nominal operation power [MW]	21.95
Pulse compression power gain	4.35
Waveguide loss [%]	15
No. of structures per RF unit	8
Structure input power [MW]	20.3

3.2.1 *RF power combination part*

The RF power comes from two X-band klystrons with peak power of 25 MW and pulse length of 2.3 μs. Each klystron has two output ports with standard dimension WR-90 (22.86 mm × 10.16 mm). A 3-dB hybrid combines the RF power from the two ports. The RF design and the S-parameters of the 3-dB hybrid are shown in Fig. 3.52. When combining the RF power, two ports are for the input RF power and one for the output power. As the 3-dB has four ports, the remaining one can be used as a vacuum pumping port.

The standard WR-90 single height version of the pumping port is shown in Fig. 3.53. The double-height pumping port is obtained by simply increasing the height of the double version by a factor of two.

This pumping port is attached to one of the ports of the 3-dB hybrid. During the RF power combination, a small amount of RF power may go into the port connecting with the pumping port. A terminator is used to absorb this. The terminator design is shown in Fig. 3.54.

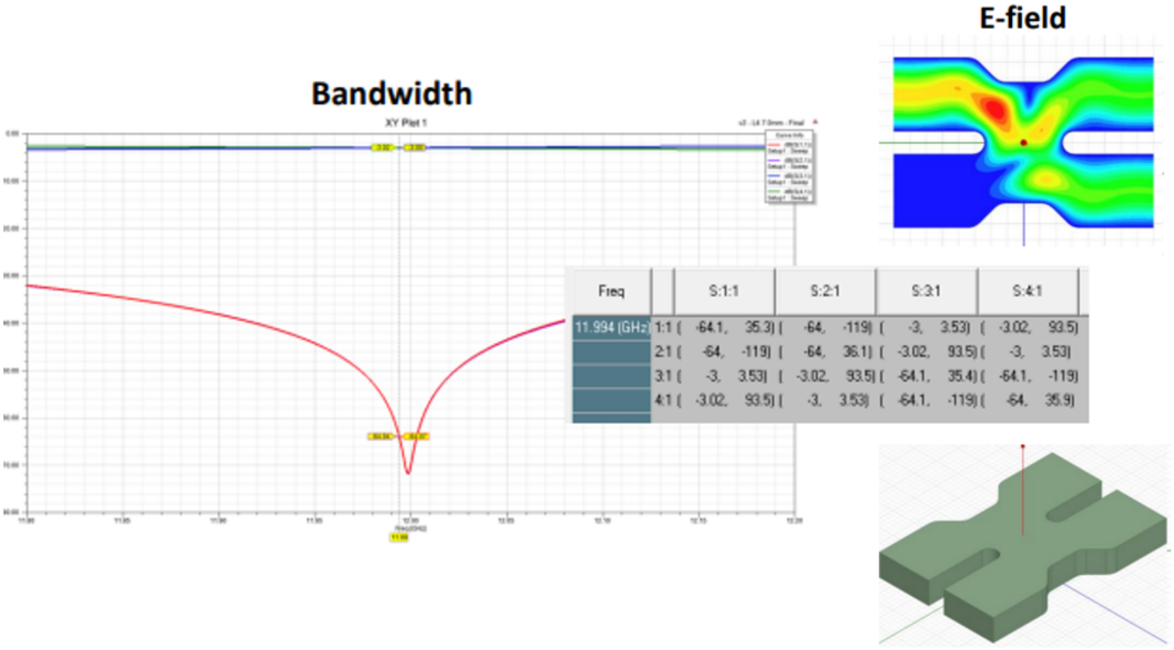

Freq		S:1:1	S:2:1	S:3:1	S:4:1
11.994 (GHz)	1:1	(-64.1, 35.3)	(-64, -119)	(-3, 3.53)	(-3.02, 93.5)
	2:1	(-64, -119)	(-64, 36.1)	(-3.02, 93.5)	(-3, 3.53)
	3:1	(-3, 3.53)	(-3.02, 93.5)	(-64.1, 35.4)	(-64.1, -119)
	4:1	(-3.02, 93.5)	(-3, 3.53)	(-64.1, -119)	(-64, 35.9)

Figure 3.52: RF design of the H-plane 3-dB hybrid.

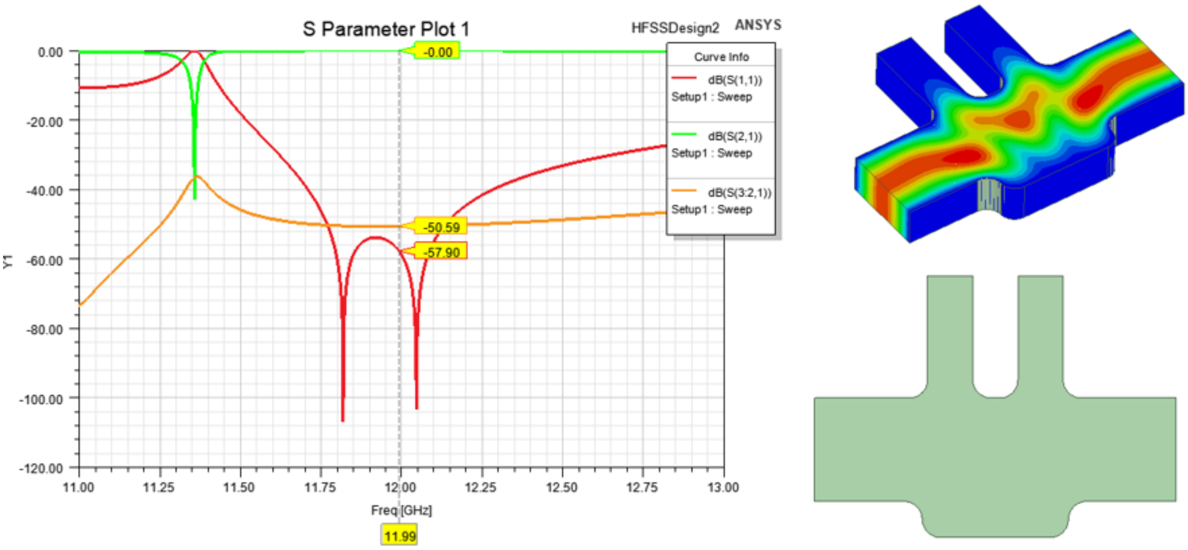

Figure 3.53: RF design of the vacuum pumping port.

After combining the RF power from the two ports of the klystron, a directional coupler is used to measure the power level as well as the phase of the RF pulses from the klystron. The RF design and the S-parameters of the directional coupler are shown in Fig. 3.55. This directional coupler has been successfully tested and widely used in high power test facilities at CERN.

After the directional couplers, the RF power will be combined by an RF network as is shown in the

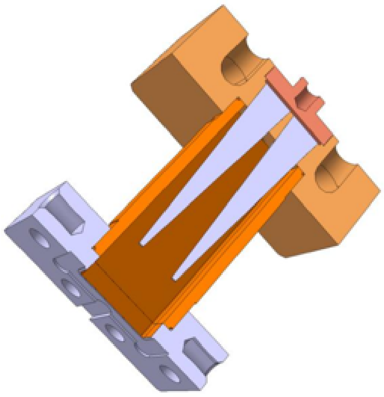

Figure 3.54: RF terminator.

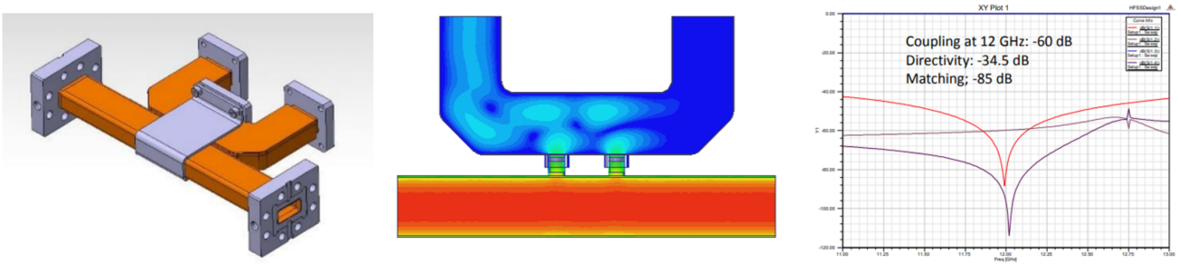

Figure 3.55: Mechanical and RF design of the directional coupler.

Fig. 3.56. This RF network consists of three RF tapers, a double-height 3-dB hybrid and a double-height pumping port. The RF taper shown in Fig. 3.57 is used to provide the transition from single to double height waveguides. The RF taper is compact, benefiting from the tangent arcs. Due to the symmetry of the geometry, the couplings to the other modes except for the working mode are negligible. The double-height 3-dB hybrid can be easily designed by just increasing the height of the 3-dB hybrid in Fig. 3.52.

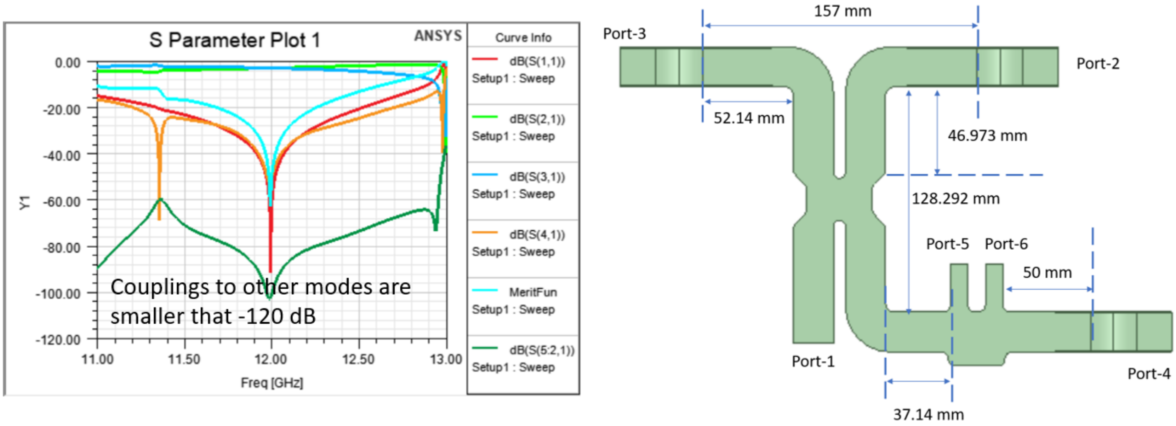

Figure 3.56: RF network for combining RF power from the two klystrons.

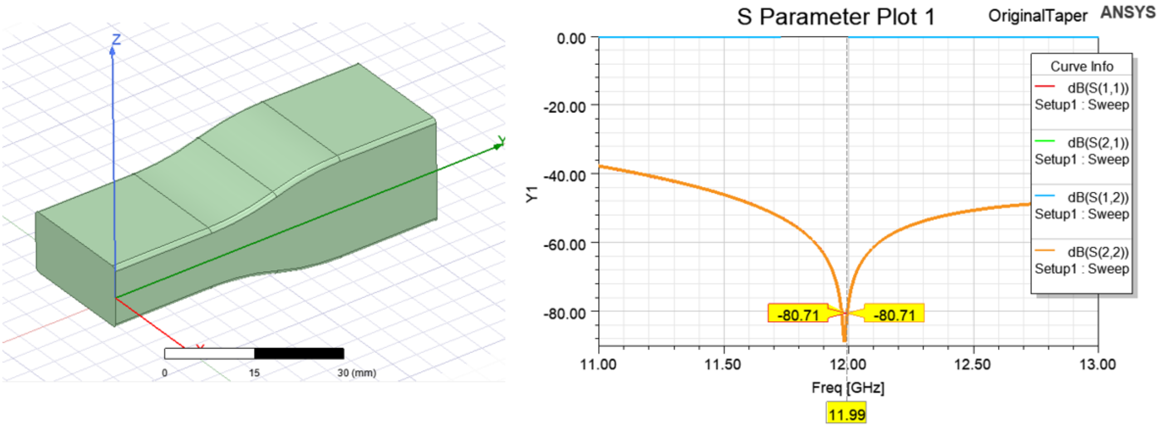

Figure 3.57: Taper from 10.16 to 20.32 mm.

After combining, the RF power level in the output port towards the accelerating structure reaches up to 50 MW. However, before operating the two klystrons, it's difficult to know their phases, which means some RF power may go to the other port of the double-height 3-dB hybrid rather than the one for the accelerating structures. In this case, a high power stainless steel (SS) RF load is used to absorb this RF power. This RF load is shown in Fig. 3.58. It has been widely used in the high power test facilities at CERN. Between the SS RF load and double-height 3-dB hybrid, a double-height pumping port is used for vacuum pumping.

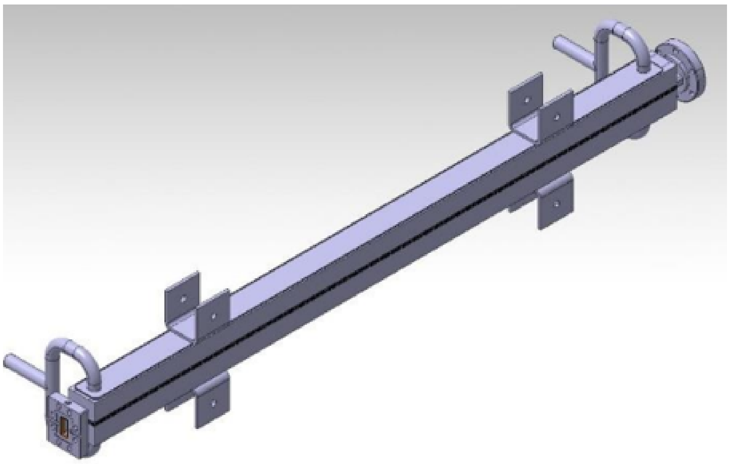

Figure 3.58: Stainless Steel RF load.

3.2.2 *RF pulse compression part*

The RF pulse compression system was discussed in the Section 3.1. It consists of a BOC pulse compressor and four spherical cavities. Before and after the pulse compression system, bending waveguides are needed for integration. The single and double-height H-plane bends are designed for this purpose. The RF design and S-parameters of the single height H-plane waveguide bend are shown in Fig. 3.59. The double height bend can be directly obtained by increasing the height of the single height bend, as in the case of the double height and single height 3-dB hybrids.

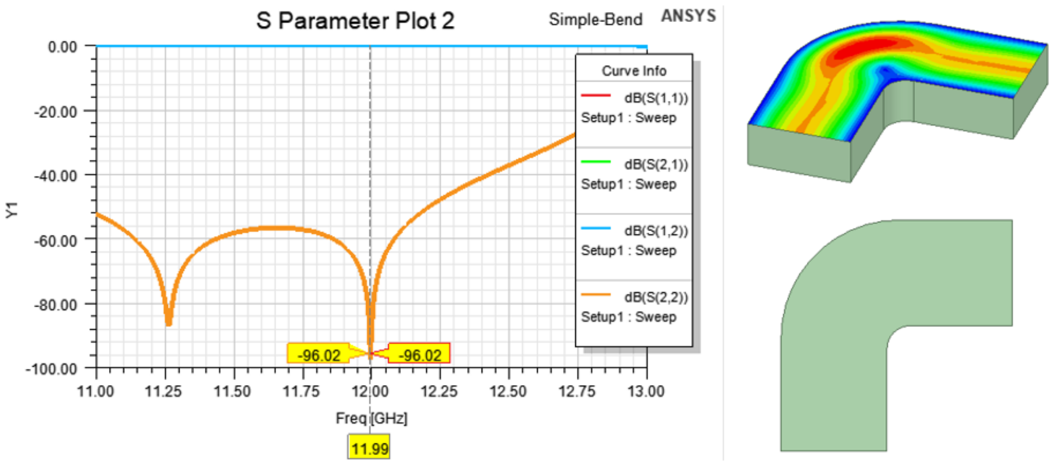

Figure 3.59: H-plane WG bend.

3.2.3 *Accelerating structure part*

The pulse compression system generates RF pulses with a peak power of about 200 MW. An RF distribution network based on 3-dB hybrids is designed for RF power distribution as shown in Fig. 3.60. This power is divided into four identical parts by three double height 3-dB hybrids. The power from each port of the Hybrid-2 and Hybrid-3 is then divided by an E-plane 3-dB hybrid into two accelerating structures. The positions of the 3-dB hybrids are carefully calculated. They are important for the phases of the accelerating structures, which affect the acceleration of the beam. The RF design and S-parameters of the E-plane 3-dB hybrid are shown in Fig. 3.61. The accelerating structures are described in Section 2.

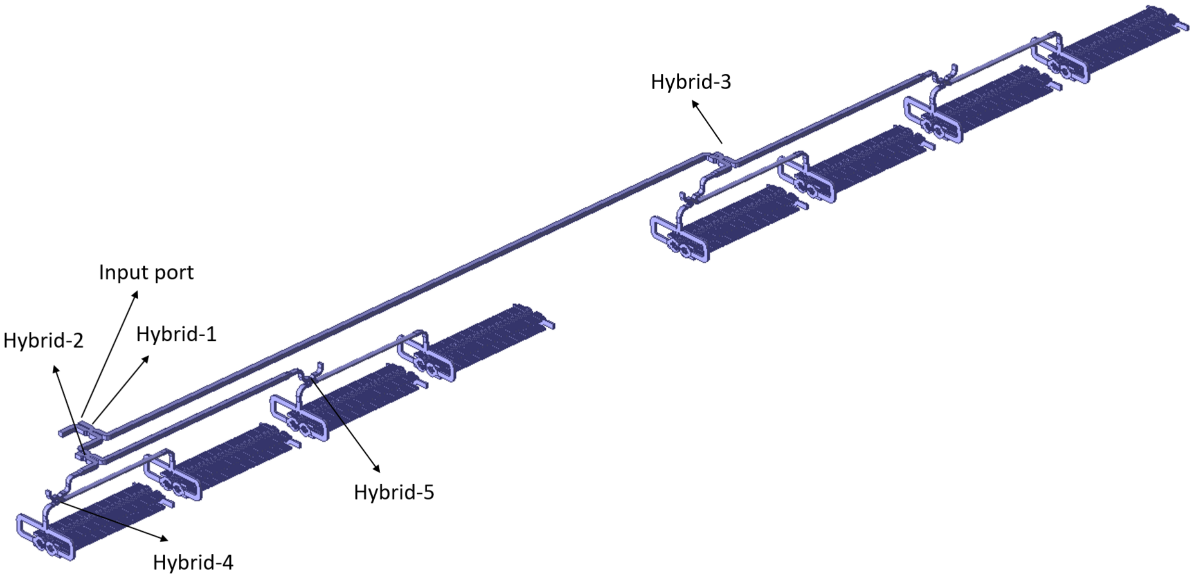

Figure 3.60: Layout of RF splitter for the eight accelerating structures.

An RF splitter, two RF tapers and four identical H-bends are used to feed the accelerating structures with four input ports as shown in Fig 3.62. The RF splitter is widely used at CERN.

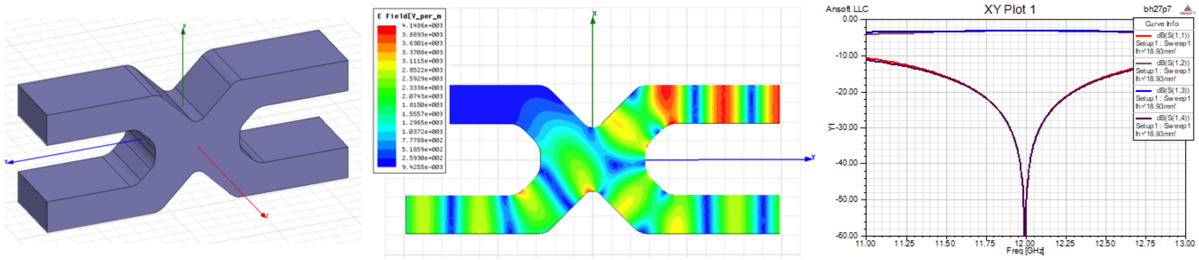

Figure 3.61: RF design and S-parameters of the E-plane 3dB hybrid.

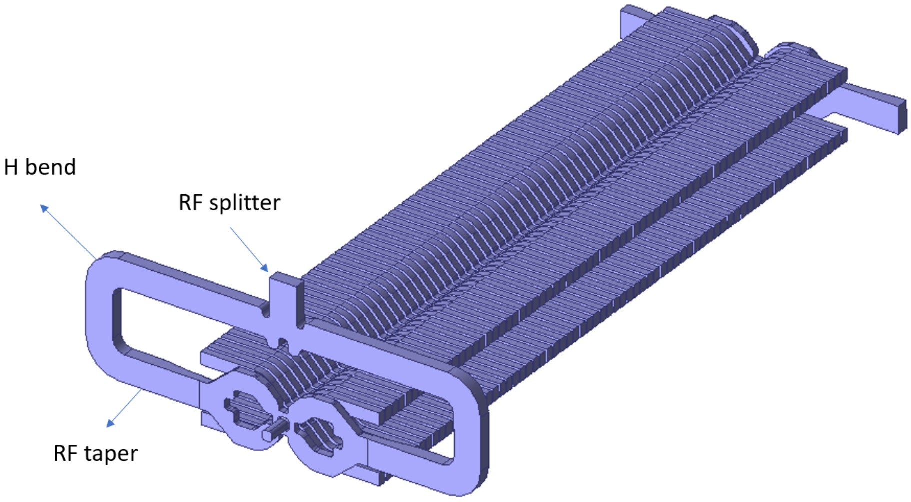

Figure 3.62: RF model of the accelerating structure with RF network around it.

Some RF power leaves the accelerating structure with or without a beam. Two spiral RF loads per structure are used to absorb the RF power from each output port. The RF design and the S-parameters are shown in Fig. 3.63. The spiral RF loads have been successfully high power tested at CERN.

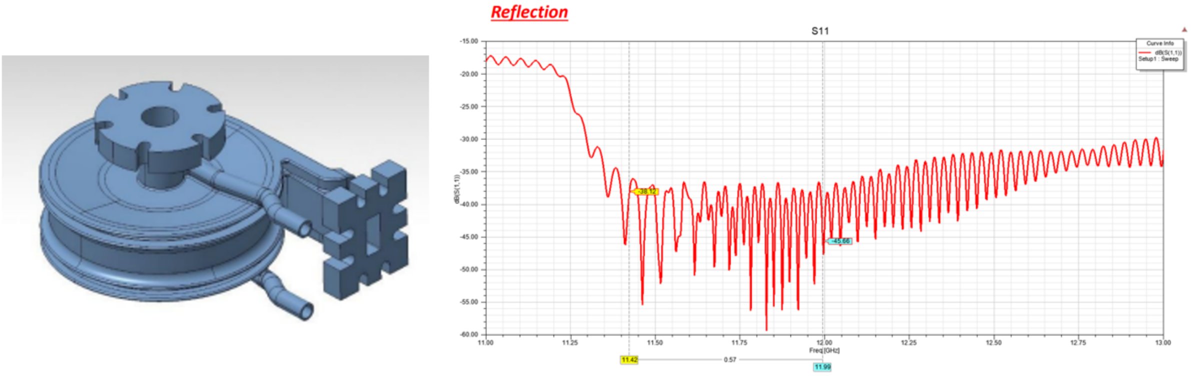

Figure 3.63: Spiral RF load.

3.2.4 *Thermal sensitivity*

Regarding the WR-90 ($a = 22.866$ mm, $b = 10.16$ mm) waveguide network, the phase shift due to thermal expansion will be given by the change in longitudinal length and cross section of the waveguide by

$$\phi+\Delta\phi = 2\pi\frac{d+\Delta d}{\lambda+\Delta\lambda} \longrightarrow \frac{\Delta\phi}{d} = 2\pi\frac{\alpha\lambda\Delta T-\Delta\lambda}{\lambda(\lambda+\Delta\lambda} \quad , \tag{3.7}$$

where d is the length of the waveguide and λ is the wavelength of the TE_{10} mode in a rectangular waveguide, which is given by

$$\lambda = \frac{2}{\sqrt{\left(\frac{2f}{c}\right)^2-\left(\frac{1}{a}\right)^2}} \quad . \tag{3.8}$$

If the temperature shift is on the order of ~ 10 K, the phase shift per kelvin and meter of waveguide will be linear, and it is given by

$$\frac{\Delta\phi}{\Delta T} = 0.292\,\frac{\text{deg}}{\text{K}{\cdot}\text{m}} \quad . \tag{3.9}$$

3.3 S-band RF waveguide distribution system

The preliminary schematic layout of the S-band RF system is shown in Fig. 3.64. It consists of a klystron with a peak power of 30 MW, two RF windows, a circulator, a directional coupler and an RF gun. The circular operates with SF_6 gas while the long waveguide and RF gun operate in a vacuum environment. Two RF windows are used to isolate the circulator from the vacuum.

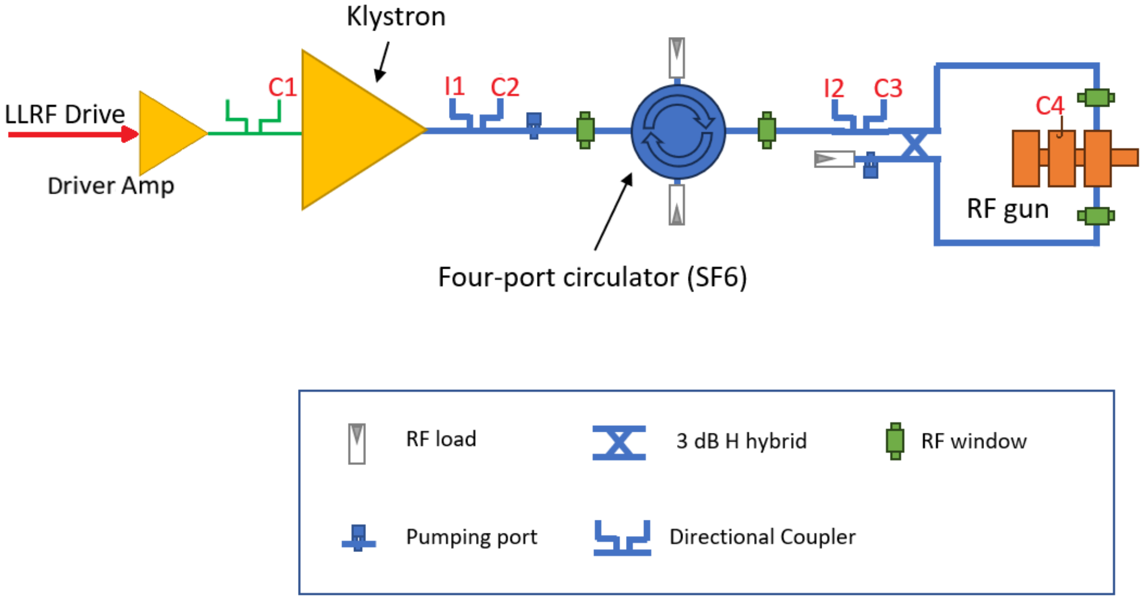

Figure 3.64: Schematic layout of the S-band RF system.

The operation frequency of the RF system is 2.998 GHz, within the range of S-band. The S-band is very common and has been used in a wide range of applications, including medical linear accelerators. The S-band RF components, except for the RF gun, can be provided by many companies, such as MAGE industries, Ferrite Microwave Technologies and CML Engineering. The S-band waveguides have ports with standard dimension WR-284 (72.136 mm × 34.036 mm). The distance between the klystron and the RF gun is about 15 m. The RF loss of the 15 m waveguide is 6.5%. One example of the circulator is shown in Fig. 3.65. The RF loss of the circulator is smaller than 0.2 dB which corresponds to 4.5%. The overall RF loss is about 10.7%.

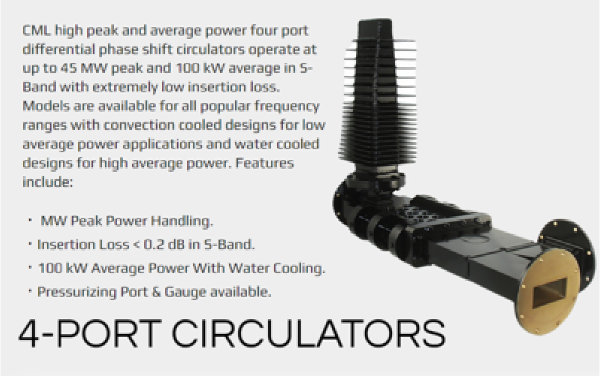

CML high peak and average power four port differential phase shift circulators operate at up to 45 MW peak and 100 kW average in S-Band with extremely low insertion loss. Models are available for all popular frequency ranges with convection cooled designs for low average power applications and water cooled designs for high average power. Features include:

- MW Peak Power Handling.
- Insertion Loss < 0.2 dB in S-Band.
- 100 kW Average Power With Water Cooling.
- Pressurizing Port & Gauge available.

4-PORT CIRCULATORS

Figure 3.65: Circulator from CML Engineering.

3.3.1 Thermal sensitivity

In the WR-284 ($a = 72.136$ mm, $b = 34.036$ mm) waveguide network RF phase shift due to thermal expansion will be given by the change in longitudinal length and cross section of the waveguide by Eq. (3.7). If the temperature shift is on the order of $\sim 10\,\mathrm{K}$, the phase shift per kelvin and meter of waveguide will be linear, and it is given by

$$\frac{\Delta\phi}{\Delta T} = 0.0849\,\frac{\mathrm{deg}}{\mathrm{K{\cdot}m}} \quad . \tag{3.10}$$

4 High power RF systems

The DEFT RF powering system must reliably provide RF pulses to drive the S-band injector and X-band accelerator. The powering system uses two types of klystron amplifiers, in S and X-band. Klystron parameters are specified in Table 3.20. These parameters correspond to commercially available klystrons in S-band and X-band, and commercial modulators are available for both. The standard, treatment, operating mode with 400 Hz bursts and a flexible number of pulses is within the specifications of commercial devices. In addition to standard operation, the powering system will be used to condition newly fabricated RF structures. Conditioning new structures may require up to a few weeks to achieve the operating gradient. During conditioning, it is advantageous to operate the RF system at a constant high repetition rate to minimize total processing time. In addition, a power overhead of 10% will allow higher gradients to be reached during conditioning, increasing stability at the nominal operating gradient.

In close communication with industry, we selected devices whose performance parameters are consistent with the specifications listed in Table 3.20. These klystrons are: 30 MW S-band klystron (Thales, France), 25 MW X-band Klystron (Canon ETD, Japan) and K200 modulator (ScandiNova, Sweden), see Fig. 3.66. The catalogue parameters of selected devices are summarised in Table 3.21. Our business partners confirmed that these devices have already been shipped to and operated by different customers. The only exception is the 25 MW X-band klystron, for which the commercialized version is delivering 20 MW (by specification). Canon ETD assured that the scaled 25 MW version of this tube will require only an additional 3-month development period (mostly tooling) with no extra risk for the tube performance. We received from the different companies the 3D drawings and files that have been

Table 3.20: Klystron parameters specification.

Frequency	3 GHz	12 GHz
Pulse length, μs	1.5	2.3
Peak power, MW	30	25
Repetition rate, Hz	400	400
Average power, kW	16.2	23
Power redundancy, %	10	10
Isolation	Circulator	None

used for RF source facility integration.

Table 3.21: Commercial Klystron and Modulator parameters. ScandiNova confirmed that 310 kV will be accessible by adjusting the HV transformer circuit.

	Modulator K200	TH2135	E37119
Frequency		3 GHz	12 GHz
Peak power, MW	80	27	22.5
Average power, kW	55	16.5	20.7
Pulse Voltage, kV	160–290	270	310
Pulse current, A	120–280	280	190
Rep. rate, Hz	0–500	400	400
Pulse length, μs	0.5–10	1.5	2.3

Figure 3.66: Images of 30 MHz S-band Thales klystron (left), 25 MW X-band Canon klystron (centre) and ScandiNova K200 modulator.

The schematic layouts of 3 GHz and 12 GHz RF power stations are shown in Figs. 3.64 and 3.51, respectively. All 3 GHz waveguide components are commercially available from various vendors worldwide. Note that commercial 3 GHz high-power RF circulators use SF6.

The particularity of the X-band klystron configuration is the fact that they will operate in pairs. This is due to the need to provide tight control on the shape of RF pulse to compensate for beam loading in the accelerating structure and to ensure high repetition rate of the individual devices. Such a mode of operation has been used at CERN´s XBOX3 with 6 MW X-band klystrons for more than a decade and is proven to be reliable.

5 Low level RF control

5.1 Introduction

The low level RF system (LLRF) controls the voltage, amplitude and phase for each klystron. It also acquires data from bi-directional couplers to implement a pulse-to-pulse feedback. The X-band part of the system is driven by the combination of two klystrons, while the S-band part is driven by a single klystron. Both systems use a pulse compressor, requiring arbitrary phase and amplitude control from the LLRF system in order to ensure the correct output pulse shape.

The current baseline for a patent's treatment consists of up to 40 RF pulses spaced at 400 Hz with up to 507 bunches per RF pulse.

The charge per bunch is constant, hence the total dose will be retrofitted to machine parameters by defining the number of pulses (integer between 0 and 40) and the number of bunches per train, which is also an integer sent to the laser. The fine-tuning on the total delivered dose will be carried out by calculating in real time the number of bunches in the last RF pulse.

The LLRF should also implement a reflection/arc detection system to stop the RF in the event of breakdowns or arcs during operation. The response time of this detection system should be such as to avoid driving the pulse immediately after the one where the breakdown was detected.

Finally, the LLRF will interface with other systems, such as Diagnostics, Timing, and Interlocks. An example is the requirement to generate LLRF synchronous triggers for the DAQ of the beam current transformer. Furthermore, the LLRF should be synchronized with the patient's movements (e.g, breathing). This will require a trigger or a similar method to tell the RF (and the laser system) to start the treatment at the next 400 Hz cycle.

5.2 LLRF channel requirements

The LLRF controls the voltage amplitude/phase of each klystron by playing a predefined IQ beam loading compensation table via an IQ vector modulator. Beam loading compensation tables for I and Q for each klystron are defined during the setup phase of the LLRF system (see below) and should be updated regularly to compensate for temperature drifts or other changes. Each table includes several [I, Q] values sufficient to cover the entire pulse at the sampling period of the DAC. For instance, up to 1000 IQ vectors will be needed at each pulse and for each klystron for a DAC sampling frequency of 250 MHz and a pulse length of 4 μs.

Diagnostics and LLRF setup are carried out by a demodulation process where two ADCs are needed per directional coupler to include both forward and reverse power. An IQ vector can be obtained from a single ADC, whilst two DACs per klystron are required for voltage control (one for I and Q, respectively).

Table 3.22 shows the maximum number of DAC and ADC channels needed for the HLRF configurations depicted respectively in Fig. 3.64 (S-band system) and Fig. 3.51 (X-band system). It should be noted that here we include an antenna pick-up in the RF gun, as shown in Fig. 3.67, that needs an additional ADC for its data acquisition.

Commercial off-the-shelf boards often have double DACs and modulators that generate the signal to the cavity controlled in amplitude and phase. The number of ADCs will typically be higher than that shown in Table 3.22. It is common practice to distribute a reference signal to each ADC board and to have it digitized there. This will allow recovering the phase in case the synchronisation between boards is lost. The need to digitize the reference will therefore increase the overall number of ADC channels required by the system, as one ADC channel per board will be dedicated to the reference. In principle, DACs do not need this reference as they are controlled in feedback and should share the same clock everywhere in the system.

Table 3.22: Maximum number of single ADC and DAC channels required to acquire the signals originating from directional couplers and to control the voltage and phase of all klystrons. The digitisation of references is not included.

		DACs	ADCs
S-Band	1 klystron	2	6
X-Band	2 klystrons	4	46

It is possible to distinguish between channels (ADCs) that will be used for setting up and others that will be important for operation. This might allow reducing the size and overall cost of the system, if needed, by replacing the setup channels with operational ones after the setup is completed. Figures 3.67 and 3.68 give an overview of the usage of the acquisition channels currently considered in the S-band and X-band systems. The function of each channel is shown via letters: “S” corresponds to setup, “C” to control, and “I” to interlock.

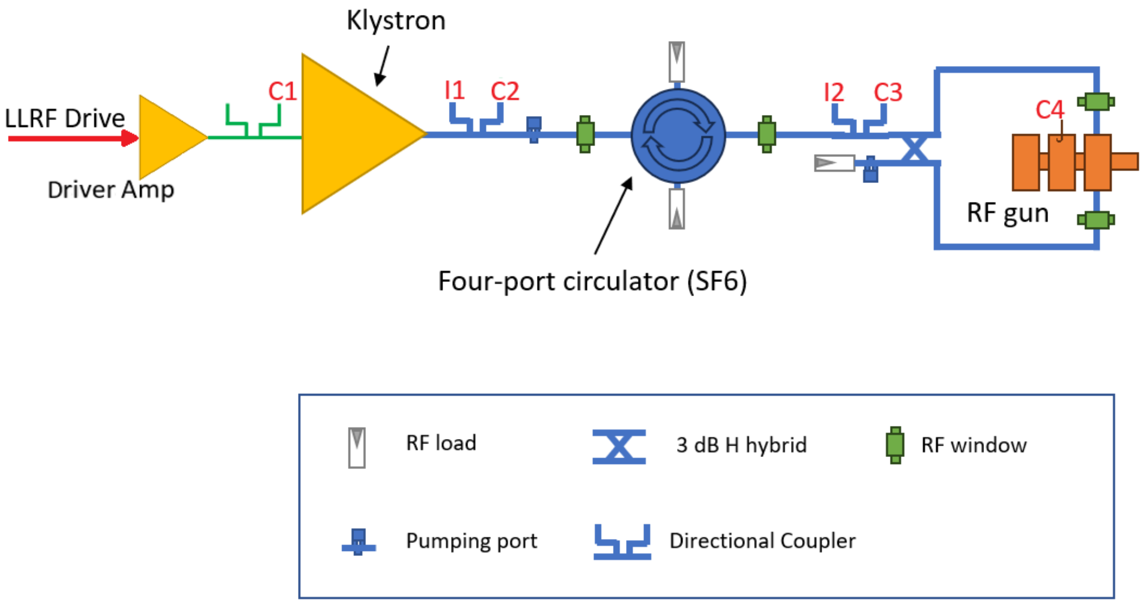

Figure 3.67: Usage of the acquisition channels foreseen in the S band system. Key: “S” = setup; “C” = control; “I” = interlock.

For the S-Band system, a "missing power interlock" can be implemented by comparing the sum of C1 and C2 with C3. An interlock could be triggered if the difference is higher than a certain threshold corresponding to losses along the line. In principle, once everything is set up, only one of C1 and C2 is

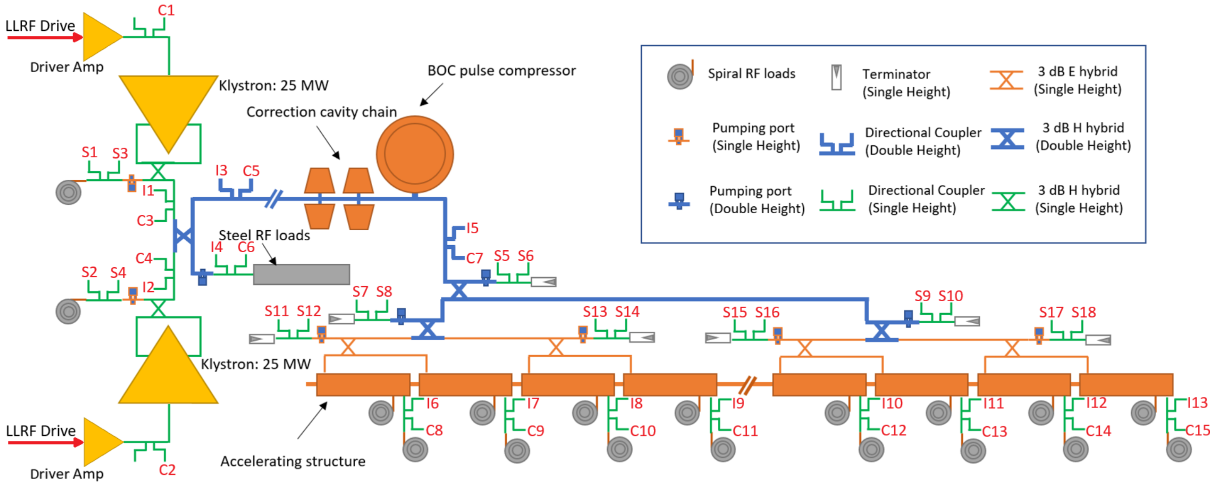

Figure 3.68: Usage of the acquisition channels foreseen in the X band system. Key: "S" = setup; "C" = control; "I" = interlock.

strictly required. Another "missing energy" interlock can be obtained thanks to the pick-up in the gun. If the integrated waveform input to the gun is higher than the integrated value of the waveform detected by the pick up, then there is missing energy indicating an arc, and the RF can then be turned off.

For the X-band system, C5 and C6 can be used to control the amount of power that goes into the waveguide after C5 and the load after C6, respectively. An important "missing power interlock" can be obtained by comparing C7 with the sum of C8 to C15. An interlock shutting down the RF could be triggered if the difference is higher than a certain threshold corresponding to losses along the line.

5.3 LLRF basic design recommendations

ADCs and DACs clocks should be synchronous with the RF to eliminate timing jitter; this can be achieved by using integer dividers, such that the RF and the trigger signals are derived from the same source.

The choice of the intermediate frequency (IF) is important, and we recommend selecting it to avoid IQ sampling, namely IQ values spaced by 90°. The IQ sampling has the advantage of simplified signal processing of I and Q values, but would "exercise" the ADCs only at four points and would cause harmonics of the signal under observation to alias the same frequency as the carrier itself, thus introducing distortion. This would have been the case if the IF had been chosen as 31.5 MHz in Fig. 3.69.

The IF in Fig. 3.69 was selected to be 25 MHz and will provide a non-IQ sampling [24] of the input signal. Retrieving the IQ data from the digitised samples requires more processing power than simply "reading out" I and Q data. The additional processing power is, however, typically present in a modern digital LLRF system, and this method greatly improves the quality as well as the repeatability of the measurement. The ADC clock of 125 MHz can be derived from the 3 GHz reference via a division by 24. The DAC clock of 250 MHz or even 500 MHz can also be obtained, as shown in Fig. 3.69.

Signals to and from the 12 GHz system can be up- and down-converted as shown in Fig. 3.70 to be treated by the same type of LLRF system used for the 3 GHz signals and described in the previous sections. The scheme shown refers to a single channel of acquisition and control. Additional channels will be needed to properly match the physical HLRF layout.

On the down-conversion path, a low-pass filter with 4 GHz cutoff is sufficient to select the relevant signal. On the up-conversion path, an 11 to 13 GHz bandpass filter would be sufficient to cut out 3n GHz

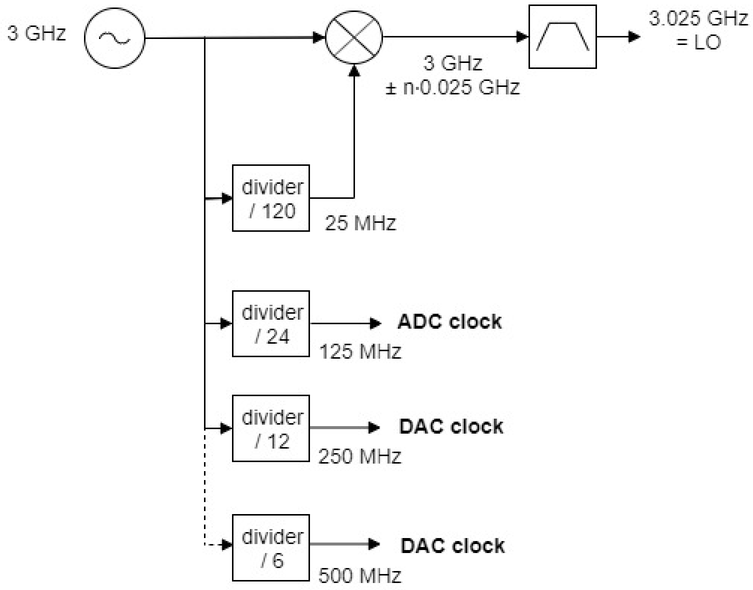

Figure 3.69: Generation of a Local Oscillator (LO) frequency at 3.025 MHz and ADC/DAC clocks. The intermediate frequency (IF) was selected to be 25 MHz and the signals to be observed are sampled with non-IQ sampling.

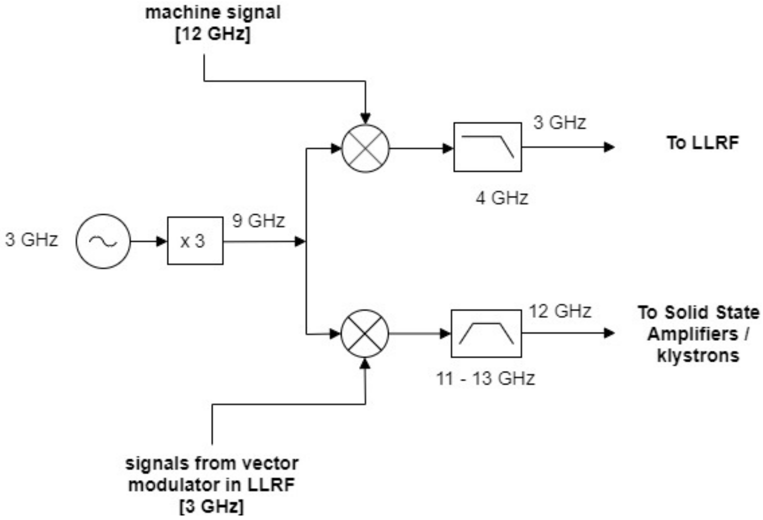

Figure 3.70: Down and up conversion of 12 GHz signals to treat them with a common LLRF system.

components.

The 9 GHz reference is shared between the up-and down-conversion paths because typically in COTS boards several down-conversion channels and one or more up-conversion channels are available. As a consequence, the 9 GHz signal can be physically the same for both paths inside the same board.

Other schemes could, of course, be implemented. The advantage of the scheme shown in Fig. 3.70 is that the IF frequency can be the same as that of the 3 GHz LLRF, hence the same LLRF system could be used for both the 3 and 12 GHz systems, the only difference being the additional up- and down-conversion stage (typically implemented in an external chassis) required by the 12 GHz acquisition and control.

5.4 LLRF design recommendations for phase and amplitude stability

Figures 2.29 and 2.30 define the most demanding requirements on the phase and amplitude stability for the X-band systems as 0.3% for the amplitude and 1° for the phase.

A factor of two on all fluctuations can be gained by operating the hybrid as a perfect combiner, i.e. sending all the power to the waveguide. Both klystrons would run at the same power level; to vary the gradient, we would then reduce the power level for both klystrons in tandem while maintaining the 90-degree phase difference between the two. As a consequence, a 0.6% amplitude variation between the two klystrons translates to only 0.3% as seen by the linac, and a 2° RF phase variation between the two klystrons translates to only 1° as seen by the linac.

Such requirements are similar to those for CERN facilities such as CLEAR, AWAKE and XBOX.

This paragraph outlines some features we recommended implementing in order to fulfil the stability requirements.

The main oscillator, which generates the RF references for both laser/gun and accelerating structure systems, should have good noise characteristics, as phase noise in the RF reference signal affects RF amplitude and phase stability. Currently, the ARES facility uses a commercial signal generator with a phase noise lower than 20 fs RMS in the 1 Hz to 10 MHz range.

The main oscillator should be located in the part of the laser room closer to the klystrons, to keep the reference distribution distance to laser/gun and klystrons as short as possible and of similar (although not identical) length. The LLRF crates should also be housed in the same room, as close as possible to the main oscillator, and should be temperature-stabilised to 1 K. Even with all channels (for setting up and for operation) fully deployed and using a micro-TCA implementation, the LLRF rack would consist of two crates.

To minimise temperature-related phase drifts of the RF reference and signal distribution, it is recommended to use cables with a stable phase for temperature variations. An example is the MegaPhase UltraPhase™ coaxial cables line (https://megaphase.com/products/ultraphase-cables-to-110-ghz) and in particular the GE12 Series, which allows a maximum frequency of 40 GHz. For these cables, a phase shift of 0.26 degrees per 1 K change in temperature is to be expected for operation at 12 GHz and for a 10 meters cable between 15–35 K, i.e 0.026 degrees/C/m. For the 3 GHz case, this shift will be only 0.0065 degrees/C/m.

Both temperature-controlled crates and cables with a stable phase for temperature variations are used in CERN's XBOX installation.

Much more demanding requirements, especially in terms of phase stability, have been satisfied in facilities such as ARES [25], an S-Band linac accelerator under commissioning at DESY, and PSI's SwissFEL [26]. To this end, these facilities implement additional features in parallel to those mentioned above. For instance, the RF reference phase is measured via an RF interferometer before the pulse. The drifts due to humidity or temperature are then compensated for by a dedicated module hosted in each LLRF crate. These additional features are not necessary for the current DEFT requirements.

5.5 Beam loading compensation tables

Due to the availability of memory in a modern digital LLRF system, it is possible to download all 40 tables for each pulse before the start of the treatment. For example, for a 4 μs pulse with a sample rate of 250 MHz, 1000 samples are required. For 32-bit IQ vectors (16 bits each), the full pulse train requires only 160 kBytes of memory.

The number of samples to be played will depend on the number of bunches in each RF pulse. This is known in advance for all RF pulses apart from the last one, where the number of bunches is an integer defined in real time to fine-adjust the total dose provided.

It is recommended that IQ samples are set to 0 after the last bunch in an RF pulse has passed to avoid over-driving the klystrons during the treatment. For the case of the last RF pulse at each energy, where the total number of bunches is decided in real-time, it is preferable to set the remaining IQ vectors to 0, also.

It should be noted that bunches are cut from the tail of the RF pulse and not from its head, hence the beam would be affected by the tables being played even after the last bunch for that pulse has passed.

At 35 MV/m with beam loading and at around 50 MV/m without beam loading, the gradient is overall rather low. As a consequence, the probability of a breakdown in the accelerating structures will be below 1E-10, i.e. comparable with the probability of a power blackout, hardware failure or bad human manipulations. For this reason, specific mechanisms to avoid over-driving the klystrons are not considered essential.

Finally, it is very important that the beam loading compensation table starts exactly when the beam arrives, so as not to affect the energy. This calls for a good stability of the rise time of the RF pulse with respect to the bunch time. This is ensured by the synchronous clock and trigger generation scheme, described previously.

5.6 Adaptive feedforward algorithms

The LLRF controls the 3 GHz klystron for the electron gun, which is static and not a travelling wave structure. As for the klystrons controlling the 12 GHz linac, they always work in pairs, so the amplitude can be controlled by de-phasing the two klystrons, and this is a linear effect. However, the relative and overall phases need to be adjusted.

An additional difficulty of the 12 GHz system is that the beam loading voltage is not in phase with the RF. As a consequence, calculating the correct amplitude and phase profile before going into a pulse compressor to get the right amplitude and phase for the rise time is a complicated task.

We recommend using an adaptive algorithm to define in an iterative manner the optimum control parameters, similarly to what has been operational for years in CERN's Linac4 [27].

A certain number of pulses with the beam, but without the patient, are needed for the adaptive feedforward to learn the best parameters, via a Multiple Inputs Multiple Outputs (MIMO) matrix. This processing is non-trivial and in CERN's Linac4 is carried out in software rather than firmware.

The train from the photoinjectors is not fully flat, as it depends on the train length. Beam loading is also present within the laser system, and the first bunches in a pulse have higher energies, which then decay for further bunches before reaching a steady state. However, as long as this effect is repeatable, machine learning will be possible and effective.

The beam loading compensation tables used during the patient treatment will require regular updates. The time interval between updates to re-learn the optimum parameters depends on the overall system stability. It is expected that at least a daily check will be required.

5.7 LLRF interlocks

Events such as arcs are expected during the structure conditioning. What is typically required in this phase is maintaining their rate below a certain level, mainly to avoid damaging the system.

A reflection/arc detection system should, however, be implemented so that the RF can be stopped if a breakdown is detected during the treatment. The reaction to this situation should be fast to avoid additional RF pulses being generated after the breakdown detection.

The detection can be carried out by having a threshold detector in the detected reflective power for each directional coupler: if a spike is detected during treatment, the treatment should be stopped by raising an interlock and/or by cutting directly the RF drive signal. The reason for this is that, as RF pulses come every 2.5 ms, the vacuum will not have the time to recover between successive pulses. If the machine is kept pulsing, it could inject megawatts of power into a plasma, causing subsequent reflections and possible damage to the waveguide system or klystrons.

If a breakdown is detected after the end of the last pulse in a treatment, there is no danger for the patient; no additional pulses would be generated, and the vacuum would recover within some tens of seconds.

On the other hand, the LLRF should also interface with interlocks coming from the vacuum system, to stop the RF as soon as a non-conformity is detected.

5.8 Some notes on LLRF operation during treatment

This section summarises some hints for the LLRF operation during a normal treatment day. It is to be underlined that some of the ideas below still need to be finalised.

During standard operation, the LLRF will play in feedforward the IQ tables prepared during the setup phase. Acquisition and detection of arcs/breakdowns will still be carried out.

It is envisaged that the validity of the beam loading compensation tables is checked at least once per day, without patients. Some checks can also be done immediately before the treatment and without a beam by de-phasing the laser.

The treatment should be synchronised to the patient's movements, such as their breathing. It is possible that for the "human response time-scale" it might be sufficient to start a treatment with a resolution of 2.5 ms; i.e. by specifying a "*initiate treatment at the next 400 Hz RF pulse*". This would require a dedicated trigger for the RF as well as the laser. This topic still needs confirmation.

As mentioned above, the accelerating structures run at a low gradient (35 MV/m with beam loading and around 50 MV/m without beam loading) and the probability of a breakdown is overall rather low. It is, however, possible to zero the IQ vectors after the last bunch in a pulse has passed. Mechanisms to detect an arc or a breakdown should, however, be implemented to immediately stop the RF, i.e. to prevent the next pulse from being generated.

5.9 Example of LLRF implementation with COTS hardware

An example of implementation within COTS boards is shown in Fig. 3.71. This could refer, for instance, to Struck (https://struck.de/) 8300KU AMC and RTM boards within a microTCA crate. The system includes 8 downconverter channels and one vector-modulator channel. The local oscillator (LO) frequency can be received by each board either from the RF backplane (as shown in the picture) or through a front-panel connector. Of the 8 ADC channels available in each board, 7 can be used for machine signals at 3 GHz whilst one should be reserved to acquire the 3 GHz reference,

An FPGA handles the digitization of the data from the ADC and the conversion of the sampled signals to IQ vectors. The feed-forward data processing could be done within the FPGA itself, but for simplicity and flexibility, it would typically be carried out by a CPU board in a different microTCA slot. The FPGA also hosts the IQ beam loading compensation tables and controls the vector-modulator channel.

A possible example of a full LLRF system implemented in a microTCA crate is shown in Fig. 3.72.

The boards marked as "LLRF" are the RTM + AMC pair, depicted in Fig. 3.72 and receive the 3 GHz reference. Ideally, a timing card could be hosted in the same crate, clocked by a 500 MHz (or lower) clock obtained by dividing the common 3 GHz reference. The timing card should also receive a 400 Hz train from the timing system. To avoid drifts, the whole crate should be kept at a stabilised and

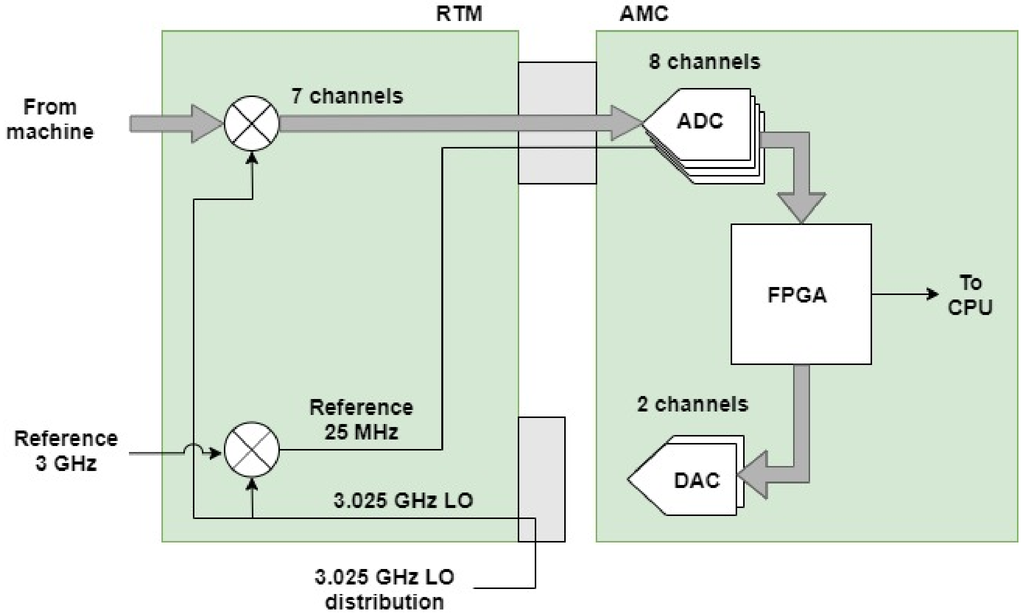

Figure 3.71: Example of implementation of ADC and DAC channels within a microTCA crate. The RTM module is a rear transition module, whilst the AMC is an advanced mezzanine card.

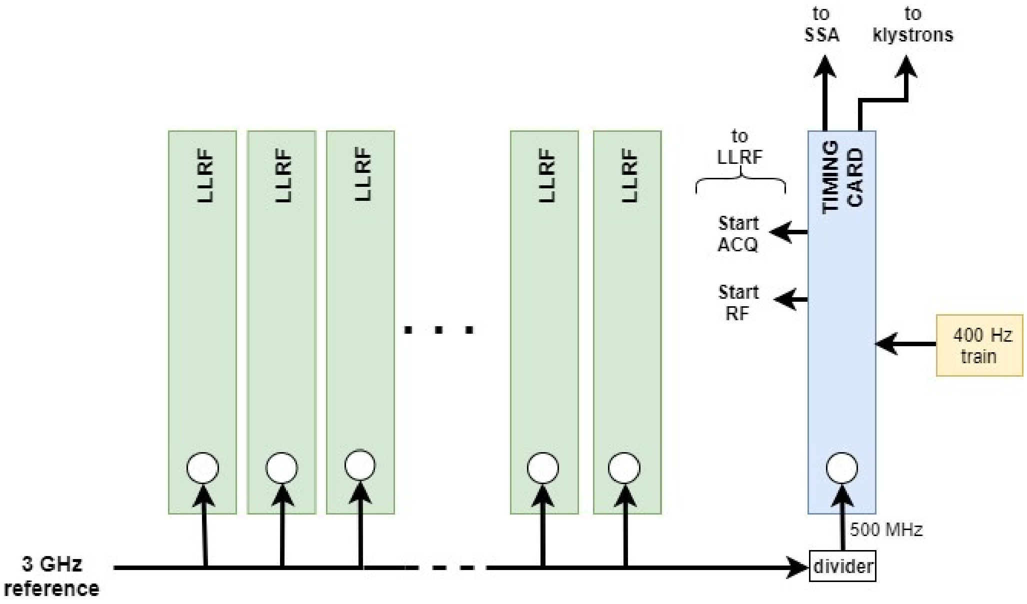

Figure 3.72: A possible implementation of LLRF and integrated timing system within a microTCA crate.

controlled temperature.

The timing card will be able to generate pulses and will integrate counters and delays. Pulses from the 400 Hz external RF train would reset the counters.

Outputs from the timing card include triggers to the solid state amplifiers (SSA) and to the klystrons. Triggers such as "*START ACQ*" and "*START RF*" are sent internally to all LLRF boards. In CERN's XBOX3, SSAs need to be started first, then a few microseconds afterwards, the klystrons are started. The "START ACQ" will follow, and finally, the "*START RF*" is sent to start the pulse.

This logic could also integrate the synchronisation of the LLRF to the patient breathing, by receiving, for instance, the “*start treatment at the next 400 Hz cycle pulse*” trigger.

LLRF systems organised as the one mentioned above have been successfully implemented, deployed and operated at CERN for many years. One example is the LLRF system for the XBOX3 test stand [28], shown in Fig. 3.73 and operating at 12 GHz.

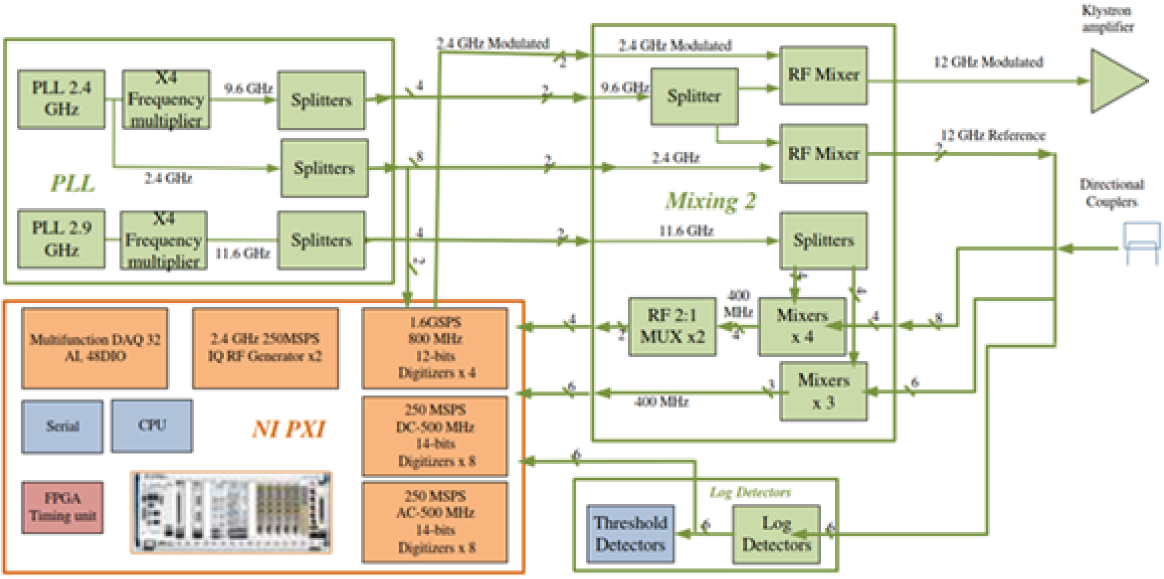

Figure 3.73: Schematic of the LLRF and signal acquisitions in CERN’s XBOX3 system.

The XBOX3 system is partially based upon National Instruments cards and relies on a 2.4 GHz master oscillator. The 1.6 Gsample (Giga sample) digitizers and a high IF frequency of 400 MHz were selected as one of the aims for this system was to study breakdowns, hence a very high bandwidth was desired. This would be a costly over-specification for DEFT, hence the implementation suggested above.

CERN has also developed an LLRF for a 3 GHz system, referred to as SBOX. This is an S-band test facility at CERN, powered by a 43 MW S-band klystron via WR-284 waveguide lines. The klystron can deliver 43 MW, 5 μs RF pulses at a repetition of 50 Hz and is protected against reflected power by a high power circulator.

6 Magnets

6.1 Solenoids

A set of two flat solenoids is positioned at the exit of the gun to focus the emitted electrons and limit their expansion due to the space charge effect. These solenoids are based on the same design principles as those used in the electron source of the CLEAR experiment at CERN, accordingly known as IS-10-4826 and IS-10-4827. Since detailed drawings or CAD files of these magnets were unavailable, the magnet designers implemented a reverse-engineering process. This involved creating an advanced parametric CAD model using CATIA® V5, allowing for precise modifications and simulations.

To ensure the reliability of the design, the models underwent rigorous validation, which included a series of electromagnetic simulations in ANSYS® Maxwell. These simulations were instrumental in verifying the combined magnetic fields generated by the solenoids, providing a quantitative assessment of their performance.

As part of the validation process, the field spectrum data calculated from the simulation software were shared with the Beam Dynamics Team. This data, illustrated in Fig. 3.74, was essential for the

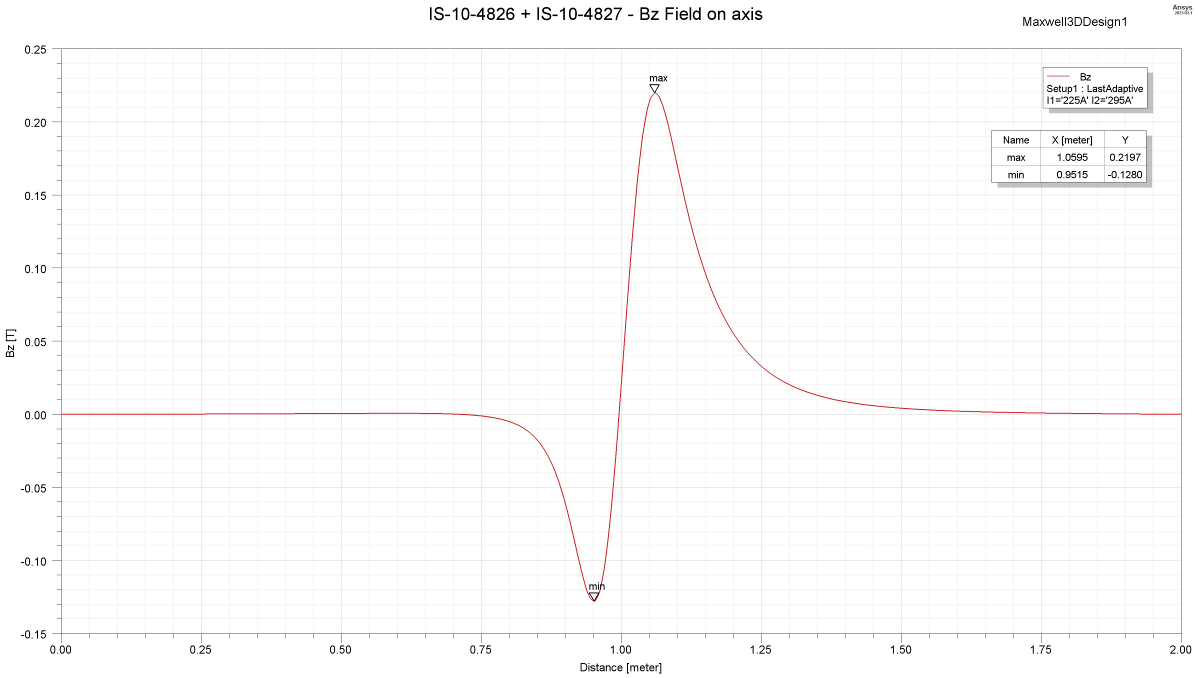

Figure 3.74: Bz field on axis of the solenoid setup at operational current.

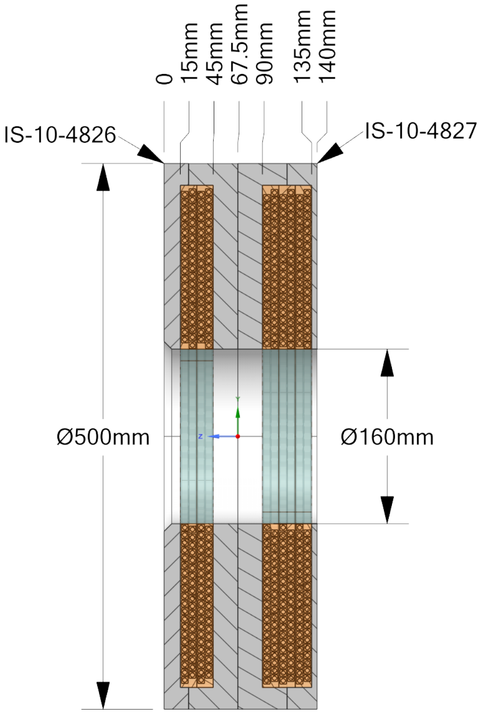

Figure 3.75: Section of the solenoid setup at the injector.

validation cycle. The results were reviewed by beam dynamics experts, who analysed the data to confirm its validity and the functionality of the 3D design of the solenoids for the DEFT machine.

These solenoids are constructed using square hollow copper conductors directly cooled with demineralized water flowing through the conductor channel. They are insulated with wrapped glass fibre tape and wound in modules. Each module consists of a continuous length of conductor wound in a double-

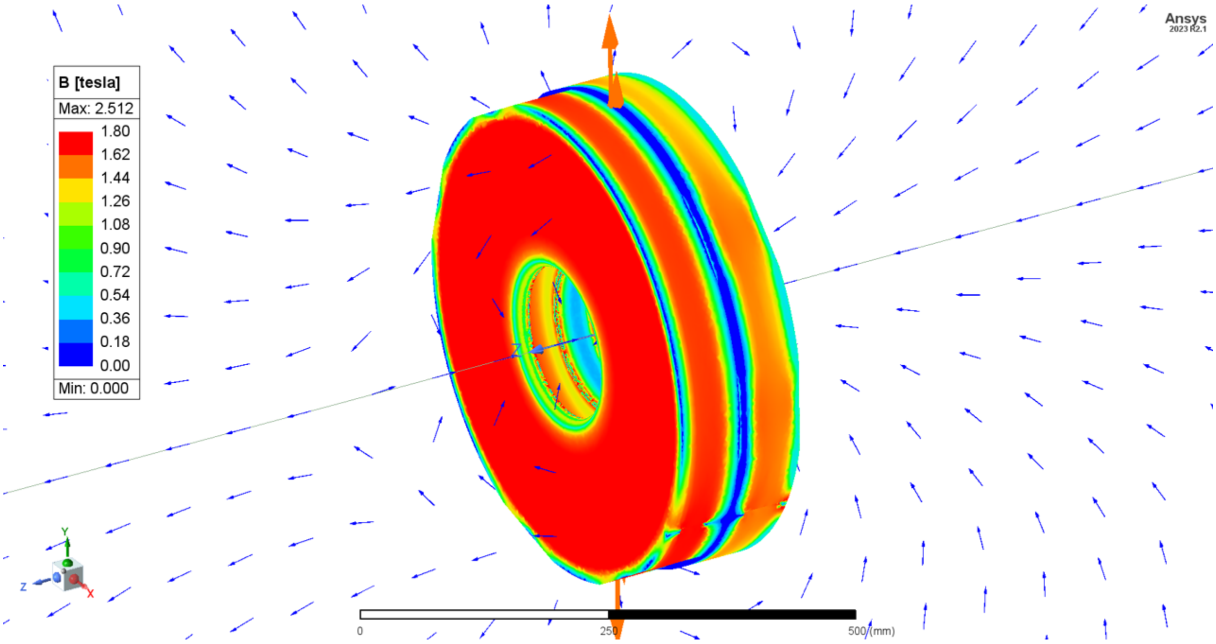

Figure 3.76: Magnetostatic simulation of the solenoids setup at the injector with operational current 225 A for IS-10-4826 and 295 A for IS-10-4827.

layer configuration, with the inlet and outlet conductor terminals exiting through what is referred to as “radial single-point leads with external access”. The layer jump from the first plane to the second occurs on the inner diameter.

The module terminals are electrically connected in series using a brazed connection busbar. Parallel cooling is provided to each coil to ensure hydraulic impedance is matched and to limit the temperature increase to a maximum of 30°C while operating at nominal current. For machine protection, these solenoids feature an interlock system that monitors the live coolant flow and temperature, which triggers automatically by cutting the current under predefined thresholds.

To aid in understanding the layout and operation of the solenoids, a section view on the XZ-plane of both solenoids in the setup is presented in Fig. 3.75. Additionally, the magnetostatic simulation of this setup, using operational currents (225 A for IS-10-4826 and 295 A for IS-10-4827), is shown in Fig. 3.76.

6.1.1 Solenoid model IS-10-4826

This solenoid is the first to encounter the beam and is a 67.5 mm long cylinder with an exterior diameter of 500 mm and an aperture diameter of 160 mm. It consists of two double-layer windings, totalling 84 turns. The square hollow conductor measures 6×6 mm with 4 mm inner diameter and is wrapped with fibreglass for inter-turn insulation, while the ground insulation is provided by epoxy resin. The production process involves vacuum impregnation with two pure iron shells that surround the coils, serving as a former during the resin potting.

Electromagnetic simulations were performed to measure and compare the field spectrum against the magnetic measurement performed by the manufacturer. The electromagnetic model is shown in Fig. 3.77. The estimated operating current is 225 A, necessary to meet the optics requirements; it can safely handle a peak current of 300 A, with a dissipated power of approximately 10 kW, at a flow rate of 5 l/min and a pressure drop of 5 bar. The flux density in iron as well as Bz profile on axis at the operational current I = 225 A is shown in Figs. 3.78 and 3.79, respectively. The parameters of the solenoid model IS-10-4826 are summarized in Table 3.23.

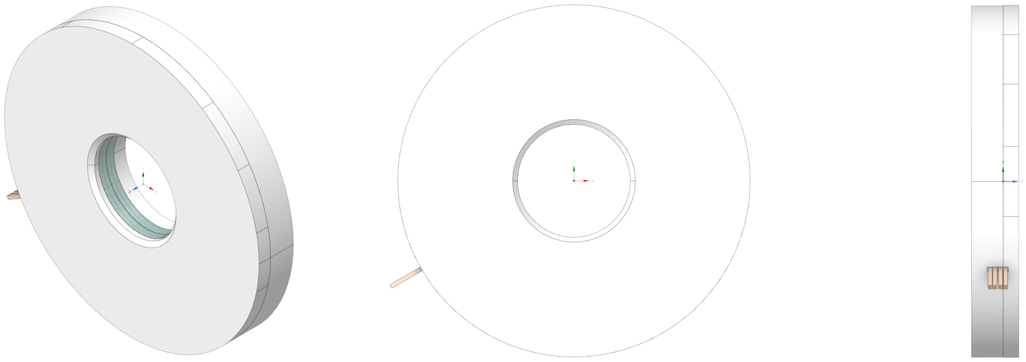

(**a**) Isometric view. (**b**) Front view. (**c**) Side view.

Figure 3.77: Views of the IS-10-4826 electromagnetic model.

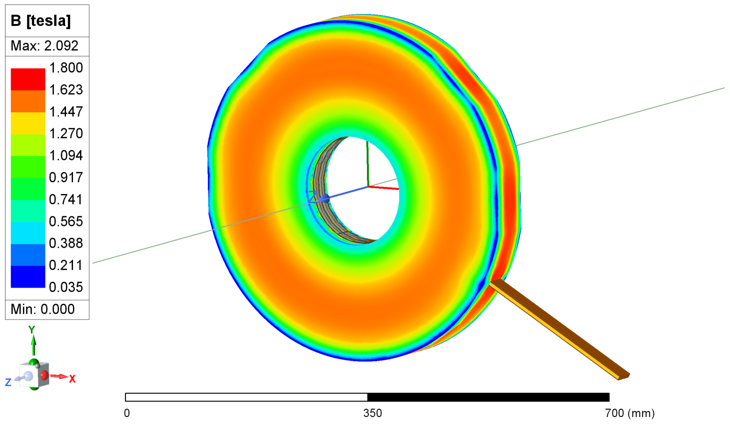

Figure 3.78: Solenoid model IS-10-4826, flux density in iron at operational current I = 225 A.

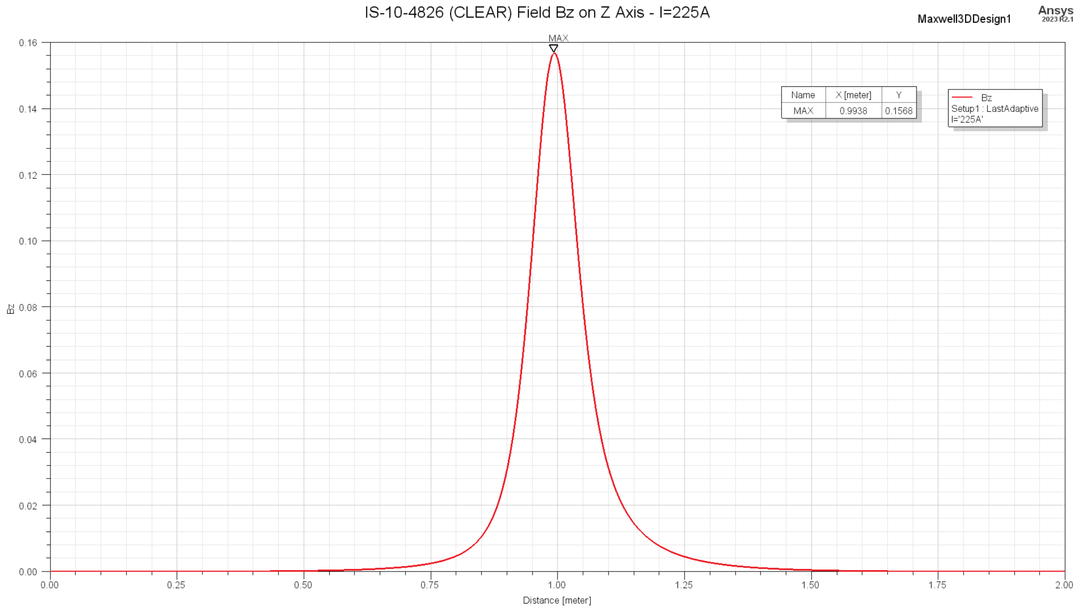

Figure 3.79: Solenoid model IS-10-4826 Bz profile on axis (Z).

Table 3.23: Parameters of the solenoid Model IS-10-4826.

Parameter	**Unit**	**Proposed design**
	Mechanical	
Overall width×height (Ancillaries excl.)	mm × mm	500 × 500
Overall length	mm	67.5
Physical aperture diameter	mm	160
Iron mass	kg	59.0
Copper mass	kg	16.8
Resin mass	kg	4.7
Total mass (Ancillaries excl.)	kg	80.5
	Conductor	
Material	-	OF copper
Type	-	Square, water-cooled
Square side	mm	6
Cooling hole diam.	mm	4
	Electrical	
Peak current (DC)	A	300
Current density peak	A/mm^2	12.9
# turns / coil	-	42
# coils	-	2
Magnet resistance peak	mΩ	70.2
Magnet DC voltage	V	21.1
Dissipated power (RMS)	kW	6.3
	Hydraulic	
Acceptable delta p	bar	4 to 10
Peak delta p	bar	8
Cooling flow at delta p peak	l/min	3.3
Delta T at delta p peak and I max.	°C	27.8

6.1.2 Solenoid model IS-10-4827

This solenoid has overall exterior dimensions of 500 mm in diameter and 72.5 mm in length, with an aperture diameter of 160 mm. It is located immediately downstream of Solenoid Model IS-10-4826 and creates a setup depicted in the accompanying figure (reference). This unit features three double-layer windings, with a total of 126 turns, using the same square hollow conductor. It is electrically insulated, assembled, impregnated, and connected in the same manner as the upstream solenoid.

Electromagnetic simulations were performed to measure and compare the field spectrum against the magnetic measurement performed by the manufacturer. The electromagnetic model is shown in Fig. 3.80. The estimated operating current for this solenoid is 295 A to meet the optics requirements; it can operate safely with a peak current of 350 A, dissipating approximately 15 kW of power, at a flow rate of 6 l/min and a pressure drop of 7 bar. The flux density in iron as well as Bz profile on axis at the operational current I = 295 A is shown in Figs. 3.81 and 3.82, respectively. The parameters of the solenoid model IS-10-4826 are summarized in Table 3.24.

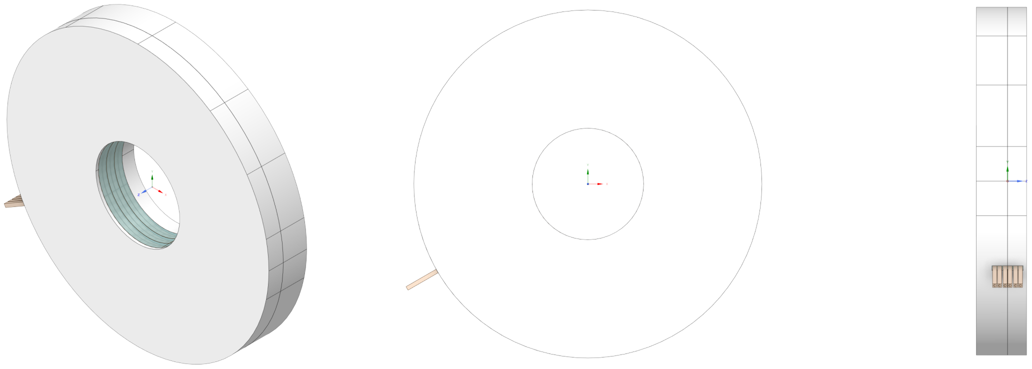

(**a**) Isometric view. (**b**) Front view. (**c**) Side view.

Figure 3.80: Views of the IS-10-4827 electromagnetic model.

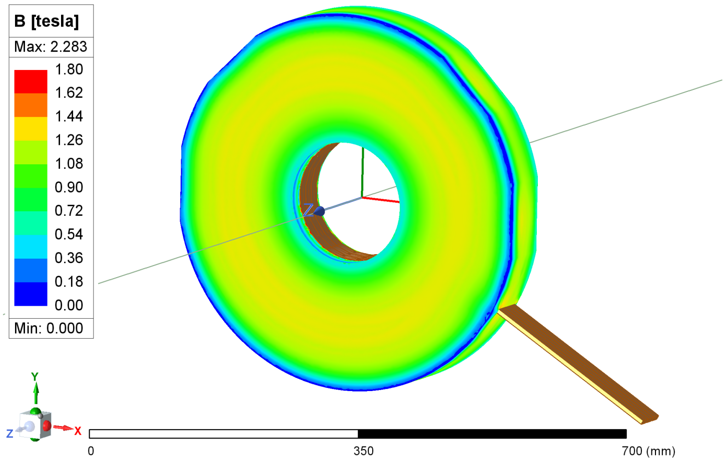

Figure 3.81: Solenoid model IS-10-4827, flux density in iron at operational current I = 295 A.

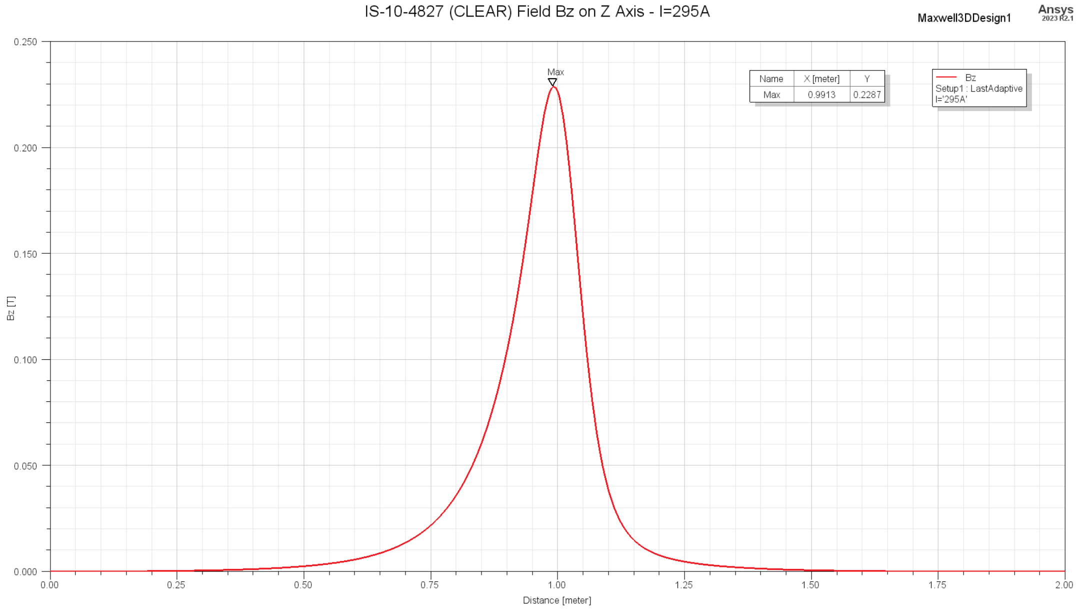

Name	X [meter]	Y
Max	0.9913	0.2287

Figure 3.82: Solenoid model IS-10-4827 Bz profile on axis (Z).

Table 3.24: Parameters of the solenoid sodel IS-10-4827.

Parameter	Unit	Proposed design
Mechanical		
Overall width×height (Ancillaries excl.)	mm × mm	500 × 500
Overall length	mm	72.5
Physical aperture diameter	mm	160
Iron mass	kg	48.7
Copper mass	kg	25.2
Resin mass	kg	7.0
Total mass (Ancillaries excl.)	kg	80.9
Conductor		
Material	-	OF copper
Type	-	Square, water-cooled
Square side	mm	6
Cooling hole diam.	mm	4
Electrical		
Peak current (DC)	A	350
Current density peak	A/mm^2	15.1
# turns / coil	-	42
# coils	-	3
Magnet resistance peak	mΩ	107.1
Magnet DC voltage peak	V	37.5
Dissipated power (RMS)	kW	13.1
Hydraulic		
Acceptable delta p	bar	4 to 10
Nominal delta p	bar	10
Cooling flow at delta p nom.	l/min	5.6
Delta T at delta p nom. and I max.	°C	33.9

6.2 Quadrupole magnets

The functional specifications of the quadrupoles have been determined based on the aperture and strength requirements defined by the beam optics (see Table 2.7). These diverse requirements are met with three different designs: two short, small-aperture quadrupoles for the linac, and a longer one for the beam delivery system (BDS). The BDS quadrupole features a larger aperture to accommodate the increased beam size and to provide large transverse beams to the isocenter.

For each design, the magnet bore apertures have been specified according to the largest beam aperture requirements of the optics, with an additional 3 mm in diameter to allow for the vacuum chamber (1 mm wall thickness) and alignment tolerances (± 0.5 mm). The field gradient homogeneity must be better than 1% across the entire dynamic range of operation.

While the design of all magnets prioritised compactness, certain constraints were imposed. The average current density in the copper conductors should not exceed 5 to 6 A/mm^2 to limit power consumption, and the flux density in the iron yokes should not exceed 1.6 T to prevent saturation. Although air-cooled versions of the quadrupoles were considered, a water-cooled design was ultimately chosen to maintain compactness and prevent heat dissipation into the facility's ventilation system.

6.2.1 Linac quadrupoles

Two quadrupole design options are proposed to meet the beam optics and integration requirements in the linac. The first design, called Q0-C4F, is 60 mm long and features a classic four-fold symmetry with 90° tapered poles and saddle coils. The second design, known as Q0-CP, is 40 mm long and utilises an unconventional claw-pole configuration with a solenoid coil. The Q0-CP design is anticipated to be more cost-effective due to its simplicity and symmetrical structure. However, it requires validation through magnetic measurements to ensure it meets the functional specifications. Two units of the selected model will be installed in the injector section, forming a quadrupole doublet.

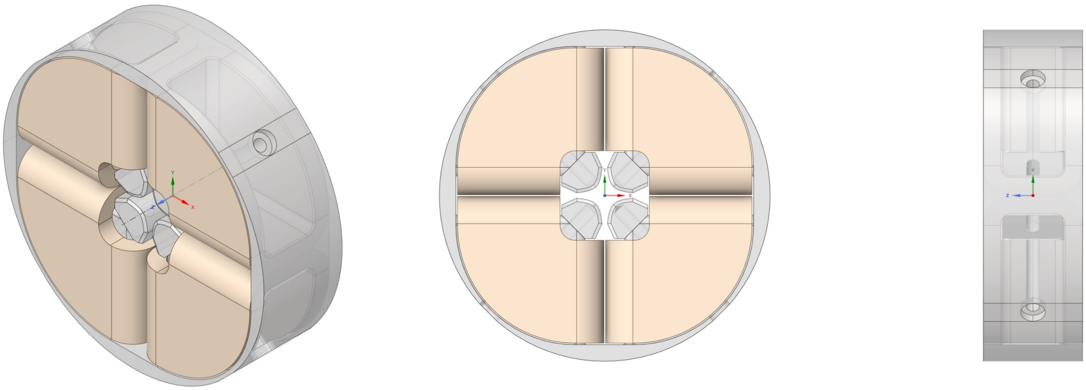

(a) Q0-C4F Isometric view. **(b)** Q0-C4F Front view. **(c)** Q0-C4F Side view.

Figure 3.83: Views of the Q0-C4F electromagnetic model.

The magnetic model of the Q0-C4F is depicted in Fig. 3.83. The flux density in the iron, when the magnet is powered at its maximum current, is shown in Fig. 3.84, with the peak field reaching 1.7 T at the base of the pole. This peak can be attributed to a mesh edge effect that creates singularities due to the rapid transition in cross-section that the flux encounters at this point. These singularities are classified as numerical artefacts and are not expected to have physical implications.

The longitudinal field profile is shown in Fig. 3.85, revealing that the field amplitude extends approximately 50 mm on either side of the magnetic centre, or about 20 mm from each yoke end.

The field quality of the 3D magnetic design is represented by the relative harmonic components of field errors with respect to the main field, as shown in Fig. 3.86. Optimisation efforts to further minimise these field errors are ongoing at the time of writing.

The mechanical parameters of the Q0-C4F magnet are listed in Table 3.25, the magnetic parameters in Table 3.26, and the electrical and cooling parameters in Table 3.27.

Table 3.25: Q0-C4F dimensions and weight.

Parameter	**Unit**	**Proposed design**
Overall width × height	mm × mm	200 × 200
Overall length	mm	60
Pole length	mm	37
Yoke mass	kg	7.6
Copper mass	kg	6
Total mass	kg	13.6

Similarly, the magnetic model of the Q0-CP is represented in Fig. 3.87. Figure 3.88 shows the flux density in the iron under maximum current, with the peak field reaching 1.5 T at the transition to

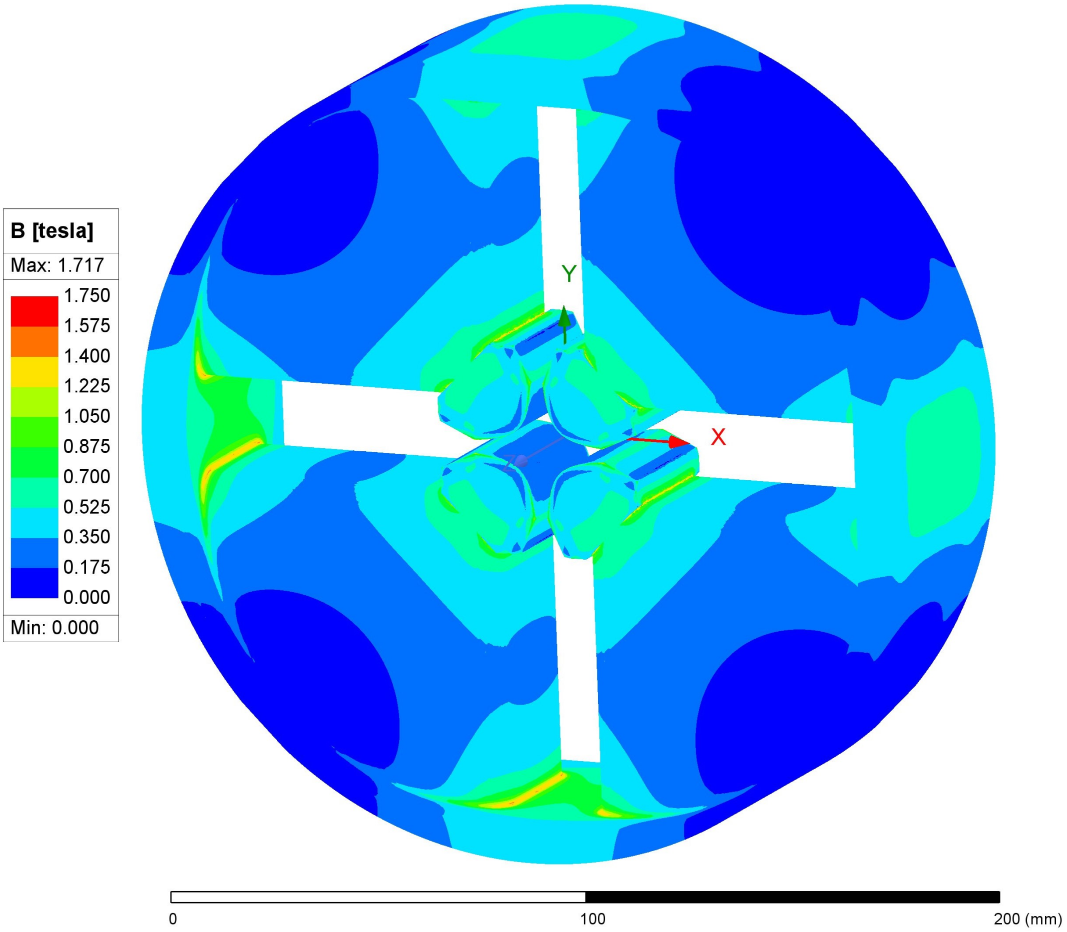

Figure 3.84: Q0-C4F, flux density in iron at peak current.

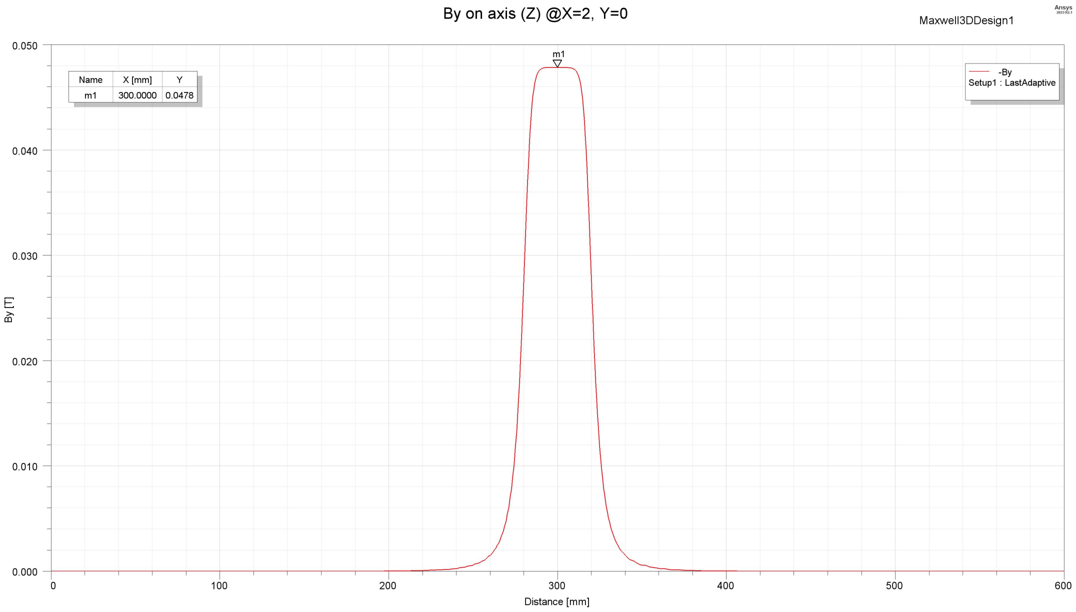

Figure 3.85: Q0-C4F longitudinal field profile, By in XZ plane at R = 2 mm along Z.

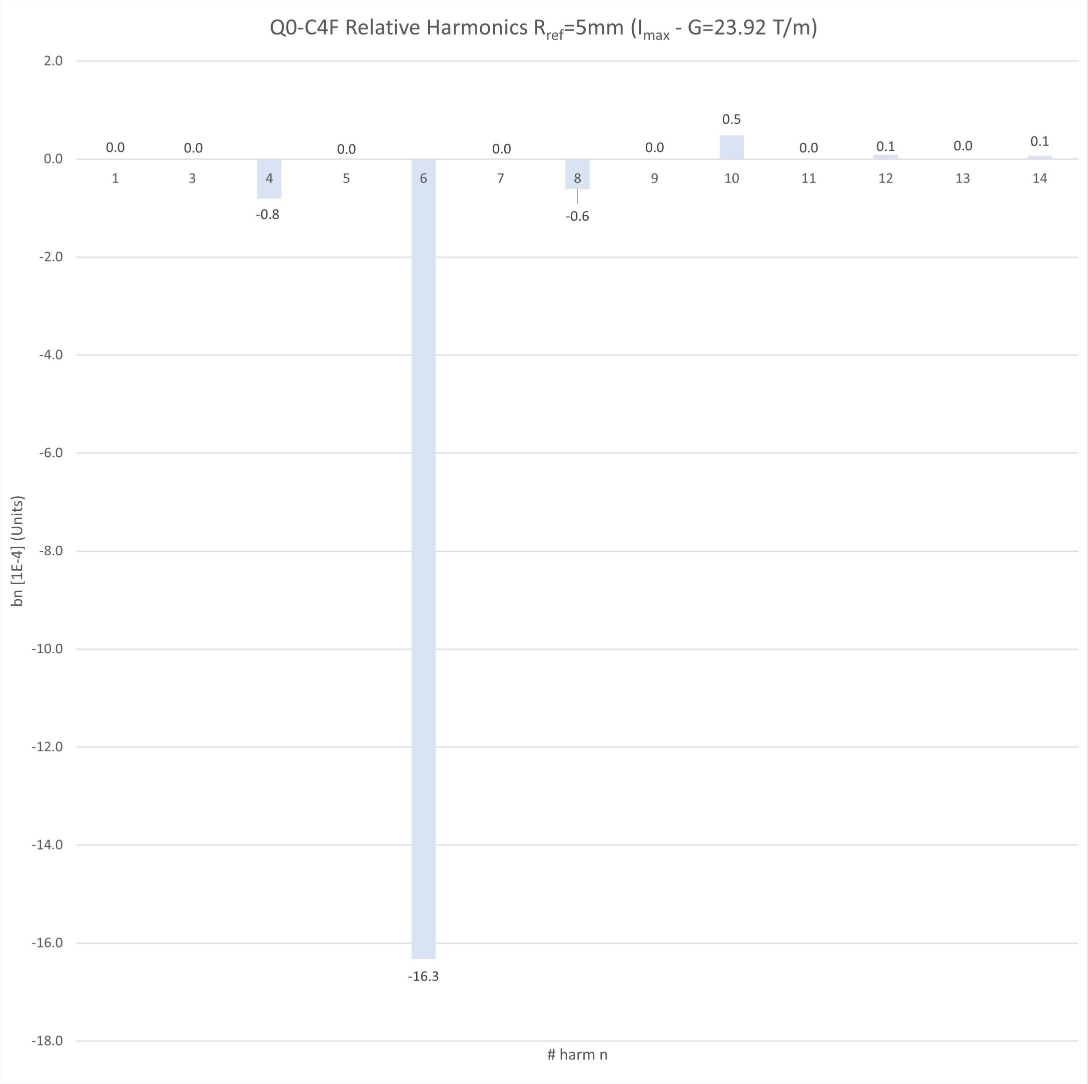

Figure 3.86: Q0-C4F Harmonics at Rref = 5 mm at peak current.

Table 3.26: Q0-C4F magnetic parameters.

Parameter	**Unit**	**Specification**	**Proposed design**	**Margin [%]**
Gradient (G)	T/m	23.4	24.1	3
Bore aperture radius	mm	6	7.5	-
Magnetic length	m	0.045	0.045	-
Integrated gradient ($\int Gdl$)	T	1.053	1.089	3.42

the pole. This peak is likely due to a mesh edge effect, which is considered a numerical artefact without expected physical consequences.

Figure 3.89 shows the longitudinal field profile, indicating that the field amplitude extends approximately 60 mm on either side of the magnetic centre, or about 40 mm from each yoke end.

The field quality of the 3D magnetic design is characterised by the relative harmonic components of field errors with respect to the main field, as shown in Fig. 3.90. Optimisation to further reduce these field errors is ongoing.

Table 3.27: Q0-C4F electrical and cooling parameters.

Parameter	**Unit**	**Proposed design**
Conductor		
Material		OF copper
Type		Rectangular, air-cooled
Rectangular size (height × width)	mm	3 × 2
Electrical		
Peak current (DC)	A	7.4
Current density	A/mm^2	1.3
# turns / coil	-	75
Coil resistance	mΩ	18.6
DC voltage	V	0.1
Thermal		
Dissipated power (RMS)	W	1

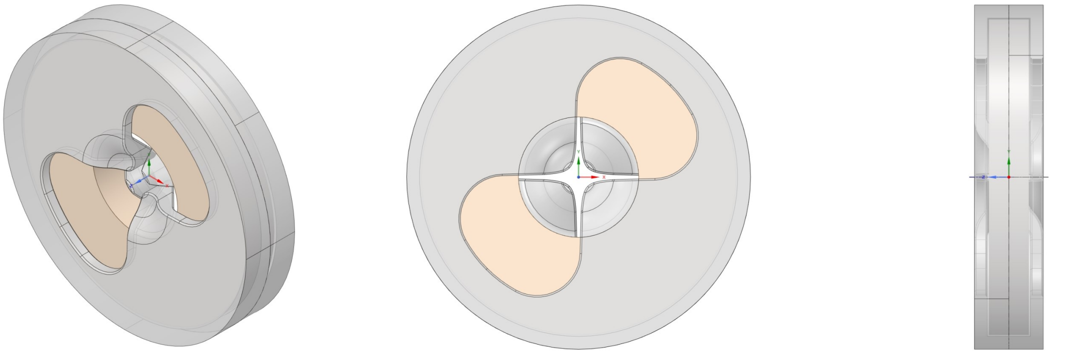
(a) Q0-CP Isometric view. **(b)** Q0-CP Front view. **(c)** Q0-CP Side view.

Figure 3.87: Views of the Q0-CP electromagnetic model.

The mechanical parameters of the Q0-CP magnet are listed in Table 3.28, the magnetic parameters in Table 3.29, and the electrical and cooling parameters in Table 3.30.

Table 3.28: Q0-CP dimensions and weight.

Parameter	**Unit**	**Proposed design**
Overall width × height	mm × mm	200 × 200
Overall length	mm	40
Pole length	mm	20
Yoke mass	kg	3.75
Copper mass	kg	4.6
Total mass	kg	8.35

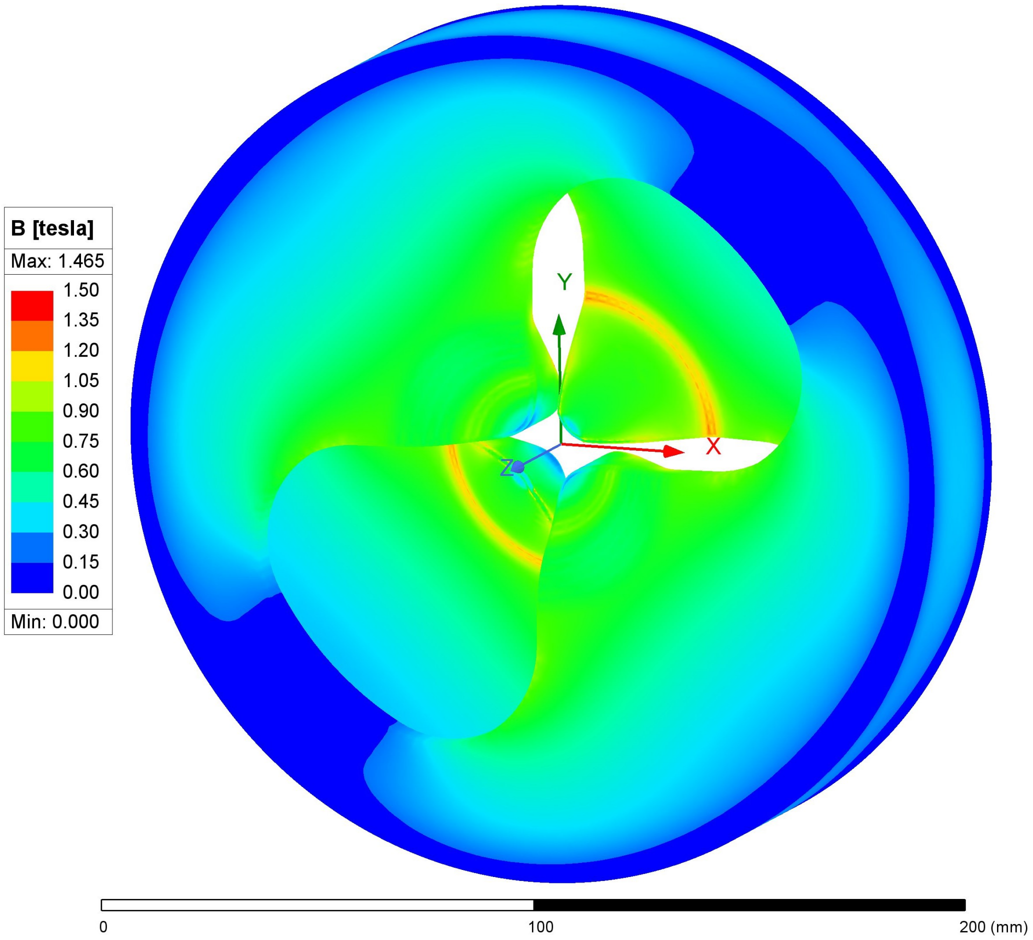

Figure 3.88: Q0-CP, flux density in iron at peak current.

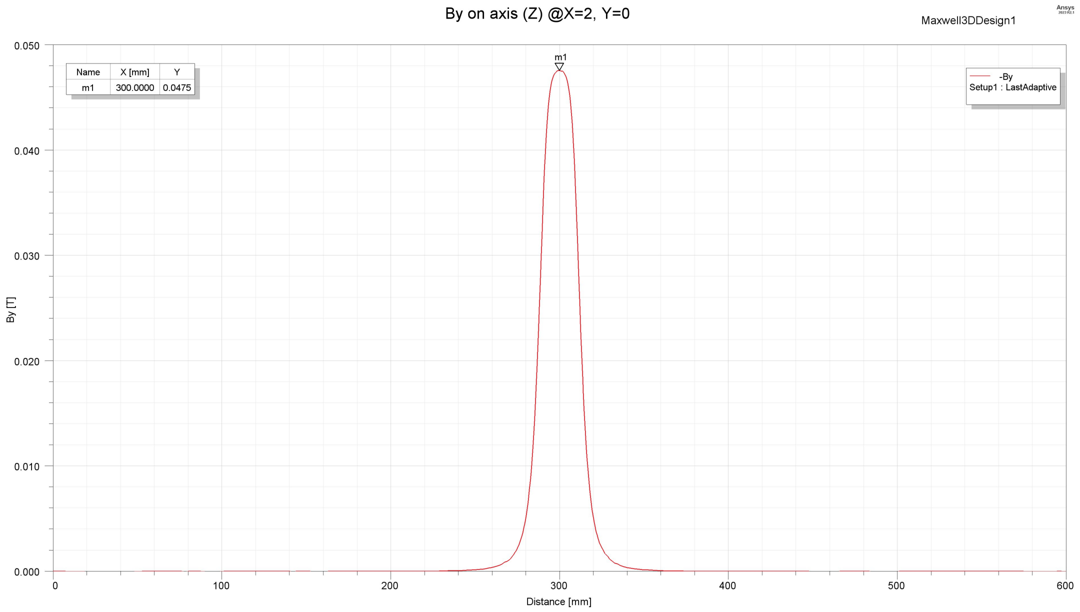

Figure 3.89: Q0-CP longitudinal field profile, By in XZ plane at R = 2 mm along Z.

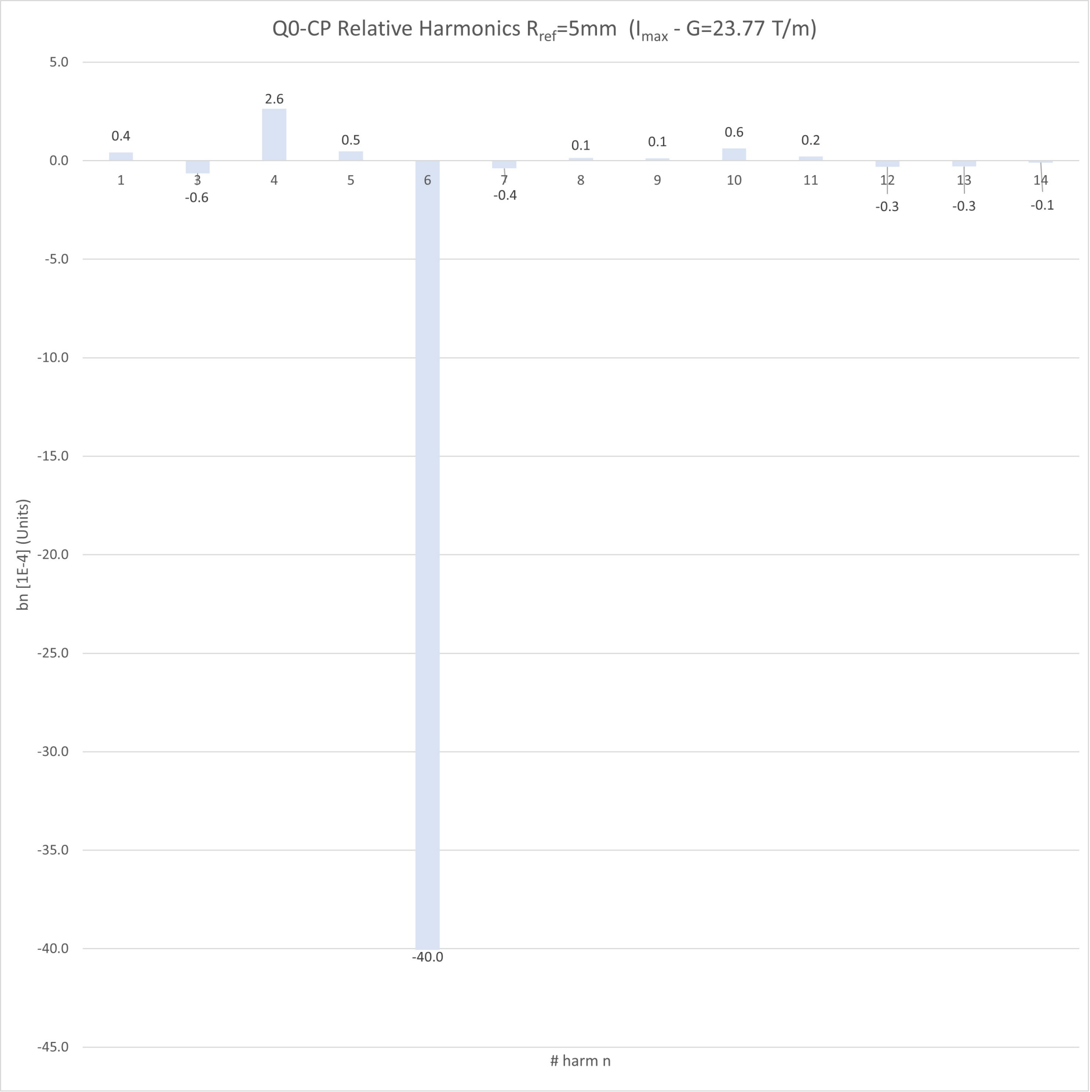

Figure 3.90: Q0-CP Harmonics at R ref = 5 mm at peak current.

Table 3.29: Q0-CP magnetic parameters.

Parameter	Unit	Specification	Proposed design	Margin [%]
Gradient (G)	T/m	23.4	23.95	2.35
Bore aperture radius	mm	6	7.5	-
Magnetic length	m	0.045	0.045	-
Integrated gradient ($\int Gdl$)	T	1.053	1.087	3.42

6.2.2 BDS quadrupoles

A quadrupole design has been developed to meet the foreseen beam optics and integration requirements for the BDS, with a total of five units scheduled for installation in the machine. This BDS quadrupole Q1 features a classical four-fold symmetry with straight poles and racetrack coils. It is designed with additional ampere-turns and a larger yoke to achieve the specifications.

The magnetic model is illustrated in Fig. 3.91. Figure 3.92 shows the flux density in the iron when the magnet is powered at its maximum current, with the peak field reaching 3.3 T at the pole edges. This

Table 3.30: Q0-CP electrical and cooling parameters.

Parameter	Unit	Proposed design
Conductor		
Material		OF copper
Type		Square, air-cooled
Square side	mm	10
Electrical		
Peak current (DC)	A	130
Current density	A/mm^2	1.3
# turns / coil	-	10
Coil resistance	mΩ	0.8
DC voltage	V	0.1
Thermal		
Dissipated power (RMS)	W	13

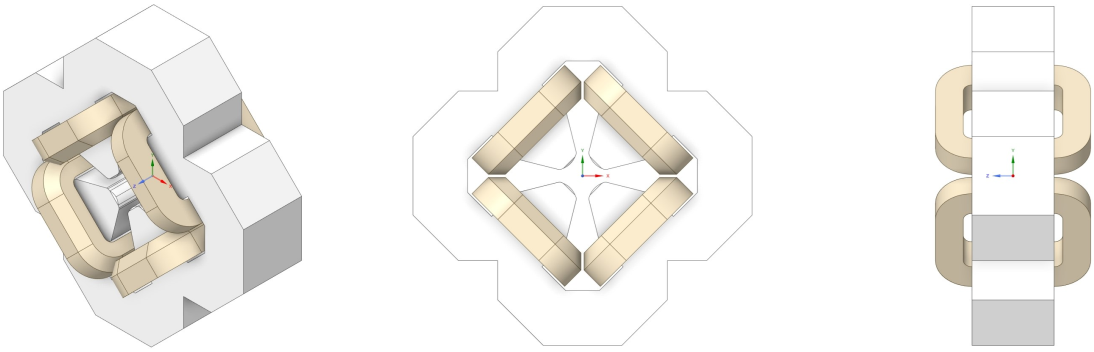
(a) Isometric view. **(b)** Front view. **(c)** Side view.

Figure 3.91: Views of the BDS quadrupole Q1 electromagnetic model.

issue will be addressed during the optimisation of field quality in the final design. The field quality of the 3D magnetic design is represented by the relative harmonic components of field errors compared to the main field, as shown in Fig. 3.93. Optimisation is ongoing to further minimise these field errors at the time of writing this chapter. The mechanical parameters of the magnet are listed in Table 3.31, the magnetic parameters in Table 3.32, and the electrical and cooling parameters in Table 3.33.

Table 3.31: Q1-C4F dimensions and weight.

Parameter	Unit	Proposed design
Overall width × height	mm × mm	560 × 560
Overall length	mm	300
Pole length	mm	150
Yoke mass	kg	195
Copper mass	kg	45
Total mass	kg	240

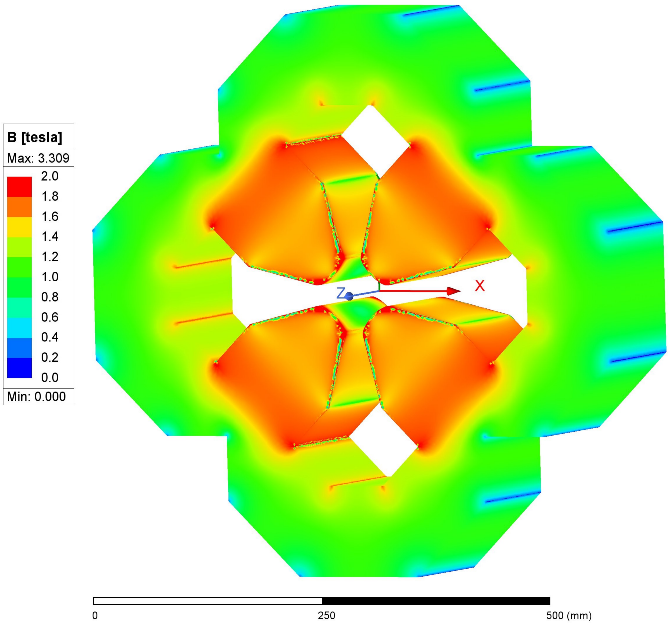

Figure 3.92: BDS quadrupole Q1, flux density in iron at peak current.

Table 3.32: Q1-C4F magnetic parameters.

Parameter	Unit	Specification	Proposed design	Margin [%]
Gradient (G)	T/m	22.2	24.0	5
Bore aperture radius	mm	30	31.5	-
Magnetic length	m	0.18	0.185	-
Integrated gradient ($\int G dl$)	T	4.00	4.44	11

6.3 Steering magnets

If additional lateral corrections to the beam motion are required, the machine will be equipped with strategically positioned steering magnets. These magnets are designed to address all electromagnetic needs across the machine through a unified design approach. A total of five “steering” or “corrector” magnets are necessary for the machine.

The design of these magnets has been optimised to fulfil the optical needs of the beamline while maintaining a compact depth of less than 180 mm, as well as all other space limitations from the integration model.

Each magnet consists of a main iron frame and two sets of coils. The frame is divided into four identical quadrants to simplify construction, thereby reducing production and maintenance costs. Each iron quadrant supports an air-cooled racetrack coil, made by winding a solid filament conductor.

Furthermore, these magnets accommodate the vacuum pipe and flanges as described in Section 8, and have been designed with a 120 mm aperture.

The magnetic model is illustrated in Fig. 3.94. Magnetostatic simulations have been conducted to optimise the magnet’s geometry. The numerical model indicates that the peak field reaches 1.4 T in normal mode depicted in Fig. 3.95, and up to 1.8 T in boost mode, as shown in Fig. 3.96. However, these peak fields are localised and represent singularity points caused by edge effects in the FEM simulation. The average magnetic field in the iron volume is below 1 T, providing a margin of approximately 0.6 T before saturation when the current is at its maximum value, as shown in Fig. 3.96.

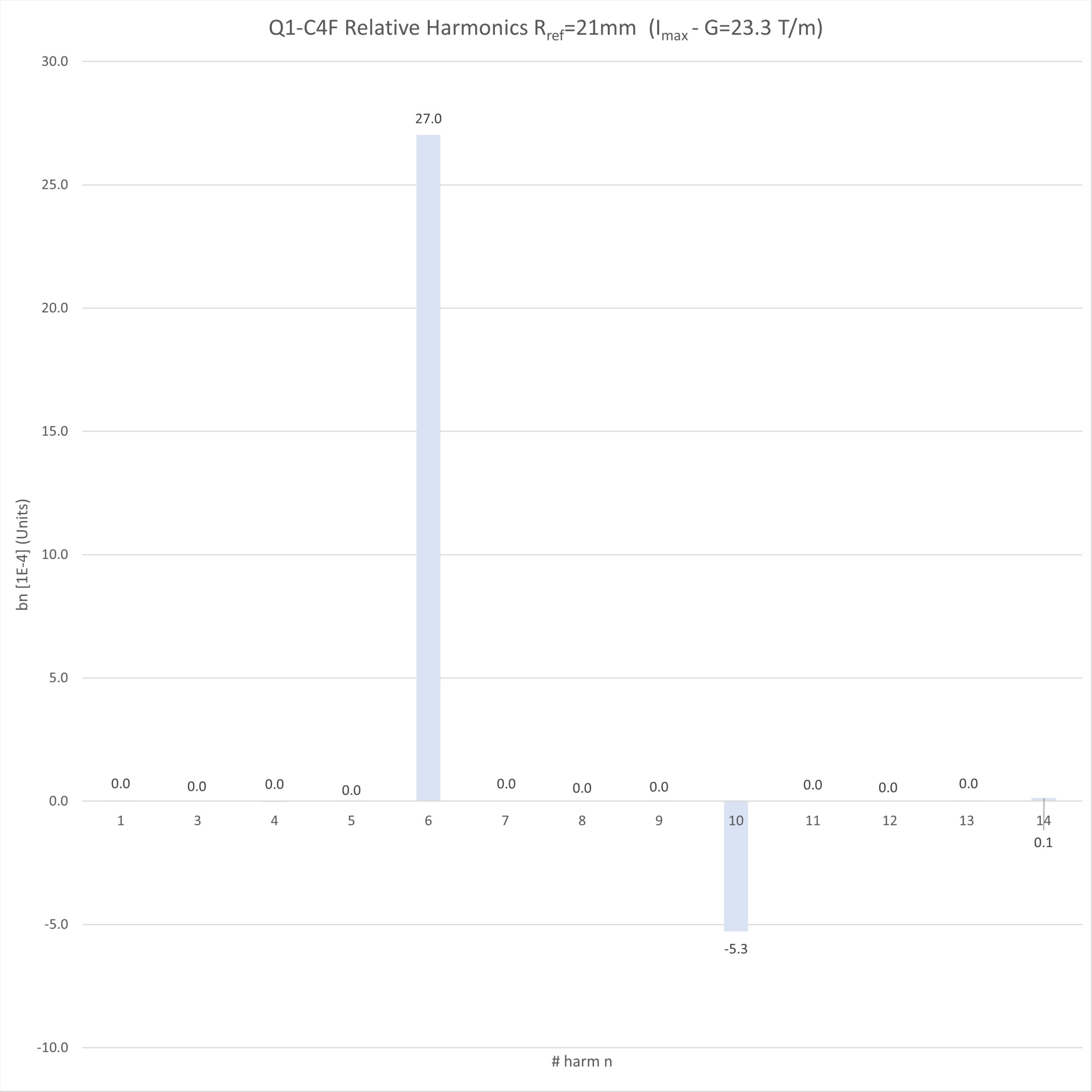

Figure 3.93: Q1, 3D simulated integrated field relative harmonics at Rref = 21 mm, at peak current.

The equivalent engineering current density J for boost mode is $J = 2\,\text{A/mm}^2$, double the maximum limit of $J = 1\,\text{A/mm}^2$ in normal operation. At the time of writing, two-way coupling multiphysics simulations are ongoing to ensure the magnet can safely operate in boost mode.

The equivalent 1D field map is shown in Fig. 3.97. This longitudinal field profile reveals that the field amplitude extends approximately 300 mm on either side of the magnetic centre, or about 280 mm from each yoke end. The stray field extension implies that the integrated field strength required by the beam optics for each corrector could be reduced due to cross-talk between nearby quadrupole magnets or other magnetic fields in the neighbourhood. Therefore, it is critical to assess the margin of the integrated field strength accordingly.

The magnet's mechanical parameters are listed in Table 3.34, the magnetic parameters in Table 3.35, and the electrical and cooling parameters in Table 3.36.

Table 3.33: Q1-C4F electrical and cooling parameters.

Parameter	**Unit**	**Proposed design**
Conductor		
Material		OF copper
Type		Square, water-cooled
Square side	mm	6
Cooling hole diam.	mm	3
Electrical		
Peak current (DC)	A	176
Current density	A/mm^2	6.25
# turns / coil		57
Coil resistance	mΩ	125
DC voltage	V	22
Dissipated power (RMS)	kW	7.8
Hydraulic		
Acceptable delta p	bar	4 to 10
Nominal delta p	bar	5
Cooling flow at delta p nom.	l/min	2.2
Delta T at delta p nom. and I max.	°C	25

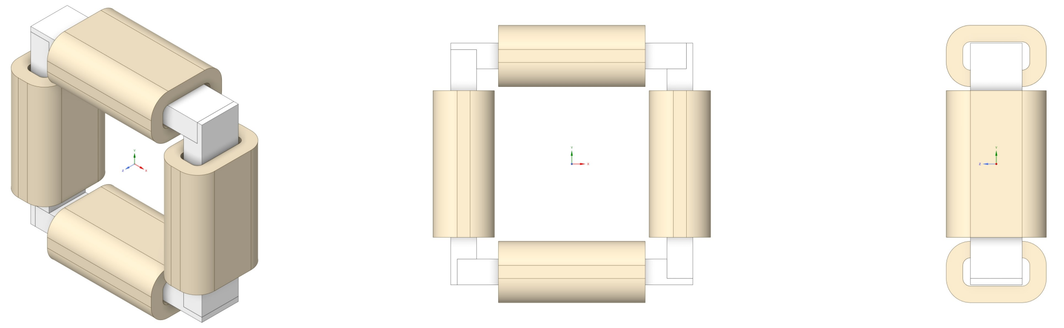

(a) Q0-CP Isometric view. **(b)** Q0-CP Front view. **(c)** Q0-CP Side view.

Figure 3.94: Views of the corrector electromagnetic model.

Table 3.34: Corrector dimensions and weight.

Parameter	**Unit**	**Proposed design**
Overall width × height	mm × mm	215.2 × 215.2
Overall length	mm	77.5
Iron length	mm	40
Physical aperture	mm × mm	120 × 120
Yoke mass	kg	4.2
Copper mass	kg	7.2
Total mass (Ancillaries excl.)	kg	11.4

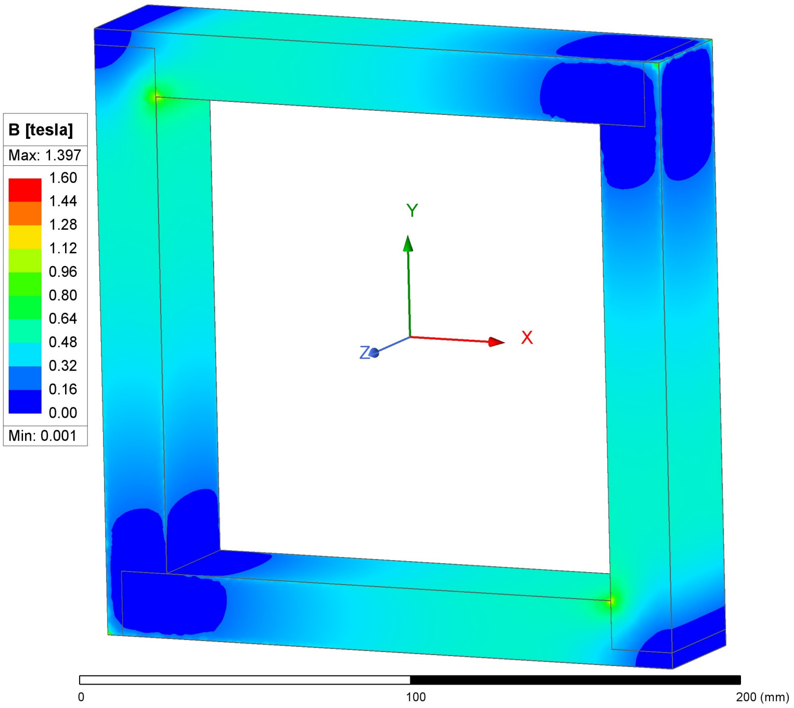

Figure 3.95: Corrector, flux density in iron at 6 A current, corresponding to the current density of $J = 1\,\mathrm{A/mm^2}$.

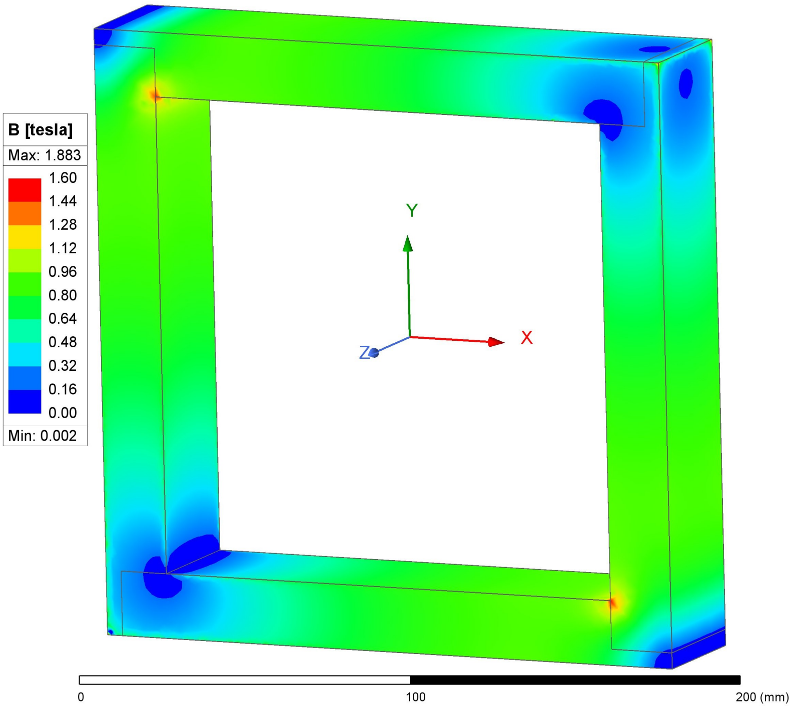

Figure 3.96: Corrector, flux density in iron at 12 A current, corresponding to the current density of $J = 2\,\mathrm{A/mm^2}$.

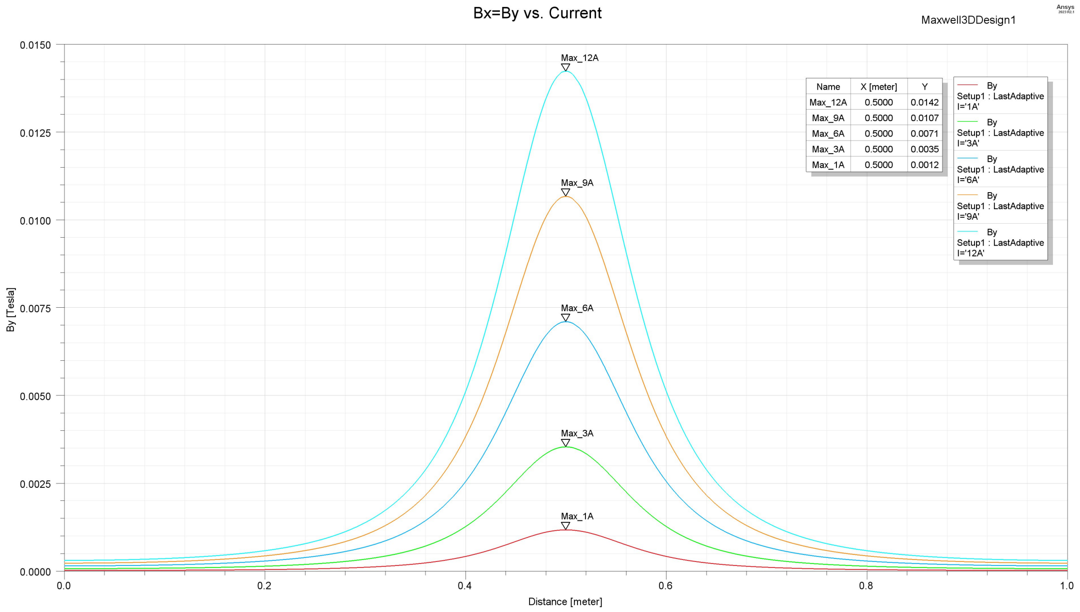

Figure 3.97: Corrector longitudinal field profile vs. current I, Bx = By on axis (Z).

Table 3.35: Corrector magnetic parameters.

Parameter	**Unit**	**Specification**	**Design**	**Margin [%]**
Peak field (B, at I = 12 A)	T	-	0.014	-
Bore aperture radius	mm	-	60	-
Magnetic length	mm	-	205	-
Integrated field strength ($\int B dl$)	T·mm	2.5	2.9	16

Table 3.36: Corrector electrical and cooling parameters.

Parameter	**Unit**	**Proposed design**
Conductor		
Material		OF copper
Type		Rectangular, air-cooled
Rectangular size (height × width)	mm	3 × 2
Electrical		
Peak current (DC)	A	12
Current density	A/mm^2	2
# turns / coil	-	175
Coil resistance	mΩ	106.1
DC voltage	V	2.5
Thermal		
Dissipated power (RMS)	W	15

6.4 Power converters

The specifications of the power converters are derived from magnet parameters, DEFT machine operating modes and equipment procurement considerations.

The design of the magnets has been optimised to enable converters to be used in “standard” voltage and current ranges, avoiding operation at very low voltages, for example. In addition, converters have been designed to operate at voltages below 50 V, to simplify the safety measures required to access and maintain this equipment and to facilitate access to the DEFT beamline area.

As regards the machine’s operating modes, it has been decided that all the converters are operated in continuous mode (DC). The main reasons for this choice are:

- to simplify the converter control by using standard control links and protocols,
- to avoid all the needs for their synchronisation and reference waveform generation in case of an eventual pulsed or cycled operating mode,
- to use commercially available converters from well-established suppliers on the market to avoid any development and associated costs and delays. This choice may allow cost reduction by putting several suppliers in competition.

Another choice was to allow maximum flexibility for the machine’s optics: the quadrupole converters are therefore bipolar so that the magnets can be used in focusing or defocusing mode. Also, each converter allows the operation at nominal magnet current, thus allowing the machine to be operated with different optics.

Concerning the magnet current precision that is required, a sensitivity study has been performed. For the quadrupoles, a ± 1 mm beam size variation has been allowed with regard to nominal beam optics. This criterion allows the definition of the converters required precision.

From a technological point of view, the choice has been made to use air-cooled converters to simplify their installation and considering that the constraints in terms of dimensions are low.

Also, for the converters of the solenoids that are the most demanding in terms of power, it was decided to use modular converters using three units in parallel. In this way, it is possible to use low power modules as spares, thereby reducing costs.

To validate the feasibility of the powering and to evaluate the requirements in terms of AC powering, space in the racks, cabling, control links, etc., a solution using commercially available power converters has been set up. Given standardisation, there are four converter types. This proposal is described below in Table 3.37 where the magnet current stability has been evaluated with 5 K temperature variation and suppliers’ parameters.

Table 3.37: Power converter requirements and specifications.

	Operational Requirements		Magnet parameters					Cable parameters	
	Magnetic Field (operational) [T or T/m]	Magnetic Field Precision	Nominal Field gradient [T or T/m]	Nominal Current [A]	Operational Current [A]	Magnet current Required Precision [A]	Magnet Resistance [mΩ]	Cable Type	Cable Resistance [mΩ]
Solenoide IS1	0.13	0.125%	0.21	340	225	0.281	69	2x120mm2 - Cu	0.02
Solenoide IS2	0.22	0.125%	0.3	400	295	0.369	105	2x120mm2 - Cu	0.02
Linac Q1	14.4	0.420%	24.2	30	18	0.076	12	2x16mm2 - Cu	120
Linac Q2	-14.6	0.210%	24.2	30	18	0.038	12	2x16mm2 - Cu	120
BDS Q1	-18.5	0.680%	24	235	144	0.979	125	2x120mm2 - Cu	0.02
BDS Q2	6.6	0.530%	24	235	46	0.244	125	2x120mm2 - Cu	0.02
BDS Q3	-5.1	0.120%	24	235	36	0.043	125	2x120mm2 - Cu	0.02
BDS Q4	6.3	0.170%	24	235	44	0.075	125	2x120mm2 - Cu	0.02
BDS Q5	-18.5	0.470%	24	235	-144	-0.677	125	2x120mm2 - Cu	0.02
Linac Steerer 1 Horizontal	0.014	0.100%	0.014	12	12	0.012	212	2x10mm2 - Cu	170
Linac Steerer 1 Vertical	0.014	0.100%	0.014	12	12	0.012	212	2x10mm2 - Cu	170
Linac Steerer 2 Horizontal	0.014	0.100%	0.014	12	12	0.012	212	2x10mm2 - Cu	170
Linac Steerer 2 Vertical	0.014	0.100%	0.014	12	12	0.012	212	2x10mm2 - Cu	170
Linac Steerer 3 Horizontal	0.014	0.100%	0.014	12	12	0.012	212	2x10mm2 - Cu	170
Linac Steerer 3 Vertical	0.014	0.100%	0.014	12	12	0.012	212	2x10mm2 - Cu	170
BDS Steerer 1 Horizontal	0.014	0.100%	0.014	12	12	0.012	212	2x10mm2 - Cu	170
BDS Steerer 1 Vertical	0.014	0.100%	0.014	12	12	0.012	212	2x10mm2 - Cu	170
BDS Steerer 2 Horizontal	0.014	0.100%	0.014	12	12	0.012	212	2x10mm2 - Cu	170
BDS Steerer 2 Vertical	0.014	0.100%	0.014	12	12	0.012	212	2x10mm2 - Cu	170

	Power Converter parameters											
	Operational Voltage [V]	Maximal Output Current [A]	Maximal Output Voltage [V]	Maximal Output Power [kW]	Estmated Output Current Stability [A]	AC input	Polarity	Commercial Type	Units in parallel	Control Link	Dimensions Height	Depth [mm]
Solenoide IS1	15.53	420	45	18.9	0.158	3 Phases - 400V / 12A (x3)	Unipolar	Model A	3	Ethernet	4U x 3	550
Solenoide IS2	30.98	420	45	18.9	0.158	3 Phases - 400V / 12A (x3)	Unipolar	Model A	3	Ethernet	4U x 3	550
Linac Q1	2.38	50	30	1.5	0.002	1 Phase - 230V / 20A	4 quadrants	Model B	no	Ethernet	2U	600
Linac Q2	2.38	50	30	1.5	0.002	1 Phase - 230V / 20A	4 quadrants	Model B	no	Ethernet	2U	600
BDS Q1	18.00	300	50	15	0.012	3 Phases - 400V / 30A	Bipolar	Model C	no	RS422	9U + 3U	575
BDS Q2	5.75	300	50	15	0.012	3 Phases - 400V / 30A	Bipolar	Model C	no	RS422	9U + 3U	575
BDS Q3	4.50	300	50	15	0.012	3 Phases - 400V / 30A	Bipolar	Model C	no	RS422	9U + 3U	575
BDS Q4	5.50	300	50	15	0.012	3 Phases - 400V / 30A	Bipolar	Model C	no	RS422	9U + 3U	575
BDS Q5	-18.00	300	50	15	0.012	3 Phases - 400V / 30A	Bipolar	Model C	no	RS422	9U + 3U	575
Linac Steerer 1 Horizontal	4.58	20	20	0.4	0.010	1 Phase - 230V / 5A	Bipolar	Model D	no	Ethernet	1U	400
Linac Steerer 1 Vertical	4.58	20	20	0.4	0.010	1 Phase - 230V / 5A	Bipolar	Model D	no	Ethernet	1U	400
Linac Steerer 2 Horizontal	4.58	20	20	0.4	0.010	1 Phase - 230V / 5A	Bipolar	Model D	no	Ethernet	1U	400
Linac Steerer 2 Vertical	4.58	20	20	0.4	0.010	1 Phase - 230V / 5A	Bipolar	Model D	no	Ethernet	1U	400
Linac Steerer 3 Horizontal	4.58	20	20	0.4	0.010	1 Phase - 230V / 5A	Bipolar	Model D	no	Ethernet	1U	400
Linac Steerer 3 Vertical	4.58	20	20	0.4	0.010	1 Phase - 230V / 5A	Bipolar	Model D	no	Ethernet	1U	400
BDS Steerer 1 Horizontal	4.58	20	20	0.4	0.010	1 Phase - 230V / 5A	Bipolar	Model D	no	Ethernet	1U	400
BDS Steerer 1 Vertical	4.58	20	20	0.4	0.010	1 Phase - 230V / 5A	Bipolar	Model D	no	Ethernet	1U	400
BDS Steerer 2 Horizontal	4.58	20	20	0.4	0.010	1 Phase - 230V / 5A	Bipolar	Model D	no	Ethernet	1U	400
BDS Steerer 2 Vertical	4.58	20	20	0.4	0.010	1 Phase - 230V / 5A	Bipolar	Model D	no	Ethernet	1U	400

7 Beam diagnostics

In order to commission and operate the facility, a number of physical properties of the beam must be measured and monitored in several locations. These include:

- Charge per pulse.
- Beam transverse position.
- Beam transverse profile.
- Beam energy.
- Bunch and train duration.

The charge will be measured using Integrating Current Transformers (ICTs). At least two such devices are needed in the accelerator part, one placed between the gun and the linac, and a second at the end of the linac. Another ICT may also be considered in the beam delivery line for beam current calibration before the patient. The beam transverse position is needed in several places along the beam lines to provide effective steering of the beam and thus compensate for position and field errors of the magnetic elements. Finally, train duration can be measured using BPMs. The beam instrumentation of the DEFT facility is summarized in Table 3.38.

Table 3.38: Beam instrumentation.

Device	Injector	Linac	Transfer lines	Total
Beam intensity monitor	1	1	1	3
Beam position monitor	1	1	3	5
Beam size monitor	1	1	1	3

Bunch length monitoring using either a screen and streak camera or an Electro-Optical technique [29] or an RF deflecting cavity [30] have been discussed, but is not in the baseline design of the machine and is not described in this document.

Beam energy and energy spread upstream and downstream of the linac could be measured using spectrometer lines equipped with BPMs and screens. The first spectrometer line would be used only during the commissioning phase of the injector and removed after validation. The second spectrometer line, after beam acceleration, could remain as part of the final facility and be used to check the final beam energy and energy spread before the beam is sent to the patient. Both spectrometer lines have been studied, but their designs are not finalised and thus not included in this report.

7.1 ICTs

The charge will be measured using integrating current transformers (ICTs). Commercial ones from Bergoz are routinely used in the CLEAR Facility [31], and provide the required precision and resolution [32]. At least two such devices are needed in the accelerator part, one placed between the gun and the linac, and a second between the end of the linac and the separator dipole. All beam delivery lines should also be equipped with one ICT each.

7.2 BPMs

The beam position monitors for DEFT will be based on electrostatic button pick-ups as depicted in Fig. 3.98. There will be two mechanical designs for the BPMs in DEFT, one for the injector and the linac with a beam pipe diameter of 22 mm and a second one in the delivery line with a larger aperture. Beam dynamics studies have shown that to achieve a good orbit correction of magnetic elements alignment errors, the BPMs must have a resolution of 10 μm with nominal beam conditions in the injector and the linac. As the beam size gets larger in the beam delivery system, the resolution can be relaxed to 100 μm

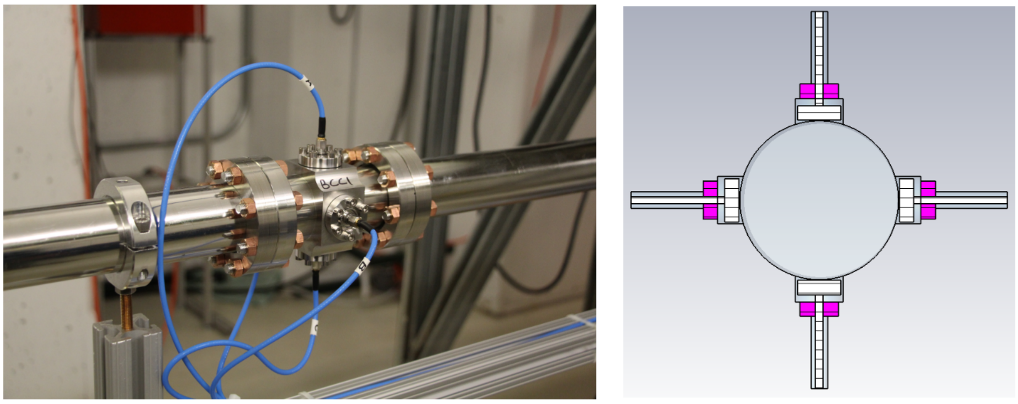

Figure 3.98: A picture of a Button BPM on the left side. The geometry of the button pick is simulated for DEFT on the right side.

The proposed button has a head diameter of 6 mm and a flat button surface for easier and cheaper manufacturing. The button capacitance will be of 2.75 pF and the button gap of 0.25 mm, comparable to the bunch length. Simulations, as shown in Fig. 3.99, indicate that with an analogue front-end consisting of a 3.8 GHz low-pass filter and 2.9 GHz bandpass filter, the system will provide signals of 375 and 45 mV peak amplitude for the 22 and 160 mm aperture BPMs, respectively. The corresponding thermal noise will then correspond to 2 and 62 μm for the 22 and 160 mm aperture BPMs respectively, well within specifications for required resolution.

7.3 Profile monitors

The standard beam profile measurement system in an electron linac is based on the use of a movable imaging screen and a digital camera. The overview of the system is depicted in Fig. 3.100. With high intensity electron beams, both optical transition radiation (OTR) and scintillating screens can be used. The final choice will depend on the final beam parameters. The OTR screen will be made out of thin silicon wafers, and YAG is a typical scintillating material used for an electron beam imaging system. The screen is installed on a remotely controlled pneumatic actuator that allows for insertion or retraction of the screen from the beam line. The screen is tilted at 45 degrees with respect to the beam trajectory such that the emitted photons are collected by an optical system installed at 90 degree angle. The optical system consists of a filter wheel equipped with a neutral density filter to control the light intensity sent to the digital camera, depending on the beam intensity. The tank is also equipped with lights that can be switched on to take a reference image and calibrate the optical system.

In the case of DEFT, as the beam intensity is relatively large, the vacuum tank is equipped with a replacement chamber that will ensure an almost perfect electrical continuity of the beam pipe when the monitor is not used. This is done to minimise beam impedance effects that may affect the beam emittance. The two positions of the system are displayed in Fig. 3.101.

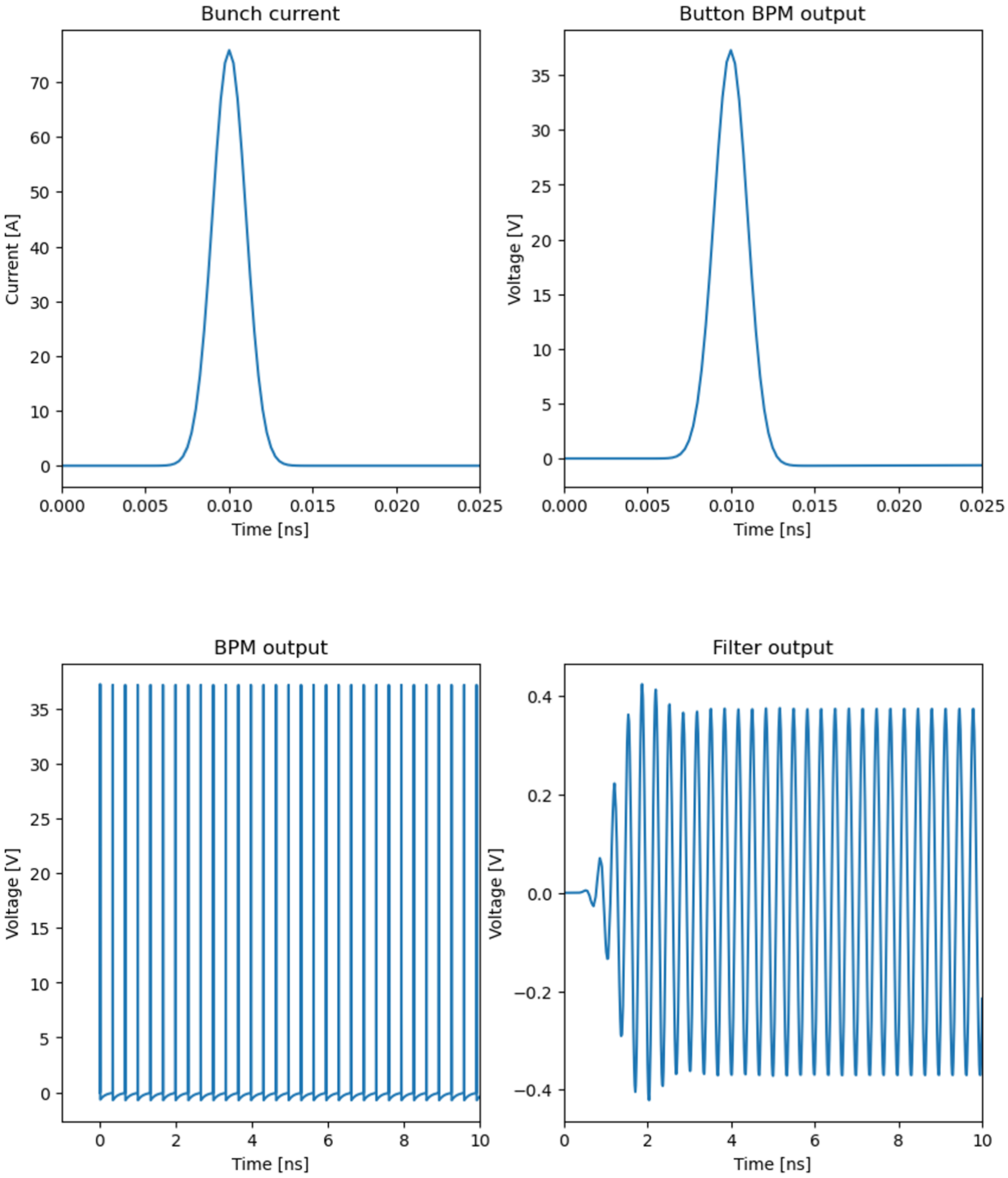

Figure 3.99: Simulations of a 22 mm aperture button BPM for DEFT.

8 Vacuum system

8.1 Introduction

DEFT vacuum requirements are similar to other electron linacs like CLEAR [31]. The lifetime of the photo-cathode is one of the main concerns for the operation of the RF-gun. The lifetime strongly depends on the pressure during operation [13]. For that reason, the pressure requirement of the RF-gun is 10^{-10} mbar in static conditions (without beam). The vacuum design study of the photoinjector is discussed in this document. The rest of the beam line has a less stringent requirement, a pressure of 10^{-9} mbar is considered enough. This vacuum level can be achieved with a vacuum system and follow-

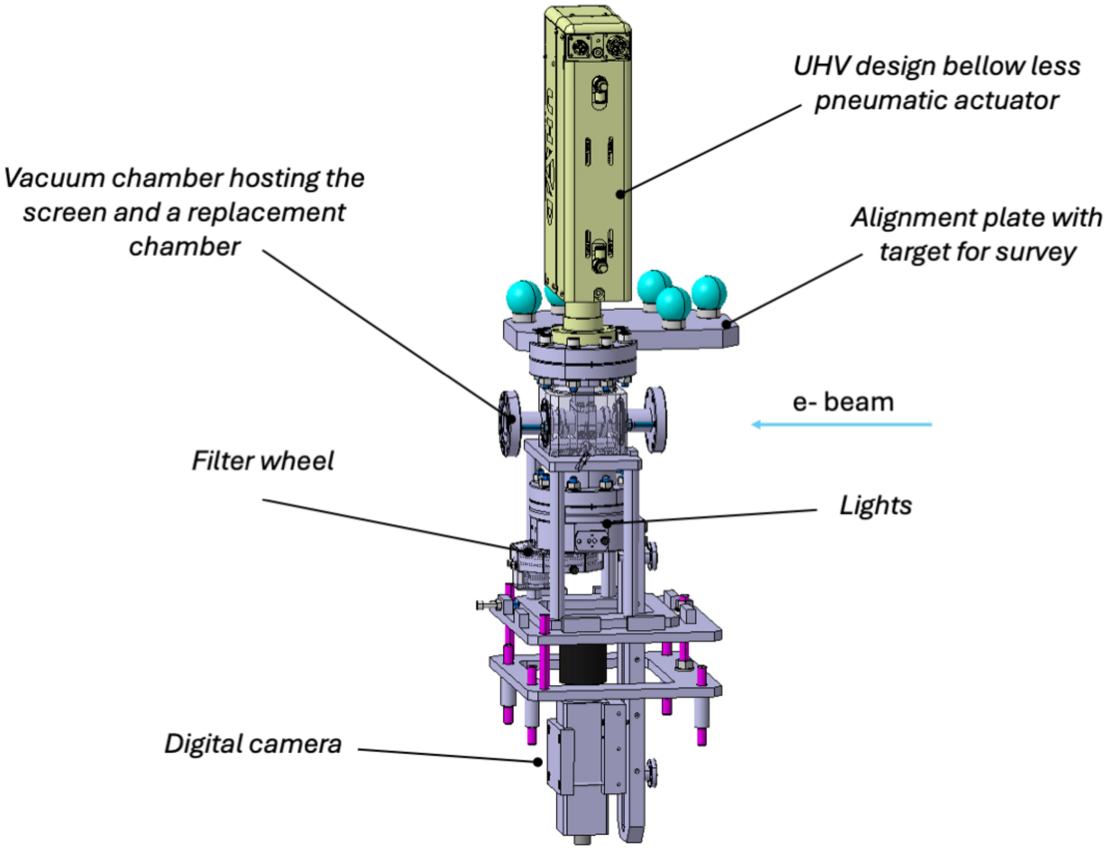

Figure 3.100: Overview of the DEFT beam imaging system using a remotely controlled screen and a digital camera.

ing the same procedures as it is done today at CLEAR.

8.2 Vacuum design of the photoinjector

The baseline for DEFT is the same design as the PHIN photoinjector [10]. The PHIN photoinjector is surrounded by a NEG-coated vacuum chamber communicating via holes with the copper internal structure (see Fig. 3.102). This chamber is also connected to two sputter ion pumps and a vacuum gauge. The two RF wave-guides and the downstream chamber are also equipped with one sputter ion pump each, as shown in Fig. 3.103. The PHIN photoinjector has experimentally achieved a pressure under static vacuum (without beam) of $\approx 10^{-10}$ mbar, and $\approx 10^{-9}$ mbar with $5.5\,\mu$C/s continuous operation. These values were achieved after a 130°C bake-out.

To study the performance of the PHIN photoinjector a 3D Monte Carlo model has been built using MOLFLOW+ [33]. The H_2 outgassing rate of the model for the copper and stainless steel surfaces was estimated as 3×10^{-12} mbar L/s [34], corresponding to values after a $150^{c}irc$C bake-out. For the first simulation, no pumping by the NEG coating was considered. This assumption is based on the low temperature bake-out [35] and the presence of a large non-coated surface that will make a good NEG activation difficult. Under the described conditions, the calculated pressure along the axis of the photoinjector is $\approx 10^{-10}$ mbar (red line in Fig. 3.104). The calculated pressure in the position of the

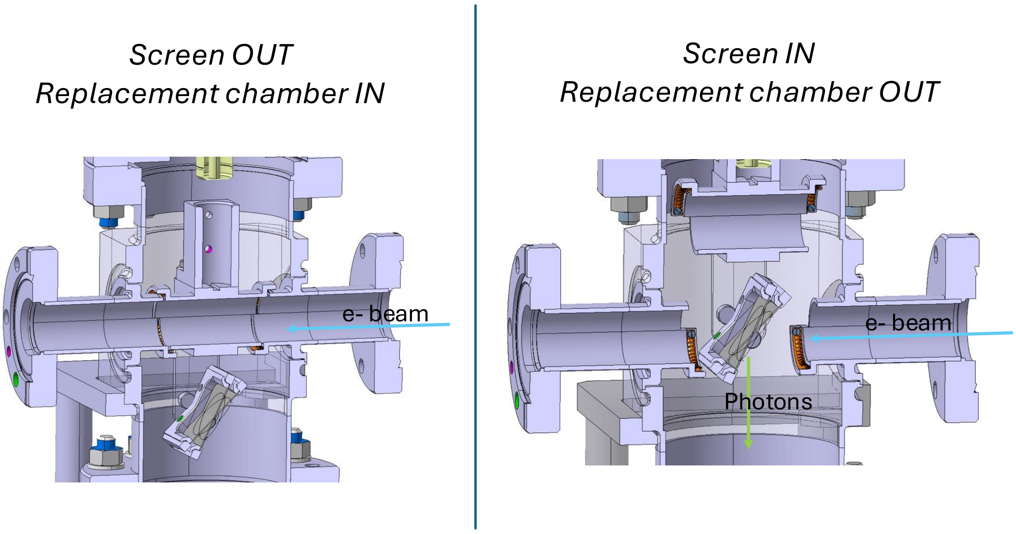

Figure 3.101: On the left side, the screen is out and the replacement chamber is in. On the right side, the screen is inserted, and transverse beam images are acquired.

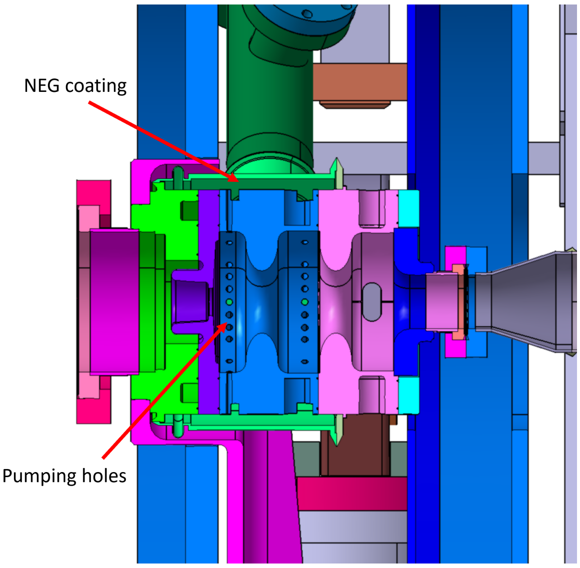

Figure 3.102: NEG coated chamber around PHIN photoinjector.

vacuum gauge was estimated as 10^{-10} mbar. Both values are consistent with the observations in PHIN.

The model also shows that the effect of NEG pumping on the surrounding chamber is modest along the beam (blue line in Figure 3.104) and significant at the gauge position ($\approx 5 \times 10^{-11}$ mbar). This proves the assumption of no NEG pumping correct.

The effect of adding a NEG coating on the downstream vacuum chamber has also been studied. Figure 3.104 shows the pressure profiles in three different scenarios, all of them with a downstream NEG-coated chamber:

- No NEG pumping on the chamber surrounding the photoinjector (green line)
- NEG pumping on the surrounding chamber (purple line)

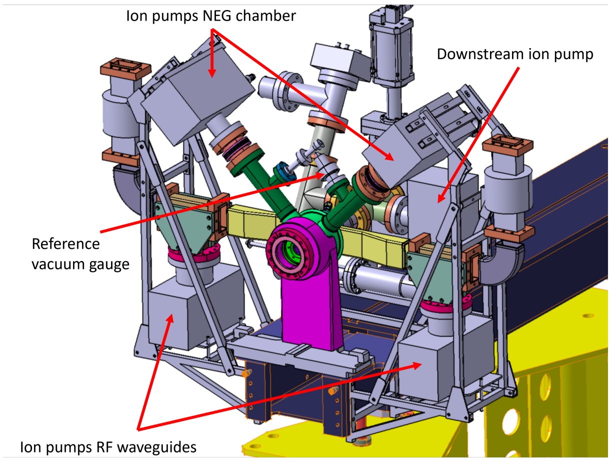

Figure 3.103: Downstream chamber showing sputter ion pumps.

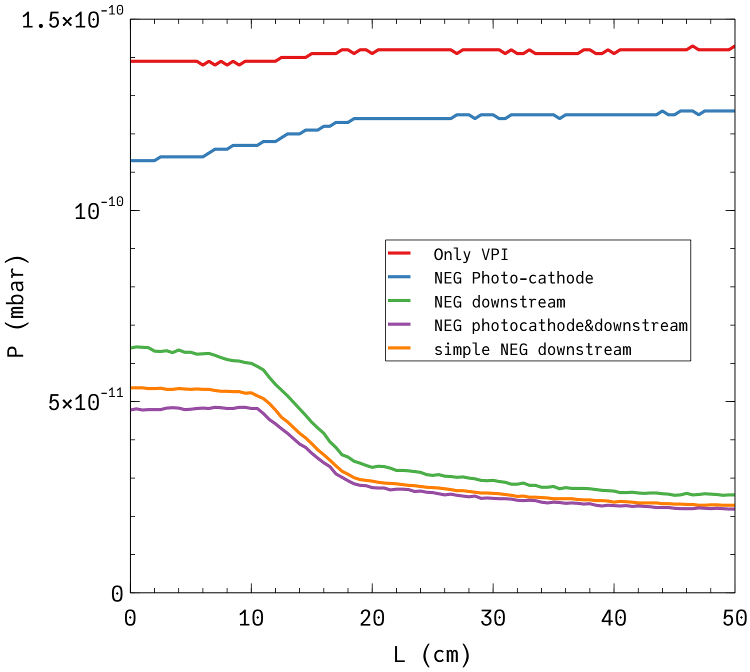

Figure 3.104: Pressure profile along the PHIN photoinjector under different scenarios.

– Simplified geometry without holes or surrounding chamber (orange line)

The NEG coating of the surrounding chamber has a small effect on the pressure profile, and this effect can be even detrimental if the coating is not active (due to the larger surface). To activate the NEG coating, the coated and all the non-coated copper surfaces are necessarily baked together at the same temperature, not providing the best conditions for the activation. The optimal vacuum configuration of the PHIN photoinjector hence, does not require a surrounding chamber, but should include NEG coating of the downstream chamber. This configuration allows for decoupling the outgassing and NEG activation phases during the bake-out.

To evaluate the effect of the dynamic outgassing due to the beam, the gas load due to the beam presence at the PHIN photoinjector was estimated using MOLFLOW+. To obtain a reading of 10^{-9} mbar on the gauge position, as observed experimentally, it is necessary to assume 3×10^{-7} mbar L/s produced at the position of the photo-cathode. This is equivalent to 0.055 mbar L/C or 0.22 molecules/e^-.

Using these values to convert the charge produced by the photoinjector and the resulting gas load, it is possible to estimate the pressure evolution inside the DEFT photoinjector during operation. Figure 3.105 shows the results for an example consisting of 20 pulses of 945 bunches/pulse and 0.3 nC/bunch that makes a total charge of 5.67 μC within a 100 ms treatment duration. The maximum pressure is always $< 10^{-7}$ mbar during the treatment with an average $< 3 \times 10^{-8}$ mbar during the first 150 ms. The pressure evolution during the treatment is dominated by the free expansion of the gas produced at the photo-cathode. The different pumping configurations have a minor impact on the dynamic pressure evolution during the beam production, but will have an important impact on the final pressure profile as shown in Fig. 3.104.

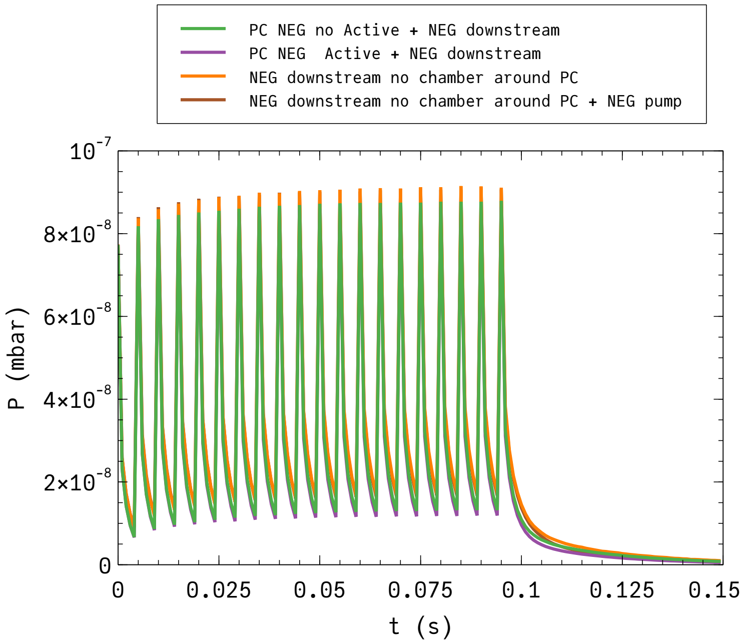

Figure 3.105: Pressure evolution next to the photo-cathode during beam delivery.

8.2.1 Recommendations for the vacuum system of DEFT photoinjector

- The quality of the materials used for vacuum applications should be controlled to ensure their performance [36]. For this application, it is recommended to use 316LN stainless steel and OFE copper, following CERN specifications for the material and cleaning.

- The stainless steel should be vacuum fired to reduce its outgassing. Non-coated components shall be vacuum fired at 950°C during 2 h and components that shall be NEG coated at 650°C during 24h [34, 36].

- To optimize the pressure profile inside the photoinjector, it is recommended to add a NEG coating on the downstream vacuum chamber.

- The effect of the NEG-coated surrounding chamber is modest, while it adds significant complexity to the mechanical design.

- The dynamic pressure evolution during the beam production is dominated by the expansion of the gas produced at the photo-cathode. The different pumping configurations have almost no impact on the pressure evolution.

8.3 Vacuum simulation of the DEFT RF cavity

The DEFT accelerating structure, based on X-band technology similar to that used in CLIC, consists of a sequence of accelerating cells with bent waveguides [37] and six ports for mounting pumping systems. The latter are essential for maintaining vacuum conditions within the volume and ensuring proper operation. The volume used for the vacuum simulations, shown in Fig. 3.106, was simplified from the original mechanical design to optimize computational efficiency while preserving critical geometrical features that influence vacuum performance.

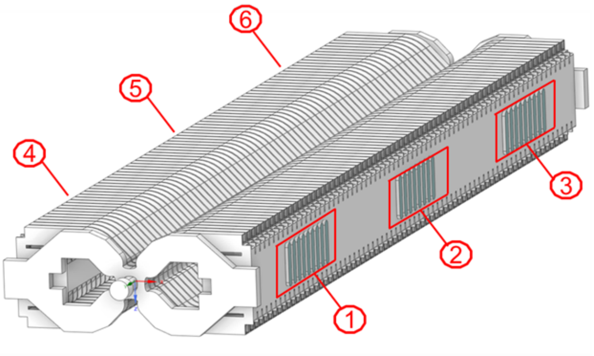

Figure 3.106: Simulated geometry for the DEFT accelerating cavity and numbering of the pumping ports.

The MOLFLOW+ [33] program was employed to simulate two pumping schemes and evaluate the corresponding cavity pressure profiles. The two configurations tested were as follows:

- Four pumps mounted on ports 1, 3, 4, and 6, with an effective total pumping speed (S_{eff}) of 80 L/s.
- Two pumps mounted on ports 2 and 5, with S_{eff} reduced to 40 L/s.

The effective pumping speed on each port (20 L/s) accounted for conductance losses in the connections. Ion pumps with nominal speeds of 40 or 55 L/s were considered suitable for achieving these values. The cavity walls were assigned an outgassing rate of $3 \times 10^{-11}\,\mathrm{mbar} \cdot L/\mathrm{s} \cdot \mathrm{cm}^2$ after 100 hours of pumping, reflecting typical values for unbaked metallic surfaces [34].

8.3.1 Simulation results

For the first simulation results (Fig. 3.107), using four pumps (S_{eff}= 80 L/s), the pressure within the DEFT chamber ranges from approximately 3.6×10^{-9} to 7.9×10^{-9} mbar. A slight asymmetry is observed due to the decreasing cross-section of the connecting pipe, which reduces conductance along the y-axis. Despite this, the pressure throughout the chamber remains within the desired UHV range.

In the second simulation (Fig. 3.108), where two pumps (S_{eff} = 40 L/s) are used, the pressure ranges from 6.6×10^{-9} to 1.4×10^{-8} mbar. The pressure distribution shows distinct pressure zones, with the higher pressures further from the central ports, but still within acceptable levels for RF cavity operation.

For both pumping schemes, the simulation results confirm that, under realistic assumptions for outgassing rates and pumping speeds, the DEFT cavity design can achieve the required vacuum levels for optimal FLASH technology performance.

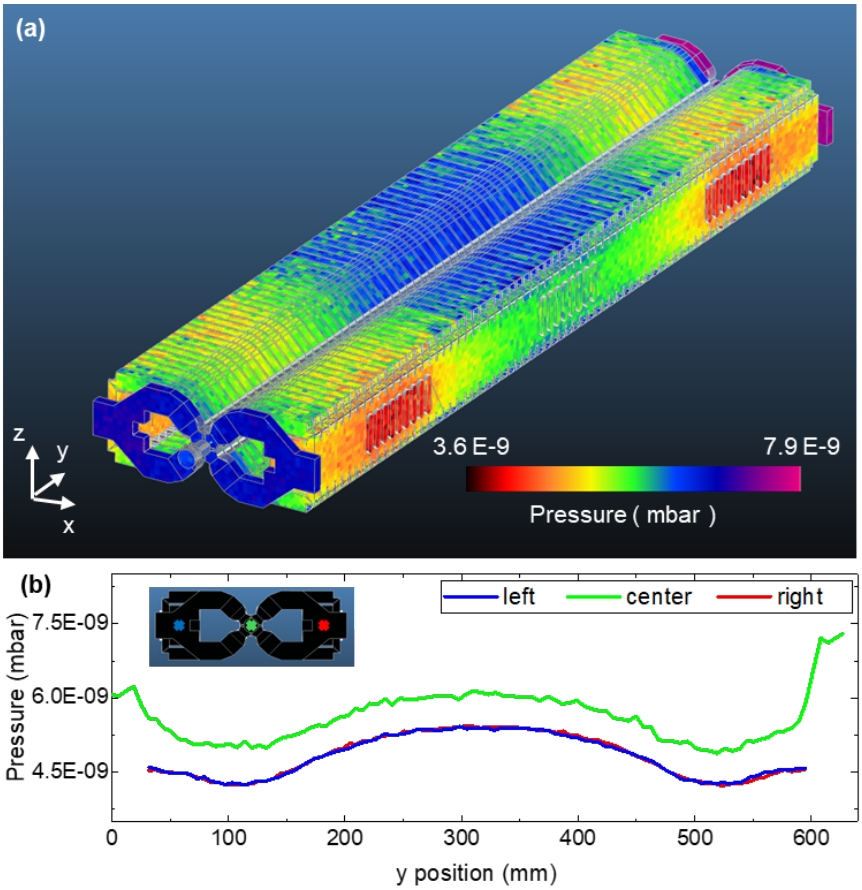

Figure 3.107: (a) Colour map describing the pressure distribution within the DEFT chamber and (b) pressure profile along three lines in the y-direction, when four pumps (S_{eff} = 80 L/s) are used to pump the structure.

9 Accelerator integration

9.1 General introduction

The integration of the facility in the building had to take into consideration a design that was based on requirements coming from a previous and more demanding configuration, with higher beam energy. In particular, the shielding topology and the wall thickness were dictated by the concept of realizing a self-contained radiation envelope for a conservative maximum beam energy of 210 MeV. The machine configuration described here rather concerns an accelerator with a single, straight beamline, with a maximum beam energy of 140 MeV.

9.2 Integration of the accelerator components

The accelerator consists of a low energy injector, a linac with two accelerating modules and a beam delivery system.

A general view of the accelerator and beam delivery system is given in Fig. 3.109.

The particle production and initial beam acceleration up to the energy of 5 MeV are assured by an RF photo-injector that is largely inspired by photo-injectors that have been studied and operated at CERN and by collaborators and that is described in Section 1. The development of the load/lock system was a collaborative effort between CERN and the company Theryq for the installation and replacement

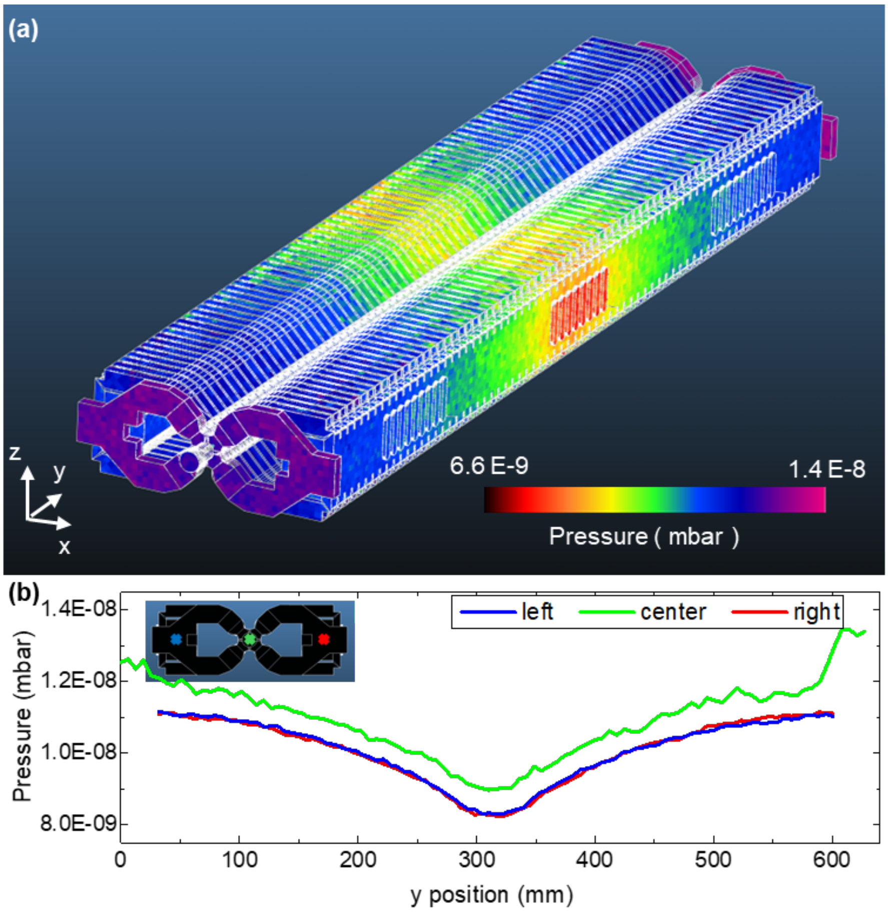

Figure 3.108: (a) Colour map describing the pressure distribution within the DEFT chamber and (b) pressure profile along three lines in the y-direction, when two pumps (S_{eff} = 40 L/s) are used to pump the structure.

of photo-cathodes. Theryq developed the design of the vacuum suitcase, which is not shown here, for the transfer of the photo-cathodes from the production site into the accelerator. Between the photo-injector and the first accelerating section, a short transport line was designed, providing vacuum pumping capability, in particular for the RF gun cavity, which requires an excellent vacuum level to maintain the expected cathode quantum efficiency. At the sector valve exit, a glass window for the laser beam injection is foreseen, equipped with an external mirror, which is followed by beam diagnostic components. A beam current measurement, a beam position monitor (BPM) and a movable beam profile monitor are foreseen for the beam characterization before it is injected into the accelerating section. The correction of the beam trajectory is provided by two steering magnets, combining horizontal and vertical steering. The first one is close to the vacuum sector valve, and the second is just in front of the first accelerating structure.

The accelerating structures are grouped in two modules; each module is made of four accelerating structures, 0.6 m long each, and connected to a dedicated RF source by double-height, WR90 waveguides, as described in Section 3. In Fig. 3.110, the two RF Modules are shown, providing details of the RF distribution network and the intra-module focusing section with beam diagnostics.

RF correction cavities and a pulse compression cavity of the BOC type (barrel open cavity) provide the necessary shaping to the RF pulse. In the beam line, two quadrupole magnets, an H+V corrector and a BPM are installed between the two modules. At the linac exit, a sector valve isolates the accelerating section vacuum from the beam delivery system (BDS) vacuum. Right at the exit of the last accelerating

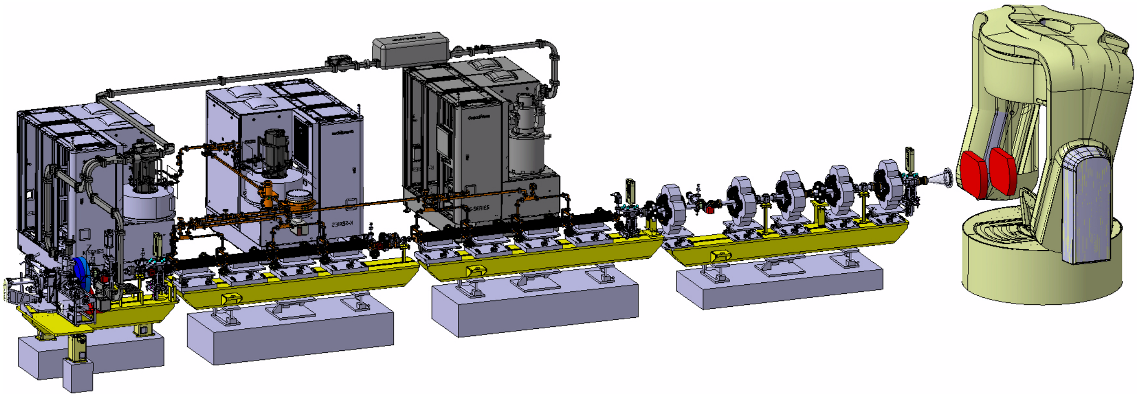

Figure 3.109: General view of the DEFT accelerator and beam delivery system. In this view, the model of the patient chair is also presented (image courtesy of Leo Cancer Care™).

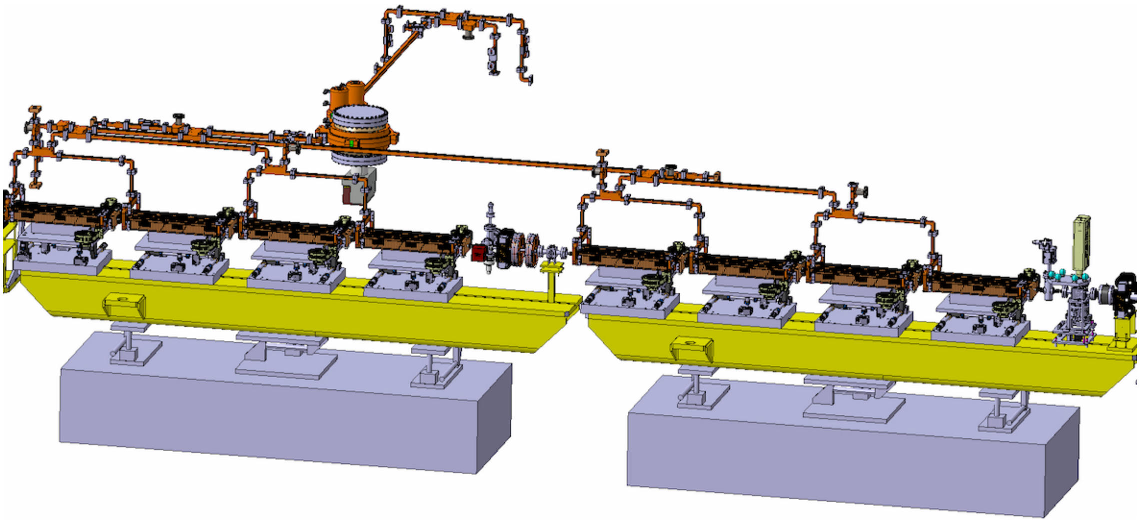

Figure 3.110: View of the two RF Modules, with intra-module focusing section and beam diagnostics.

section, a beam profile monitor provides the possibility to check the quality of the beam before it reaches the BDS.

The general support and alignment system was initially identified in order to provide an alignment precision better than ± 0.1 mm. All accelerating structure and beam line elements are supported by long girders, which can be aligned by means of universal alignment platforms (UAP) [38]. Critical components, like accelerating structures and BDS quadrupoles, are also individually supported and aligned by UAPs, while other components, like small quadrupoles and BPMs, adopt more conventional stands. A preliminary view of the two RF modules is provided in Fig. 3.110. Beam dynamics error studies could confirm that this alignment strategy is adequate and allows for achieving the required alignment tolerances.

A detailed view of the BDS sector is provided in Fig. 3.111. The two red boxes in front of the patient's chair represent the two positions of the beam collimator.

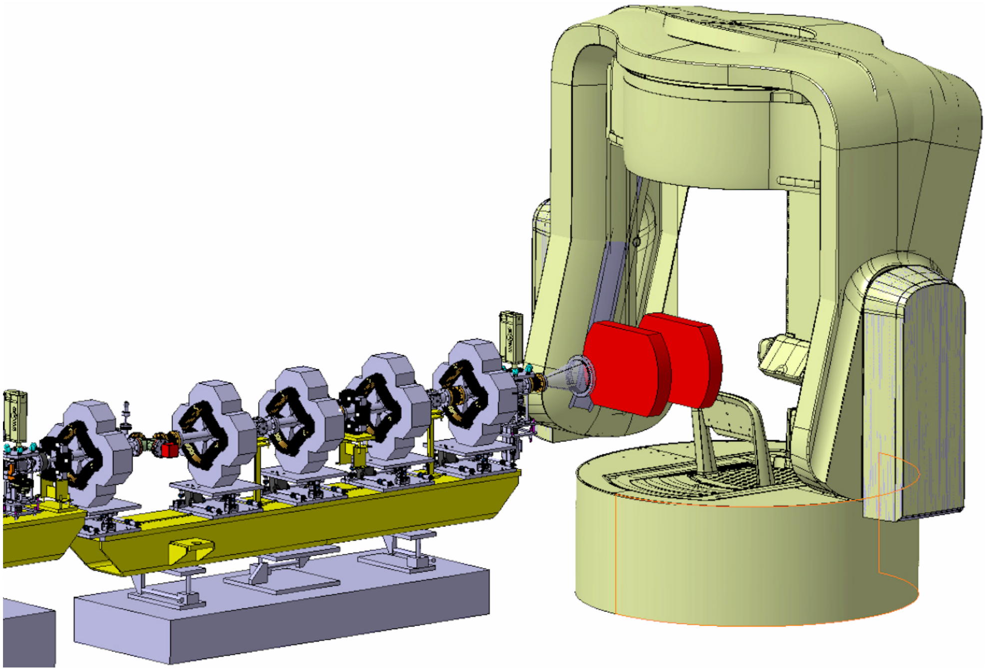

Figure 3.111: View of the DEFT BDS sector, the two red boxes materialize the limits of the collimator position. The model of the chair is also visible, with the scanner (image courtesy of Leo Cancer Care™).

9.3 The building and the technical infrastructure

The facility has been designed to fit into the limited space that can be made available by an existing hospital, in this case, the CHUV of Lausanne. Additional requirements that were considered are the possibility of a direct connection between the facility and the hospital and the need to keep the new building under the road level, to ensure free access to the hospital.

Figure 3.112 visualizes the site constraints that were assigned to the design. The existing CHUV main entrance is on the right, while the Children's Hospital is shown on the top-left side of the picture. The access to the existing Radio-Oncology Department, on the right side in grey, is visible.

Specific simulations were performed with the beam energy of 140 MeV and the single beamline configuration by the Radiation Protection Team. This was done, in particular, to assess the possible radiation load in the area occupied by klystron modulators and associated electronics, with respect to their capability to operate reliably in such conditions. The thermal neutron fluence for one year of irradiation with $1.3\times10^{17}\,e^-$ is shown in Fig. 3.113.

A view of the layout for the accelerator room, the klystron room and the patient treatment area for the single beamline configuration is shown in Fig. 3.114.

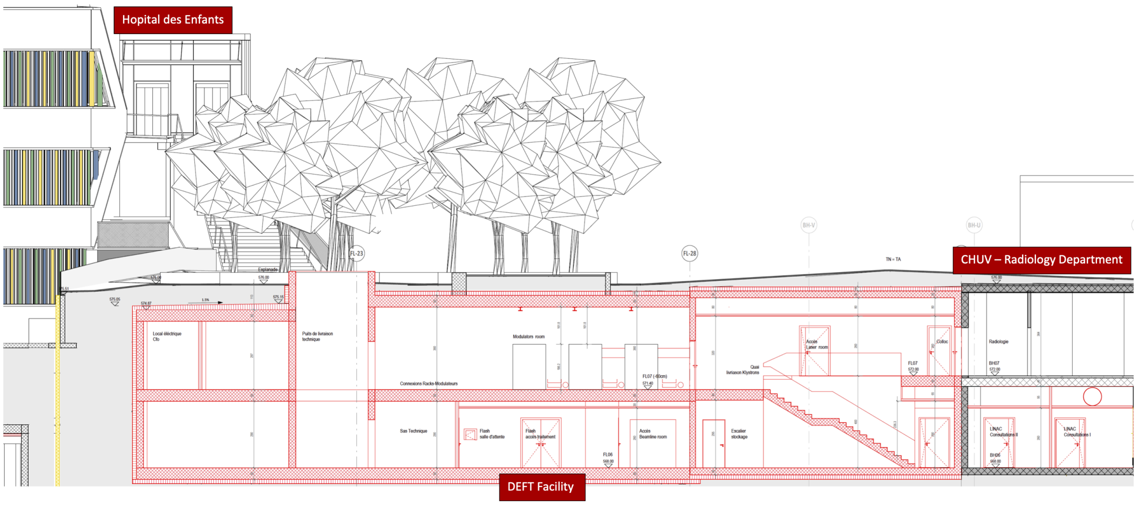

Figure 3.112: The DEFT building. A side view of the facility showing the access to the existing CHUV areas of the Radiology and Radio-Oncology Departments - courtesy Ferrari Architects.

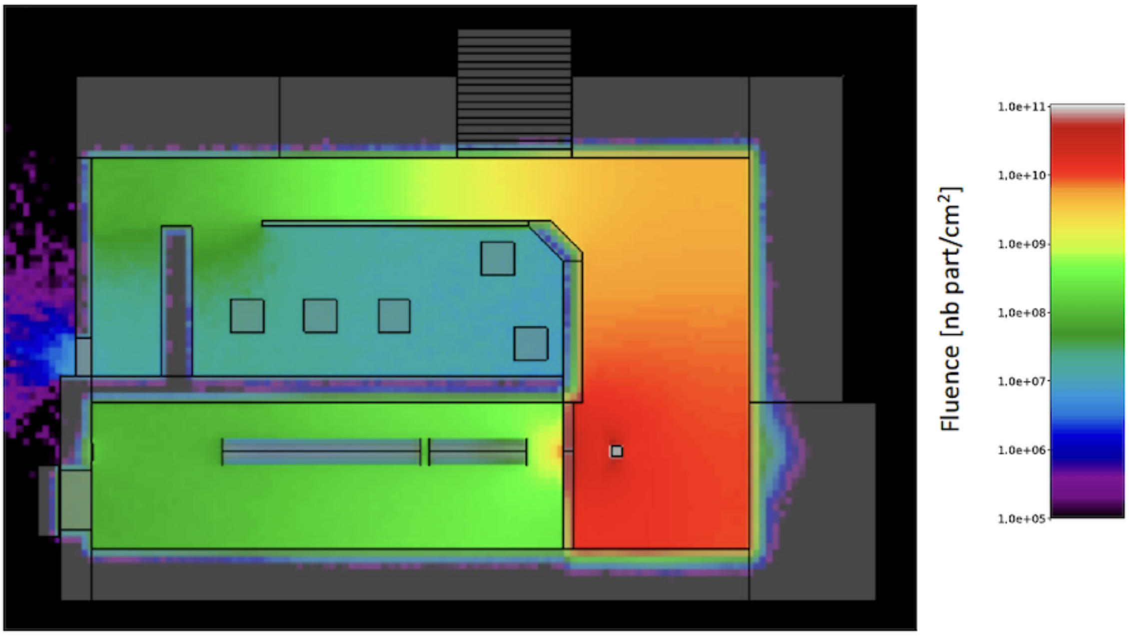

Figure 3.113: Thermal neutron fluence in the klystron room for the single beamline configuration and in the DEFT area as provided by L. Desorgher (IRA/CHUV).

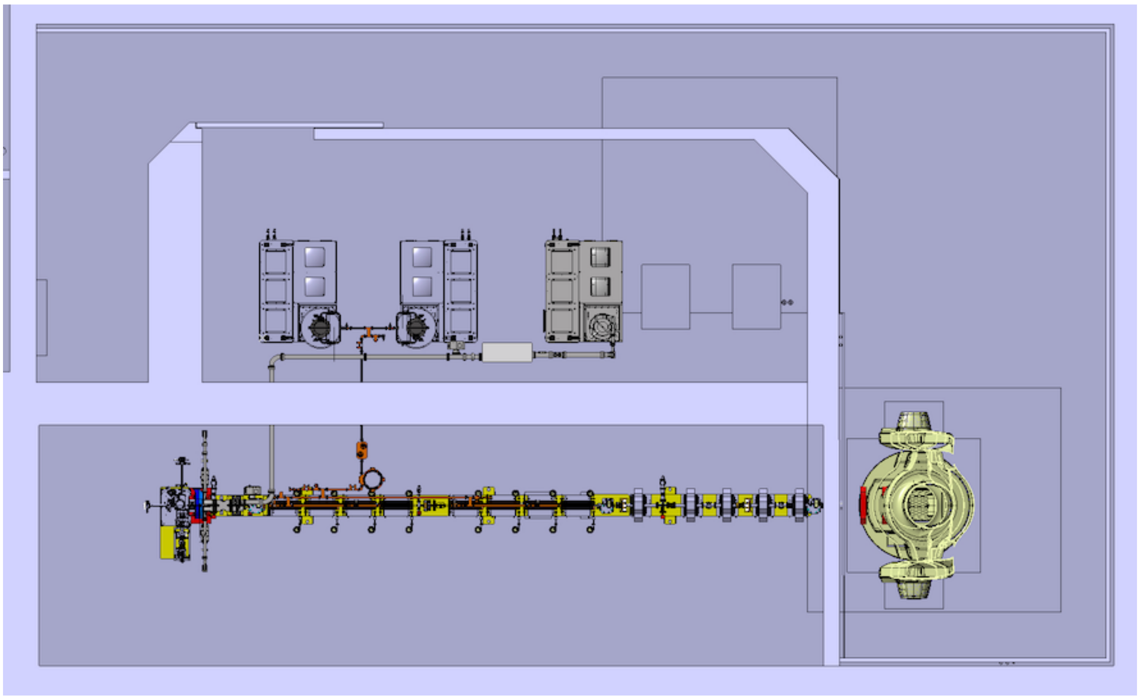

Figure 3.114: A view of the accelerator room, klystron room and patient treatment area from above.

Bibliography

[1] V. Favaudon et al. “Ultrahigh dose-rate FLASH irradiation increases the differential response between normal and tumor tissue in mice”. In: *Sci. Transl. Med.* 6 (2014), 245ra93. doi: 10.1126/scitranslmed.3008973.

[2] M.-C. Vozenin, J. Bourhis, and M. Durante. “Towards clinical translation of FLASH radiotherapy”. In: *Nat. Rev. Clin. Oncol.* 19 (2022), pp. 791–803. doi: 10.1038/s41571-022-00697-z.

[3] M. Aicheler et al. *A multi-TeV linear collider based on CLIC technology: CLIC conceptual design report*. Tech. rep. CERN-2012-007. SLAC-R-985. KEK-Report-2012-1. PSI-12-01. JAI-2012-001. Geneva: CERN, 2012. doi: 10.5170/CERN-2012-007.

[4] CompactLight Collaboration. *CompactLight project*. `https://www.compactlight.eu/Main/HomePage`. Last accessed 18 Sep. 2025.

[5] P. Craievich et al. “Status of the Polarix-TDS Project”. In: *9th International Particle Accelerator Conference (IPAC 2018)*. CERN-ACC-2018-157. 2018, pp. 3808–3811. doi: 10.18429/JACoW-IPAC2018-THPAL068.

[6] Andrzej Wolski. *Beam Dynamics in High Energy Particle Accelerators*. London: Imperial College Press / World Scientific, 2014. ISBN: 978-1-78326-277-9. doi: 10.1142/p899.

[7] A. Latina. *RF-track reference manual*. Version 2.5. June 2020. doi: 10.5281/zenodo.4580369.

[8] A. Chao et al. *Handbook of accelerator physics and engineering; 2nd ed.* Singapore: World Scientific, 2013. doi: 10.1142/8543.

[9] O. Mete et al. “Production of long bunch trains with 4.5 μC total charge using a photoinjector”. In: *Phys. Rev. ST Accel. Beams* 15 (2012), p. 022803. doi: 10.1103/PhysRevSTAB.15.022803.

[10] E. Chevallay et al. “PHIN photo-injector as the CLIC drive beam source”. In: *J. Phys.: Conf. Ser.* 347 (2012), p. 012036. doi: 10.1088/1742-6596/347/1/012036.

[11] E. Chevallay. “Production of a high current electron beam with caesium telluride photocathodes”. In: *CTF3 Note 20* (2000). doi: 10.17181/CERN.36SJ.RTBM.

[12] C. Heßler. “Study of the performance of caesium telluride cathodes in the PHIN RF photoinjector using long pulse trains”. In: *7th International Particle Accelerator Conference (IPAC 2016)*. 2016, pp. 3960–3963. doi: 10.18429/JACoW-IPAC2016-THPOW015.

[13] E. Chevallay. *Experimental Results at the CERN Photoemission Laboratory with co-deposition photocathodes in the frame of the CLIC studies*. Tech. rep. Internal Note CTF3-Note-2012-104. CERN, 2012. doi: 10.17181/CERN.FP2J.FYI7.

[14] S. Schreiber et al. “Update on the lifetime of caesium telluride photocathodes operated at FLASH”. In: *38th International Free-Electron Laser Conference*. 2018, pp. 407–410. doi: 10.18429/JACoW-FEL2017-WEP003.

[15] S. Lederer et al. “Update on the photocathode lifetime at FLASH and European XFEL”. In: *39th International Free Electron Laser Conference*. 2019, pp. 427–429. doi: 10.18429/JACoW-FEL2019-WEP047.

[16] E. Prat et al. “Measurements of copper and cesium telluride cathodes in a radio-frequency photoinjector”. In: *Phys. Rev. ST Accel. Beams* 18 (2015), p. 043401. doi: 10.1103/PhysRevSTAB.18.043401.

[17] F. Zhou et al. “Commissioning of the SLAC Linac Coherent Light Source II electron source”. In: *Phys. Rev. Accel. Beams* 24 (7 July 2021), p. 073401. doi: 10.1103/PhysRevAccelBeams.24.073401.

[18] E. Wisniewski et al. “Caesium telluride photocathode performance in the AWA high-charge high-gradient drive gun”. In: *6th International Particle Accelerator Conference*. 2015, pp. 3283–3285. doi: 10.18429/JACoW-IPAC2015-WEPTY013.

[19] N. Terunuma et al. “Improvement of an S-band RF gun with a Cs2Te photocathode for the KEK-ATF”. In: *Nucl. Instrum. Meth. A* 613 (2010), pp. 1–8. doi: https://doi.org/10.1016/j.nima.2009.10.151.

[20] V. Fedosseev et al. “Generation and delivery of an ultraviolet laser beam for the RF-photoinjector of the AWAKE electron beam”. In: *10th International Particle Accelerator Conference (IPAC 2019)*. 2019, pp. 3709–3712. doi: 10.18429/JACoW-IPAC2019-THPGW054.

[21] C. Heßler. “Status of the polarized electron gun at the S-DALINAC”. In: *10th European Particle Accelerator Conference (EPAC 06)*. 2006, pp. 3173–3175. URL: `https://proceedings.jacow.org/e06/PAPERS/THPCH161.pdf`.

[22] M. Martinez-Calderon et al. “Fabrication and rejuvenation of high quantum efficiency caesium telluride photocathodes for high brightness and high average current photoinjectors”. In: *Phys. Rev. Accel. Beams* 27 (2024), p. 023401. doi: 10.1103/PhysRevAccelBeams.27.023401.

[23] E. Granados et al. *Capabilities and performance of the CLEAR facility photo-injector*. Tech. rep. CERN-OPEN-2020-002. Geneva: CERN, 2019. doi: 10.17181/CERN.KPD2.MM9H.

[24] L. Doolittle, H. Ma, and M.S. Champion. “Digital low-level RF control using non-IQ Sampling”. In: *Proc. of Linear Accelerator Conference (LINAC6), Knoxville, Tennessee, USA, August 2006* (Knoxville, Tennessee, USA). `https://accelconf.web.cern.ch/l06/PAPERS/THP004.pdf`. 2006, pp. 568–570.

[25] S. Pfeiffer et al. “LLRF control and synchronisation system for the ARES facility”. In: *12th International Particle Accelerator Conference (IPAC 2021)*. 2021, pp. 3347–3350. doi: 10.18429/JACoW-IPAC2021-WEPAB294.

[26] T. Berenc, T. Plawski, and D. Teytelman. *9th Low-Level RF Workshop (LLRF2019)*. 2019. doi: 10.48550/ARXIV.1909.06754.

[27] Bartosz Bielawski, Philippe Baudrenghien, and Robert Borner. “Development of LLRF for CERN’s Linear Accelerator 4”. In: *Low-Level Radio Frequency Workshop*. Sept. 2019. arXiv: `1909.12541 [physics.acc-ph]`.

[28] N. Catalán Lasheras et al. “Commissioning of XBOX-3: A very high capacity X-band test stand”. In: *28th International Linear Accelerator Conference (LINAC16)*. 2017, pp. 568–571. doi: 10.18429/JACoW-LINAC2016-TUPLR047.

[29] R. Pan et al. *Electro-optical bunch profile measurement at CTF3*. Tech. rep. CERN-ATS-2013-054. CLIC-Note-1015. CERN, May 2013, 3 p. doi: 10.17181/CERN.1KKC.SUU8.

[30] P. Arpaia et al. “Enhancing particle bunch-length measurements based on radio frequency deflector by the use of focusing elements”. In: *Sci. Rep.* 10 (2020), p. 11457. doi: 10.1038/s41598-020-67997-1.

[31] CERN. *CLEAR*. `https://home.cern/science/accelerators/clear`. Last accessed 18 Sep. 2025.

[32] BERGOZ Instrumentation. *ICT & BCM-IHR-E*. `https://www.bergoz.com/products/ict/`. Last accessed 19 Sep. 2025.

[33] M. Ady (contact person). *MOLFLOW+*. `https://molflow.docs.cern.ch/`. Last accessed 18 Sep. 2025.

[34] P. Chiggiato. *Outgassing properties of vacuum materials for particle accelerators*. June 2020. doi: 10.48550/arXiv.2006.07124. arXiv: `2006.07124 [physics]`.

[35] C. Benvenuti et al. “Vacuum properties of TiZrV non-evaporable getter films”. In: *Vacuum* 60 (2001), pp. 57–65. doi: 10.1016/S0042-207X(00)00246-3.

[36] S. Sgobba. *Vacuum for accelerators: Introduction to materials and properties*. June 2020. doi: 10.48550/arXiv.2006.02212. arXiv: `2006.02212 [physics]`.

[37] C. Rossi et al. “The deep electron FLASH therapy facility”. In: *32nd Linear Accelerator Conference (LINAC 2024)*. 2024, pp. 551–556. doi: 10.18429/JACoW-LINAC2024-WEYA002.

[38] M. Sosin et al. “Design and study of a 6 Degree-of-Freedom universal adjustment platform for HL-LHC components”. In: *International Particle Accelerator Conference, Melbourne*. 2019, pp. 3720–3722. doi: 10.18429/JACoW-IPAC2019-THPGW058.